# Spectro-spatial observations of galaxy clusters with *Planck* and CCAT-prime

Dissertation
zur
Erlangung des Doktorgrades (Dr. rer. nat.)
der
Mathematisch-Naturwissenschaftlichen Fakultät
der
Rheinischen Friedrich-Wilhelms-Universität Bonn

von
Jens Erler
aus
Simmerath

Bonn, September 2019

Die vorliegende Dissertation wurde mit Genehmigung der Mathematisch-Naturwissenschaftlichen Fakultät der Rheinischen Friedrich-Wilhelms-Universität Bonn angefertigt und ist über eine persistente URN elektronisch publiziert.
https://nbn-resolving.org/urn:nbn:de:hbz:5-58609

| | |
|---|---|
| 1. Gutachter: | Prof. Dr. Frank Bertoldi |
| 2. Gutachter: | Prof. Dr. Thomas H. Reiprich |
| Tag der Promotion: | 15.05.2020 |
| Erscheinungsjahr: | 2020 |

*If you want to go deeply into any subject, you need a lot of time, and in particular you need the privilege of wasting time. You need to experiment with unproductive paths, explore dead ends, make space for doubts and boredom, and allow little seeds of insight to slowly grow and blossom. If you cannot afford to waste time, you will never find the truth.*

— Yuval Noah Harari, *21 Lessons for the 21st Century*

## Abstract

The Sunyaev-Zeldovich (SZ) effect is a spectral distortion of the cosmic microwave background (CMB) caused by inverse Compton scattering of CMB photons by free electrons in the hot intracluster medium (ICM) of galaxy clusters. The last two decades have seen dramatic improvements in the quality of SZ data and the galaxy cluster sample size obtained through SZ observations. The obtained cluster samples are important probes for cosmological studies, which help to unravel the illusive nature of dark matter and dark energy, measure the masses of light relativistic particles, and more. The research presented in this work consists of three parts, focusing on observations of the thermal SZ (tSZ) effect of clusters with data from the *Planck* space telescope, the development of new techniques for the extraction of SZ images, and forecasts for the next-generation of SZ surveys.

The first part of this thesis is a detailed study of the average tSZ spectrum of 772 massive galaxy clusters observed with the *Planck*, IRAS, and *AKARI* space telescopes. Of particular interest for this study are distortions of the tSZ spectrum caused by special-relativistic effects that allow to measure the ICM temperature. The tSZ effect spectra are extracted from multifrequency images of clusters using matched filters (MFs), which allow for an optimal removal of contaminating astrophysical emission while only making assumptions on the spatial signature of the observed clusters. The extracted average spectrum clearly traces the characteristic shape of the tSZ spectrum and reveals the presence of an additional far-infrared (FIR) excess due to thermal emission from warm dust grains in and around the clusters. Relativistic distortions of the tSZ effect are measured at a significance of $2.2\sigma$, constraining the average SZ-measured ICM temperature of the cluster sample to $k_\mathrm{B}T_\mathrm{e} = 4.4^{+2.1}_{-2.0}\,\mathrm{keV}$. The analysis of a smaller sub-sample of clusters containing the hottest 100 objects delivered a measurement at a similar significance of $2.0\sigma$ and constrained the clusters' mean ICM temperature to $k_\mathrm{B}T_\mathrm{e} = 6.0^{+3.8}_{-2.9}\,\mathrm{keV}$. The observed FIR excess was well modelled by a modified blackbody spectrum, implying an average dust grain temperature $\approx 18\,\mathrm{K}$ in the rest-frame of the clusters.

The second part of this work presents an extension of the MF technique used in the first part. It is shown that the matched filter algorithm can be generalised to allow for the extraction or suppression of multiple components at the same time if the corresponding sources can also be approximated by spatial templates. Using simulated microwave data, the unbiased tSZ-photometry of clusters with central radio sources is demonstrated and the dependence of the noise level of the obtained maps on the spatial resolution of the telescope is explored. The new method is further exemplified using *Planck* observations of the Perseus galaxy cluster, which harbours a bright central radio source. The new technique, called constrained MF (CMF), is also applicable to X-ray data of galaxy clusters and could offer improved separation of galaxy clusters and active galactic nuclei, which is investigated using mock data for the recently launched eROSITA X-ray space telescope.

The third and final part of this work presents detailed forecasts for the expected galaxy cluster sample size and SZ-spectral constrains for future microwave surveys with the upcoming CCAT-prime telescope, which will perform a submillimeter survey of a large fraction of the sky from the summit of the Cerro Chajnantor at 5600 m above sea level. Using a self-developed pipeline for the generation of mock observations of the microwave sky and the MF techniques developed before, it is found that CCAT-prime will detect and characterise between 2000 and 10 000 galaxy clusters, depending on the assumed survey area and potential synergies with other microwave observatories. Furthermore, it is shown that CCAT-prime data will allow to perform measurements of the spectrum of the SZ effect of clusters in much greater detail than the ones obtained from *Planck*-data presented in the first part of this work.

# List of publications relevant to this thesis

Chapter 4 of this work is a reproduction of the article

- **Erler J.**, Basu K., Chluba J., Bertoldi F., 2018, *Planck's* view on the spectrum of the Sunyaev–Zeldovich effect, MNRAS, 476, 3360.

Author contributions: J.E. conducted the data reduction and analysis, while K.B., J.C., and F.B. provided supervision and contributed to the interpretation of the obtained results. The published article was largely written by J.E., with K.B. and J.C. providing parts of the discussion and conclusion. Valuable feedback on the manuscript was given by F.B..

Chapter 5 of this work is a reproduction of the article

- **Erler J.**, Ramos-Ceja M. E., Basu K., Bertoldi F., 2019, Introducing constrained matched filters for improved separation of point sources from galaxy clusters, MNRAS, 484, 1988.

Author contributions: J.E. derived, implemented, and explored the new constrained matched filtering techniques and prepared the open-source implementation PyMF. K.B. contributed ideas for plots that demonstrate the benefits of the new filtering techniques. M.E.R.C. provided eROSITA mock data and shared valuable insights into X-ray data reductions and source detection. The published article was written mostly by J.E. with contributions by M.E.R.C. to the X-ray sections and by K.B. to the discussion and conclusion. Feedback from F.B. helped to improve the quality of the manuscript.

The methods and tools developed in Chapter 6 were used to produce results presented in

- Stacey G. J., Aravena M., Basu K., Battaglia N., Beringue B., Bertoldi F., ... , **Erler J.** et al., 2018, CCAT-Prime: science with an ultra-widefield submillimeter observatory on Cerro Chajnantor, Proc. SPIE, 10700, 107001M,
- Aravena M., Austermann J., Basu K., Battaglia N., Beringue B., Bertoldi F., ... , **Erler J.** et al., 2019, The CCAT-Prime Submillimeter Observatory, arXiv:1909.02587,
- Basu K., **Erler J.**, Chluba J. et al., 2019, "SZ spectroscopy" in the coming decade: Galaxy cluster cosmology and astrophysics in the submillimeter, arXiv:1809.06446.

Contributions by J.E.: As a member of the CCAT-prime collaboration, J.E. participates in the development of the galaxy cluster science case for CCAT-prime and provided spectroscopic forecasts for the former two articles. The latter article is an outlook on spectroscopic observations of the SZ effect beyond CCAT-prime and contains several forecasts and figures provided by J.E., which have been created using the techniques presented in Chapter 6.

# Additional publications

### Articles by the CCAT-prime Collaboration

- Parshley S. C., Niemack M., Hills R., Dicker S. R., Dünner R., **Erler J.** et al., 2018, The optical design of the six-meter CCAT-prime and Simons Observatory telescopes, Proc. SPIE, 10700, 1070041.
- Parshley S. C., Kronshage J., Blair J., Herter T., Nolta M., Stacey G. J., ... , **Erler J.** et al., 2018, CCAT-prime: a novel telescope for sub-millimeter astronomy, Proc. SPIE, 10700, 107005X.
- Vavagiakis E. M., Ahmed Z., Ali A., Basu K., Battaglia N., Bertoldi F., ... , **Erler J.** et al., 2018, Prime-Cam: A first-light instrument for the CCAT-prime telescope, Proc. SPIE, 10708, 107081U.

Contributions by J.E.: J.E. has made contributions to the development of the galaxy cluster science case for CCAT-prime and provided feedback on the manuscript of all three articles.

### Works on galaxy cluster radio emission and shock waves

- **Erler J.**, Basu K., Trasatti M., Klein U., Bertoldi F., 2015, Evidence for a pressure discontinuity at the position of the Coma relic from *Planck* Sunyaev–Zel'dovich effect data, MNRAS, 447(3), 2497–2502.

  Contributions by J.E.: Published master's thesis results. J.E. carried out all data analyses presented in the article and wrote parts of the manuscript.

- Basu K. Vazza F., **Erler J.**, Sommer M., 2016, The impact of the SZ effect on cm-wavelength (1-30 GHz) observations of galaxy cluster radio relics, A&A, 591, A143.

  Contributions by J.E.: J.E. provided some numerical tools for the modelling and simulations of shock waves in SZ data and assisted in the creation of the manuscript.

- Basu K., Sommer M., **Erler J.**, Eckert D., Vazza F., Magnelli B., Bertoldi F & Tozzi P., 2016, ALMA-SZ Detection of a Galaxy Cluster Merger Shock at Half the Age of the Universe, ApJ, 829, L23.

  Contributions by J.E.: Most calculations for the successful ALMA proposal, which led to the observations presented in the article, were carried out by J.E.. After the data were collected, J.E. provided some numerical tools for the data analysis and helped with the creation of figures and the manuscript.

- Basu K., Sommer M., **Erler J.**, Eckert D., Vazza F., Magnelli B., Bertoldi F & Tozzi P., 2016, First ALMA Detection of a Galaxy Cluster Merger Shock, The Messenger, 166, 53.

  Contributions by J.E.: Abridged version of the previous article with identical contributions by J.E..

- Basu K., Sommer M., **Erler J.**, Eckert D., Vazza F., Magnelli M., Bertoldi F. & Tozzi P., 2016, Galaxy Cluster Outskirts from the Thermal SZ and Non-Thermal Synchrotron Link, Galaxies, 4, 73.

  Contributions by J.E.: J.E. provided some numerical tools for the modelling and simulations of shock waves in SZ data and assisted in the creation of the manuscript.

### Other works

- Basu K., Remazeilles M., Melin J. B., Alonso D., Bartlett J. G., Battaglia N., ... , **Erler J.** et al., 2019, A Space Mission to Map the Entire Observable Universe using the CMB as a Backlight, arXiv:1909.01592.

  Contributions by J.E.: J.E. provided two figures and assisted in the creation of the manuscript.

- Delabrouille J., Abitbol M. H., Aghanim A., Ali-Haimoud Y., Alonso D., Alvarez M., ... , **Erler J.** et al., 2019, Microwave Spectro-Polarimetry of Matter and Radiation across Space and Time, arXiv:1909.01591.

  Contributions by J.E.: J.E. provided feedback on the manuscript.

- Battaglia N., Hill J. C., Amodeo S., Bartlett J. G., Basu K., **Erler J.** et al., 2019, Probing Feedback in Galaxy Formation with Millimeter-wave Observations, Astro2020 white paper, arXiv:1903.04647.

  Contributions by J.E.: J.E. provided feedback on the manuscript.

- **Erler J.**, Unruh S., 2017, Der Bulletcluster, *Astronomie+Raumfahrt*. (Outreach article)

  Contributions by J.E.: J.E. wrote half of the article.

- Buddendiek A., Schrabbrack T., Greer H.,Hoekstra H., Sommer M., Eifler T., Erben T., **Erler J.** et al., 2015, Optical and Sunyaev–Zel'dovich observations of a new sample of distant rich galaxy clusters in the ROSAT All Sky, MNRAS, 450(4), 4248–4276.

  Contributions by J.E.: J.E. provided *Planck* SZ-maps for all galaxy clusters that were observed with CARMA. The ILC method used for the extraction of the images was described by J.E. in a brief appendix.

# Contents

CHAPTER 1

# Introduction

## 1.1 The basics of modern physical cosmology

Throughout the history of mankind, our picture of the Universe and our place in in has steadily evolved. With the rapid technological and theoretical progress during the 20$^{\text{th}}$ and early 21$^{\text{st}}$ century the discipline of cosmology was transformed from a field driven by myths and religion a to physical science firmly backed by observational evidence. Today, cosmology is defined as the branch of physics that aims to describe the origin and evolution of the Universe as a whole.

At the cornerstone of modern cosmology lies the cosmological principle, which assumes that the Universe is homogeneous and isotropic on large scales. In this context, isotropy states that properties of the distant universe, e.g. the distribution of galaxies, are the same in all directions of the sky. On the other hand, homogeneity means that the energy density of the Universe is constant when averaged over large scales. The cosmological principle therefore implies that we do not occupy a special place in the Universe, as opposed to common believes throughout history. When applied to Einstein's field equations of general relativity, an exact solution, which was derived independently by Alexander Friedmann, Georges Lemaître, Howard P. Robertson, and Arthur Geoffrey Walker, can be found (e.g. Robertson, 1935; Walker, 1935)

$$\mathrm{d}s^2 = \mathrm{c}^2\mathrm{d}t^2 - a^2(t)\left[\mathrm{d}D_{\mathrm{C}}^2 + D_{\mathrm{M}}^2(D_{\mathrm{C}})(\mathrm{d}\theta^2 + \sin(\theta)^2\mathrm{d}\phi^2)\right], \tag{1.1}$$

where c is the speed of light, $t$ is the cosmic time, $a(t) = \frac{r(t)}{r(t_0)}$ is the cosmic scale factor that is normalised to be 1 at the current point in time $t_0$, $\theta$ and $\phi$ are the angular coordinates on a unit sphere, $D_{\mathrm{C}}$ is the radial comoving distance, and $D_{\mathrm{M}}$ is the transverse comoving distance, a concept that is introduced later in Section 1.1.3. This solution is known as the *Friedmann–Lemaître–Robertson–Walker* (FLRW) metric and provides the theoretical foundation for the current standard model of cosmology, which is referred to as $\Lambda$ *cold dark matter* ($\Lambda$CDM).

A fundamental aspect of cosmological models build from the FLRW metric is an expanding or contracting spacetime. First observational evidence for an expanding Universe was obtained by Vesto Slipher, who found the light of most nearby galaxies to be redshifted, which was subsequently interpreted by Edwin Hubble as a receding motion relative to the Milky Way with the velocity $v = z\mathrm{c}$,

where

$$z = \frac{\lambda_{\text{obs.}} - \lambda_{\text{em.}}}{\lambda_{\text{em.}}} \tag{1.2}$$

is the measured redshift that is obtained from the observed wavelength $\lambda_{\text{obs.}}$ and the one emitted in the rest-frame of the galaxies $\lambda_{\text{em.}}$. Combining measurements of the redshifts of other galaxies with distances estimated via the period of variations in the intrinsic luminosity of rare stars known as Cepheid variables revealed that the recessional velocity of galaxies increases with their distance in a linear way, a relationship that today is known as Hubble's law

$$z\,\mathrm{c} = H_0\, D_{\mathrm{C}}, \tag{1.3}$$

where $H_0$ is called the local Hubble constant. These observations lead to the conclusion that the Universe is expanding, i.e. the space between galaxies is constantly growing. In this picture, the observed redshift of other galaxies is a direct consequence of this expansion which stretches the wavelength of light and is related to the cosmic scale factor via

$$1 + z = \frac{1}{a}. \tag{1.4}$$

The (current) rate of this expansion is given by the Hubble constant and is commonly expressed as $H_0 = h\,100\,\mathrm{km\,s^{-1}\,Mpc^{-1}}$ with $h \approx 0.7$. The Hubble constant $H_0$ represents the value of the generalised Hubble parameter $H(t)$ at the current point in cosmic time $t_0$, which is connected to the cosmic scale factor by

$$H(t) = \frac{\dot{a}(t)}{a(t)}. \tag{1.5}$$

The evolution of the cosmic scale factor, and therefore the Hubble parameter, is described by the first and second Friedmann equations, which are given by

$$H(t)^2 = \frac{\dot{a}(t)^2}{a(t)^2} = \frac{8\pi\mathrm{G}}{3}\rho(t) - \frac{K\mathrm{c}^2}{a(t)^2}\left(+\frac{\Lambda\mathrm{c}^2}{3}\right), \tag{1.6}$$

$$\frac{\ddot{a}(t)}{a(t)} = -\frac{4\pi\mathrm{G}}{3}\left[\rho(t) + \frac{3p(t)}{\mathrm{c}^2}\right]\left(+\frac{\Lambda\mathrm{c}^2}{3}\right), \tag{1.7}$$

where G is the gravitational constant, $\rho(t)$ is the average matter and energy density, $p(t)$ is the pressure, $\Lambda$ is the cosmological constant and $K$ is the curvature parameter that can take on the values $+1$, 0, or $-1$ for positively curved, flat, and negatively curved space, respectively. The first Friedmann equation is derived from the law of energy conservation and indicates that the curvature of the Universe is closely linked to its total energy density. The special case of a flat universe with $K = 0$ requires a precise value for the average density, known as the critical density

$$\rho_{\text{crit.}}(t) = \frac{3H(t)^2}{8\pi G}. \tag{1.8}$$

Since the critical density depends on the value of the time-dependent Hubble parameter, its value changes with cosmic time as well. Using the approximate value $h = 0.7$ of today's Hubble constant, we find the critical density to be $\approx 9.2 \times 10^{-27}\,\mathrm{kg\,m^{-3}}$, or alternatively $1.4 \times 10^{11}\,\mathrm{M_\odot\,Mpc^{-3}}$. A

universe that exceeds the critical density inevitably has a closed geometry, while a universe with a lower average density has an open geometry. However, note that a perfectly flat universe remains flat indefinitely.

The second Friedmann equation can be derived from the first one together with the fluid equation

$$\dot{p}(t) + 3\frac{\dot{a}(t)}{a(t)}\left(\rho(t) + \frac{p(t)}{c^2}\right) = 0. \tag{1.9}$$

The dynamics of the expansion of the Universe depend on its composition and the properties of the individual components. The next section gives a brief overview on the most important constituents of our Universe.

### 1.1.1 The composition of the Universe

When looking at the composition of the Universe it is useful to compare the energy density $\rho_i(t)$ of each individual component $i$ to the critical density and define unitless density parameters

$$\Omega_{i,0} = \frac{\rho_i(t_0)}{\rho_{\text{crit.}}(t_0)}. \tag{1.10}$$

In general, the values of these density parameters are time-dependent (see left-hand panel of Fig. 1.2). The values provided here refer explicitly to the densities at $t = t_0$. The total energy density of the Universe is subsequently defined as

$$\Omega_0 = \sum_i \Omega_{i,0}. \tag{1.11}$$

The most recent measurements find the total energy density of the Universe to be very close to unity with $\Omega_0 = 0.9993 \pm 0.0019$ (Planck Collaboration, 2018b), suggesting that we live in a spatially flat universe.

Each component of the Universe can be characterised by an *equation of state* (EOS), which relates pressure and density

$$p = wc^2\rho, \tag{1.12}$$

where $w$ is the dimensionless EOS parameter. Plugging equation (1.12) into (1.9) leads to the differential equation

$$\frac{\dot{\rho}}{\rho} = -3\frac{\dot{a}}{a}(1 + w), \tag{1.13}$$

which can be solved by

$$\rho = \rho_0\, a^{-3(1+w)}. \tag{1.14}$$

Equation (1.14) allows to characterise the evolution of the energy density of a given component with cosmic expansion, provided the EOS parameter is known and constant in time.

#### Baryonic matter

This summary of the constituents of the known Universe starts with the components we are most familiar with, ordinary matter that is made from atoms or non-relativistic charged particles and makes up all the luminous stars and gas clouds we see with our telescopes. Cosmologists refer to this as

baryonic matter and its distinct feature is that it takes part in electromagnetic interactions that are mediated by photons. Observations indicate that baryons make up approximately 5% of the total energy density of the Universe with $\Omega_{\mathrm{b},0} = 0.0489 \pm 0.0003$ (Planck Collaboration, 2018b). Since we restrict the definition of baryons to non-relativistic particles they can be considered pressureless, implying $w = 0$ and therefore

$$\rho_{\mathrm{b}}(t) = \rho_{\mathrm{b},0}\, a^{-3}(t). \tag{1.15}$$

The change in baryon density is thus directly proportional to the change in cosmic volume.

The baryonic matter we observe as galaxies only makes up a fraction of the total baryon density. Observations of the absorption spectrum of high-redshift quasars suggest ~two times more baryons than we observe in the local Universe. These missing baryons are thought to reside in a warm phase in the space between galaxies, which is difficult to observe.

#### Dark matter

The existence of additional matter that can not be observed directly but indirecly through its gravitational interactions with baryonic matter was first proposed by Fritz Zwicky in 1933 (Zwicky, 1933). Today, the gravitational impact of dark matter is observed on scales ranging from stellar orbits in galaxies to the large-scale structure of the Universe, out to the highest observable redshifts. Recent observations find roughly five times more dark matter than baryons with $\Omega_{\mathrm{m},0} = \Omega_{\mathrm{dm},0} + \Omega_{\mathrm{b},0} = 0.311 \pm 0.006$ (Planck Collaboration, 2018b). In regards to cosmic expansion, dark matter behaves like a pressureless fluid with $w = 0$ and

$$\rho_{\mathrm{dm}}(t) = \rho_{\mathrm{dm},0}\, a^{-3}(t). \tag{1.16}$$

Dark matter is widely believed to consist of currently unknown *weakly interacting massive particles* (WIMPs, see Bertone et al. 2005 for an overview over particle candidates). If dark matter particles are massive, they are classified as cold dark matter, while light particles are referred to as hot dark matter. An example of hot dark matter are neutrinos at the current epoch of cosmic time. Cold and hot dark matter differ in the way they form structures, as is explained in detail in Section 1.4.1. Besides their gravitational influence, many candidates for these particles, like the lightest stable particle predicted by supersymmetry, the neutralino, are postulated to also interact via the weak nuclear force.

Currently, several long-term experiments are being conducted that aim at a direct detection of dark matter particles by observing rare collisions with regular atoms in deep underground detectors, which are shielded from cosmic rays and ambient nuclear radiation (e.g. Edelweiss; Armengaud et al. 2019, XENON1T; Aprile et al. 2017), while the upgraded High-Luminosity Large Hadron Collider (HL-LHC) will attempt to generate dark matter particles in high-energy Proton-Proton collisions in the time after 2026. A great review on the status of direct detection of WIMPs is provided by Schumann (2019). In addition to the direct detection of dark matter in laboratories, X-ray and gamma-ray telescopes are used in the search for the spectral signature of dark matter self-annihilation towards large concentrations of dark matter in the cores of galaxies and clusters of galaxies.

Besides unknown particles, there are several astrophysical candidates for dark matter, most prominently primordial black holes and brown dwarfs. However, microlensing studies suggest that these *massive compact halo objects* (MACHOs) at most represent a small fraction of the total amount of dark matter (Alcock et al., 2000; Tisserand et al., 2007; Niikura et al., 2019).

A number of observations that imply the existence of dark matter are alternatively explained by modified laws of gravity, e.g. through *Modified Newtonian Dynamics* (MOND, Milgrom, 1983).

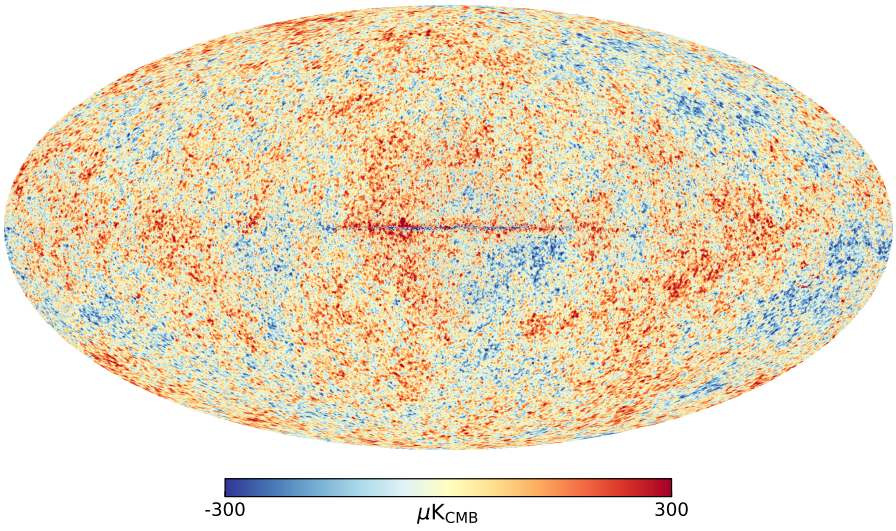


Figure 1.1: Mollweide projection of the temperature anisotropies of the cosmic microwave background radiation in Galactic coordinates. The map has been reconstructed using an ILC algorithm (Bennett et al. 2003; see Section 2.3 for details) from data gathered by the *Planck* satellite (second data release; Planck Collaboration 2016a). Some Galactic foreground residuals from the brightest parts of the Galactic disc close to the centre of the Milky Way can be seen in the map. Those regions are masked for the cosmological analysis and usually replaced by constrained random realisations for press release images.

However, since the year 2000 a number of observations like the dynamics of colliding galaxy clusters (Angus et al., 2006) or most recently the propagation velocity of gravitational waves through space (Boran et al., 2018), as well as theoretical inconsistencies (e.g. Scott et al., 2001) have strongly disfavoured MOND, or require the addition of dark matter to it.

#### Radiation

Radiation consists of all particles with zero rest mass, most importantly photons, as well as massive particles with relativistic energies. Throughout early cosmic history, the number or relativistic species therefore changes as the Universe cools. Depending on their still unknown rest mass, the lightest neutrino family might stay relativistic until the current epoch. Radiation is a pressurised fluid with $p_\mathrm{r} = \rho_\mathrm{r} c^2/3$, resulting in $w = 1/3$. The radiation energy density is therefore given by

$$\rho_\mathrm{r}(t) = \rho_{\mathrm{r},0}\, a^{-4}(t). \tag{1.17}$$

The radiation density in the current Universe is mostly provided by the cosmic microwave background (CMB, see Fig. 1.1) with $\Omega_{\mathrm{r},0} \approx 10^{-5}$ and has a neglectable impact on the current dynamics of cosmic expansion. However, the early Universe at $z \gtrsim 3000$ was dominated by radiation.

### Neutrinos

In the standard model of particle physics, neutrinos are massless particles and would thus be designated as radiation in cosmology. However, the observation of neutrino oscillations requires neutrinos to have a non-zero rest mass, a discovery that was awarded with the Nobel Price in Physics in 2015 (Ahmad et al., 2001; Fukuda et al., 1998). Neutrinos of all types were produced in the early Universe in large amounts and, depending on their rest mass, could constitute a relevant fraction of the dark matter density. These primordial neutrinos form a neutrino background with a thermal energy distribution of a temperature that is slightly colder than the one of the CMB.

Observations of the CMB suggest that there are no more than three neutrino families with $N_{\mathrm{eff}} = 3.0 \pm 0.3$ (Planck Collaboration, 2018b), consistent with the Standard Model of particle physics. Although none of the individual neutrino masses has been measured directly, cosmological observations provide the best constraints on the upper limit of the sum of neutrino masses (e.g. Lesgourgues & Pastor, 2014; Lattanzi & Gerbino, 2017) with $\sum m_\nu < 0.12\,\mathrm{eV}$ at 95% confidence level (Planck Collaboration, 2018b). At the same time, neutrino oszillation experiments imply a lower bound of $\sum m_\nu > 0.06\,\mathrm{eV}$, suggesting the actual value to be $O(0.1\,\mathrm{eV})$. At the current epoch, at least two neutrino families are non-relativistic and contribute to warm dark matter. At early times, neutrinos contribute to the energy density of radiation and are crucial for the production of helium in the early Universe.

### Dark energy

Dark energy is a term coined for the mysterious component that dominates the energy budget of our Universe, with $\Omega_{\Lambda,0} = 0.6889 \pm 0.0056$ (Planck Collaboration, 2018b), and drives its observed accelerated expansion. The cosmic acceleration was discovered independently by two research groups who studied the cosmic expansion history using the distance-redshift relation of Type Ia supernovae with the intend of measuring the rate of deceleration, which was the standard paradigm up to that point in time (Riess et al., 1998; Perlmutter et al., 1999).

From the second Friedmann equation, it can be shown that an accelerated expansion of space, i.e. $\ddot{a} > 0$, requires an energy component with negative pressure, which implies $w < -1/3$. In case the EOS parameter of dark energy has a value of $-1$, its energy density would be constant in time

$$\rho_{\mathrm{DE}}(t) = \rho_{\mathrm{DE},0} \quad \text{for } w = -1. \tag{1.18}$$

Dark energy could therefore be identified with a positive cosmological constant $\Lambda$ and its density parameter would be given by

$$\Omega_{\Lambda,0} = \frac{\rho_\Lambda}{\rho_{\mathrm{crit.}}(t_0)} = \frac{\Lambda\,\mathrm{c}^2}{3H_0^2}. \tag{1.19}$$

In contrast to the other components that make up the Cosmos, the EOS parameter of dark energy is not precisely known at the current point in time. However, a wide range of cosmological probes are consistent with a cosmological constant (see right-hand panel of Fig.1.3). Some models also propose a time evolution of the state parameter of dark energy, which is why its current value is sometimes referred to as $w_0$.

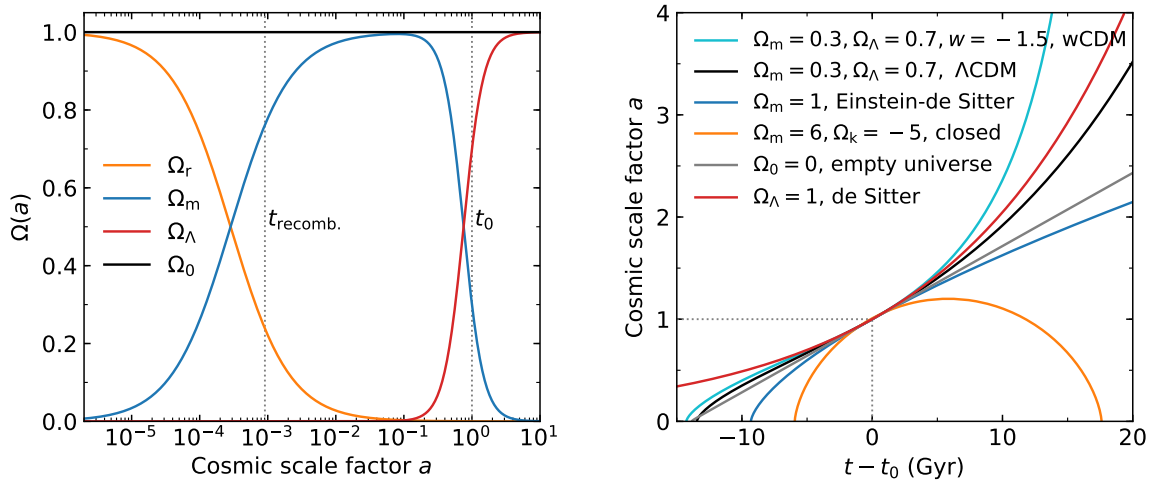


Figure 1.2: **Left-hand panel:** Evolution of the composition of the Universe for a flat ΛCDM cosmology with $h = 0.7$ and $\Omega_{m,0} = 0.3$. Shortly after the Big Bang, the Universe first entered a radiation dominated phase, followed by a matter dominated one and recently entered its current phase dominated by dark energy. The dotted lines mark the epoch of recombination at $z \approx 1100$ and the current point in time at $z = 0$. Note that the sum of all components, $\Omega_0$, remains constant for a flat universe. **Right-hand panel:** Evolution of the size of the Universe, described by the cosmic scale factor, as a function of cosmic time for a range of cosmological models build on the FLRW metric. Note that the predicted age of the Universe, given by the x-axis intercept, varies widely between models and can be compared e.g. to the age of the oldest known stars. The ultimate fate of the Universe in models without dark energy depends purely on the geometry of space, leading to a future collapse (closed), a stop of the expansion in the infinite future (flat), or eternal decelerating expansion (open). An empty universe on the other hand has an open geometry but will forever expand at a constant rate. Models that include dark energy, like the cosmological standard model ΛCDM, allow for a future eternal accelerated expansion and can even avoid a big bang in the past. If dark energy is not a cosmological constant and has an equation of state parameter $w$ that is smaller than $-1$, the Universe will grow to infinite size in a finite amount of time, leading to a scenario called the "Big Rip".

### 1.1.2 The standard model of cosmology

The current standard model of cosmology is referred to as ΛCDM, where Λ stands for a cosmological constant with a small positive value and CDM refers to cold dark matter, implying that the majority of dark matter is dynamically cold. The standard model assumes a flat universe and has a total of six free parameters, namely the Hubble constant $H_0$, the amount of baryons $\Omega_\mathrm{b}$, the amount of matter (including the aforementioned baryons) $\Omega_\mathrm{m}$, the optical depth at the epoch of reionisation $\tau$, the amplitude of the power spectrum $A_\mathrm{s}$ and the spectral index of the linear power spectrum $n_\mathrm{s}$. As can be seen from the Friedmann equations, not all of these parameters affect the expansion history of the Universe directly, but instead influence the formation of structures or the temperature fluctuations of the CMB. Modern cosmology therefore relies on a number of independent probes that provide estimates of the values of these six free parameters. An example of the combination of multiple cosmological probes is shown in Fig. 1.3.

Using the unitless density parameters defined in equation (1.10) the first Fiedmann equation can be

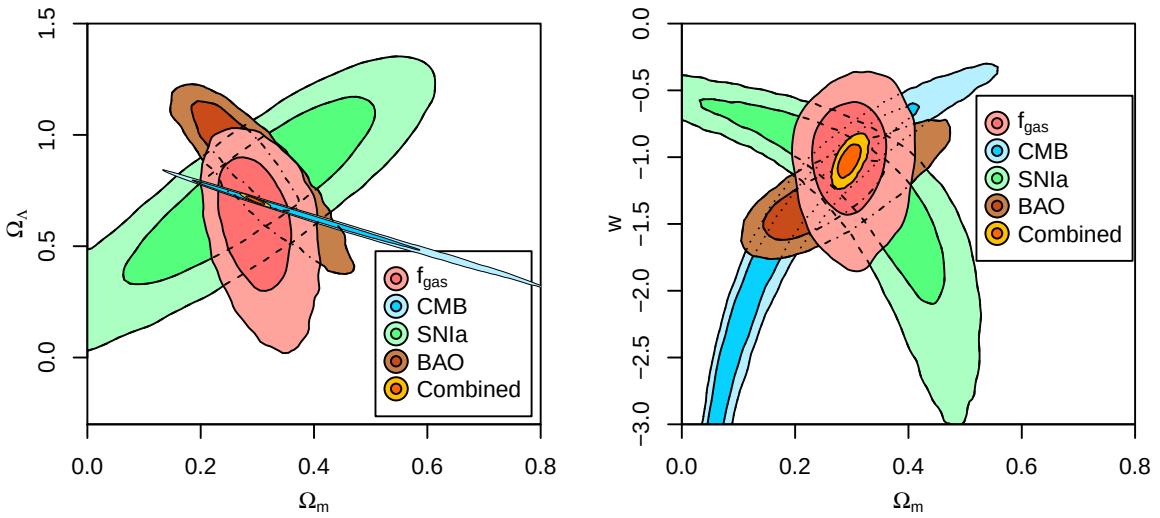


Figure 1.3: Constraints on properties of dark matter and dark energy by different cosmological probes. Each probe provides a different test for the ΛCMB model and the constraints are often complementary. The combined constraints suggest that we live in a universe that consists to ∼ 70% of dark energy and to ∼ 30% of a mixture of (mostly) dark matter and baryons. The constraints on the EOS parameter $w$ of dark energy are are consistent with a cosmological constant. The figures have been adopted from Mantz et al. (2014).

recast into

$$H^2(a) = \left(\frac{\dot{a}}{a}\right)^2 = H_0^2 \left(\frac{\Omega_{\mathrm{r},0}}{a^4} + \frac{\Omega_{\mathrm{m},0}}{a^3} + \Omega_{\Lambda,0} + \frac{1-\Omega_0}{a^2}\right), \tag{1.20}$$

which, assuming a flat universe and a neglectable radiation energy density at present times, is sometimes also written as $H(z) = H_0\, E(z)$, where

$$E(z) = \left(\Omega_{\mathrm{m},0}\,(1+z)^3 + \Omega_{\Lambda,0}\right)^{\frac{1}{2}} \tag{1.21}$$

is called the *cosmic evolution function*.

One inevitable consequence of the ΛCDM model and our best values for its parameters is that the Universe began with a hot big bang and has been expanding and cooling down ever since. The theory of the Big Bang has lead to a series of predictions like the helium mass fraction of primordial gas and the existence of the CMB. Although our current understanding of physics does not permit us to understand the first moments that followed the Big Bang, to this date there is no robust observational evidence that contradict it.

The postulation of a big bang suggests that the Universe has a finite age which can be computed via

$$t(a) = \int_0^a \frac{\mathrm{d}a}{a\,H(a)}. \tag{1.22}$$

The current age of the Universe $t_0$ is obtained for $a = 1$ and is found to be $13.787 \pm 0.020$ billion years (Planck Collaboration, 2018b).

While the beginning of the Universe is at least conceptually understood, its ultimate fate depends on the nature of dark energy. If dark energy indeed is just a cosmological constant and space is

geometrically flat, the Universe expands forever with the Hubble parameter approaching a constant value. This scenario is called the *Big Freeze* and predicts an empty and cold universe in the distant future. In case the dark energy equation of state parameter $w$ is smaller than $-1$ its energy density would increase with the expansion of space, leading to a scenario that is refereed to as the *Big Rip* during which the cosmic scale factor grows to infinity in a finite time, ripping even atoms apart (Caldwell et al., 2003). This objectively terrifying event could happen soon on cosmological time scales. For $w = -1.5$, the Big Rip would occur $\approx 21.7$ billion years from now, which is a short time span compared to the lifetime of the lowest-mass stars that are expected to live for more than a trillion years. A deceleration of cosmic expansion followed by a reversal that would lead to a collapse of the Universe, called a *Big Crunch*, has been excluded by observations. The evolution of the scale factor in each of these cases is illustrated in the right-hand panel of Fig. 1.2.

### 1.1.3 Distances in an expanding spacetime

The expansion history of the Universe can be reconstructed by measurements of the distance-redshift relation, extending on the original work by Slipher and Hubble. Measuring distances to Galactic and extragalactic sources is one of the key challenges in astronomy. The most common techniques rely either on the dimming of the observed flux $S$ of a sources with known intrinsic luminosity $L$ according to the inverse square of its distance:

$$D_{\mathrm{L}} = \sqrt{\frac{L}{4\pi S}}, \tag{1.23}$$

which is called the *luminosity distance*, or on comparing the intrinsic diameter $d$ of a distant object (e.g. in units of parsec) to its observed angular diameter $\theta$ (in radians)

$$D_{\mathrm{A}} = \frac{d}{\theta}, \tag{1.24}$$

which is referred to as the *angular diameter distance*. Both the luminosity distance and the angular diameter distance are connected to the *transverse comoving distance* $D_{\mathrm{M}}$ via the redshift of the source:

$$D_{\mathrm{L}}(z) = (1+z)\, D_{\mathrm{M}}(z), \tag{1.25}$$

$$D_{\mathrm{A}}(z) = \frac{D_{\mathrm{M}}(z)}{1+z} = \frac{D_{\mathrm{L}}(z)}{(1+z)^2}. \tag{1.26}$$

The value of the transverse comoving distance at a given redshift depends on the geometry of the space:

$$D_{\mathrm{M}}(z) = \begin{cases} \frac{D_{\mathrm{H}}}{\sqrt{\Omega_{\mathrm{k}}}} \sinh\left(\sqrt{\Omega_{\mathrm{k}}} \frac{D_{\mathrm{C}}(z)}{D_{\mathrm{H}}}\right) & \Omega_0 < 1 \\ D_{\mathrm{C}}(z) & \Omega_0 = 1 \\ \frac{D_{\mathrm{H}}}{\sqrt{|\Omega_{\mathrm{k}}|}} \sin\left(\sqrt{|\Omega_{\mathrm{k}}|} \frac{D_{\mathrm{C}}(z)}{D_{\mathrm{H}}}\right) & \Omega_0 > 1 \end{cases} \tag{1.27}$$

where $D_{\mathrm{H}} = \mathrm{c}/H_0$ is the Hubble radius and $D_{\mathrm{C}}$ is the *radial comoving distance*, which is defined as

$$D_{\mathrm{C}}(z) = D_{\mathrm{H}} \int_0^z \frac{\mathrm{d}z'}{E(z')}. \tag{1.28}$$

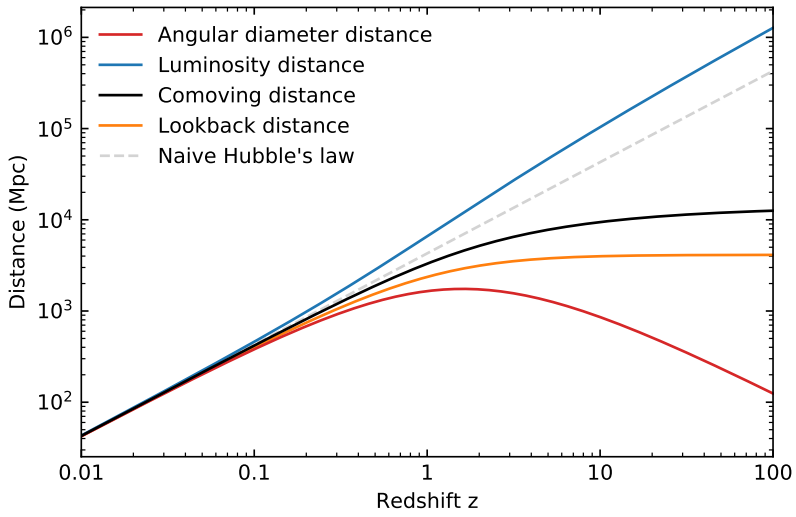


Figure 1.4: Comparison of the different cosmological distance measures as a function of redshift, computed for a flat ΛCDM cosmology with $h = 0.7$, $\Omega_{\mathrm{m},0} = 0.3$, $\Omega_{\Lambda,0} = 0.7$. For small redshifts, all distance measures are in agreement with each other. At high redshifts, the comoving distance converges towards the size of the observable Universe, while the luminosity distance diverges and the angular diameter distance starts to decrease after reaching a maximum value at $z \approx 1.5$. The lookback distance converges towards $t_0\, c$, where $t_0$ is the age of the Universe. Finally, the naive distance computed via Hubble's law, which assumes $H(z) = H_0$, diverges.

The integral in equation (1.28) has to be solved numerically for ΛCDM cosmologies. An additional but less commonly used distance measure is the *lookback distance*, which is simply defined as the *lookback time* to redshift $z$ multiplied with the speed of light:

$$D_{\mathrm{T}} = \mathrm{c}\,(t_0 - t(z)). \tag{1.29}$$

If space is static, all of these distance measures have the same value, except for the lookback distance, which is zero in that case. However, in an expanding space the numbers are no longer equal. For that reason, it is paramount to clarify what kind of distance measure is used when stating cosmological distances. Also note that objects at cosmological distances are separated from us not only in space but also vastly in time. If we could stop the expansion of space and travel towards a galaxy at $z = 1$ instantaneously to measure its distance with a giant ruler we would find an evolved galaxy, now roughly twice the age of the galaxy we saw though our telescope, and find the distance to be identical to its comoving distance of 3.3 Gpc. The distance of the galaxy at the time the light that we observe today was emitted is sometimes called the proper distance and is identical to the angular diameter distance of 1.65 Gpc. This gedankenexperiment illustrates that the angular diameter distance underestimates and the luminosity distance overestimates the current (comoving) distance of the galaxy. Fig. 1.4 shows the four distance measures introduced in this section, together with the naive estimate of the comoving distance obtained via Hubble's law, as functions of the redshift. An excellent introduction to cosmological distance measures is provided by Hogg (1999).

## 1.2 A brief overview of the thermal history of the Universe

While the previous sections summarised our understanding of the expansion of the Universe and its contents, we now summarise the most important events that occurred shortly after the Big Bang, when the Universe was hot and energetic. In the early Universe, radiation was in thermal equilibrium with matter particles. The expansion of the Universe preserves the blackbody spectrum of the CMB and change its temperature according to

$$T(a) = \frac{T_0}{a}, \tag{1.30}$$

where $T_0 = 2.7255\,\mathrm{K}$ is the CMB temperature we measure today. While the scale factor approaches 0 at the moment of the Big Bang, the temperature grows to infinity. At high temperatures, it is useful to compare the typical photon energy $k_\mathrm{B}T$ to the rest mass of particles. If the energy exceeds a particle's rest mass, particle - anti-particle pairs can be created, which can annihilate again and create a pair of photons. An example for this is the production/annihilation of electron-positron pairs at $k_\mathrm{B}T \gtrsim 1\,\mathrm{MeV}$:

$$\mathrm{e}^+\,\mathrm{e}^- \leftrightarrow \gamma\,\gamma. \tag{1.31}$$

Some interactions are not mediated by electromagnetism and therefore do not involve photons. An example for this is the production/annihilation of electron-positron pairs by neutrino-anti-neutrino pairs mediated through the weak nuclear force:

$$\mathrm{e}^+\,\mathrm{e}^- \leftrightarrow \nu\,\bar{\nu}, \tag{1.32}$$

As long as the temperature of the Universe is sufficiently high, such reactions are in equilibrium, i.e. both directions are equally likely. During the radiation-dominated epoch, the expansion rate evolves as $H(a) \propto a^{-2}$, while the rate of reactions such as the electron-positron creation/annihilation depends on particle number densities and energies and therefore decrease much faster (at least $\propto a^{-3}$). If reaction rates drop below the rate of expansion, the reactions become very unlikely and the participating particle species cease to interact, which is referred to as a freeze-out. This can happen at times during which typical particle energies exceed particle rest masses and depends on the detailed cross sections.

### 1.2.1 From the Big Bang to the first atoms

The immediate time after the Big Bang called the *Planck epoch*, when the Universe was $\lesssim 10^{-43}$ s old and reached typical particle energies of $1.2 \times 10^{19}$ GeV, is governed by the unknown laws of Quantum gravity. At these energies, all four fundamental forces are hypothesised to be unified and no distinct particles could have existed.

Gravity decoupled first, which happened at the end of the Planck epoch leading to the era of *grand unification*, during which the remaining three forces stay unified as a hypothetical electronuclear force. At the end of the epoch of grand unification, $\lesssim 10^{-36}$ s after the Big Bang, two important events are thought to have happened. Driven by the symmetry breaking phase transition caused by the decoupling of the strong nuclear force from the electroweak force, a small asymmetry in the matter-antimatter abundance by one in a billion led to the matter-dominated Universe we observe today, in an event called baryogenesis. The second event is a period of rapid exponential expansion of space by at least 26 orders of magnitude, which is referred to as *inflation*. Inflation was initially postulated to explain the lack of observational evidence for topological defects like cosmic strings or magnetic monopoles,

which are believed to be produced in large amounts during the aforementioned phase transition, as well as the remarkable isotropy of the CMB and the flatness of space (Guth, 1981; Linde, 1982).

After the end of inflation at $10^{-32}$ s, the Universe enters the electroweak epoch, which ends roughly $10^{-12}$ s after the Big Bang with the decoupling of the weak nuclear force from electromagnetism. With $\sim 250$ GeV, electroweak unification marks the highest energies that are experimentally probed with particle accelerators. Shortly after this point in time, the postulated CDM particles with rest masses of $\gtrsim 100$ GeV are no longer produced and freeze-out due to their negligible cross section with standard model particles. The CDM particles now stream freely through the Universe and form a homogenious and isotropic background. As these particles self-annihilate, their density gradually decreases with the currently remaining relic abundance depending on their time of freeze-out.

Roughly $10^{-6}$ s after the Big Bang, the Universe is cold enough to allow quarks and gluons to form protons, neutrons, and their respective anti-particles, leading into the hadron epoch. Initially, the temperature during this epoch was high enough to allow the production of hadron/antihadron pairs. As the Universe cooled, reaction rates slowed down until an equilibrium was no longer possible. The slight overabundance of matter at the end of the epoch on grand unification now leads to the annihilation of all antihadrons. This process ends roughly $\sim 1$ s after the Big Bang and left the Universe dominated by leptons. The ratio of the number of baryons after and before this event is observable today as the baryon-to-photon ratio of the Universe. The remaining protons and neutrons are in equilibrium with the remaining particles and convert into one another via the $\beta$- and the inverse $\beta$-decay.

At energies of 1 MeV, which occurred $\sim 1$ s after the Big Bang, neutrinos decouple from the other particles and form an additional background. Following the freeze-out of the neutrinos, neutrons can no longer be produced via the inverse $\beta$-decay. Protons and neutrons are therefore no longer in equilibrium with the available neutrons starting to decay with a mean lifetime of 881.5 s. The lepton epoch ends $\sim 10$ s after the Big Bang when energies drop below 0.5 MeV, which no longer allows for the production of electron-positron pairs. The following annihilation of the vast majority of leptons leaves the Universe dominated by photons with a temperature that has been slightly elevated by a factor of 1.4. The already decoupled neutrinos stay unaffected by the electron-positron annihilation and keep their previous temperature.

As the temperature of the Cosmos continued to drop and energies reached 0.1 MeV about 3 min after the Big Bang, free protons and all remaining neutrons can combine into deuterium, which can avoid fission for a long enough time at these energies to allow for the efficient production of stable $^4$He and small amounts of $^3$He and $^7$Li. The abundance of helium and these other light elements, which we can observe in gas clouds that were not later enriched by stars, is the direct result of this event called *Big Bang nucleosynthesis* (BBN, Alpher et al., 1948). The predicted mass fraction of hydrogen and helium with $\sim 75\%$ and $\sim 25\%$ provide strong evidence in favour of big bang cosmology and depend, among others, on the number of relativistic species during nucleosynthesis, placing strong constraints on the number of neutrino families.

For the next 380 000 years the Universe remains filled with a hot plasma composed of free electrons and nuclei, which were coupled to photons via Compton scattering and bremsstrahlung mechanisms. At energies of $\sim 0.3$ eV, electrons and nuclei combine to form the first atoms. The evolution of the fraction of free electrons as a function of redshift is depicted in Fig. 1.5. With the decreasing abundance of free electrons and the continued cooling of the Universe, the mean free path of the photons grows to exceed the Hubble radius. The Universe thus became transparent for the first time and the free streaming photons from this epoch, named the *epoch of recombination*, continued to

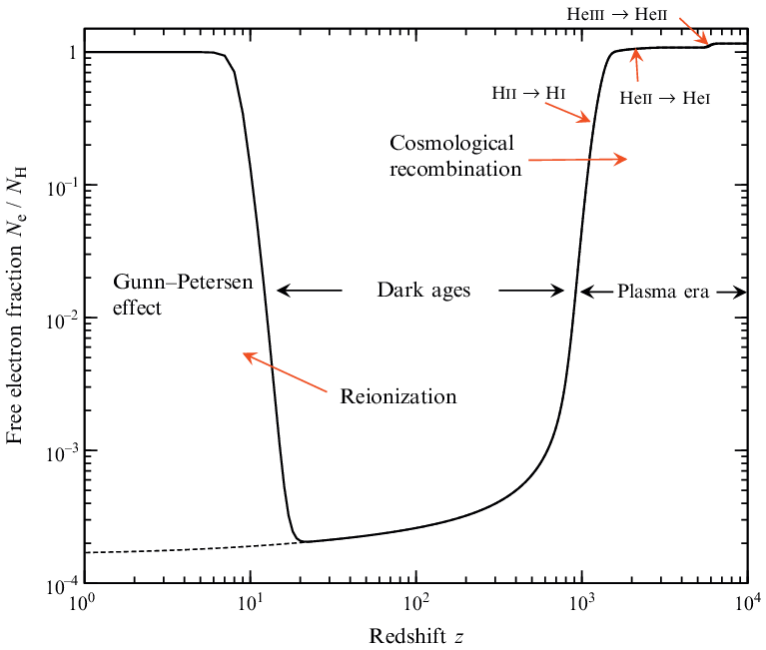


Figure 1.5: Ionisation history of the Universe. In the time after the formation of the first atomic nuclei around 1 s after the Big Bang, the Universe remained a hot plasma until cosmic expansion lowered its temperature to ≈ 3000 K and the first atoms could form. This event is referred to as cosmic recombination and occurred roughly 380 000 years after the Big Bang at a redshift of ≈ 1080. The photons that were strongly coupled to the baryonic matter before recombination are free-streaming afterwards and form the CMB we observe today. At the current epoch, the Universe is highly ionised again due to the UV radiation emitted by the first stars, which formed several hundred million years after the Big Bang. The time between recombination and the reionisation of the Universe is called the *dark ages* due to the absence of visible light as soon as the CMB has been redshifted to infrared wavelengths. The figure has been adopted from Sunyaev & Chluba (2009).

cool and are observable today as the CMB. The observation of the CMB, its characteristic blackbody spectrum, and its pattern of small temperature anisotropies are the strongest piece of evidence in favour of a hot big bang.

## 1.3 The cosmic microwave background

Since its initial discovery, the study of the CMB has become the backbone of empirical cosmology and the smoking gun for the occurrence of a hot big bang. The CMB is an isotropic background with a *spectral energy distribution* (SED) that, with current technology, is indistinguishable from a blackbody with a temperature of (2.726 ± 0.005) K (Mather et al., 1994, see Fig. 1.6). The existence of the CMB as a consequence of the Big Bang was first predicted by Asher Alpher, George Gamow, and Robert Herman in a series of publications in which they investigated the physics of the early Universe and BBN (Alpher & Herman, 1948b,a; Gamow, 1948a,b). The CMB was first detected in 1965 by Arno Penzias and Robert Wilson (Penzias & Wilson, 1965), who received the 1978 Nobel Price in Physics for their discovery.

The CMB photons we observe today decoupled from baryonic matter during the epoch of

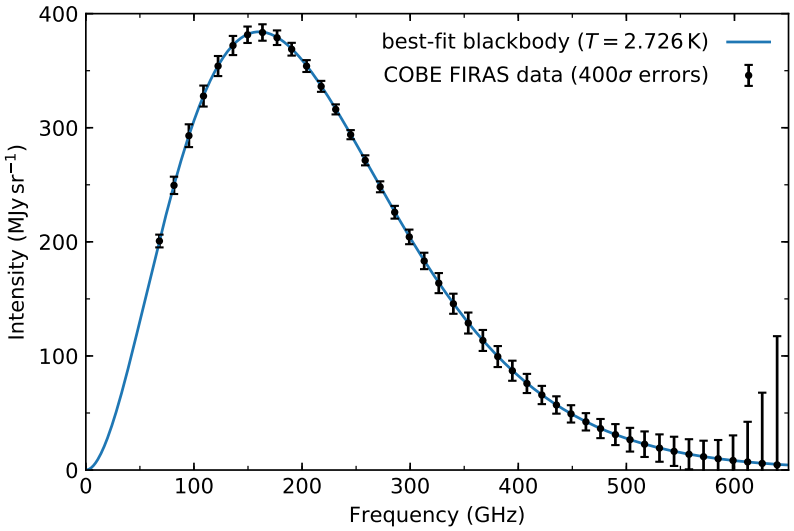


Figure 1.6: Observed all-sky average spectral energy distribution of the CMB as measured by the COBE FIRAS instrument (Fixsen et al., 1996). The original $1\sigma$ errors are invisible on the scale shown here and were thus multiplied with a factor of 400. The solid blue line shows the best-fit blackbody spectrum with a temperature of 2.726 K.

recombination, roughly 380 000 years after the Big Bang, when the Universe became cold enough for the formation of the first atoms. In the time before this event, photons and baryons formed a tightly coupled fluid that was able to oscillate when disturbed, e.g. by gravitational potentials. These so-called *baryon acoustic oscillations* (BAOs) are the source of the specific pattern of small temperature anisotropies that were first observed by the Cosmic Background Explorer (COBE) satellite observatory. These primordial fluctuations in CMB temperature are referred to as *primary* anisotropies and have a typical amplitude of $\Delta T/T_0 \approx 10^{-5}$. The CMB can be thought of as emitted from the surface of a thin spherical shell, in which centre we, the observer, reside. This shell is called the *last scattering surface* (LSS) and located at $z \approx 1080$. The LSS defines the edge of the part of the Universe that can be observed through electromagnetic radiation. The primary anisotropies of the CMB provide us with a snapshot of the distribution of matter on the LSS at the time of recombination. The most recent observations of the CMB temperature anisotropies by the *Planck* satellite are shown in Fig. 1.1.

### 1.3.1 The CMB power spectrum

The statistical nature of the CMB temperature fluctuation pattern can be described through an expansion of the observed temperature map in spherical harmonics $Y_m^\ell(\theta, \phi)$

$$\Delta T(\theta, \phi) = T(\theta, \phi) - T_0 = \sum_{\ell=1}^{\infty} \sum_{m=-\ell}^{\ell} a_{\ell m} Y_m^\ell(\theta, \phi), \tag{1.33}$$

where the coefficients $a_{\ell m}$ carry information about the size of fluctuations as a function of angular scale. The angular scale is approximately given by $180^\circ/\ell$. The statistical properties of the coefficients

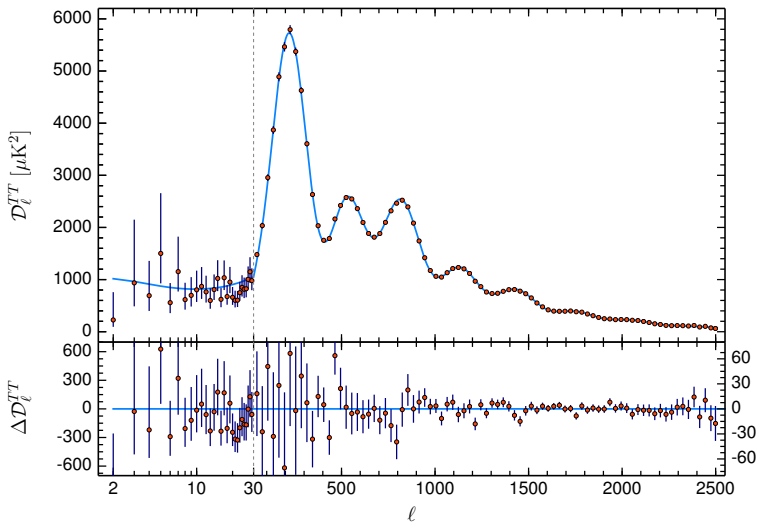


Figure 1.7: Angular power spectrum of the CMB temperature anisotropies measured by *Planck* with the best-fit ΛCDM cosmology shown as the blue solid line (Planck Collaboration, 2018b). The plot shows $D_\ell^{TT} = \ell(\ell+1)C_\ell^{TT}/(2\pi)$ and demonstrates the impressive agreement of the observed and predicted spectrum.

are quantified by the angular power spectrum, which is defined by

$$C_\ell = \langle |a_{\ell m}|^2 \rangle. \tag{1.34}$$

The most recent measurement of the CMB angular power spectrum by the *Planck* satellite is shown in Fig. 1.7.

The shape of the angular power spectrum is determined by a multitude of phenomena that convert the primordial fluctuations in matter density to fluctuations in temperature, either through the scattering of photons by baryons or through effects of gravity. In the tightly coupled baryon-photon fluid, the photons interacted with free electrons via Thomson scattering, while free electrons engaged with nucleons via Coulomb scattering. Disturbances in the density field propagated through this fluid at the speed of sound, which was $\approx c/\sqrt{3}$. The maximum distance a sound wave could have traveled from the moment of the Big Bang to the time of recombination is given by the sound horizon. The temperature anisotropies can therefore be categorised into fluctuations on super- and sub-horizon scales.

Super-horizon fluctuations are imprinted to the CMB by the Sachs-Wolfe effect (Sachs & Wolfe, 1967), which is a combination of gravitational redshift and time dilation, as well as the Doppler effect caused by the peculiar motion of gas in large-scale gravitational potentials. The power spectrum on super-horizon scales is expected to be directly related the power spectrum of the matter distribution, leading to

$$\ell(\ell+1)C_\ell \approx \text{const.} \quad \text{for } \ell \lesssim 100 \tag{1.35}$$

On sub-horizon scales, the most important effect are the aforementioned BAOs. After the postulated CDM particles decoupled from the other species less than 1 s after the Big Bang, dark matter was free-streaming and small initial disturbances in its density field started to grow slowly, but unimpeded.

Baryonic matter is prevented from falling into the dark matter potential wells by the pressure exerted by the photons. Instead, the baryon-photon fluid starts to oscillate. Adiabatic compression and expansion of the fluid during the oscillations raises and lowers its temperature. At the moment of recombination, the pattern of sound waves generated by the oscillations gets frozen in time by the escaping photons. Sound waves that have traveled a distance corresponding to the sound horizon are observed as temperature fluctuations of $\approx 1^\circ$ in scale, leading to a characteristic peak in the CMB angular power spectrum at $\ell_1 \approx 200$, the multipole moment of which is very sensitive to the geometry on the Universe. Additional peaks are expected at integer multiples of $\ell_1$ and correspond to different stages in the compression/expansion cycle of the oscillations. The amplitude of higher-order peaks is predicted to decrease rapidly due to the weaker coupling of photons at small scales, a process called Silk damping (Silk, 1968). These so-called acoustic peaks are the most important cosmological probe of the CMB. Their most recent measurement is shown in Fig. 1.7.

A variety of processes can lead to additional CMB temperature anisotropies after the epoch of recombination. These so-called *secondary* anisotropies include Thomson scattering after the reionization of the Universe, gravitational lensing, the integrated Sachs-Wolfe effect, the Rees-Sciama (Rees & Sciama, 1968) effect and the Sunyaev-Zeldovich effect, the latter of which is introduced in detail in Section 1.7. A detailed review on CMB anisotropies is provided by Hu & Dodelson (2002).

### 1.3.2 Observations of the CMB

After its initial discovery by Penzias and Wilson in 1965, the study of the CMB has moved to the centre of cosmological research. A major breakthrough were the all-sky observations performed from space by COBE, the first satellite observatory dedicated to cosmology. As mentioned previously, the COBE FIRAS instrument obtained the most precise measurement of the CMB SED to this date and verified its predicted blackbody nature. COBE's Differential Microwave Radiometer (DMR) on the other hand was the first instrument that detected the predicted temperature anisotropies of the CMB, laying the foundation for the detailed study of its angular power spectrum in the coming decades. For their discoveries, the principle investigators of the two instruments, John Mather and George Smoot, were awarded the 2006 Nobel Prize in Physics with the price committee stating "the COBE project can also be regarded as the starting point for cosmology as a precision science".

The first high-resolution measurements of the CMB were carried out during the early 2000s with balloon experiments like MAXIMA (Hanany et al., 2000) and BOOMERanG (Netterfield et al., 2002). By 2002 the first three accoustic peaks were discovered by a combination of instruments, providing strong evidence that we live in a spatially flat universe that is dominated by dark energy (Wang et al., 2003). The Wilkinson Microwave Anisotropy Probe (WMAP) was the second satellite observatory dedicated to the study of the CMB and strongly improved on COBE with an increase in spatial resolution by a factor of 33 and an increase in sensitivity by a factor of 45. WMAP observed the sky for nine years and provided the first percent-level constraints for cosmological parameters. WMAP's successor, and final CMB satellite observatory for the foreseeable future, has been the *Planck* satellite. *Planck* provided another improvement in spatial resolution and sensitivity over WMAP and observed the sky out to much higher frequencies for improved removal of contamination by other astrophysical emission. The measured angular power spectrum, shown in Fig. 1.7, extends out to $\ell \approx 2500$ and allowed for the detection of the first seven acoustic peaks. In addition to measurements of the temperature anisotropies, *Planck* allowed for the measurements of the polarization of the CMB and the observed polarization auto- and cross-spectra presented by the Planck Collaboration (2018b)

show excellent agreement with the prediction.

### 1.3.3 Galactic and extragalactic foregrounds

The cosmic microwave emission we receive with our telescopes is a superposition of the CMB and emission from Galactic and extragalactic sources. When the sky is observed close to the Galactic disk, those Galactic foregrounds dominate the measured signal. At high Galactic latitudes, the contamination by Galactic foregrounds weakens. The foreground emission by our Galaxy can be broken down into several components with distinct SEDs, many of which are well approximated by power laws $I(\nu) \propto \nu^{\alpha}$ (see Fig. 1.8), that allow them to be modelled and removed from CMB observations with sufficient frequency coverage. The relevant components are

- Galactic synchrotron radiation from electrons that are accelerated to relativistic velocities in supernova explosions. Synchrotron emission dominates at frequencies below $\sim 30\,\mathrm{GHz}$ and follows a power law SED with $\alpha \approx -0.8$.
- Galactic bremsstrahlung radiation from hot ($T \approx 10^4\,\mathrm{K}$) plasma around young massive stars. At frequencies relevant to the study of the CMB, the SED of bremsstrahlung is almost flat (i.e. $\alpha \approx 0$).
- Thermal emission from warm ($T \approx 20\,\mathrm{K}$) interstellar dust grains that are heated by UV emission of young stars. Emission from dust dominates at frequencies $\gtrsim 300\,\mathrm{GHz}$ and approximately follows a *modified blackbody* SED $I(\nu) \propto \nu^{\beta} B(\nu, T)$, where $\beta \approx 1.5$ depends on the composition and grain size distribution of the dust and $B(\nu, T)$ is the blackbody SED. In the Rayleigh-Jeans regime, the SED is well approximated by a power law with $\alpha \approx 3.5$.
- Anomalous Microwave Emission (AME) in the frequency range 10–60 GHz, first detected by Kogut et al. (1996). The most natural explanation of AME is rotational emission from ultra-small dust grains ("spinning dust", e.g. Dickinson et al., 2018).
- Line emission from $^{12}$CO molecules in molecular clouds. A number of rotational transitions of $^{12}$CO lie at frequencies that are relevant to CMB observations, ranging from $J = 1 \rightarrow 0$ with $\nu_0 = 115.3\,\mathrm{GHz}$ to $J = 9 \rightarrow 8$ with $\nu_0 = 1036.9\,\mathrm{GHz}$.

The most important extragalactic signal for observations of the CMB is the near-isotropic *cosmic infrared background* (CIB), which is composed of countless unresolved dusty starforming galaxies at high redshift. Like thermal dust emission from the Milky way, the CIB is well approximated by a modified blackbody SED.

Besides these diffuse fore- and backgrounds, emission from Galactic and extragalctic point sources is a relevant contaminant for high-resolution CMB surveys. These point sources can the broadly divided into radio point sources with falling power law SEDs and dusty point sources with rising power law SEDs.

## 1.4 From CMB anisotropies to galaxy clusters: structure formation

Observations of the CMB temperature anisotropies show that matter was distributed very smoothly at $z \sim 1100$, a few hundred thousand years after the Big Bang. In contrast, the distribution of matter in

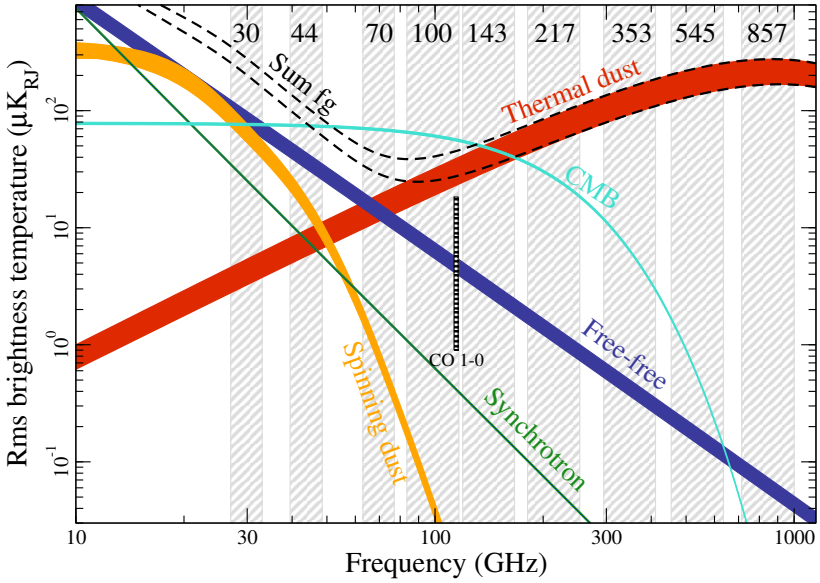


Figure 1.8: Frequency dependence of the CMB and the most-relevant diffuse Galactic foregrounds. The $y$-axis gives the Rms of the brightness temperature in the Rayleigh-Jeans limit computed from individual *Planck* components maps that were smoothed to a spatial resolution of 1°, while the width of the bands indicates the variance of the individual component SEDs. The grey vertical bands indicate the channels of the *Planck* satellite. The figure has been adopted from the Planck Collaboration (2018a).

the local Universe is strongly inhomogeneous on small scales, with stars inside of galaxies, which, in turn, form groups and clusters along a web-like filamentary structure that surrounds large, mostly empty regions called voids. This so-called *cosmic web* can be seen clearly in the three-dimensional distribution of galaxies that has been mapped by various galaxy redshift surveys like the 2 degree Field Galaxy Redshift Survey (2dFGRS, Colless et al., 2001) and the Sloan Digital Sky Survey (SDSS, Lundgren et al., 2015). The distribution of galaxies obtained by the 2dFGRS is shown in Fig. 1.9. This section provides a brief outline how the large-scale structure of the Universe evolved from the epoch of recombination to the current epoch. A compact introduction to the topic is provided by Schneider (2015).

### 1.4.1 The matter power spectrum

Perturbations in the matter density field and their evolution in time is quantified by the so-called *density contrast* $\delta(\boldsymbol{x}, t)$ at the comoving coordinate $\boldsymbol{x}$ and time $t$

$$\delta(\boldsymbol{x}, t) = \frac{\rho(\boldsymbol{x}, t) - \rho_{\mathrm{m}}(t)}{\rho_{\mathrm{m}}(t)}, \tag{1.36}$$

where $\rho(\boldsymbol{x}, t)$ is the matter density at a given location and time and $\rho_{\mathrm{m}}(t) = \Omega_{\mathrm{m}}(t)\rho_{\mathrm{crit.}}(t)$ is the mean matter density of the Universe at the time $t$. The CMB temperature anisotropies suggest that at the time of recombination ($z \approx 1080$), typical values were $|\delta| \sim 10^{-5}$. Driven by self-gravity, these small perturbations continued to grow to eventually form the large-scale structures we observe in the local Universe. In that process, overdense regions experience a reduced local expansion rate,

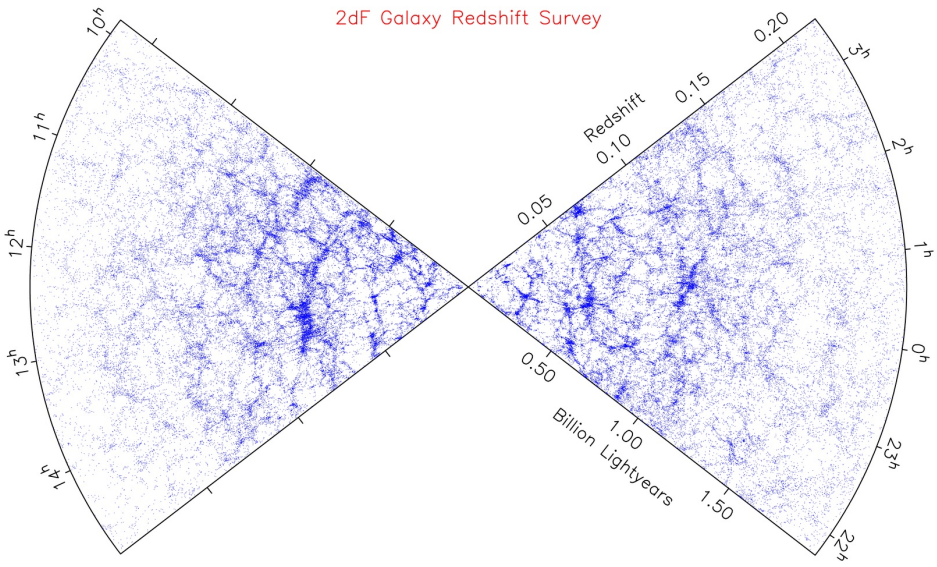


Figure 1.9: The distribution of galaxies in the complete 2dF Galaxy redshift survey. The radial axis of the image indicates the redshift of the galaxies, while the tangential axis shows their right ascension. The survey was performed along two bands close to the Galactic north and south pole. The original 3D structure was projected along the declination axis. Note that the true radial coordinate differs from the redshift-derived one, shown in the image, due to redshift-space distortions. The survey measured the sky position and redshift of more than 350 000 galaxies in the time between 1997 and 2002. The figure was created by the 2dFGRS collaboration and is based on the results presented by Colless et al. (2001).

further increasing their density contrast, while the density contrast of underdense regions continues to decrease due to a locally faster expansion rate. The absolute value $|\delta|$ therefore grows in both cases. The evolution of structures in the Universe is therefore driven by the effect of gravitational instability.

On scales smaller than the Hubble radius the growth of structure can be described in the framework of Newtonian gravity. Assuming that the matter in the Universe can be described as a pressureless fluid (i.e. $\boldsymbol{P}(\boldsymbol{x},t) = 0$) with the density field $\rho(\boldsymbol{x},t)$, its velocity field $\boldsymbol{v}(\boldsymbol{x},t)$ is described by the continuity equation

$$\frac{\partial \rho}{\partial t} + \nabla \cdot (\rho\, \boldsymbol{v}) = 0, \tag{1.37}$$

which implies conservation of matter. In addition, the Euler equation applies, which describes the behaviour of a fluid under the influence of forces and implies the conversation of angular momentum

$$\frac{\partial \boldsymbol{v}}{\partial t} + (\boldsymbol{v} \cdot \nabla)\boldsymbol{v} = -\frac{\nabla \boldsymbol{P}}{\rho} - \nabla\Phi. \tag{1.38}$$

Since we only consider pressureless matter, the pressure gradient vanishes. The gravitational potential $\Phi$ is given as a modified version of the Poisson equation that accounts for a cosmological constant $\Lambda$

$$\partial^2\Phi = 4\pi \mathrm{G}\rho - \Lambda. \tag{1.39}$$

When combined, these three equations allow for the description of a self-gravitating fluid. In general, they can not be solved analytically, in which case one has to use numerical methods. However, an

analytic solution can be found for the special case of a homogeneous expanding cosmos with the velocity field $\boldsymbol{v}(\boldsymbol{x},t) = H(t)\boldsymbol{x}$ and for small values of the density contrast, $|\delta| \ll 1$ (linear regime). It can be shown that this solution leads to a second-order differential equation for the density contrast

$$\frac{\partial^2\delta}{\partial t^2} + \frac{2\dot{a}}{a}\frac{\partial\delta}{\partial t} - \frac{3H(a)^2\Omega_m}{2a^3}\delta = 0. \tag{1.40}$$

This linear equation has two linearly independent solutions, one that describes a growth of the density contrast with time, while the other describes a decrease. At later times, the growing solution, which is denoted with a +, always dominates. After separating the spatial- and time-dependencies in equation (1.40), the solution for the density contrast is given by

$$\delta(\boldsymbol{x},t) = D_+(t)\,\delta_0(\boldsymbol{x}), \tag{1.41}$$

where $\delta_0(\boldsymbol{x})$ is the linearly extrapolated density fluctuation field and $D_+(t)$ is called the *growth factor*, a function that describes the time evolution of the density contrast and is normalised to $D_+(t_0) = 1$.

An important concept for the formation of structures is the *particle horizon*, which is defined by

$$r_\mathrm{H} = \int_0^t \frac{c\,\mathrm{d}t}{a(t)}, \tag{1.42}$$

and gives the largest (comoving) distance at which particles could have been in causal contact in the past. At early times, fluctuations of all scales $\lambda$ are larger than the horizon and as the Universe expands, the horizon outgrows first the smallest perturbations and later the largest. As long as fluctuations are on superhorizon scales, dark matter and baryonic matter behave the same way and their perturbations grow as

$$\begin{aligned} &\delta \propto a^2 \quad \text{during the radiation dominated epoch,} \\ &\delta \propto a \quad \text{during the matter dominated epoch,} \end{aligned} \tag{1.43}$$

due to the different expansion rates in the respective eras. When the horizon outgrows a specific pertubation scale during the radiation-dominated epoch, baryonic perturbations stop growing due to the pressure of the photons in the baryon-photon fluid and start to oscillate. The behaviour of dark matter on sub-horizon scales depends on its nature. If dark matter predominantly consists of light, fast-moving particles, it is free-streaming on sub-horizon scales and thus only able to form large structures. This type of dark matter is commonly called hot dark matter and an example for it are neutrinos. Cold dark matter made from WIMPs, on the other hand, is not free-streaming and can be bound in gravitational potentials. Observations of low mass galaxies combined with the absence of massive galaxy clusters at high redshifts suggests that dark matter is at least mostly composed out of high-mass particles. We therefore expect dark matter perturbations to continuously grow during the radiation dominated epoch, although at a reduced, logarithmic rate. By the time recombination occurs, the baryons are no longer impeded by photon pressure and fall into the potential wells formed by dark matter. Both components then continue to grow at the same rate during the matter-dominated epoch. Since pertubation on scales larger than the particle horizon at the moment of equal matter and radiation energy density $z_\mathrm{eq}$ enter the horizon in the matter-dominated epoch, their growth is not affected by sub-horizon physics, while the growth on all scales that are smaller is suppressed.

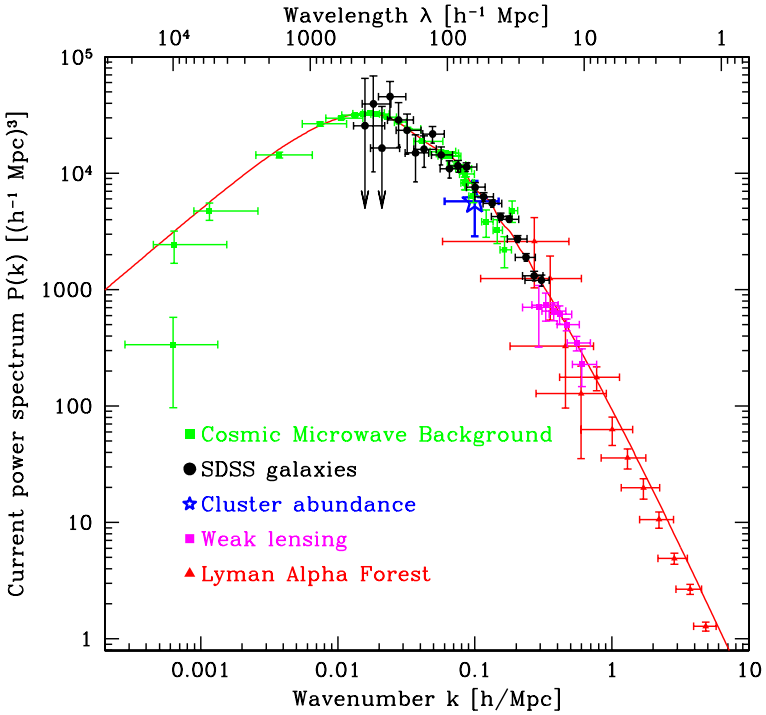


Figure 1.10: Observational constraints on the matter power spectrum $P(k)$ from different probes of the large-scale structure of the Universe. The red solid line shows the predicted spectrum for a flat ΛCDM cosmology with $h = 0.72$, $\Omega_{m,0} = 0.28$, $\Omega_{b,0} = 0.448$, $\tau = 0.17$ and $n_s = 1$. The figure has been adopted from Tegmark et al. (2004).

These effects are accounted for in the *transfer function* T(k), where $k = 2\pi/\lambda$ is the wave number for a pertubation of scale $\lambda$

$$\frac{\delta_0(k)}{\delta_0(k_s)} = T(k)\frac{\delta_i(k)}{\delta_i(k_s)}, \tag{1.44}$$

where the indices i and 0 denote inital and current values, respectively, and $k_s$ denote the small wavenumbers of superhorizon fluctuations. A variety of efficient codes for the computation of the transfer function exist, the most popular of which is the Code for Anisotropies in the Microwave Background (CAMB; Lewis et al., 2000)

With these definitions, the matter power spectrum $P(k,t)$ is given by

$$P(k,t) = A\,k^{n_s}\,D_+^2(t)\,T(k)^2, \tag{1.45}$$

where $k^{n_s}$ is the initial power spectrum after the Big Bang with $n_s = 1$ (Harrison–Zeldovich approximation) and A is its amplitude, which has to be constrained through observations. Measurements of $P(k)$ are shown in Fig. 1.10. The idea that $n_s$ should be unity was originally put forward to evoke scale invariance at early times. However, theories of inflation predict that $n_s$ should be slightly smaller than unity, with the most recent measurements performed with the *Planck* satellite finding $n_s = 0.9665 \pm 0.0038$ providing strong evidence in favor of inflation. These initial, perturbations are commonly assumed to be caused by quantum fluctuations, which are inflated to macroscopic scales.

Such quantum fluctuations generate Gaussian random fields that are fully characterised by their power spectrum. Observations demonstrating the necessity of higher-order spectra for the description of the observed fields would provide evidence for primordial non-Gaussianity, predicted by models of chaotic inflation (e.g. Bartolo et al., 2004).

The power spectrum amplitude A is commonly estimated through observations of the standard deviation of matter fluctuations on scales with radius $R = 8\,h^{-1}$ Mpc, which is referred to as $\sigma_8$. In general, the standard deviation of matter fluctuation at the scale $R$ is defined as

$$\sigma(R,t) = \frac{1}{2\pi^2} \int_0^\infty \mathrm{d}k\, P(k,t)\, |\hat{W}(kR)|^2\, k^2, \tag{1.46}$$

where $\hat{W}(kR)$ is the Fourier transform of the real-space top-hat window function of radius $R$, given by

$$\hat{W}(kR) = 3\,\frac{\sin(kR) - kR\,\cos(kR)}{(kR)^3}. \tag{1.47}$$

The convolution of $P(k,t)$ with $\hat{W}(kR)$ allows to select only the specific scale of interest, $R$. Combining equations (1.45) and (1.45) yields

$$\sigma_8^2 = \frac{A}{2\pi^2} \int_0^\infty \mathrm{d}k\, k^{2+n_\mathrm{s}}\, T(k)^2\, |W(kR)|^2. \tag{1.48}$$

Therefore, measuring $\sigma_8^2$ at the current epoch with $D_+(t_0) = 1$ allows to empirically determine the amplitude $A$ of the matter power spectrum.

### 1.4.2 Dark matter halos

The linear theory of structure formation presented in the previous section describes the growth of perturbations for $|\delta| \ll 1$. While their density contrast is increasing, overdense regions still follow the expansion of the Universe at a reduced pace. In order to form bound structures, those overdensities have to decouple from the Hubble flow and collapse under their own gravity after reaching a maximum expansion at $t_\mathrm{max}$. An accurate description of the gravitational collapse is no longer possible using linear theory and, in general, numerical techniques are required. However, an analytical solution for the non-linear evolution of overdense regions can be found for spherical overdensities in an otherwise homogeneous universe. After reaching its maximum size, an overdense sphere collapses to a single point at $t_\mathrm{coll} = 2t_\mathrm{max}$ under idealised conditions. For the galaxies and clusters of galaxies that we observe today, this turnover happened during the matter-dominated epoch, which is well approximated by an EdS universe. For the case of an EdS universe one can show that overdensities with a linearly extrapolated critical overdensity of $\delta_\mathrm{c} = 1.69$ at the current epoch collapse within the age of the Universe $t_0$.

Since particles do not perfectly follow radial orbits during the collapse and the matter distribution inside the collapsing sphere is not perfectly homogeneous, the particles scatter and eventually virialize. Using energy conservation and the virial theorem $E_\mathrm{pot} = -2E_\mathrm{kin}$, the non-linear theory of the spherical collapse predicts that after this process, called violent relaxation, the average density of the collapsed structure exceeds the average density of an EdS universe by a factor of $\Delta_\mathrm{vir} = 178$. In a ΛCDM universe this value is lower. However, a common approximation for the mass of virialized structures is

$M_{\rm vir} \approx M_{178} \approx M_{200}$, where $M_\Delta$ is the mass of a sphere of radius $R_\Delta$ within which the average density exceeds the critical density of the Universe at the redshift of the structure by a factor of $\Delta = 200$:

$$M_{200} = 200\,\rho_{\rm crit.}(z)\frac{4}{3}\pi R_{200}^3. \tag{1.49}$$

These collapsed, virialized structures are called dark matter halos.

Deviations from the idealised scenario of the spherical collapse, like non-spherical inhomogeneous perturbations and baryonic feedback, can no longer be treated analytically. For this reason, non-linear structure formation has been studied in great detail using large-scale three-dimensional numerical simulations. Due to the enormous computational resources required, early simulations focused on the dynamics of dark matter particles, which only interact gravitationally, and were able to reproduce the properties of the cosmic web seen in galaxy redshift surveys (e.g. Millennium simulation, Springel et al., 2005). More recent (magneto-)hydrodynamical simulations model the complex interactions of baryons and include many sub-grid phenomena like star-formation and feedback from supermassive black holes (SMBHs), allowing to reproduce e.g. the shapes and stellar populations of galaxies that are observed throughout cosmic time (e.g. Illustris, Vogelsberger et al. 2014; Illustris TNG, Pillepich et al. 2018). An example of a cutting-edge hydrodynamical simulation is given in Fig. 1.11.

Using numerical simulations, Navarro et al. (1996) showed that dark matter halos, on average, follow a universal density profile given by

$$\rho(r) = \frac{\rho_0}{\frac{r}{R_{\rm s}}\left(1+\frac{r}{R_{\rm s}}\right)^2}, \tag{1.50}$$

where $\rho_0$ is the characteristic density, $R_{\rm s} = R_{\rm vir}/c$ is the scale radius, and $c$ is the dark matter concentration parameter. This profile is named the Navarro–Frenk–White (NFW) profile. Assuming the average overdensity $\Delta_{\rm vir}$ inside the virial radius to be 200, the concentration parameter defines the value of $\rho_0$ by

$$\frac{\rho_0}{\rho_{\rm crit}} = \frac{200}{3}\frac{c^3}{\ln(1+c) - c/(1+c)}. \tag{1.51}$$

The concentration parameter $c$ therefore is the only free parameter that varies from halo to halo. The mass of a dark matter halo inside a sphere of radius $R_{\rm max}$ is given by

$$M(<R_{\rm max}) = 4\pi\int_0^{R_{\rm max}}\rho(r)r^2{\rm d}r = 4\pi\rho_0 R_s^3\left[\ln\left(\frac{R_{\rm s}+R_{\rm max}}{R_{\rm s}}\right) - \frac{R_{\rm max}}{R_{\rm s}+R_{\rm max}}\right] \tag{1.52}$$

For a given value of the concentration parameter, the NFW profile allows to convert masses and radii for different overdensities by equating (1.52) and (1.49) and solving for $R_{\rm max}$, which is demonstrated in Appendix A.2.

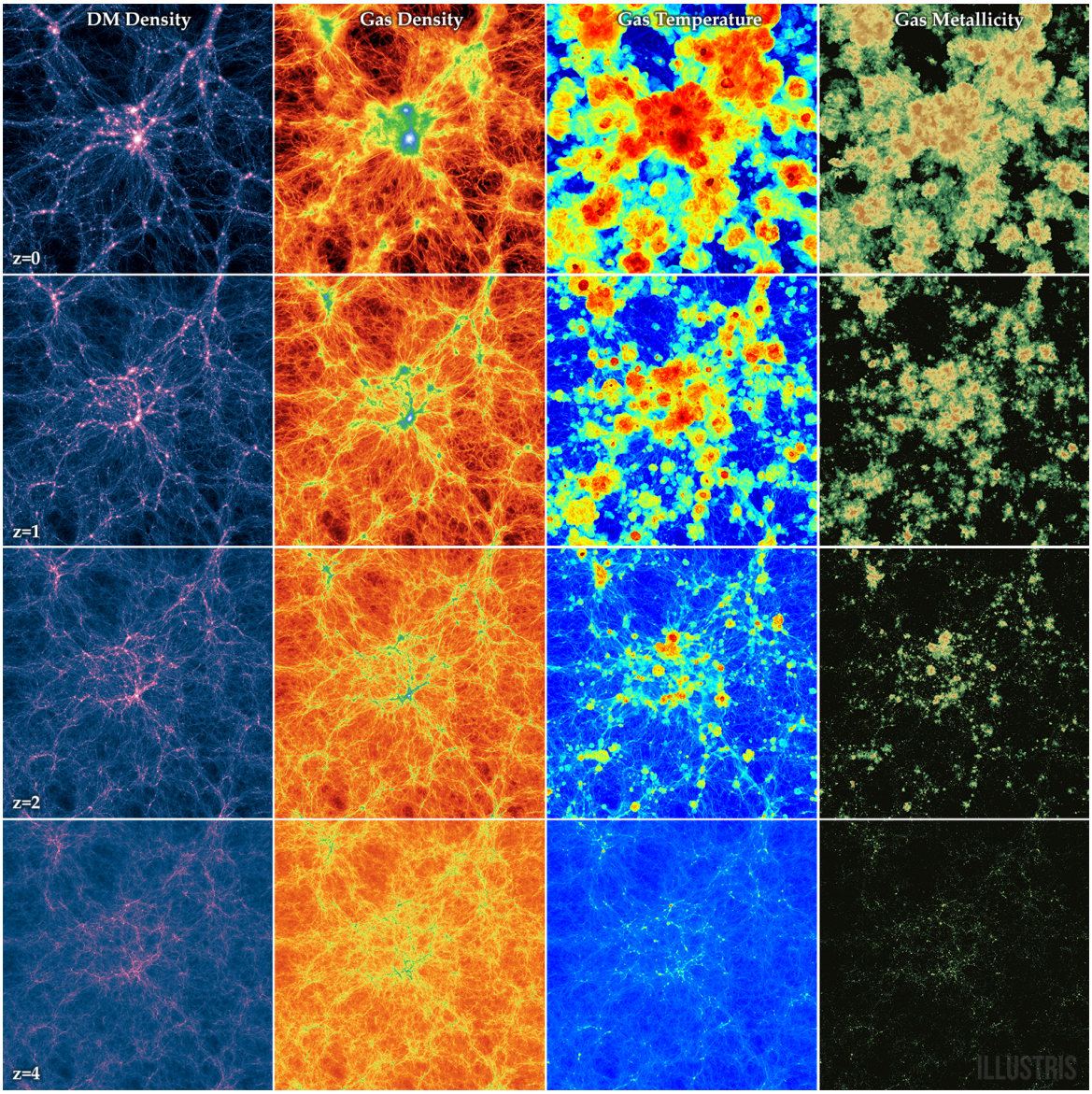


Figure 1.11: State-of-the-art hydrodynamical simulation of the large-scale structure of the Universe. The panels show thin slices of the projected (from left to right) dark matter density, gas density, gas temperature, and gas metallicity in the simulated volume of the Illustris simulation (Vogelsberger et al., 2014) at (from top to bottom) $z = 0$, 1, 2, and 4, centred on a massive galaxy cluster. Following the principles of cosmic structure formation, the contrast in all four fields increases with cosmic time from a smooth initial state to the large-scale structure we observe in the local Universe.

## 1.5 The halo mass function

The number density of dark matter halos as a function of halo mass $M$ and redshift $z$ is given by the *halo mass function* (HMF), which is generally written as (Sheth & Tormen, 1999)

$$\frac{\mathrm{d}n}{\mathrm{d}M}(M,z) = f(\sigma)\,\frac{\Omega_\mathrm{m}\rho_\mathrm{crit.}(z=0)}{M}\,\frac{\mathrm{d}\ln\left[\sigma^{-1}(R,z)\right]}{\mathrm{d}M}, \tag{1.53}$$

where $f(\sigma,z)$ is the differential mass function and $\sigma(R,z)$ is the dispersion of the matter field at redshift $z$, which was defined previously in equation (1.46). The dispersion is smoothed over the scale $R$, which is related to the mass of a halo by

$$R(M) = \left(\frac{3\,M}{4\pi\,\Omega_\mathrm{m}\rho_\mathrm{crit.}(z=0)}\right)^{\frac{1}{3}}. \tag{1.54}$$

The strong dependence of the HMF on the underlying cosmological model enters through the matter power spectrum $P(k)$ in the definition of $\sigma$, making it sensitive to all previously introduced cosmological parameters ($h$, $\Omega_\mathrm{m}$, $\Omega_\mathrm{b}$, $\Omega_\Lambda$, $w$, $\sigma_8$ and $n_\mathrm{s}$).

An analytic expression for the HMF was first derived by Press & Schechter (1974) using the non-linear model of spherical collapse that was introduced in the previous section. In the notation adopted in this work, their result translates into the differential mass function

$$f(\sigma) = \sqrt{\frac{2}{\pi}}\,\frac{\delta_\mathrm{c}}{\sigma}\,\exp\left(-\frac{\delta_\mathrm{c}^2}{4\sigma^2}\right). \tag{1.55}$$

Alternative HMF models derived from the abundance of dark matter halos in numerical simulations provide a better description of the observed halo counts. Detailed comparisons of analytic and numerical HMF models demonstrated deviations by up to 50% of the Press–Schechter model from numerical models (e.g. Jenkins et al., 2001). For this reason, all modern HMF models are obtained from large cosmological simulations (e.g. Jenkins et al., 2001; Reed et al., 2003, 2007; Warren et al., 2006; Tinker et al., 2008; Watson et al., 2013; Bocquet et al., 2016) with good agreement between them (Pillepich et al., 2010). This work adopts the widely used model for the HMF that was presented by Tinker et al. (2008), who use the notation introduced in equation (1.53) and find

$$f(\sigma) = A_\mathrm{T}\left[\left(\frac{\sigma}{b_\mathrm{T}}\right)^{-a_\mathrm{T}} + 1\right]\exp\left(-\frac{c_\mathrm{T}}{\sigma^2}\right). \tag{1.56}$$

The parameters $A_\mathrm{T}$, $a_\mathrm{T}$, and $b_\mathrm{T}$ are defined as

$$\begin{aligned} A_\mathrm{T} &= A_{\mathrm{T},0}\,(1+z)^{-0.14}, \\ a_\mathrm{T} &= a_{\mathrm{T},0}\,(1+z)^{-0.06}, \\ b_\mathrm{T} &= b_{\mathrm{T},0}\,(1+z)^{-\alpha}, \end{aligned} \tag{1.57}$$

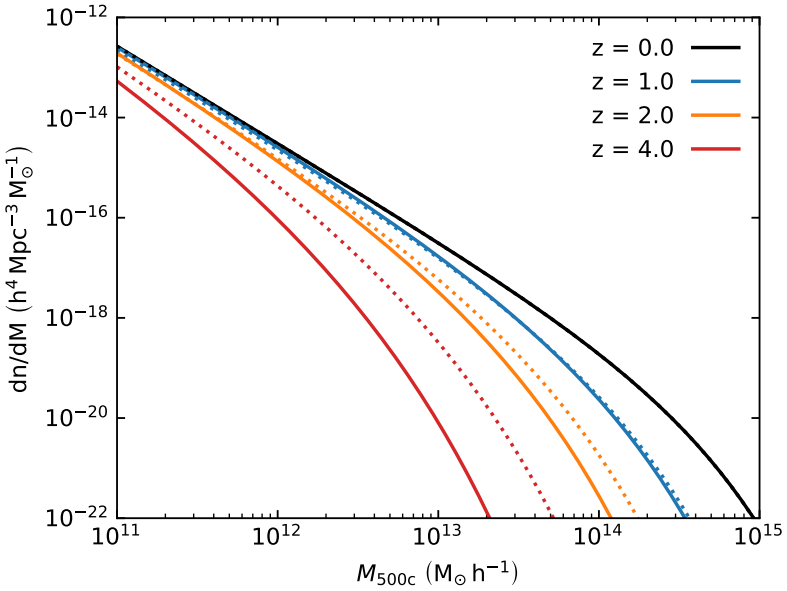


Figure 1.12: Redshift evolution of the halo mass function according to Tinker et al. (2008) for the best-fit Planck 2018 + BAO flat ΛCDM cosmology (solid lines) and for a derived open CDM cosmology that adopts all Planck 2018 + BAO best-fit values but assumes $\Omega_\Lambda = 0$ (dotted lines). The halo mass function quantifies the number of dark matter halos in a comoving volume per mass interval. The example shown here demonstrates that a dark energy-less open CDM cosmology predicts a higher number of dark matter halos across all halo masses with increasing redshift.

where $\alpha$ is a function that depends on the overdensity $\Delta_\mathrm{m}$ of the halo, defined as

$$\Delta_\mathrm{m}(z) = \frac{3M_{\Delta_\mathrm{m}}}{4\pi\, R^3_{\Delta_\mathrm{m}}\, \Omega_\mathrm{m}\rho_{\mathrm{crit.}}(z)}, \tag{1.58}$$

$$\log_{10}(\alpha(\Delta_\mathrm{m})) = -\left(\frac{0.75}{\log_{10}(\Delta_\mathrm{m}/75)}\right)^{1.2}. \tag{1.59}$$

Values for the parameters $A_{\mathrm{T},0}$, $a_{\mathrm{T},0}$, $b_{\mathrm{T},0}$, and $c_\mathrm{T}$ are given in Table 2 of Tinker et al. (2008) for different values of the overdensity $\Delta_\mathrm{m}$ with respect to the mean matter density $\Omega_\mathrm{m}\,\rho_{\mathrm{crit.}}(z)$. This work adopts an overdensity of 500 times the critical density of the Universe, which we denote as $\Delta_c = 500 = \Delta_\mathrm{m}/\Omega_\mathrm{m}$. Of particular importance for this work is the total number of halos predicted by the HMF in a redshift- and mass-interval, which is given by

$$N = f_\mathrm{sky}\, 4\pi \int_{z_\mathrm{min}}^{z_\mathrm{max}} \mathrm{d}z \int_{M_\mathrm{min}}^{M_\mathrm{max}} \mathrm{d}M \frac{\mathrm{d}n}{\mathrm{d}M} \frac{\mathrm{d}V_\mathrm{C}}{\mathrm{d}\Omega\,\mathrm{d}z}, \tag{1.60}$$

where $f_\mathrm{sky}$ is the fractional sky coverage of a given survey and

$$\frac{\mathrm{d}V_\mathrm{C}}{\mathrm{d}\Omega\,\mathrm{d}z} = D_\mathrm{H}\frac{(1+z)^2\, D_\mathrm{A}^2}{E(z)}, \tag{1.61}$$

is the comoving volume for a flat universe.

The redshift evolution of the HMF is shown in Fig. 1.12 for the Tinker et al. (2008) model using the best-fit Planck 2018 + BAO flat ΛCDM cosmology and an open cosmology without dark energy. As seen from the parametrizations of the HMF given in equation (1.55) and (1.56), the HMF predicts a rapid exponential decrease of the number density of dark matter halos with increasing mass at all redshifts. This is a consequence of the bottom-up scenario of structure formation that applies to CDM, in which small structures form first and, in time, merge to produce larger structures. The abundance of galaxy clusters, which are residing in the most massive and therefore rare dark matter halos that only formed recently, is a very sensitive probe of the shape of the HMF and especially suited to constrain the parameters $\Omega_m$ and $\sigma_8$. The biggest challenge in constraining the shape of the HMF with obervations is the accurate determination of galaxy cluster masses, an issue that is discussed in Section 1.6.5.

## 1.6 Clusters of galaxies

The previous section described the origin and evolution of the large-scale structure of the Universe. Large galaxy-redshift surveys showed that galaxies are not distributed randomly, but follow a web-like pattern. The galaxies we observe trace the underlying distribution of dark matter, which has been reproduced in great detail by hydrodynamic numerical simulations. At the nodes of this cosmic web, we observe large concentrations of galaxies, which are classified either as galaxy groups or galaxy clusters. The basic definitions are:

- **Galaxy groups** contain a few up to $\sim 50$ luminous galaxies and have a total mass of $\sim 10^{12}$ to $\sim 5 \times 10^{13}\,M_\odot$.
- **Galaxy clusters** contain between $\gtrsim 50$ and $\sim 1000$ luminous galaxies and show total masses from $\sim 5 \times 10^{13}$ to $\sim 10^{15}\,M_\odot$.

The total masses of galaxy groups and clusters refer to the sum of the mass of the dark matter halo and all baryonic matter that is bound in it.

In addition to galaxy groups and clusters, there are also galaxy super clusters. These even larger structures contain many sub-groups and clusters of galaxies, but are in the early stages of their gravitational collapse and are therefore not virialized systems. In addition, many super clusters never fully collapse, but instead will be unbound in the distant future by the accelerated expansion of the Universe. Clusters of galaxies are therefore the most massive virialized systems that are bound by gravity.

### 1.6.1 The composition of galaxy clusters

Galaxy clusters were first identified as overdensities in the distribution of galaxies. Today we know that these galaxies only contribute $\sim 5\%$ of the total mass of clusters. Multi-wavelength observations of clusters revealed their composition to be:

- **Galaxies:** First defined as agglomerations of galaxies, clusters contain $\gtrsim 50$ and $\sim 1000$ luminous galaxies (excluding dwarf galaxies) that move through their gravitational potential in complex orbits, with typical velocity dispersions of $\sim 1000\,\mathrm{km/s}$. The majority of cluster members at low redshifts are evolved elliptical galaxies with old stellar populations and a low

star formation rates (Butcher & Oemler, 1978a,b, 1984). The *brightest cluster galaxy* (BCG) is usually a giant elliptical galaxy that is often located in the centre of clusters. Many BCGs have an active galactic nucleus that can strongly affect other baryonic components of clusters. Cluster member galaxies are the most prominent component observed at optical and infrared wavelengths.

- **Intracluster medium:** Most of the baryonic matter observed in galaxy clusters is a hot, optically thin gas that is not bound to the individual member galaxies, but instead is smoothly distributed along the gravitational potential of the dark matter halos of clusters and called the *intracluster medium* (ICM). The ICM contributes $\sim 15\%$ to the total mass of a typical cluster, which is commonly defined as the gas mass fraction $f_\mathrm{g} = M_\mathrm{gas}/M_\mathrm{total}$. This gas has a typical temperatures of $10^7$–$10^8$ K, which is usually expressed in terms of equivalent energies of $k_\mathrm{B}T = 1$–$10$ kev. These high temperatures are caused by the release of gravitational potential energy during the formation of clusters, which is dissipated by shockwaves in the ICM. At these high temperatures, primordial hydrogen and helium atoms, which make up the majority of the ICM, are fully ionized. In addition to these two light elements, the ICM contains highly-ionized heavy elements e.g. iron, with average metallicities around $Z \approx 0.3\,Z_\odot$ (e.g. Urban et al., 2011). These heavy elements are thought to be stripped from infalling galaxies by ram pressure (Abadi et al., 1999) or ejected from them by supernovae explosions. Due to its high temperature, the ICM emits observable X-ray radiation and scatters CMB photons.
- **Dark matter:** The dark matter halo of typical galaxy clusters contributes roughly 80% of their total mass. Galaxy clusters were the first systems that were discovered to show signs of missing mass. Dark matter inside galaxy clusters was first proposed by Fritz Zwicky (Zwicky, 1933) to explain the high velocity dispersion of the galaxies within the Coma Cluster.
- **Relativistic particles:** Radio observations showed that some galaxy clusters are sources of diffuse radio synchrotron emission (e.g. van Weeren et al., 2019). The observed spectra suggest that the emission is caused by a population of relativistic electrons with energies in the ~GeV range that move though intracluster magnetic fields with flux densities of a few $\mu$G. These relativistic electrons are thought to be accelerated by *diffusive shock acceleration* (DSA, Blandford & Eichler, 1987) during cluster mergers as well as by AGN. Although they give rise to interesting phenomena, their contribution to the total mass of clusters is negligible.

### 1.6.2 Observations of galaxy clusters

Galaxy clusters can be observed over the entire electromagnetic spectrum, ranging from radio waves to Gamma-ray radiation. Besides enhancing our understanding of clusters and the processes inside them, multi-wavelength observations have delivered e.g. direct observational evidence for the existence of dark matter. Through a combination of X-ray and optical observations of a colliding system of galaxy clusters nicknamed the *Bullet Cluster*, Clowe et al. (2006) showed that the mass distribution of the colliding system differs from the distribution of the ICM, which got separated from the two main dark matter halos and optical galaxies by the collision. An example for multi-wavelength observations of the cluster Abell 2219 is shown in Fig. 1.13. This section provides a brief overview on the emission mechanisms at each wavelength regime and what we can learn about clusters through their observations.

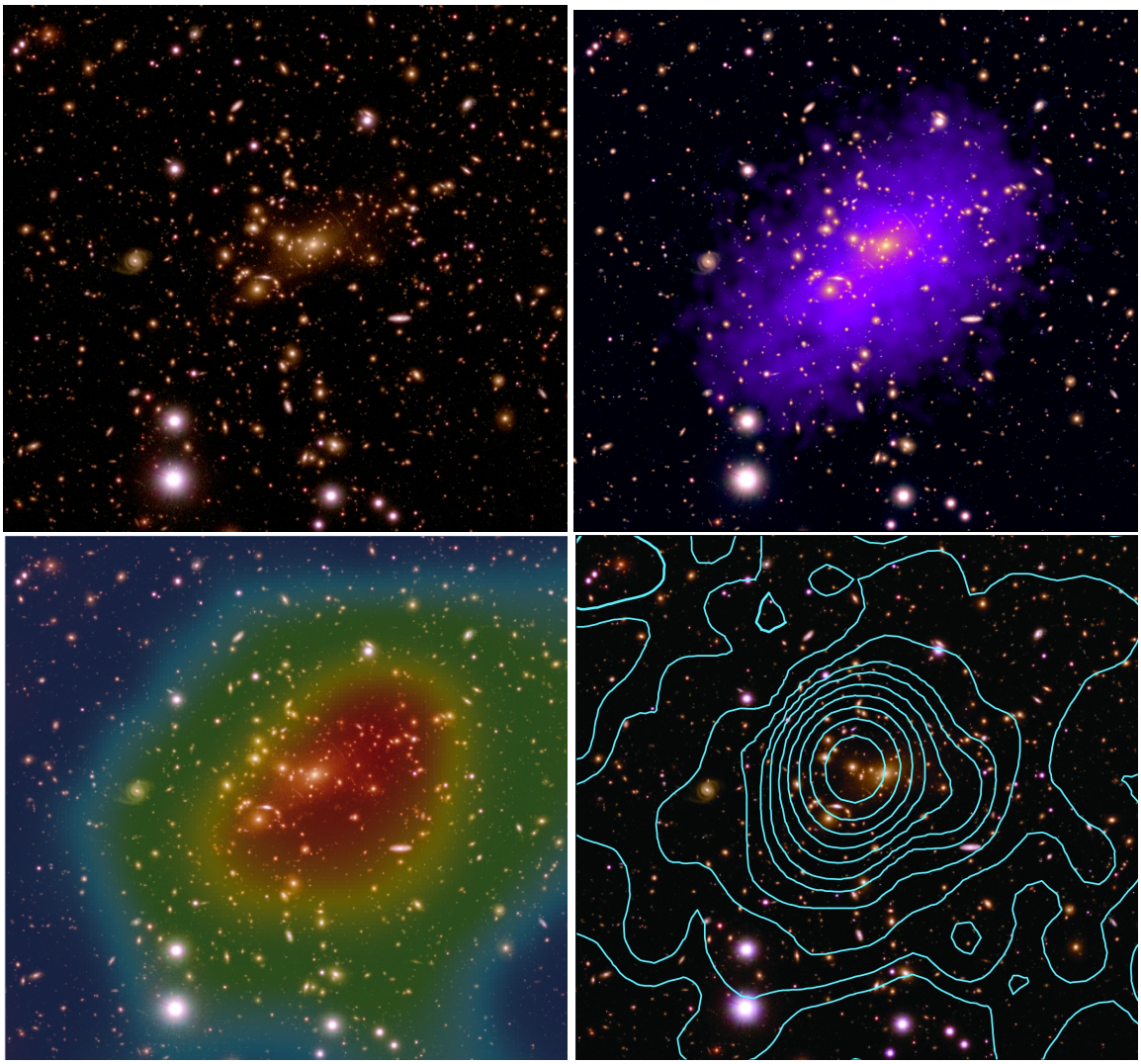

Figure 1.13: Multi-wavelength observations of the massive galaxy cluster Abell 2219. Each of the four panels shows the same three-colour optical image taken with the Subaru telescope through combination of data from the Rc, V and B filters (top-left, von der Linden et al., 2014a). The optical image has been overlaid with the X-ray surface brightness as seen by Chandra (top-right, Canning et al. 2015), the Sunyaev-Zeldovich temperature-decrement measured by the Combined Array for Research in Millimeter-Wave Astronomy (CARMA, bottom-left, credit: M. Sommer), and 1.4 GHz observations of the cluster's giant radio halo (bottom-right, Bacchi et al. 2003). The size of the field is identical across all four panels.

### Radio waves

Some galaxy clusters harbour ~Mpc scale sources of diffuse radio synchrotron emission with steep spectra ($I \propto \nu^{-\alpha}$ with $\alpha > 1$) that, depending on their morphology, are classified as *radio halos* or *radio relics*. Radio halos are located in the centres of many clusters, are mostly spherical, and show unpolarized emission of low surface brightness. Based on their size, radio halos are split into two sub-classes. *Giant radio halos* are observed in disturbed clusters, while *radio mini-halos* are more compact objects seen in relaxed systems. Radio relics, on the other hand, are elongated features that are observed on the periphery of clusters and emit highly polarized emission. There is a growing amount of evidence that the relativistic particles that give rise to relics are accelerated *in situ* by shock waves that propagate through the ICM. A recent review on diffuse radio emission from clusters has been published by van Weeren et al. (2019). Besides these diffuse radio sources in the ICM, member galaxies of some clusters, e.g. the Perseus Clusters, harbour radio-loud AGN, which are observed as radio point sources.

### Microwaves

At millimetre wavelengths, galaxy clusters appear as CMB cold spots, while at submillimetre wavelengths they are observed as CMB hot spots. This peculiar phenomenon is caused by inverse Compton scattering of CMB photons by hot electrons of the ICM and is referred to as the Sunyaev-Zeldovich effect (Sunyaev & Zeldovich, 1970, 1972). Since this effect is the main observable used in this work, it is introduced in detail in Section 1.7.

### Infrared, optical and UV

For the most part, observations at infrared, optical and UV wavelengths trace the stellar population inside and around clusters. The redshift of clusters is usually obtained through direct spectroscopic measurements, or through ratios of photometric observations at multiple wavelengths. Large-area optical surveys were the first to produce large catalogs of galaxy clusters (Abell, 1958; Abell et al., 1989), with recent ones, like the SDSS redmapper catalog (Rykoff et al., 2014a), listing several $10^4$ objects. High-resolution optical images of clusters often show arc-like features around their centres. These arcs are background galaxies that were highly distorted and multiply-imaged through *strong gravitational lensing* by the deep gravitational well of clusters. The less-obvious displacement and slight distortion caused by weak gravitational lensing in the periphery of clusters has become an important tool to provide accurate measurements of the total mass of clusters (e.g. Bacchi et al., 2003; von der Linden et al., 2014a). Furthermore, the study of the morphology and colour of cluster member galaxies showed that star formation ceases in galaxies after they enter cluster environments. This *quenching* of star formation is not fully understood at the current point in time (Taranu et al., 2014), but thought to be a combination of ram pressure stripping of the ISM by the ICM (e.g. Abadi et al., 1999) and the ejection of gas and stars during mergers between galaxies (e.g. Kauffmann et al., 1993). While this stripped gas mixes and enriches the ICM with heavy elements, the ejected stars can be observed as *intracluster light* (ICL), which is a potential tracer of the distribution of dark matter in galaxy clusters (Montes & Trujillo, 2019).

### X-rays

Galaxy clusters are the brightest extended extragalactic X-ray sources in the sky, with typical X-ray luminosities of $10^9$–$10^{11}\,L_\odot$. Since X-ray photons are unable to pass through the Earth's atmosphere, they can only be detected by balloon or space observatories. The extended X-ray emission from the ICM of clusters was first discovered in observations performed with the *Uhuru* satellite in the early 70s of the last century (Forman et al., 1972; Kellogg et al., 1972). X-ray radiation is produced in the ICM by three main processes, thermal bremsstrahlung from free electrons (free-free emission), line emission (bound-bound emission), and recombination emission (free-bound emission, see Sarazin 1986; Reiprich et al. 2013 for reviews). The contribution of each mechanism depends on the plasma temperature (see Fig. 1.14). For massive clusters with electron temperatures of $k_\mathrm{B}T_\mathrm{e} \gtrsim 2\,\mathrm{keV}$ the main emission mechanism is thermal bremsstrahlung, with its total emissivity given by

$$\epsilon^\mathrm{ff} = \frac{\mathrm{d}L}{\mathrm{d}V} \propto n_\mathrm{e}^2 T_\mathrm{e}^{1/2}, \tag{1.62}$$

where $n_\mathrm{e}$ is the free electron number density of the ICM and $T_\mathrm{e}$ is the electron temperature. The observed X-ray surface brightness $S_\mathrm{X}$ is given by the line-of-sight integral of the X-ray emissivity

$$S_\mathrm{X} = \frac{1}{4\pi\,(1+z)^4} \int_{-\infty}^{\infty} \epsilon\,\mathrm{d}l. \tag{1.63}$$

The free electron number density $n_\mathrm{e}$ is proportional to the gas density $\rho_\mathrm{g}$, which is commonly approximated by a $\beta$-model (Cavaliere & Fusco-Femiano, 1976)

$$n_\mathrm{e}(r) \propto \rho_\mathrm{g}(r) = \rho_{\mathrm{g},0} \left(1 + \frac{r^2}{r_\mathrm{c}^2}\right)^{-\frac{3}{2}\beta}, \tag{1.64}$$

where $\rho_{\mathrm{g},0}$ is the central gas density, $r_\mathrm{c}$ is the core radius, and $\beta \approx 2/3$ (Voit, 2005). The temperature of the ICM can be estimated by measuring and modelling of the X-ray spectrum. Since the emissivity of thermal bremsstrahlung is proportional to the square of the gas density, the dense core of clusters is particularly bright in X-rays. If left undisturbed, the dense core cools through the emission of X-ray photons, allowing its density and therefore its cooling rate to increase further, boosting its X-ray luminosity. X-ray observations are particularly sensitive towards these *cool core* clusters, which are often classified as dynamically relaxed systems.

X-ray observations performed with e.g. the *Chandra* space telescope can reach a high spatial resolution of $< 1$ arcsec, allowing to resolve substructures like shockwaves and gas clumps. Measurements of spectral lines in the X-ray spectrum of clusters can provide estimates of the redshift and the chemical composition of the ICM.

### Gamma-rays

Through the observations of radio halos, mini halos and relics, it has been shown that galaxy clusters harbour a population of relativistic particles. These highly energetic electrons and protons are expected to produce gamma rays through inverse Compton scattering of CMB photons and inelastic *pp* collisions (see Brunetti & Jones 2014 for a recent review). Diffuse gamma ray emission from clusters has

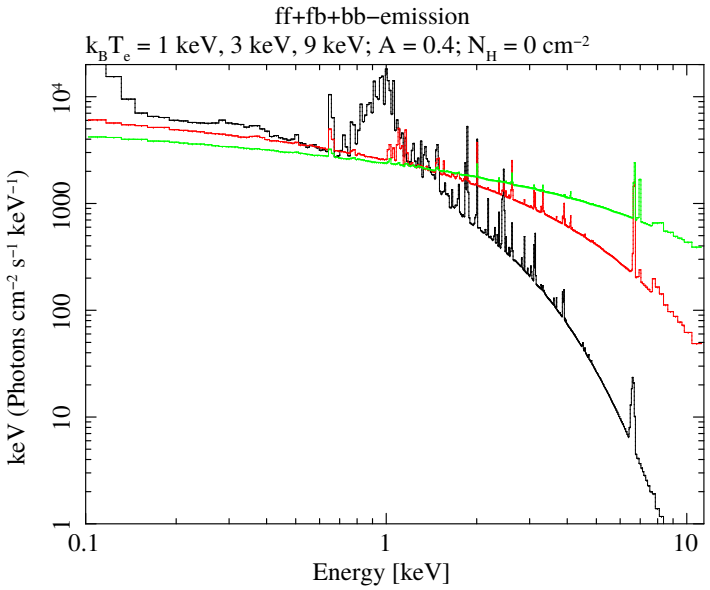


Figure 1.14: Predicted X-ray spectra of hot plasmas with $k_\mathrm{B}T_\mathrm{e} = 1$ keV (black), 3 keV (red), and 9 keV (green) at $z = 0$ for a metallicity of $\mathrm{Z} = 0.4\,Z_\odot$. The spectra are computed as the superposition of free-free (ff), free-bound (fb) and bound-bound (bb) emission. Free-free emission shows a characteristic exponential cutoff towards high energies, which can be used to estimate the temperature of the emitting gas. The strength of emission lines depends on the metallicity and temperature of the plasma. The figure has been adopted from Reiprich et al. (2013).

not been conclusively detected so far, with empirical upper limits for the observed flux starting to challange our understanding of gamma ray production. Most recently, detections of gamma rays from clusters have been claimed by Reiss & Keshet (2018) and Xi et al. (2018).

### 1.6.3 Self-similar evolution of galaxy clusters

The properties of DM halos are determined by their mass, which can be estimated using observables like the temperature of the ICM, its X-ray luminosity, or the integrated SZ signal via simple power laws. This property is referred to as *self-similarity* (Kaiser, 1986). Assuming that gravity is the only force affecting the formation of halos, we can derive several key relations.

Following Voit (2005) and Nagai et al. (2007), a relation between the mass and temperature of clusters can be derived from a simple self-similar model. The characteristic temperature $T_{500}$ of a singular isothermal sphere of mass $M_{500}$ and radius $R_{500}$ is given by

$$k_\mathrm{B}T_{500} = \frac{\mu\, m_\mathrm{p}\, \mathrm{G}\, \mathrm{M}_{500}}{2\, R_{500}}, \tag{1.65}$$

where $\mu\, m_\mathrm{p}$ defines the average particle mass as the product of the proton mass $m_\mathrm{p}$ and the mean molecular weight $\mu = 0.59$. Combining equation (1.65) with equation (1.49) yields

$$T_{500} = 11.05\,\mathrm{keV} \left( \frac{M_{500}}{10^{15}\, h^{-1}\, \mathrm{M}_\odot} \right)^{2/3} E(z)^{2/3}. \tag{1.66}$$

The characteristic pressure is then given by $P_{500} \equiv n_{\mathrm{g},500} k_{\mathrm{B}} T_{500}$, where $n_{\mathrm{g},500} = 500\,\Omega_{\mathrm{b}}/\Omega_{\mathrm{m}}\,\rho_{\mathrm{crit.}}/(\mu m_{\mathrm{p}})$. Combining the definition of the characteristic pressure with equation (1.66) reveals that $P_{500}$ scales with the cluster mass as

$$P_{500} = 0.91\,\mathrm{keV\,cm^{-3}} \left( \frac{M_{500}}{10^{15}\,h^{-1}\,\mathrm{M}_{\odot}} \right)^{2/3} E(z)^{8/3}. \tag{1.67}$$

Finally, the entropy of the ICM is defined as $K_{500} \equiv k_{\mathrm{B}} T_{500} / n_{\mathrm{e},500}^{2/3}$ with $n_{\mathrm{e},500} = \mu/\mu_{\mathrm{e}}\, n_{\mathrm{g},500}$, where $\mu_{\mathrm{e}} = 1.14$ is the mean molecular weight per free electron. The entropy-mass relation is therefore given by

$$K_{500} = 1963\,\mathrm{keV\,cm^{-2}} \left( \frac{M_{500}}{10^{15}\,h^{-1}\,\mathrm{M}_{\odot}} \right)^{2/3} E(z)^{-2/3}. \tag{1.68}$$

### 1.6.4 The pressure profile of galaxy clusters

Of particular importance for this work is the pressure profile of galaxies. As shown in Section 1.7.1, the amplitude of the thermal SZ effect is proportional to the projected electron pressure of the ICM. The most widely used parametrization of the pressure profile of galaxy clusters is the *generalized* NFW model, which was introduced by Nagai et al. (2007) and is given by

$$\mathcal{P}(x) = \frac{P(r)}{P_{500}} = \frac{P_0}{x^{\gamma}(1 + x^{\alpha})^{(\beta-\gamma)/\alpha}}, \tag{1.69}$$

where $x \equiv r/r_{\mathrm{s}}$, $r_{\mathrm{s}} = r_{500}/c_{500}$ is the scale radius, and $P_{500}$ is given by equation (1.67). For a cluster of given mass $M_{500}$ and redshift $z$, the model has five free parameters. These parameters are the pressure amplitude $P_0$, the concentration parameter[1] $c_{500}$, and the slopes $(\gamma, \alpha, \beta)$ that determine the shape of the profile at $(r \ll r_s, r \sim r_s, r \gg r_s)$.

This parametric model was adopted by Arnaud et al. (2010) to fit the average pressure profile of a representative sample of the 33 local ($z < 0.2$) clusters with $10^{14}\,\mathrm{M}_{\odot} < M_{500} < 10^{15}\,\mathrm{M}_{\odot}$ from the REXESS sample (Böhringer et al., 2007). Arnaud et al. (2010) reconstructed the pressure profiles from the 3D gas density and temperature profiles, $n_{\mathrm{e}}(r)$ and $T(r)$, as $P(r) = n_{\mathrm{e}}(r)\, k_{\mathrm{B}} T(r)$. The 3D gas density profiles were derived by Croston et al. (2006) from XMM-Newton observations of the clusters' surface brightness profiles using a non-parametric deprojection technique. The 3D temperature profiles were obtained by Arnaud et al. (2010) by fitting the parametric model presented by Vikhlinin et al. (2006) to XMM-Newton X-ray spectroscopic temperature maps of the clusters, taking into account projection and PSF effects. The obtained pressure profiles were scaled by their characteristic pressure $P_{500}$ and radius $R_{500}$ using the standard self-similar model. Since the XMM-Newton data were only able to measure $P(r)$ out to $\sim R_{500}$ and a comparison with the pressure profile of simulated clusters from hydrodynamical simulations showed good agreement for $r \gtrsim 0.2\,R_{500}$, Arnaud et al. (2010) used the average profile of simulated clusters to constrain the pressure profile at large radii. This scaled and averaged hybrid-profile is referred to as the *universal pressure profile* (UPP) by Arnaud et al. (2010)

[1] The concentration parameter $c_{500}$ is not to be confused with the concentration parameter $c$ of the NFW-profile.

and was modelled using

$$\begin{aligned} P(r) &= P_{500} \left[ \frac{M_{500}}{3 \times 10^{14}\, h_{70}^{-1}\, \mathrm{M}_\odot} \right]^{\alpha_\mathrm{p}+\alpha'_\mathrm{p}(x)} \mathcal{P}(x) \\ &= 1.65 \times 10^{-3} E(z)^{8/3} \left[ \frac{M_{500}}{3 \times 10^{14}\, h_{70}^{-1}\, \mathrm{M}_\odot} \right]^{2/3+\alpha_\mathrm{p}+\alpha'_\mathrm{p}(x)} \mathcal{P}(x) \;\; h_{70}^2\, \mathrm{keV\,cm^{-3}}, \end{aligned} \tag{1.70}$$

where $\alpha_\mathrm{p} = 0.12$ and

$$\alpha'_\mathrm{p}(x) = 0.10 - (\alpha_\mathrm{p} + 0.10) \frac{(x/0.5)^3}{1 + (x/0.5)^3} \tag{1.71}$$

account for deviations from the predicted self-similar evolution of the characteristic pressure of clusters. The individual cluster profiles and the best-fit model are shown in Fig. 1.15. The best-fit profile parameters reported by Arnaud et al. (2010) are

$$(P_0, c_{500}, \gamma, \alpha, \beta) = (8.403\, h_{70}^{-3/2}, 1.177, 0.3081, 1.0510, 5.4905). \tag{1.72}$$

This specific profile is used on many occasions throughout this work to simulate the expected SZ effect signal from galaxy clusters. Since parameter uncertainties were unfortunitly not provided by Arnaud et al. (2010), the values given above are considered to be exact.

The pressure profile of clusters has also been investigated by the Planck Collaboration (2013a), who used SZ effect data from the *Planck* 14-month nominal survey of a sample of 62 nearby massive clusters and found their average profile to be flatter at large radii compared to the *universal pressure profile* reported by Arnaud et al. (2010). While *Planck* was able to measure the pressure profile to a maximum radius of $\sim 3\, R_{500}$, its low spatial resolution does not allow to resolve the core of the clusters in the sample. For that reason, additional pressure data reconstructed from X-ray observations with XMM-Newton was used by the Planck Collaboration (2013a) at $0.01 < R_{500} < 1$. Keeping the inner slope $\gamma$ fixed to the value reported by Arnaud et al. (2010), their best-fit parameter values are $(P_0, c_{500}, \gamma, \alpha, \beta) = (6.41, 1.81, 0.31, 1.33, 4.13)$.

Other recent studies have focussed exclusively on measuring the outer slope $\beta$ of the GNFW model, while keeping the other parameters fixed to the ones given in equation (1.72). Ramos-Ceja et al. (2015) report $\beta = 6.35 \pm 0.19$ obtained from an analysis of the thermal SZ power spectrum measured by the SPT-SZ survey. A similar value of $\beta = 6.13 \pm 0.16$ was obtained by Sayers et al. (2016) using a combination of SZ effect data from *Planck* and the ground-based Bolocam receiver on the APEX telescope.

### 1.6.5 Galaxy clusters as probes for cosmology

Cosmological models are commonly tested either by constraining the distance-redshift relation using standard candles or rulers, or by measuring the evolution of structures. Galaxy clusters can be used in both ways through a variety of techniques, which is briefly summarized in the following. A comprehensive review on cosmological tests with galaxy clusters is given by Allen et al. (2011)

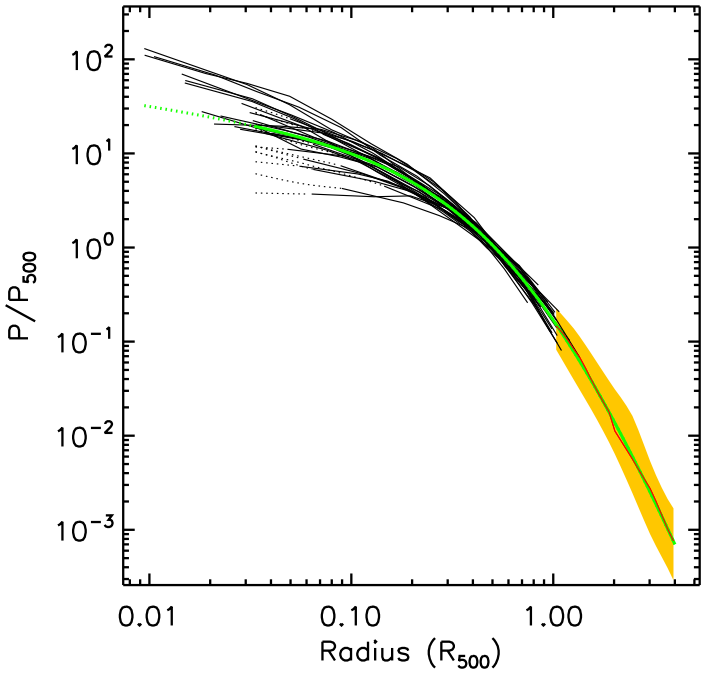


Figure 1.15: Best-fitting GNFW model of the *universal pressure profile* (green line) that has been derived from the average of the scaled pressure profiles of the clusters in the REXESS sample (black lines), combined with the average profile obtained from simulated clusters beyond $R_{500}$ (red line). The orange area indicates the dispersion of the pressure profile of the simulated clusters. For $r \gtrsim 0.2\,R_{500}$, observed and simulated profiles are found to be in good agreement and show low scatter. At smaller radii, the observed profiles show large scatter due to differences in the dynamical state of the clusters in the sample. The figure has been adopted from Arnaud et al. (2010).

### Cluster counts

The number density of galaxy clusters provides a sensitive probe of the high-mass end of the HMF (see Fig. 1.16), which was introduced in Section 1.5. In general, a single high-mass cluster that is incompatible with the halo mass function computed for a given cosmology can be sufficient to falsify it. Using galaxy cluster number counts requires accurate mass estimates, which are often obtained using scaling relations that relate low-scatter mass-proxies like the X-ray luminosity $L_X$ and the integrated SZ signal $Y_{SZ}$, both of which are easy to measure, to the total halo mass. These scaling relations are calibrated using small samples of clusters that have direct constraints on their masses. The mass of a cluster can be directly measured in multiple ways, e.g.

- **X-ray hydrostatic mass:** If left undisturbed, the ICM of a cluster settles into hydrostatic equilibrium between the pressure gradient of the gas and the gravitational potential $\Phi(r)$:

$$\frac{1}{\rho_g(r)}\,\frac{\mathrm{d}P(r)}{\mathrm{d}r} = -\frac{\mathrm{d}\Phi(r)}{\mathrm{d}r}. \tag{1.73}$$

  Assuming the ICM can be described as an ideal gas, the hydrostatic mass of a cluster can be

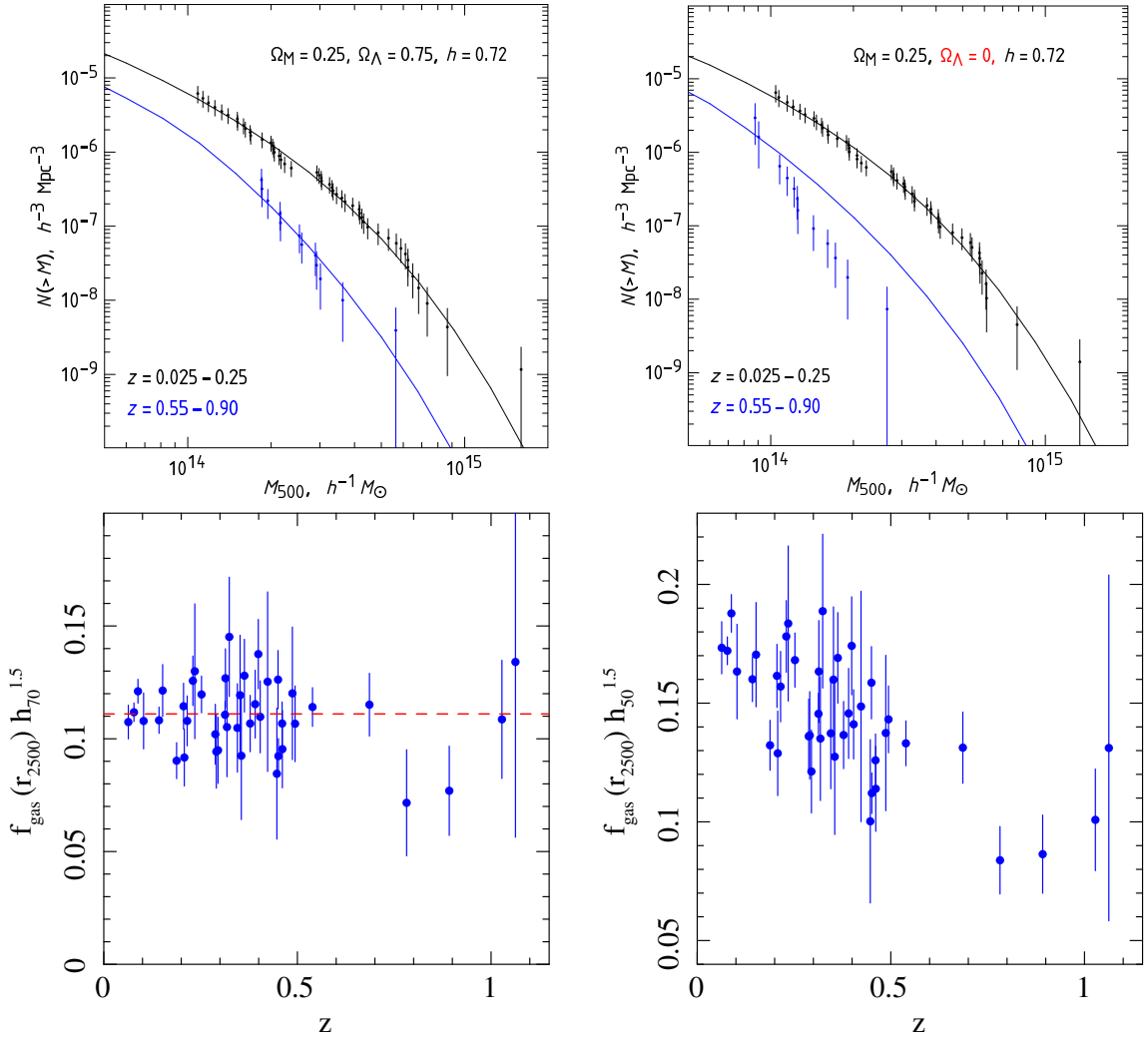


Figure 1.16: Examples of cosmological tests using samples of galaxy clusters. **Top panels:** Constraints on the halo mass function using galaxy clusters. The blue and black solid lines indicate the predicted function at two different redshift ranges. The right-hand panel shows the predicted curves for a ΛCDM cosmology that fits the observed data well, while the left-hand panel shows curves that are derived for an open universe with $\Omega_\Lambda = 0$, which does not fit the data. The two panels were adopted from Vikhlinin et al. (2009). **Bottom panels:** Measurements of the gas mass fraction $f_{\rm gas}$ of galaxy clusters. The left-hand panel shows $f_{\rm gas}$ for a sample of clusters derived using a flat ΛCDM cosmology with $\Omega_m = 0.3$, $\Omega_\Lambda = 0.7$, and $h = 0.7$. The obtained values for $f_{\rm gas}$ show no evolution with redshift, which is consistent with expectations and suggests the assumed cosmology describes our Universe well. The $f_{\rm gas}$ values shown in right-hand panel were obtained using an EdS cosmology with $\Omega_m = 1.0$, $\Omega_\Lambda = 0$, and $h = 0.5$. The resulting redshift evolution is neither supported by theory nor simulations and is therefore an artefact caused by a mismatch in real and assumed cosmology. The two panels were adopted from Allen et al. (2008).

derived from the previous equation and is given by

$$M(< r) = -\frac{k_\mathrm{B} T\, r}{\mathrm{G}\, \mu\, m_\mathrm{p}} \left( \frac{\mathrm{d}\ln(\rho_\mathrm{g}(r))}{\mathrm{d}\ln(r)} + \frac{\mathrm{d}\ln(T(r))}{\mathrm{d}\ln(r)} \right). \tag{1.74}$$

The required gas density and temperature profiles of the ICM can be derived from observations of the X-ray surface brightness and the measured X-ray spectra in concentric annuli around a cluster's centre. A problem with this method is the fact that the ICM is never truly in hydrostatic equilibrium because of the continued growth of clusters through mergers, gas accretion, turbulence, and gas flows induced by radiative cooling. These effects, together with other phenomena like non-thermal pressure support, give rise to the hydrostatic mass bias, the characterization of which is an ongoing area of research (e.g. Nelson et al., 2014).

- **Dynamical mass:** The observed velocity dispersion $\sigma$ of cluster member galaxies can be related to the total mass of the galaxy clusters via the virial theorem, which yiels the expression

$$M \propto \frac{r\sigma^2}{\mathrm{G}}. \tag{1.75}$$

- **Weak gravitational lensing:** The light of distant background galaxies is deflected by in the curved spacetime in the gravatational potential of galaxy cluster, leading to images that are displaced, distorted, magnified and sometimes appear multiple times. These effects define the *strong*-regime of gravitational lensing, which is observed in the centres of clusters. In their outskirts, *weak gravitational lensing* leads to more subtle changes in the shapes of background galaxies, which can only be measured statistically using large samples. Mapping these distortions allows us to reconstruct the total mass of a cluster, as well as its mass distribution. In general, masses estimated using gravitational lensing are considered to be the most accurate since they don't hold any assumption on the dynamical state of clusters. Recent studies have found mass estimates obtained through weak gravitational lensing to be higher than X-ray hydrostatic masses by up to 20% (e.g. Hoekstra et al., 2015; von der Linden et al., 2014c), which is attributed to the aforementioned hydrostatic mass bias.

For precise cosmological tests using cluster counts, any potential bias in the mass calibration needs to be carefully characterized and modelled. Furthermore, the selection function of the cluster survey must be understood in order to estimate the completeness of the cluster sample. A survey is considered complete if all clusters in the surveyed volume are detected down to a specified lower mass limit. Recent examples for cosmological studies with cluster counts include Planck Collaboration (2014c, 2016f) and Schellenberger & Reiprich (2017).

#### Angular diameter distance

Both X-ray and SZ effect observations trace the same free thermal electrons in the ICM. While the X-ray surface brightness is proportional to $n_\mathrm{e}^2$, the signal of the thermal SZ effect is proportional to $n_\mathrm{e}$. It can be shown that the angular diameter distance of a cluster can be derived from a combination of X-ray and SZ effect observations. Assuming an isothermal $\beta$-model for the density profile of the ICM,

one finds

$$D_{\mathrm{A}} \propto \frac{y_0^2}{S_{\mathrm{X}}(0)} \frac{1}{T_{\mathrm{e}}^2 (1+z)^4 \theta_{\mathrm{c}}}, \tag{1.76}$$

where $y_0$ is the observed central Comptonization parameter (the thermal SZ amplitude), $S_{\mathrm{X}}(0)$ is the observed central X-ray surface brightness, and $\theta_{\mathrm{c}}$ is the angle corresponding to the core radius $r_{\mathrm{c}}$ of the $\beta$-model. Equivalent expressions can be found for other density and temperature profiles for the ICM. However, this technique assumes clusters to be spherical. This approach has been used by many authors to estimate the value to the Hubble parameter $H_0$ (e.g. Bonamente et al., 2006; Kozmanyan et al., 2019), but, in general, allows to measure the expansion history of the Universe and therefore other parameters like the $\Omega_{\mathrm{m}}$, $\Omega_{\Lambda}$, and $w$.

#### $f_{\mathrm{gas}}$-test

The matter content of large galaxy clusters is thought to reflect the average matter content of the Universe. The observed baryon-to-total mass of clusters should therefore closely match the ratio $\Omega_{\mathrm{b}}/\Omega_{\mathrm{m}}$. If combined with independent measurements of the baryon density of the Universe, e.g. via constraints from the CMB or BBN, X-ray measurements of the gas mass fraction $f_{\mathrm{gas}}$ allow a direct and simple way to determine the total matter density $\Omega_{\mathrm{m}}$ of the Universe, which provided first evidence for $\Omega_{\mathrm{m}} < 1$ (White et al., 1993).

Furthermore, as first described by Sasaki (1996) and Pen (1997), measurements of $f_{\mathrm{gas}}$ can be used to constrain the expansion history of the Universe. This arises from the dependence of X-ray measurements of $f_{\mathrm{gas}}$ on the angular diameter distance to clusters:

$$f_{\mathrm{gas}}(z) \propto D_{\mathrm{A}}(z)^{3/2}. \tag{1.77}$$

The theory of structure formation and cosmological simulations both predict $f_{\mathrm{gas}}$ to be invariant with redshift for the largest clusters (Eke et al., 1998) and an observed apparent evolution would therefore reveal a mismatch in assumed and true underlying cosmology (see Fig. 1.16). This method was used by Allen et al. (2004) to provide first evidence from galaxy clusters for a universe dominated by dark energy. More recent results include e.g. Allen et al. (2008) and Mantz et al. (2014, see Fig. 1.3).

## 1.7 The Sunyaev-Zeldovich effect

The *Sunyaev-Zeldovich* (SZ) effect is a secondary anisotropy of the CMB that was first predicted by Rashid Sunyaev and Yakov Zeldovich (Sunyaev & Zeldovich, 1970, 1972). It is caused by the scattering of CMB photons by energetic free electrons in the ICM, which leads to a characteristic distortion of the SED of the CMB towards galaxy clusters. A schematic illustration of this process is shown in the left-hand panel of Fig. 1.17. This process conserves the number of photons that we receive from the CMB in the direction of a cluster since, on average, for every photon that is scattered away from our *line of sight* (l.o.s.) another photon that would not have reached us otherwise is scattered towards us. The SZ effect can be divided into several sub-components, the most important of which being the *thermal* SZ (tSZ), *kinetic* SZ (kSZ) and *non-thermal* SZ (ntSZ) effects. The combined signal is observed as fluctuations of the observed CMB temperature (see right-hand panel of Fig. 1.17), the amplitude of which is independent of the redshift of the source. The redshift invariance stems from

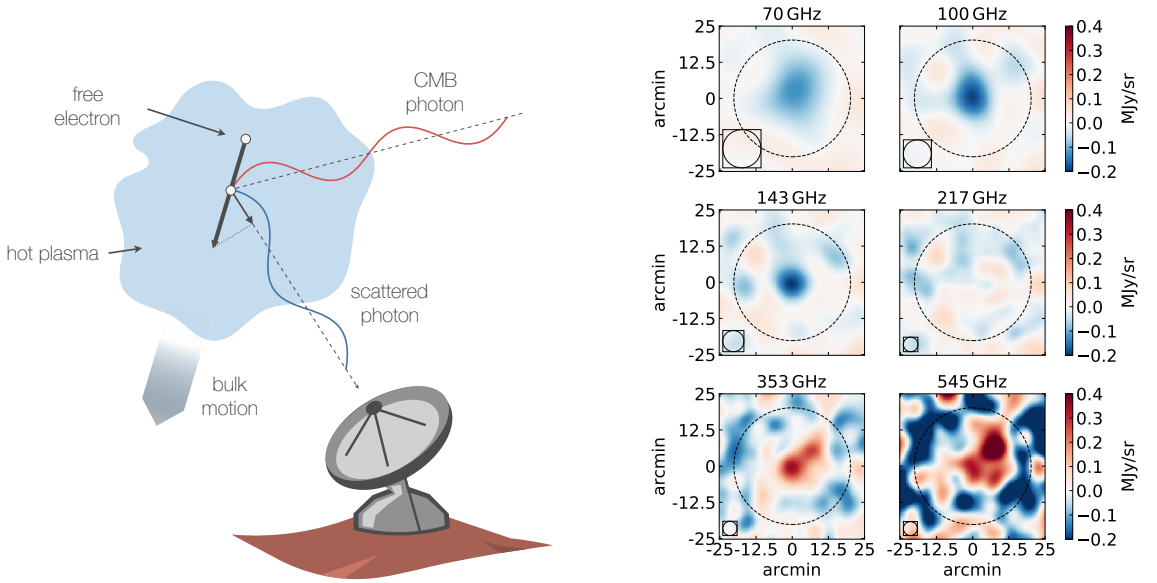


Figure 1.17: **Left-hand panel:** Illustration of the mechanism that gives rise to the Sunyaev-Zeldovich effect, adopted from Mroczkowski et al. (2019). A CMB photon (red) enters a galaxy cluster in a random direction and interacts with a free electron (black) of the ICM of the cluster via Compton scattering, leading to a deflection of the photon's trajectory and, on average, a small gain in energy of the outgoing photon (blue). While the thermal SZ effect is due to the random thermal motions of the ICM electrons, the kinetic SZ effect is due to any superimposed bulk motion of clusters in the rest frame of the CMB and allows to measure the l.o.s. component of that motion. **Right-hand panel:** *Planck* observations of the SZ signal of the massive galaxy cluster Abell 2319 at $z = 0.0557$. The characteristic spectral signature of the tSZ effect is clearly visible, with a decrement in observed intensity at 70-143 GHz, no signal at 217 GHz, and an increment in intensity at 353 & 545 GHz. The dashed black circles indicate the clusters $\theta_{500} = 20$ arcmin that has been derived from its mass measured by *Planck*. The maps are centred at (RA, Dec.) = (19h21m9.6s, +43°58′29.5″).

the fact that both the scattered and unscattered CMB cools at the same rate with the expansion. The contrast introduced by the SZ effect is therefore preserved. The characteristic spectral shape of the SZ effect is shown in Fig. 1.18 and broken down into its most relevant components.

This section introduces the central components of the SZ effect, with special attention to the tSZ effect and its relativistic corrections, which are a central aspect of this work. Excellent reviews on the theory and observations of the SZ effect are presented by Sunyaev & Zeldovich (1981), Birkinshaw (1999), Carlstrom et al. (2002), and Mroczkowski et al. (2019).

### 1.7.1 The thermal Sunyaev-Zeldovich effect

For typical galaxy clusters, the tSZ effect is the dominent component of the SZ effect. It is caused by Compton scattering of CMB photons by the thermal electrons in the ICM that follow an isotropic Maxwell–Boltzmann distribution. These elastic collisions transfer a small amount of the momentum from an electron to a photon, leading to a deflection of the photon path and a gain in energy. The maximum photon energy after scattering occurs for photons that are back-scattered after a head on collision with a free electron, while the lowest transfer of momentum occurs for photons scattered into the same direction as the incoming electron. The impact on the energy and trajectory of the scattered

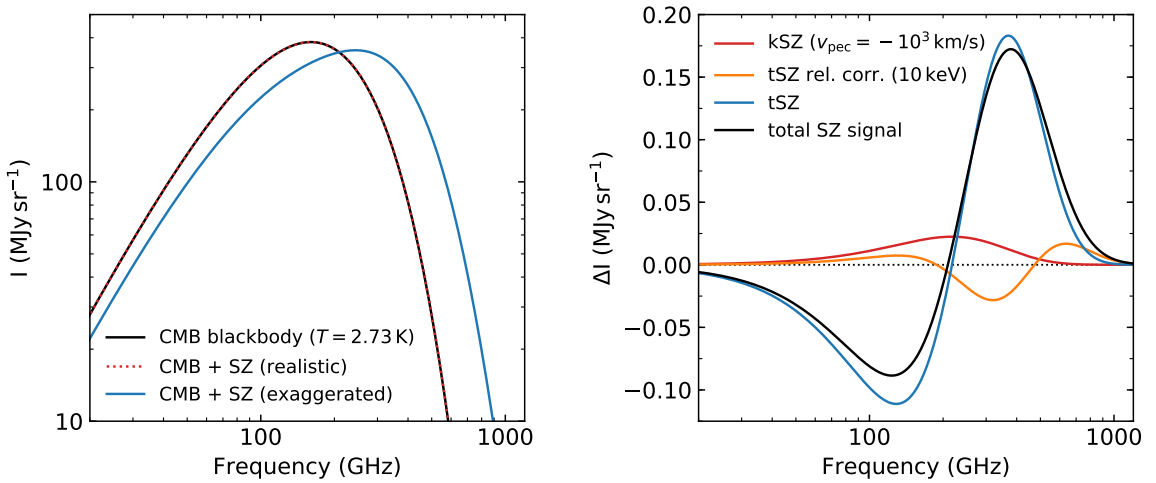


Figure 1.18: **Left-hand panel:** Comparison of the average ≈ 2.73 K CMB blackbody spectrum (black solid line) and the distorted CMB spectrum towards a massive galaxy cluster caused by the SZ effect (red dotted line). This realistic picture demonstrates that the distortion caused by the SZ effect is very small and therefore exaggerated by a factor of 1000 (blue solid line) in order to make the spectral changes visible. At frequencies below ∼ 217 GHz, the SZ effect causes a decrement in observed intensity compared to the average CMB and an increment in observed intensity at frequencies above. By subtracting the average CMB blackbody, clusters therefore become visible as CMB cold spots at low and CMB hot spots at high frequencies, as seen in the observations of Abell 2319 shown in the right-hand panel of Fig 1.17. **Right-hand panel:** Change in observed intensity of the CMB caused by the SZ effect. The total SZ signal shown in black represents the difference of the distorted (red dotted line) and undistorted CMB in the left-hand panel. The total SZ signal shown here is the sum of the tSZ effect for $y = 10^{-4}$ (blue line), the corresponding tSZ relativistic corrections for $k_B T_e = 10$ keV (orange line) and the kSZ signal for $v_{pec} = -1000$ km/s (red line).

electron is neglectable. This process is commonly referred to as *inverse* Compton scattering and gives rise to the other components of the SZ effect as well. About 1% of the CMB photons that cross through the ICM of a cluster scatter of an electron. Multiple scatterings are therefore rare and usually not considered.

As the photons propagate through the ICM and scatter of electrons, they are uplifted to higher energies. At frequencies below ∼ 217 GHz, this redistribution of photon energies is observed as a characteristic decrement in CMB temperature compared to the unscattered reference CMB in the direction of a galaxy cluster. At frequencies above ∼ 217 GHz, it causes an increment in observed temperature compared to the unscattered reference CMB. This frequency-dependent shift in observed temperature $\Delta T_{tSZ} = T(\nu) - T_{CMB}$ is commonly expressed by

$$\frac{\Delta T_{tSZ}}{T_{CMB}} = y\, f(x), \tag{1.78}$$

where $x(\nu) = h\nu/(k_B T_{CMB})$ is the dimensionless frequency and $f(x)$ gives the frequency dependence of the tSZ effect in the non-relativistic limit:

$$f(x) = x\frac{e^x + 1}{e^x - 1} - 4. \tag{1.79}$$

The tSZ signal is proportional to the *Compton-y parameter*, which is a dimensionless measure of the electron pressure $P_e = n_e k_B T_e$ integrated along the l.o.s.:

$$y = \frac{\sigma_T}{m_e c^2} \int_{\text{l.o.s.}} P_e(r)\, \mathrm{d}l. \tag{1.80}$$

Here, $k_B$ is the Boltzmann constant, $T_e$ is the electron temperature, $m_e$ is the rest mass of the electron, $\sigma_T$ is the Thomson cross section, and $h$ is Planck's constant. Note that the Compton-$y$ parameter is not just a single number for a given cluster, but rather corresponds to a 2D projected image $y(x_1, x_2)$ of the electron pressure, which is similar in its concept to the X-ray surface brightness. A Compton-$y$ map of a cluster can be simulated by l.o.s. projection of a model for the cluster's pressure profile, like the GNFW-model that was introduced in Section 1.6.4 (see Appendix A.4). Typical peak values observed along the central l.o.s. of massive clusters are $\sim 10^{-4}$, leading to a distortion $\Delta T_{tSZ}/T_{CMB}$ of the same order of magnitude, which is shown in the left-hand panel of Fig. 1.18.

Using the derivative of the CMB blackbody SED (see Appendix A.1), the shift in CMB temperature introduced by the tSZ effect can be converted to a shift in observed intensity via

$$\Delta I = \Delta T \left.\frac{\partial B(\nu, T)}{\partial T}\right|_{T=T_{CMB}}, \tag{1.81}$$

which leads to

$$\frac{\Delta I_{tZE}}{I_0} = y f(x) h(x), \tag{1.82}$$

where $I_0 = 2(k_B T_{CMB})^3/(hc)^2 \approx 270\,\mathrm{MJy/sr}$, and

$$h(x) = \frac{x^4 e^x}{(e^x - 1)^2}. \tag{1.83}$$

The characteristic frequency-dependent shift of observed CMB intensity towards a massive cluster can be seen in the *Planck* observations of Abell 2319 shown in the right-hand panel of Fig. 1.17.

Unlike the X-ray surface brightness of clusters, the tSZ signal is not dimmed with redshift, making it an ideal tool for the detection and characterization of clusters at high $z$. The integrated Compton-$y$ parameter $Y_{SZ}$ is an important mass-proxi for cosmological studies and can be defined in multiple ways (see Section A.3), e.g. via the aperture integral over the observed Compton-$y$ radial profile $y(\theta)$.

$$Y_{SZ}(< \theta_{max}) = 2\pi \int_0^{\theta_{max}} y(\theta)\theta\, \mathrm{d}\theta. \tag{1.84}$$

### 1.7.2 The kinetic Sunyaev-Zeldovich effect

The kSZ effect is caused by scattering of CMB photons by a population of hot electrons that undergoes bulk motion relative to the CMB rest-frame (Sunyaev & Zeldovich, 1980). In that case, the velocity distribution of the electrons is no longer isotropic, which leads to a linear Doppler term that is proportional to the velocity $\beta = v/c$ of the electrons. Like the tSZ effect, the kSZ effect leads to a shift in observed CMB temperature towards a cluster with a non-zero l.o.s. peculiar velocity. Unlike the tSZ effect, the kSZ temperature fluctuations are independent of observed frequencies and can be

written as

$$\frac{\Delta T_{\mathrm{kSZ}}}{T_{\mathrm{CMB}}} = -\tau_{\mathrm{e}} \frac{v_{\mathrm{pec}}}{\mathrm{c}}, \tag{1.85}$$

which can be written as a frequency-dependent shift in observed intensity using equation (1.81),

$$\frac{\Delta I_{\mathrm{kSZ}}}{I_0} = -\tau_{\mathrm{e}} \frac{v_{\mathrm{pec}}}{\mathrm{c}} h(x), \tag{1.86}$$

where $v_{\mathrm{pec}}$ is the l.o.s. component of the peculiar velocity and $\tau_{\mathrm{e}}$ is the *optical depth*, which is defined as the l.o.s. integral over the electron number density

$$\tau_{\mathrm{e}} = \sigma_{\mathrm{T}} \int_{\mathrm{l.o.s.}} n_{\mathrm{e}}(r)\, \mathrm{d}l. \tag{1.87}$$

For isothermal clusters, the optical depth and Compton-$y$ parameters are related as $y = \tau_{\mathrm{e}} k_{\mathrm{B}} T_{\mathrm{e}} / (m_{\mathrm{e}} \mathrm{c}^2)$. The kSZ signal either appears as a CMB cold spot ($v_{\mathrm{pec}} > 0$) or a CMB hot spot ($v_{\mathrm{pec}} < 0$), making its spectral signature indistinguishable from that of primary CMB temperature fluctuations to first order, requiring either spatial information or the correlation with other data sets for a detection. Typical cluster peculiar velocities are expected to be a around several 100 km/s (e.g. Peel, 2006). The value of $\tau$ lies in the range of $10^{-3}$ to $\sim 10^{-2}$ for massive clusters, resulting in a signal that is lower than that of the tSZ effect by ∼one order of magnitude.

### 1.7.3 Relativistic corrections to the tSZ and kSZ effects

The tSZ and kSZ signals introduced previously are derived assuming the scattering electrons move at non-relativistic speeds. The expected bulk motion of clusters satisfies this assumption well enough, with typical speeds of $v_{\mathrm{pec}}/\mathrm{c} \sim 10^{-3}$. However, at the temperatures found in the ICM, the thermal motion of the electrons is mildly relativistic with $\beta = v/\mathrm{c} \sim 0.1$. In this case, the non-relativistic approximations are no longer valid and special-relativistic corrections are required in order to accurately describe the spectral shape of the tSZ and kSZ effects (e.g. Wright, 1979; Rephaeli, 1995). Since the change in the kSZ spectrum is ∼one order of magnitude smaller than the change in the tSZ spectrum, we focus on the latter. The relativistic tSZ spectrum can be written as

$$f(x, T_{\mathrm{e}}) = \left( x \frac{e^x + 1}{e^x - 1} - 4 \right) + \delta_{\mathrm{rel}}(x, T_{\mathrm{e}}). \tag{1.88}$$

The relativistic corrections $\delta_{\mathrm{rel}}(x, T_{\mathrm{e}})$ of the tSZ effect are obtained by assuming the scattering electrons follow an isotropic Maxwell–Jüttner distribution (Jüttner, 1911a,b), which is the special-relativistic generalisation of the Maxwell–Boltzmann distribution. The resulting modified spectrum can no longer be derived analytically. Its computation requires to solve the 5D collision integral using numerical integration techniques, providing accurate results (e.g. Wright, 1979; Rephaeli, 1995; Pointecouteau et al., 1998; Enßlin & Kaiser, 2000). Although the dimensionality of the collision integral can be reduced by the use of symmetries, computing the relativistic SZ spectrum via direct integration techniques can be very time consuming. Some authors have provided fitting functions to numerical results (e.g. Nozawa et al., 2000) or finite-order asymptotic series expansions (e.g. Challinor & Lasenby, 1998; Sazonov & Sunyaev, 1998; Itoh et al., 1998) that give good results for $k_{\mathrm{B}} T_{\mathrm{e}} \lesssim 5\,\mathrm{keV}$.

In this work, we make use of SZPACK (Chluba et al., 2012, 2013), which allows the fast and precise computation of the relativistic corrections using pre-computed basis functions.

The relativistic corrections introduce a temperature dependence to the spectrum of the tSZ effect, which is shown in Fig. 4.1. With increasing temperature, the tSZ null shifts towards higher frequencies, the amplitude of both the tSZ decrement and increment is lowered (e.g. by $\sim 10\%$ for $k_\mathrm{B}T_\mathrm{e} = 10\,\mathrm{keV}$), and the increment becomes broader. Precise observations of the spectrum of the tSZ effect of clusters would allow to measure the pressure-weighted l.o.s. averaged temperature $T_\mathrm{SZ}$ of the scattering gas (e.g. Pointecouteau et al., 1998; Hansen, 2004)

$$T_\mathrm{SZ} \approx \langle T_\mathrm{e} \rangle_{P_\mathrm{e}} = \frac{\int_\mathrm{l.o.s.} n_\mathrm{e} T_\mathrm{e}^2 \,\mathrm{d}l}{\int_\mathrm{l.o.s.} n_\mathrm{e} T_\mathrm{e} \,\mathrm{d}l}. \tag{1.89}$$

### 1.7.4 Non-thermal and polarized SZ effects

Both the tSZ and kSZ effect introduced in the previous sections are due the scattering of CMB photons by the population of thermal electrons in the ICM. As was mentioned in Section 1.6.1, radio observations of radio halos and relics revealed that clusters harbour a population of highly relativistic particles. The scattering of CMB photons by this population of high-energy non-thermal electrons gives rise to the ntSZ effect (e.g. Enßlin & Kaiser, 2000). Assuming an isotropic power-law-shaped momentum distribution for the non-thermal electrons, the spectrum of the ntSZeffect shows a temperature/intensity decrement and increment. For relativistic electron energies, the zero-point shifts towards THz frequencies and the increment becomes much wider. Under extreme conditions, the ntSZ increment can even extend to X-ray frequencies, where it is just referred to as inverse-Compton (IC) emission (Felten & Morrison, 1966). However, the exact shape the ntSZ spectrum can become very complex and depends on the details of the energy distribution of the scattering electrons. It is estimated that the amplitude of the ntSZ effect typically is $\lesssim 1\%$ of that of the tSZ effect (Enßlin & Kaiser, 2000; Shimon & Rephaeli, 2002).

In the presence of a quadrupole anisotropy in the local radiation field, the scattering of CMB photons by free electrons leads to polarisation of the outgoing light (Sunyaev & Zeldovich, 1980, 1981). This mechanism is very similar to the one that gives rise to primordial $E$-mode polarization (Bond & Efstathiou, 1984). This *polarised* SZ (pSZ) effect is generated predominantly by the local primordial CMB quadrupole and is expected to reach a typical signal amplitude that is 10 000 times smaller than that of the tSZ effect. Furthermore, the frequency dependence of the pSZ effect is identical to that of primordial CMB polarisation anisotorpies, increasing the difficulty of a detection. If measured, it would allow to observe the primordial CMB quadrupole in the restframe of clusters, bypassing the limitations of cosmic variance (e.g. Meyers et al., 2018). Several other local quadrupole anisotropies could in principle give rise to a pSZ signal. Among these is a quadrupole that is induced by the peculiar motion of clusters inside the CMB restframe. The polarisation signal caused by the motion of the clusters could allow to measure the tangential component of their velocity vector on the plane of the sky (Sunyaev & Zeldovich, 1980).

### 1.7.5 Observations of the SZ effect

Early attempts of observing the SZ effect of clusters were conducted with radio telescopes at low-frequencies around 15 GHz, a few years after the effect was first postulated (e.g. Pariiskii, 1973;

Birkinshaw et al., 1978). The first unambiguous detection of the tSZ decrement of three clusters was reported by Birkinshaw et al. (1984), roughly one decade after the postulation of the SZ effect. The first observation of the tSZ increment became possible in the coming decade with observations by the PRONAOS balloon experiment, which observed the cluster Abell 2163 at 350 GHz Lamarre et al. (1998).

Driven by rapid progress in detector technology, the first large-scale SZ cluster surveys were conduced during the last decade by the South pole telescope (SPT), the Atacama cosmology telescope (ACT), and the *Planck* satellite , delivering sample sizes of several hundred (ACT & SPT) to ~ 1000 (*Planck*) objects (Hasselfield et al., 2013; Planck Collaboration, 2014d; Bleem et al., 2015).

In the advent of high-resolution single-dish and interferometric observations at millimetre and submillimetre wavelengths, the measurement of cluster sub-structures became feasible. Since the tSZ effect allows to measure the l.o.s. integral of the ICM pressure, it can provide constraints on pressure discontinuities like shockfronts, with several reported detections by e.g. Korngut et al. (2011), Planck Collaboration (2013b), Erler et al. (2015), Basu et al. (2016), and Di Mascolo et al. (2019).

With the tSZ effect being observed routinely today, attempts of measuring the other aspects of the SZ effect have intensified. To this date, robust evidence for the kSZ effect has only been presented for a single system, the l.o.s. triple merger MACS J0717.5+3745. Observations conducted by Sayers et al. (2013) find a $4.2\sigma$ measurement of the peculiar velocity of one of the merging sub-clusters with $v_{\rm pec} = (3450 \pm 900)\,{\rm km/s}$. However, the kSZ effect has been detected at higher significance using statistical methods by measuring the mean pairwise momentum of optically selected clusters (Hand et al., 2012).

Several attempts have been made to measure the relativistic distortions of the tSZ effect. A $3\sigma$ measurement of the shift of the tSZ null caused by the relativistic effects was reported by Zemcov et al. (2012) using data from the Z-spec instrument. Assuming a neglectable kSZ signal, the authors constrain the ICM temperature of the cluster RX J 1347.5-1145 to $(17.1 \pm 5.3)\,{\rm keV}$. Using data from the *Planck* satellite, Hurier et al. (2014) placed constrains on the average temperature of a sample of clusters in a study that focused on measuring the evolution of $T_{\rm CMB}$. Recently, Hurier (2016) claimed the first high-significance detection of the relativistic tSZ effect based on the analysis of the average spectrum of a large sample of clusters observed with *Planck*. Chapter 4 of this work presents the most recent attempt of detecting the relativistic tSZ effect of a stacked sample of galaxy clusters using data from the *Planck* satellite.

CHAPTER 2

# Instruments, tools, and techniques

## 2.1 The Planck mission

The European Space Agency's (ESA) *Planck* Surveyor (Tauber et al., 2010a) is the third-generation space telescope dedicated to observations of the CMB. Initially proposed as two instruments named the Cosmic Background Radiation Anisotropy Satellite (COBRAS) and the Satellite for Measurement of Background Anisotropies (SAMBA), which were competing for an medium-sized mission slot of ESA's Horizon 2000 program, the two collaborations were recommended to join their efforts and propose for a single telescope. The combined COBRAS/SAMBA mission (Tauber et al., 1994) was selected in 1996 as the third and final medium-sized mission of the Horizon 2000 program and was subsequently renamed *Planck*. It was launched on the 14$^{\text{th}}$ of May 2009 together with the *Herschel* Space Telescope onbord of an Ariane 5 ECA launch vehicle to the second Earth-Sun Lagrange Point $L_2$. An artist's impression of the spacecraft is shown in Fig. 2.1.

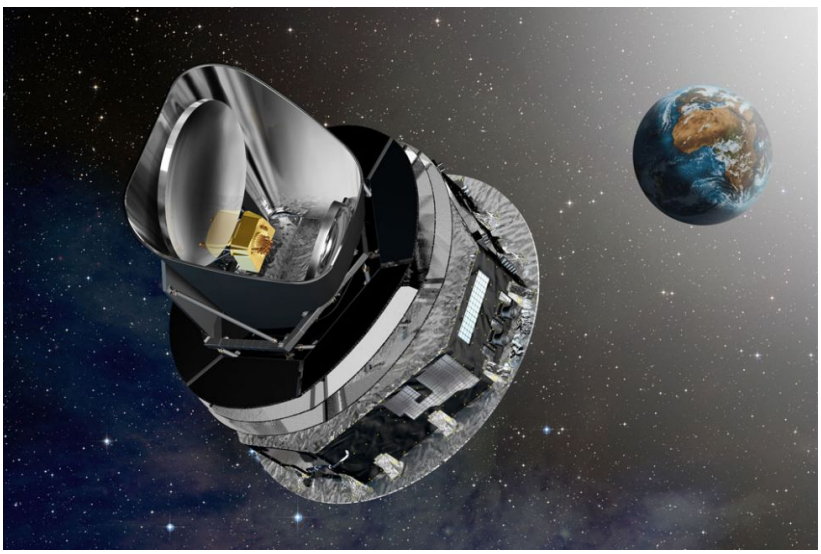

Figure 2.1: Artist's impression of the *Planck* satellite. *Planck* observed the microwave sky from the Sun-Earth Lagrange point $L_2$ from 2009 until 2013, completing multiple all-sky surveys. Credit: ESA

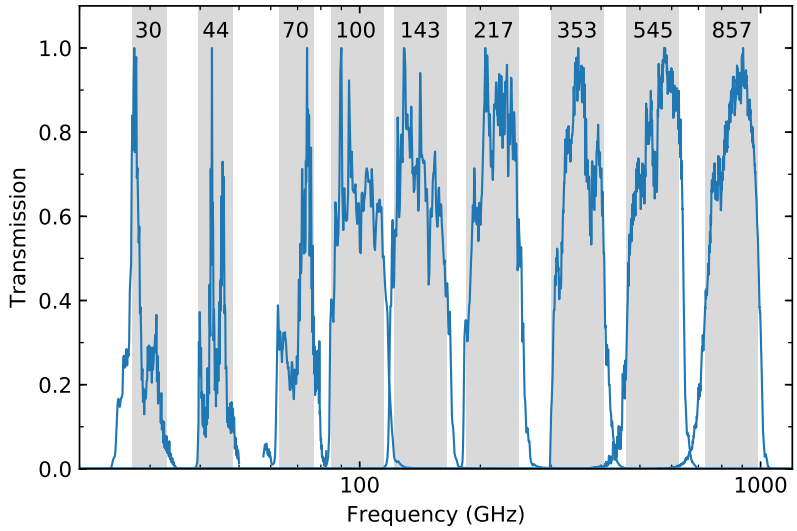


Figure 2.2: Transmission curves of the bandpass filters for the nine *Planck* frequency channels (blue curves). The grey boxes indicate the approximate width and position of the bands and are reproduced in Fig. 4.1 , 4.14, & 6.1.

From the $L_2$, *Planck* performed multiple six-month all-sky surveys in nine distinct frequency bands grouped in two main instruments. *Planck's* Low Frequency Instrument (LFI , Mandolesi et al. 2010) was derived from COBRAS and used actively-cooled pseudo-correlation radiometers that operated at a temperature of 20 K. It observed the sky at three frequency bands centred around 30, 44, and 70 GHz. The LFI was complemented by the High Frequency Instrument (HFI , Lamarre et al. 2010), which was based on SAMBA and observed in six bands centred at 100, 143, 217, 353, 545, and 857 GHz. The HFI used a total of 50 bolometers, which required active cooling to 0.1 K. The transmission curves of the bandpass filters of all nine channels are shown in Fig. 2.2. All three bands of the LFI and the first four bands of the HFI were sensitive to the linear polarization of the CMB. Both instruments shared the focal plane of *Planck's* off-axis Gregorian optics that featured an unblocked aperture of 1.5 m (Tauber et al., 2010b).

*Planck* started its first all-sky survey on the 13$^{th}$ of August 2009. Its nominal mission ended in November of 2010, after which *Planck's* operation was extended until the depletion of all cryogenic consumables. After completing its fifth all-sky survey, the HFI coolant supply exhausted on the 14$^{th}$ of January 2012, ending *Planck's* cryogenic mission. The LFI continued its operation and completed two additional all-sky surveys. The scientific mission finally ended in October of 2013, after which the spacecraft was subsequently de-orbited from the $L_2$ and placed in a heliocentric graveyard orbit.

*Planck*'s main scientific objective was to measure the angular power spectrum of the primary temperature and polarization anisotropies of the CMB with much higher sensitivity and spatial resolution compared to its predecessors COBE and WMAP. Besides its main science case, *Planck* left behind a rich scientific legacy, ranging from various source catalogs over the study of galaxy clusters detected via the tSZ effect to maps of galactic foregrounds and studies of the CIB.

The observational data obtained by *Planck* were published in multiple data releases. The first took place in 2013 and covered the data obtained during the 15 month nominal mission, excluding the

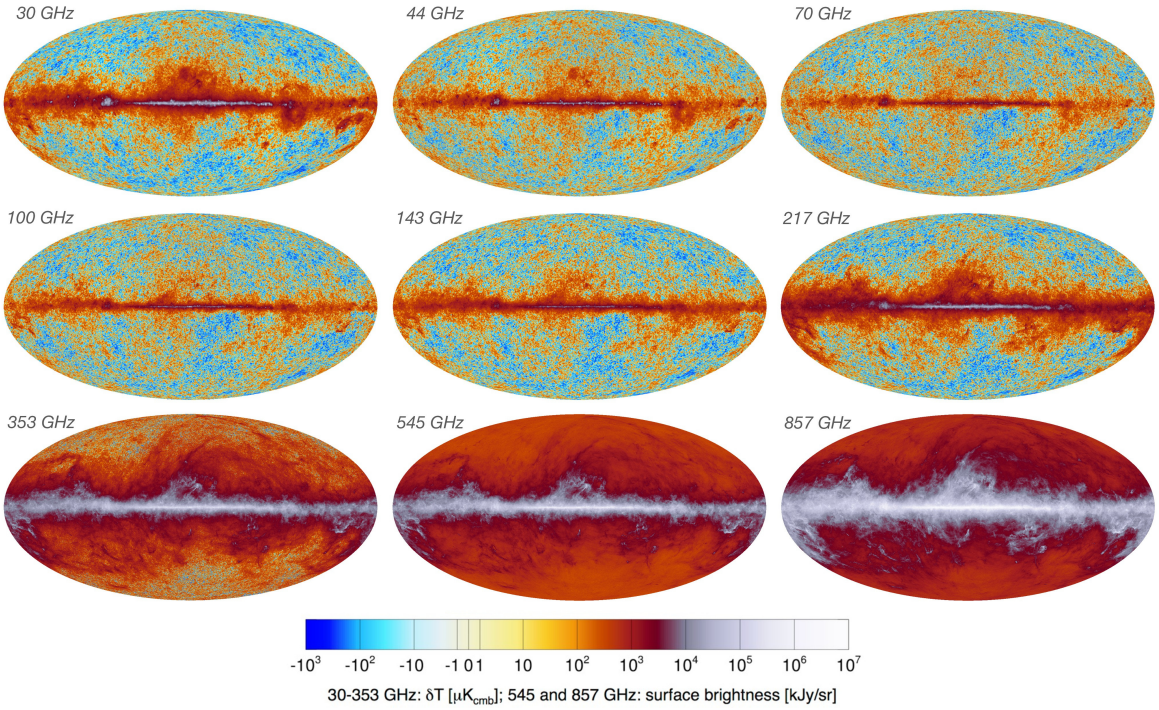


Figure 2.3: All-sky maps of the sky at microwave frequencies as seen by the *Planck* satellite after the removal of the monopole and dipole components. *Planck* observed the sky in nine different bands using two instruments. The *Planck* LFI observed the sky in three channels from 30 to 70 GHz, while the *Planck* HFI covered the range from 100 to 857 GHz using six channels. The maps are provided in units of temperature variation relative to the 2.73 K CMB blackbody up to 353 GHz to highlight variations in the SEDs of different sky components. The two highest frequencies are given in units of specific brightness. The images were taken from the Planck Collaboration (2018a).

polarization data (Planck Collaboration, 2014a). In 2015, the second data release contained all data that was collected during *Planck's* 50 months of observations with its LFI and 29 months with the HFI, including all polarization data (Planck Collaboration, 2016a). The final data release took place in 2018 and featured improved data processing and reduced systematics (Planck Collaboration, 2018a). The nine all-sky maps of the final data release are shown in Fig. 2.3. If not mentioned otherwise, some of the results presented in this work are based on *Planck* data products from the second data release.

## 2.2 CCAT-prime

CCAT-prime is a 6 m aperture survey telescope that will be constructed 40 m below the summit of the Cerro Chajnantor at an altitude of ~ 5600 m above sea level. This exceptional site is considered the best location for ground-based microwave observations (Bustos et al., 2014) and opens the possibility for observations in the terahertz regime, which can be seen in Fig. 2.4. CCAT-prime will be the first of a series of large aperture mm/sub-mm telescopes (e.g. the Simons Observatory large aperture telescope, Dicker et al. 2018) that deploy a high-throughput crossed-Dragone optical design proposed by Niemack (2016). These optics provide a large focal plane with a diameter of ~ 1.2 m and a field of

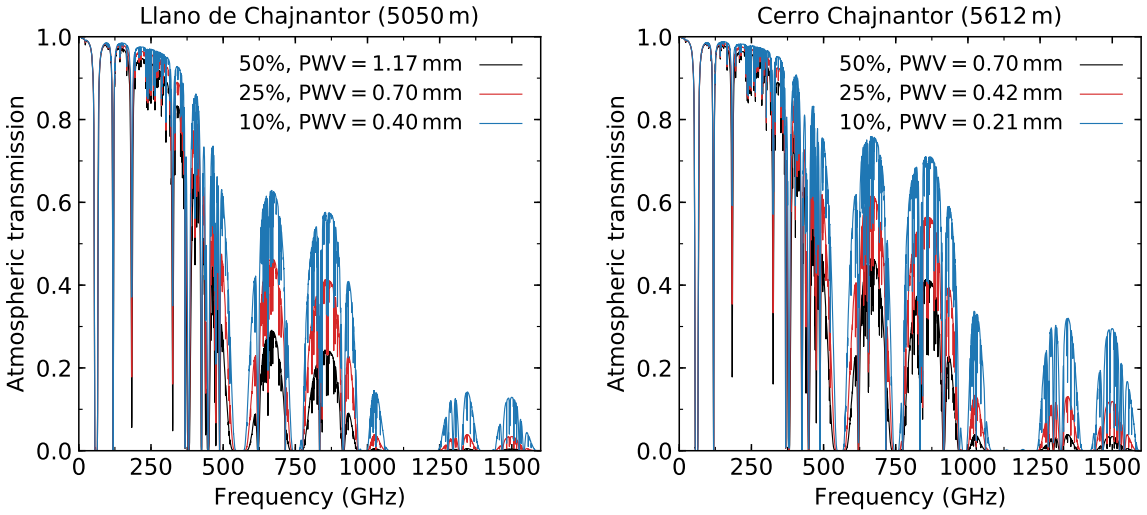


Figure 2.4: Atmospheric transmission in the millimetre and submillimetre regime at the ALMA site (Llano de Chajnantor; left-hand panel) and the Cerro Chajnantor (right-hand panel). The transmissions have been computed using the ATM model (Pardo et al., 2001), using measurements of the zenith optical depth at 350 $\mu$m presented by Bustos et al. (2014). The *black*, *red* and *blue* curves show the transmission for the 50%, 25% and 10% best weather quartiles, respectively. The weather conditions are quantified by the total atmospheric water vapour contained in a vertical column with an area of 1 m$^2$, known as *precipitable water vapour* (PWV), which is measured in millimetres. Although the ALMA site offers excellent conditions for observations at millimetre and submillimetre wavelengths the higher Cerro Chajnantor site provides clear advantages, especially in the terahertz windows.

view with a diameter of 7.8° at 100 GHz, allowing to illuminate large multifrequency instruments with up to $\sim 10^5$ detectors (Parshley et al., 2018b,a). The telescope is currently under construction with the contractor Vertex Antennentechnik GmbH in Duisburg, Germany. Fig. 2.5 shows the most recent computer aided design (CAD) study of CCAT-prime.

At first-light, which is currently expected to take place in 2021, CCAT-prime is going to host two primary instruments. The first instrument, Prime-Cam, houses up to seven instrument modules in a 1.8 metre diameter cryostat (Stacey, 2014; Vavagiakis et al., 2018). Each instrument module either hosts broadband dual-polarization detectors, or narrow-band detectors using a Fabry-Perot interferometer. The detectors are multichroic transition-edge sensor (TES) bolometers operating between 190 and 450 GHz and kinetic induction detectors (KIDs) operating at 860 GHz. The second instrument is the CCAT Heterodyne Array Instrument (CHAI), a dual colour (500 and 850 GHz) large format heterodyne array that serves as a high resolution spectrometer.

With its novel optics, cutting edge instruments and exceptional site, CCAT-prime will address five main science cases that have been presented by Stacey et al. (2018). These science cases are:

1. By providing high-frequency observations that complement the millimetre-wavelength observations by advanced ACT and the Simons Observatory, CCAT-prime allows the observation of the thermal and kinetic SZ effects of several thousands of galaxy clusters. These observations will advance our understanding of dark matter and dark energy, tighten the constraints on $\sigma_8$ and the sum of neutrino masses, expose feedback processes in the ICM, and reveal the nature of cluster

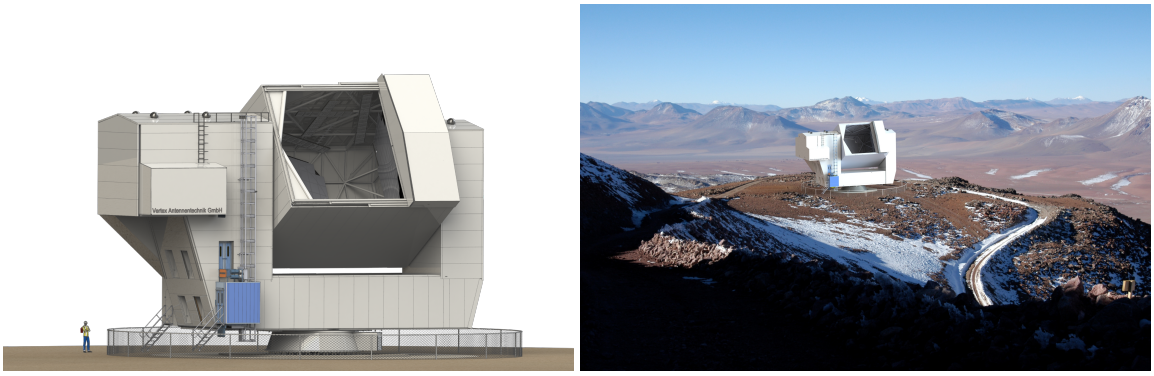

Figure 2.5: Illustrations of the CCAT-prime telescope. **Left-hand panel:** CAD study of the CCAT-prime telescope with a human to scale. CCAT-prime uses a crossed-Dragone optical system with an aperture of six metres, allowing for a large field of view of up to 7.8°at 100 GHz and a large and flat focal plane. **Right-hand panel:** Artist's impression of the assembled telescope close to the summit of the Cerro Chajnantor at an elevation of ~ 5600 m above sea level and about ~ 600 m above the ALMA site. Images courtesy of Vertex Antennentechnik GmbH.

FIR emission. Detailed forecasts for observations of galaxy clusters with CCAT-prime were conducted by Mittal et al. (2018) and Erler et al. (2018) and additional ones are presented in Chapter 6 of this work.

2. By mapping the emission of spectral lines over tens of square degrees and across a wide range of redshifts using a Fabry-Perot interferometer in conjunction with Prime-Cam, CCAT-prime will reveal the formation, evolution, and three dimensional large-scale clustering properties of the earliest star forming galaxies out to redshift ~ 9.

3. CCAT-prime will aid the search for primordial gravitational waves that are predicted by inflationary models by providing multi-frequency measurements of Galactic dust polarization.

4. Using its broad frequency coverage, CCAT-prime will perform photometric measurements of dusty star forming galaxies out to the epoch of galaxy formation more than 10 billion years ago, allowing to reconstruct the history of star formation across cosmic time.

5. CCAT-prime will investigate the physics of star formation in the Milky Way and nearby galaxies through spectrally resolved mapping of [CI] and CO line emission at high frequencies.

The first four science cases are addressed using Prime-Cam, while the Galactic ecology science case is investigated using CHAI.

CCAT-prime evolved from the previously proposed 25 m aperture Cerro Chajnantor Atacama Telescope (CCAT), which was supposed to operate at the same site but perform deeper, high resolution observations of smaller patches of the sky. Although it received high marks for the telescope concept and the proposed science case and was recommended in the Astro2010 report, *New Worlds, New Horizons in Astronomy and Astrophysics* (National Research Council, 2011), the CCAT consortium was not able to secure a key grant by the US National Science Foundation (NSF) in 2016, which lead to the fracturing and subsequent reformation of the consortium that gave birth to CCAT-prime within

the same year. Recently, new efforts for a future European large aperture submillimetre telescope called the Atacama Large-Aperture Submm/mm Telescope (AtLAST)[1] have been initiated.

## 2.3 ILC techniques

An important technique that is used throughout this work for the extraction of Compton-$y$ maps from microwave observations or simulated observations of clusters are *internal linear combination* (ILC) algorithms. ILC algorithms are simple and elegant so-called semi-blind approaches to data reduction. In its simplest form, an ILC algorithm only requires accurate knowledge of the SED of the targeted astrophysical signal like the CMB or the tSZ effect. The SED of other contaminating astrophysical signals like Galactic foregrounds and extragalactic backgrounds are estimated in a non-parametric approach from the empirical covariance of observations at multiple frequencies. The method therefore requires no prior information or external data from other instruments, which coined the term "internal". The original ILC algorithm allows for the extraction of a single component and was first introduced by Bennett et al. (2003) for the extraction of CMB maps from WMAP data. In the advent of the *Planck* mission, the ILC algorithm was further developed and generalised to allow for the extraction/suppression of multiple components (Tegmark et al., 2003; Delabrouille et al., 2013; Remazeilles et al., 2011a,b; Hurier et al., 2013) and the usage of spatial information (Remazeilles et al., 2011b; Hurier et al., 2013). This section provides the derivation of the single- and multi-component variants of the ILC algorithm and introduces basic concepts of spatial decomposition and all-sky data handling.

### 2.3.1 Single-Component ILC

The original ILC technique introduced by Bennett et al. (2003) allows for the extraction of a single component of interest based on its SED from a multifrequency data set and is based on two key assumptions:

1. The observed maps are a linear mixture of astrophysical components and instrumental noise.
2. The individual components of the maps are uncorrelated.

The first assumption states that the $N_\nu$ observed temperature maps $\mathbf{T}$ can be written for each pixel $p$ as

$$\boldsymbol{T}(p) = \boldsymbol{a}S(p) + \boldsymbol{N}(p), \tag{2.1}$$

where $\boldsymbol{a}$ is the mixing vector that contains the SED of the target component at the $N_\nu$ observed frequencies, $S(p)$ is a map that contains the target signal amplitude at each pixel, and $\boldsymbol{N}(p)$ is a vector that contains the remaining astrophysical signals and instrumental noise of the $N_\nu$ observations.

The goal of the ILC algorithm is to find a linear combination of the $N_\nu$ observed maps $\boldsymbol{T}(p)$, each multiplied with a specific weight $\omega_\nu$, that provides an unbiased and optimal estimate $\hat{S}_{\mathrm{ILC}}(p)$ of the target signal $S(p)$

$$\hat{S}_{\mathrm{ILC}}(p) = \boldsymbol{\omega}^{\mathrm{T}}\boldsymbol{T}(p) = \boldsymbol{\omega}^{\mathrm{T}}\boldsymbol{a}S(p) + \boldsymbol{\omega}^{\mathrm{T}}\boldsymbol{N}(p). \tag{2.2}$$

[1] More information on AtLAST can be found in the presentation slides from a recent ESO workshop at http://www.eso.org/sci/meetings/2018/AtLAST2018.html

Obtaining an unbiased estimate of the target signal therefore requires the ILC weights $\boldsymbol{\omega}$ to have unit response to the mixing vector $\boldsymbol{a}$

$$\boldsymbol{\omega}^{\mathrm{T}}\boldsymbol{a} = \boldsymbol{a}^{\mathrm{T}}\boldsymbol{\omega} = 1 \tag{2.3}$$

and minimize the impact of astrophysical contaminants and noise. This is achieved in an optimal way by demanding the estimated map of the signal to have minimum variance. Using the second assumption made at the beginning of this section, Eriksen et al. (2004) showed that the variance of the estimated signal map can be written as

$$\mathrm{Var}\Big(\hat{S}_{\mathrm{ILC}}(p)\Big) = \mathrm{Var}\Big(S(p)\Big) + \mathrm{Var}\Big(\boldsymbol{\omega}^{\mathrm{T}}\boldsymbol{N}(p)\Big) = \boldsymbol{\omega}^{\mathrm{T}}\hat{\mathbf{C}}\boldsymbol{\omega}, \tag{2.4}$$

where $\hat{\mathbf{C}}$ is the empirical estimate of the noise covariance matrix $\mathbf{C}$ of the observed maps

$$\hat{\mathbf{C}}_{ij} = \mathrm{Cov}\Big(\mathbf{T}_i, \mathbf{T}_j\Big) = \frac{1}{N_{\mathrm{pix}}}\sum_{p=1}^{N_{\mathrm{pix}}}\Big(T_i(p) - \langle\mathbf{T}_i\rangle\Big)\Big(T_j(p) - \langle\mathbf{T}_j\rangle\Big), \tag{2.5}$$

where $N_{\mathrm{pix}}$ denotes the number of pixels in a single map. The variance of $\hat{S}_{\mathrm{ILC}}(p)$ can therefore be minimized by determining the weights $\boldsymbol{\omega}$ such that

$$\frac{\partial}{\partial\,\omega_{\mathrm{i}}}\Big[\boldsymbol{\omega}^{\mathrm{T}}\hat{\mathbf{C}}\boldsymbol{\omega}\Big] = 0, \tag{2.6}$$

while also satisfying equation (2.3). This minimization problem can be solved by the use of a Lagrange multiplier $\lambda$

$$\frac{\partial}{\partial\,\omega_{\mathrm{i}}}\Big[\boldsymbol{\omega}^{\mathrm{T}}\hat{\mathbf{C}}\boldsymbol{\omega} + \lambda\Big(1 - \boldsymbol{\omega}^{\mathrm{T}}\boldsymbol{a}\Big)\Big] = 0. \tag{2.7}$$

Calculating the derivative yields

$$2\hat{\mathbf{C}}\boldsymbol{\omega} - \lambda\boldsymbol{a} = 0 \tag{2.8}$$

$$\Leftrightarrow \frac{\lambda}{2}\hat{\mathbf{C}}^{-1}\boldsymbol{a} = \boldsymbol{\omega}. \tag{2.9}$$

An expression for the Lagrange multiplier $\lambda$ can be found by applying equation (2.3):

$$\frac{\lambda}{2} = \frac{1}{\boldsymbol{a}^{\mathrm{T}}\hat{\mathbf{C}}^{-1}\boldsymbol{a}}. \tag{2.10}$$

The desired weights are then found by combining equation (2.9) and (2.10)

$$\boldsymbol{\omega} = \frac{\hat{\mathbf{C}}^{-1}\boldsymbol{a}}{\boldsymbol{a}^{\mathrm{T}}\hat{\mathbf{C}}^{-1}\boldsymbol{a}}. \tag{2.11}$$

The algorithm presented here can be applied both in Fourier and pixel space. An implementation in Fourier space offers the benefit of combining the multifrequency data at their native resolution, while a pixel space implementation requires smoothing all maps to match the beam of the one with the lowest resolution. Furthermore, the SED of the target component has to be corrected for instrumental effects

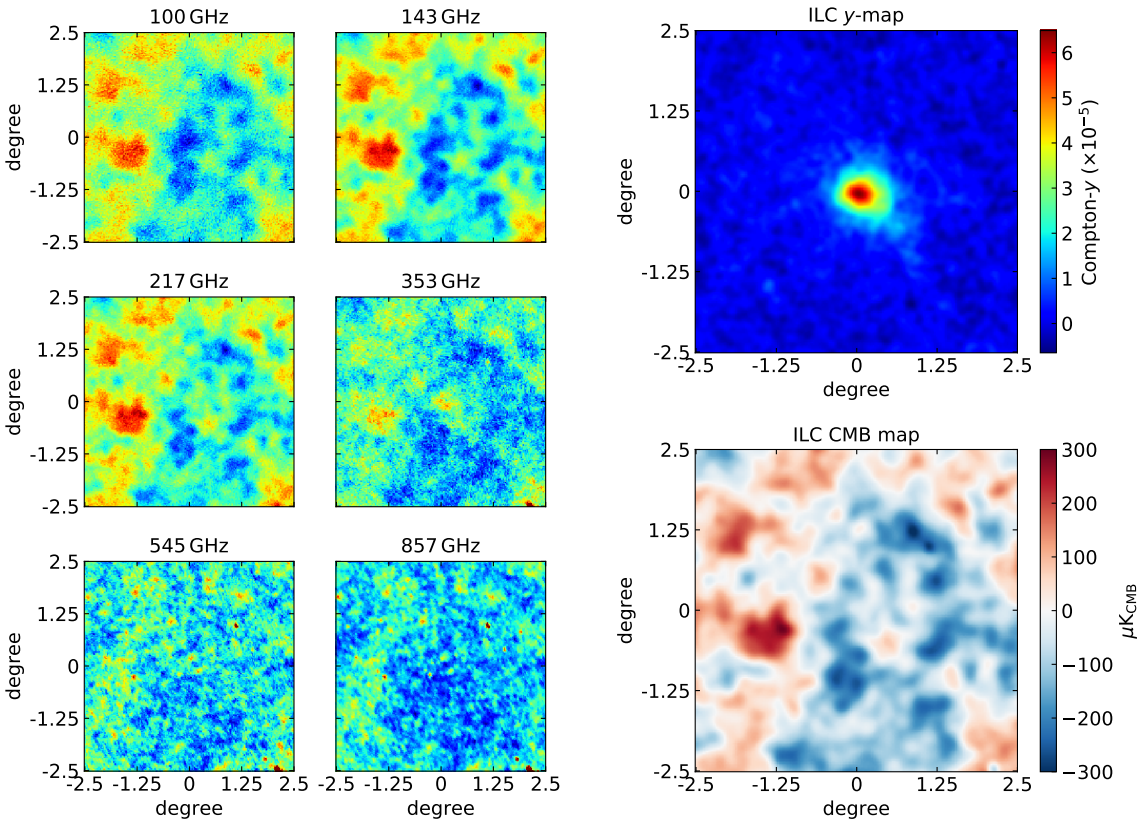


Figure 2.6: Example of the application of the ILC algorithm to a multifrequency data set. The left-hand panel shows the field around the Coma cluster at (RA, Dec.) = (12h59m48s, +27°58′50.5″) seen in the six *Planck* HFI channels. The maps are $5^\circ \times 5^\circ$ cut-outs of larger $10^\circ \times 10^\circ$ fields extracted from the maps of the *Planck* 2015 data release. The right-hand panel shows a map of the Compton-$y$ parameter (top) and a map of the primary CMB temperature anisotropies (bottom). Both maps were obtained by computing a weighted linear combination of the six maps on the left. The necessary ILC weights were computed following equation (2.11) using the (non-relativistic) spectrum of the tSZ effect and a flat spectrum (in units of $K_{CMB}$), respectively.

like the transmission characteristics of bandpass filters (e.g. see Fig. 2.2). In some cases, ILC maps may contain an arbitrary offset that does not affect the variance of the ILC map and is thus not removed by the method. Such an offset is introduced if one or several input maps have a non-zero mean and can be removed in several ways, e.g. by centreing the noise peak of a pixel histogram at a value of zero as is illustrated in Appendix A.6. Examples of a Compton-$y$ map and a CMB temperature map extracted with the ILC algorithm presented here are shown in Fig. 2.6.

### 2.3.2 Multi-Component ILC

One of the key benefits of semi-blind techniques like ILC algorithms is that a detailed understanding and SEDs of contaminating astrophysical signals is not required. Contaminants in the multifrequency data-set are instead reduced in a non-parametric way by demanding minimum variance of the desired map. Computing the ILC-weighted linear combination of the observed maps effectively reduces

contaminants that are intrinsically bright, extended, and show large variance since such components strongly affect the variance of the ILC-estimate of the target signal. However, the ILC algorithm might fail to effectively reduce components that only have a minor impact on the variance of the output map. This becomes a problem if such contaminants are spatially correlated with the target signal. An example that is relevant to this work are compact radio sources that are found in the centres of many galaxy clusters and can bias the ILC estimate of their tSZ amplitude. Another example are residuals of the SZ signal of clusters that are found in ILC CMB maps (Remazeilles et al., 2011a). If the SED of one or several particularly problematic contaminants, which are not sufficiently reduced by a standard ILC algorithm, are known, the ILC weights can be tuned to have zero response to their mixing vectors $\boldsymbol{b}_i$

$$\begin{aligned} \boldsymbol{\omega}^{\mathrm{T}}\boldsymbol{a} &= 1, \\ \boldsymbol{\omega}^{\mathrm{T}}\boldsymbol{b_1} &= 0, \\ &\vdots \\ \boldsymbol{\omega}^{\mathrm{T}}\boldsymbol{b_N} &= 0. \end{aligned} \tag{2.12}$$

This idea was put forth independently by Remazeilles et al. (2011a,b) and Hurier et al. (2013) and is referred to as constrained ILC (CILC) in this work. The $N$ additional constraints on well-characterised contaminants can be used to define a matrix $\mathbf{F}$ of dimensions $N_\nu \times (1+N)$ that contains the mixing vectors of all known components:

$$\mathbf{F} = \begin{pmatrix} a[1] & b_1[1] & \dots & b_N[1] \\ \vdots & \vdots & \ddots & \vdots \\ a[N_\nu] & b_1[N_\nu] & \dots & b_N[N_\nu] \end{pmatrix} \tag{2.13}$$

The ILC weights can be found analogously to the single-component case by minimising the variance of the desired map of the target component defined in equation (2.6) while satisfying the spectral constraints in equation (2.12). The resulting minimisation problem is again solved by introducing large multiplyers $\boldsymbol{\lambda}$

$$\begin{pmatrix} 2\cdot\hat{\mathbf{C}} & -\mathbf{F} \\ \mathbf{F}^{\mathrm{T}} & 0 \end{pmatrix} \begin{pmatrix} \boldsymbol{\omega} \\ \boldsymbol{\lambda} \end{pmatrix} = \begin{pmatrix} 0 \\ \boldsymbol{e} \end{pmatrix}, \tag{2.14}$$

where $\boldsymbol{e} = (1,0,\dots,0)^{\mathrm{T}}$ is a vector that contains the response of the ILC weights to the individual mixing vectors of the known components. The solution for the ILC-weights is given by:

$$\boldsymbol{\omega}^{\mathrm{T}} = \boldsymbol{e}^{\mathrm{T}} \left(\mathbf{F}^{\mathrm{T}}\hat{\mathbf{C}}^{-1}\mathbf{F}\right)^{-1} \mathbf{F}^{\mathrm{T}}\hat{\mathbf{C}}^{-1}. \tag{2.15}$$

For the single-component case, this expression for the ILC weights is reduced to the one given in equation 2.11. An example for the application of the CILC algorithm is given in Fig. 2.7.

However, it is important to note that constraining additional components does result in a degradation of the SNR of sources in the CILC map since fewer degrees of freedom are available to achieve minimum variance. A formal discussion of this issue is presented by Hurier et al. (2013). In general, the SNR that is achieved in an ILC map depends on the number of channels and their noise level. While the former determines the effectiveness of the reduction of contaminating astropysical emission,

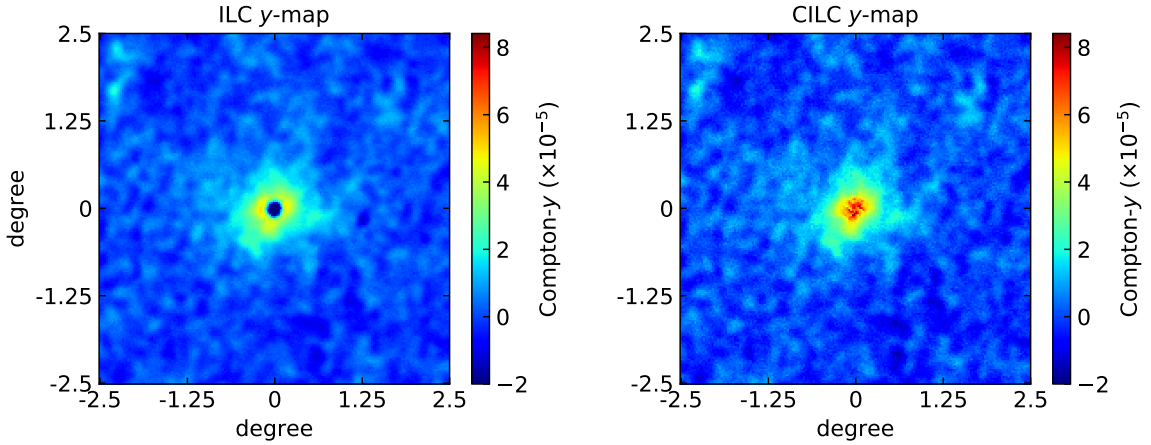


Figure 2.7: Compton-$y$ maps of the Perseus cluster created with two different variants of the ILC-algorithm. Both maps are $5^\circ \times 5^\circ$ cut-outs from larger $10^\circ \times 10^\circ$ maps that are centred at (RA, Dec.) = (03h19m47.2s, $+41^\circ 30' 47''$). The left-hand panel was created by applying the single-component algorithm that was introduced in Section 2.3.1 to *Planck* HFI data from the 2015 data release. The bright radio source Perseus A in the centre of the cluster was not sufficiently removed by the algorithm since its contribution to the variance of the map is negligible. The right-hand panel shows the same field around the Perseus cluster, but was created using a CILC algorithm that allows to place a constrain on the SED of Perseus A. Using the SED presented by Erler et al. (2018) the central Compton-$y$ parameter of the cluster can be recovered.

map noise can only be averaged down. Since the ILC weights are built to return minimum variance solution, particularly noisy channels receive a low weight. Including additional maps therefore always improves the final ILC result as long as there are no systematic issues with the data.

### 2.3.3 All-sky strategies

The ILC algorithms presented previously can be applied straightforwardly to multifrequency all-sky data sets. However, due to the multitude of different astrophysical sources in the sky and variance in their SEDs as a function of position, a strong improvement can be achieved by applying the ILC algorithm to smaller sub-fields of the sky and reconstruct the final all-sky map from these smaller patches. By doing so, the ILC-weights are always optimized to the local sky in each field. A convenient way of tesselating the sky is offered by the "nested"-binning scheme in HEALPix (Górski et al., 2005). HEALPix, the Hierarchical Equal Area isoLatitude Pixelization, is a software package available for IDL and Python (healpy) that provides a versatile structure for pixelization of data and mathematical operations on the sphere. HEALPix subdivides the sphere into 12 curvilinear quadrilaterals, each of which can be subdivided into four sub-elements (pixels hereafter), thus building a hierarchical tree. The total number of pixels is then given by:

$$N_{\rm pix} = 12\, N_{\rm side}^2, \tag{2.16}$$

where $N_{\rm side}$ is the HEALPix resolution parameter:

$$N_{\rm side} = 2^k, \text{ with } k \in [0, 1, 2, ..., 29]. \tag{2.17}$$

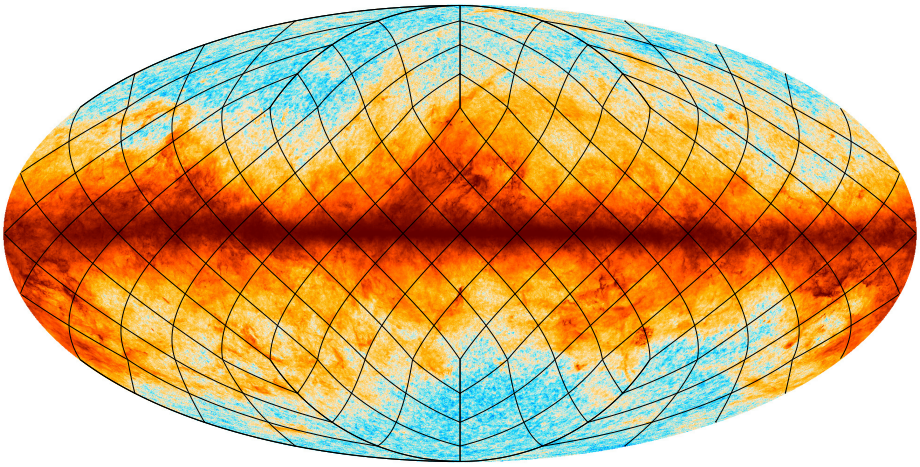

Figure 2.8: Illustration of the HEALPix tessellation of the sphere. The image shows a Mollweide projection of the *Planck* HFI 353 GHz all-sky map from the 2015 data release in Galactic coordinates. The overplotted lines show the boundaries of the HEALPix pixels for $N_{\mathrm{side}} = 4$. Using the nested indexing scheme offered by HEALPix, the sky can be subdivided into fields with equal area. In the example shown here, the all-sky map is partitioned into 192 individual fields, each covering an area of $\approx 215\,\mathrm{deg}^2$ and containing 262 144 pixels.

The properties of HEALPix all-sky map with different resolution parameter are summarised in Table A.3. Due to its hierarchical nature, the "nested"-binning scheme offered by HEALPix can be used to divide an all-sky map with $N_{\mathrm{side}} > 1$ into smaller sub-fields and perform calculations on them, which is illustrated in Fig. 2.8. Eriksen et al. (2004) first used the HEALPix nested scheme to improve their ILC-based map of the CMB, by subdividing the sky into 12 fields. The ILC algorithm is applied to multifrequency data of each field independent of the others yielding 12 CMB maps for individual regions on the sky. To minimize discontinuities along the edges of the fields, Eriksen et al. (2004) constructed all-sky ILC weight maps, which were smoothed with a Gaussian kernel with a FWHM equal to the diameter of the 12 sub-fields, i.e. $58.6^\circ$, before applying the weights to the data. In many cases the number of sub-fields can be significantly higher. Fig. 2.9 shows an all-sky map of the Compton-$y$ parameter that was created from *Planck* HFI data by applying an ILC algorithm to 192 sub-fields, each covering an area of $\approx 215\,\mathrm{deg}^2$. An all-sky CMB temperature map created from running the ILC algorithm on 12 sub-fields was shown at the very beginning in Fig. 1.1.

### 2.3.4 Spatial decomposition

The single- and multi-component variations of the ILC algorithms exclusively utilise spectral information to separate the targeted component from other contaminating signals and noise. However, the performance of the ILC algorithms can be enhanced further by leveraging spatial information. This is especially effective if the target signal has a spatial scale that is very distinct and differs from that of (some) important contaminants. This is the case for galaxy clusters, which have a typical scale of a few arcminutes to $\sim 1^\circ$, while e.g. Galactic foregrounds vary over scales of multiple degrees and (radio) point sources match the scale of the instrument beam.

A simple way of using spatial information is to perform a spatial decomposition of the multifrequency data set that conserves information on all scales. The ILC algorithm is then applied to each scale

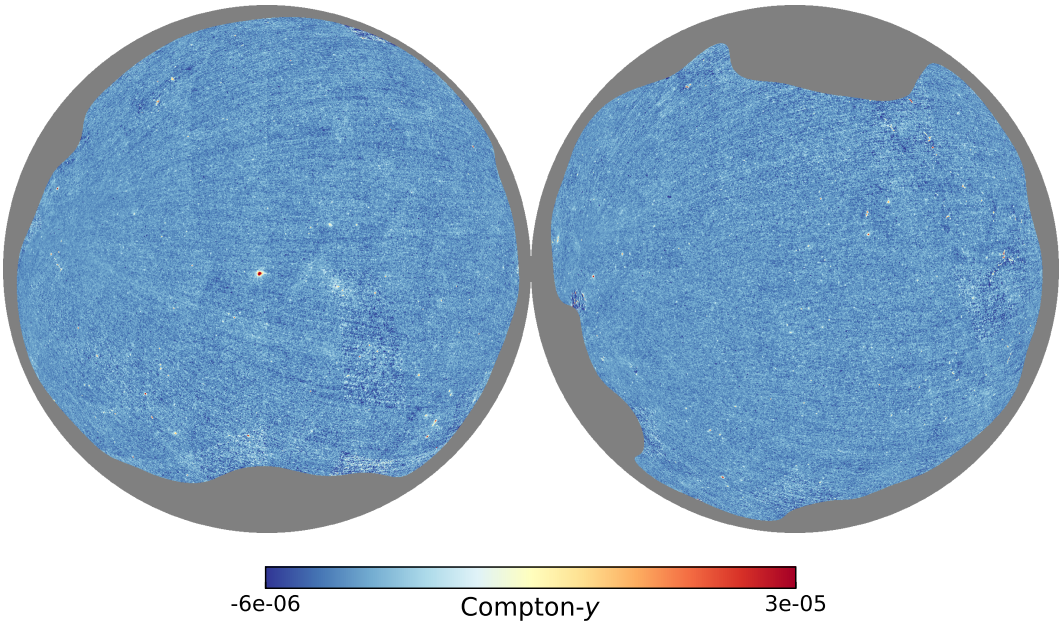


Figure 2.9: Orthographic projection of an all-sky Compton-$y$ map. The two panels show the northern and southern Galactic hemisphere and are centred on the respective poles. The grey area marks regions of the sky that have been masked due to bright Galactic foreground emissions. The all-sky Compton-$y$ map was created by applying the ILC algorithm to *Planck* HFI data from the 2015 data release. In order to ensure the ILC weights are optimized to reduce the local contaminants around each cluster, the sky was partitioned into 192 individual fields using the HEALPix nested indexing scheme as illustrated in Fig. 2.8. The resulting all-sky ILC weight maps were not smoothed.

independently and the resulting images are summed up to obtain the final image. The easiest way of performing such a spatial decomposition is by computing the pairwise difference of images smoothed with a series of Gaussians. If applied to the sphere, equivalent spatial localization is achieved by convolving the multifrequency data with a set of window functions $F_i(\ell)$ built from the difference of pairs of Gaussians $B_i(\ell)$ in spherical harmonic space:

$$F_i(\ell) = B_i(\ell) - B_{i+1}(\ell), \tag{2.18}$$

$$B_i(\ell) = \exp\left(-\frac{\ell(\ell+1)}{2\sigma_i^2}\right), \tag{2.19}$$

$$\sigma_i = \frac{\mathrm{FWHM}_i}{2\sqrt{2\ln(2)}}, \tag{2.20}$$

where the choice of the FWHM of the Gaussians is tuned according to the scale of the target sources and the spatial resolution of the instrument. Like before, a set of ILC weights is computed for each

spatial scale $i$ and the final map is obtained by summation over all scales:

$$y = \sum_i \boldsymbol{\omega}_i \boldsymbol{T}_i. \tag{2.21}$$

A series of possible window functions is shown in the left-hand panel of Fig. 2.10.

Similar principles of spatial decomposition were first used in the Needlet ILC (NILC, Delabrouille et al. 2009; Remazeilles et al. 2011b) and Modified ILC Algorithm (MILCA, Hurier et al. 2013). These two methods differ in the choice of window functions that are used to perform the decomposition (see right-hand panel of Fig. 2.10) and were both made available in the 2015 data release (Planck Collaboration, 2016d). More recently, Rogers et al. (2016) presented a CMB map build using the Scale-discretised, directional wavelet ILC (SILC) algorithm that, as the name suggests, uses directional wavelets to perform the spatial localization.

Finally, it is important to note that the empirical estimate of the covariance matrix departs from its ensemble average due to the finite number of pixels. A discussion and mitigation strategies of this ILC bias are provided by Delabrouille et al. (2013). On the other hand, if the field size is chosen too large in practice, the ILC weights are no longer tuned to minimize local contamination. It is therefore necessary to find a field size that balances these two aspects. The situation becomes somewhat more complex if spatial decomposition is applied, since the number of modes in a field of constant size changes as a function of spatial scale. When applying the ILC algorithm to the sphere, the number of sub-fields should therefore be decreased for large spatial scales.

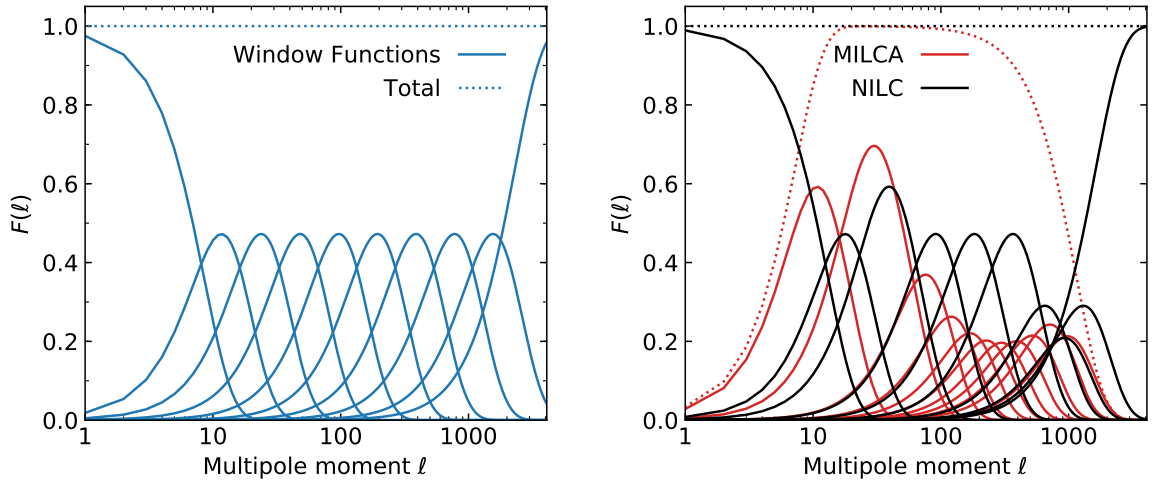


Figure 2.10: **Right-hand panel:** A set of ten window functions computed from the difference of pairs of Gaussian beams in spherical harmonic space with FWHM = $[1280', 640', 320', 160', 80', 40', 20', 10', 5']$. The first and the last window are chosen to satisfy flux conservation at all $\ell$. Sets of filters similar to the one shown can be applied to multifrequency data sets to improve the performance of ILC algorithms. **Left-hand panel:** Window functions used for the MILCA (red curves, 11 windows) and NILC (black curves, 10 windows) all-sky Compton-$y$ maps published by the Planck Collaboration (2016d). The dotted lines indicate the sum of the respective windows. Both are built from the difference of Guassian beams like the windows shown in the example on the left. While the NILC windows conserve the flux on all scales, the MILCA windows suppress both the largest and the smallest scales.

## 2.4 Bayesian statistics and Markov-Chain Monte Carlo techniques

A cornerstone of the analysis presented in this work is data regression and parameter estimation. The data sets investigated in this work are microwave spectra with correlated data points that are fit with high-dimensional spectral models. In order to make use of prior information and obtain robust parameter constraints despite parameter degeneracies, all data analysis is carried out in a Bayesian framework featuring *Markov-Chain Monte Carlo* (MCMC) techniques. This section introduces both concepts and provides technical remarks on the details of the employed samplers and the evaluation of the obtained results. Good introductions on Bayesian data analysis and MCMC techniques are given by Hogg et al. (2010) and Hogg & Foreman-Mackey (2018).

### 2.4.1 Bayesian inference

Bayesian statistics is a school of statistics that emerged from the works of Thomas Bayes during the 18th century. In Baysian statistics, probabilities represent degrees of certainty rather than frequency of occurrence, with 1 and 0 representing absolute certainty and uncertainty, respectively. Assume we want to analyse a data set that contains $n$ observations of the observable $y$ that is a function of the parameter $x$. We expect the observed values of $y$ to be related to the values of $x$ by a model $f$, which is a function of $x$ and a set of $m$ model parameters $\boldsymbol{p}$. In the Bayesian way of thinking, the observations $\boldsymbol{y}$ are given and the goal is to find the most probable model that explains the obtained data. The probability of the set of model parameters $\boldsymbol{p}$ given the observed data $\boldsymbol{y}$ is described by the *posterior probability distribution*, or just *posterior*, $P(\boldsymbol{p}|\boldsymbol{y})$. In contrast, the alternative Frequentist school of statistics assumes that there is a given "real" model and aims at understanding the probability of the observed data to occur in a set of trials. The principle of Bayesian inference is centred around Bayes' theorem

$$P(\boldsymbol{p}|\boldsymbol{y}) = \frac{P(\boldsymbol{y}|\boldsymbol{p})\,P(\boldsymbol{p})}{P(\boldsymbol{y})}, \tag{2.22}$$

where $P(\boldsymbol{y}|\boldsymbol{p})$ is called the likelihood function, $P(\boldsymbol{p})$ is called the *prior*, and $P(\boldsymbol{y})$ is referred to as the *evidence*.

The likelihood function gives the probability of obtaining the observed data given a specific set of model parameters. A common approach is to assume that the model that most closely describes the data is most likely one to generate it. We therefore aim to find the set of model parameters that maximise the likelihood. In Gaussian statistics, the likelihood function is commonly chosen to be a Gaussian

$$P(\boldsymbol{y}|\boldsymbol{p}) = \exp\left(-\frac{\chi^2}{2}\right). \tag{2.23}$$

In order to achieve maximum likelihood we therefore need to minimize

$$\chi^2 = \sum_{i=1}^{n} \frac{\big(y_i - f(x_i, \boldsymbol{p})\big)^2}{\sigma_i^2}, \tag{2.24}$$

where $\sigma_i$ is the variance of the measured $y_i$. In case the observed $y_i$ are correlated, $\chi^2$ is computed as

$$\chi^2 = [\boldsymbol{y} - f(\boldsymbol{x}, \boldsymbol{p})]^{\mathrm{T}} \mathbf{C}^{-1} [\boldsymbol{y} - f(\boldsymbol{x}, \boldsymbol{p})], \tag{2.25}$$

where **C** is the covariance matrix of the observed data

$$C_{i,j} = \langle (x_i - \langle \boldsymbol{x_i} \rangle)(x_j - \langle \boldsymbol{x_j} \rangle) \rangle. \tag{2.26}$$

As a rule of thumb, a good fit is achieved when the value of $\chi^2$ matches the number of degrees of freedom $(n - m)$.

As mentioned previously, Bayes' theorem allows the inclusion of priors on the parameter values. Priors are functions that represent knowledge we have on the model parameters before we conduct our measurements and could be based both on theoretical and empirical foundations, such as the posterior obtained by a previous experiment. If all possible parameter values are equally probable a priori, one speaks of a flat prior. If a prior provides stronger constraints on the value of a parameter than the collected experimental data, a prior is referred to as informative.

The evidence $P(\boldsymbol{y})$ is the probability of obtaining the observed data under all possible parameter values and combinations. It therefore serves as a normalisation that ensures that the integral of the posterior over all possible parameter values yields unity:

$$\frac{1}{P(\boldsymbol{y})} \int P(\boldsymbol{y}|\boldsymbol{p})\, P(\boldsymbol{p})\, \mathrm{d}\boldsymbol{p} = 1. \tag{2.27}$$

The 1D posteriors of individual parameters is obtained from the full posterior through integration over the remaining parameters, which is referred to as marginalization:

$$P(p_i|\boldsymbol{y}) = \int P(\boldsymbol{p}|\boldsymbol{y})\, \mathrm{d}p_1 \ldots \mathrm{d}p_{i-1} \mathrm{d}p_{i+1} \ldots \mathrm{d}p_n. \tag{2.28}$$

In general, computing posteriors quickly becomes computationally demanding if the number of model parameters becomes large. In those cases, one needs to resort to numerical techniques like MCMC techniques, which are introduced in the next section.

### 2.4.2 Markov-Chain Monte Carlo sampling

An elegant way of estimating complex high-dimensional posterior probability distributions is to draw random samples from them, which can be done with Markov-Chain Monte Carlo (MCMC) sampling techniques. A *Markov-Chain* is a sequence of numbers, e.g. random samples drawn from a distribution, each of which only depends on the previous one. *Monte Carlo* methods is a general term that refers to a broad class of numerical techniques that use (pseudo) random numbers. The modern form of Monte Carlo methods was invented by Stanislaw Ulam and received significant contributions from John von Neumann during their work on neutron diffusion at the Manhattan Project in the late 1940s.

One of the simplest MCMC methods is the Metropolis algorithm invented by Nicholas Metropolis (Metropolis et al., 1953), which is outlined below:

1. Start with initial guess for parameters $\mathbf{p}_0$
2. Compute initial Likelihood $P_0(\boldsymbol{y}|\boldsymbol{p_0})$
3. For $i = 1$ until $N$, with $N$ being the number of MCMC samples to generate, do

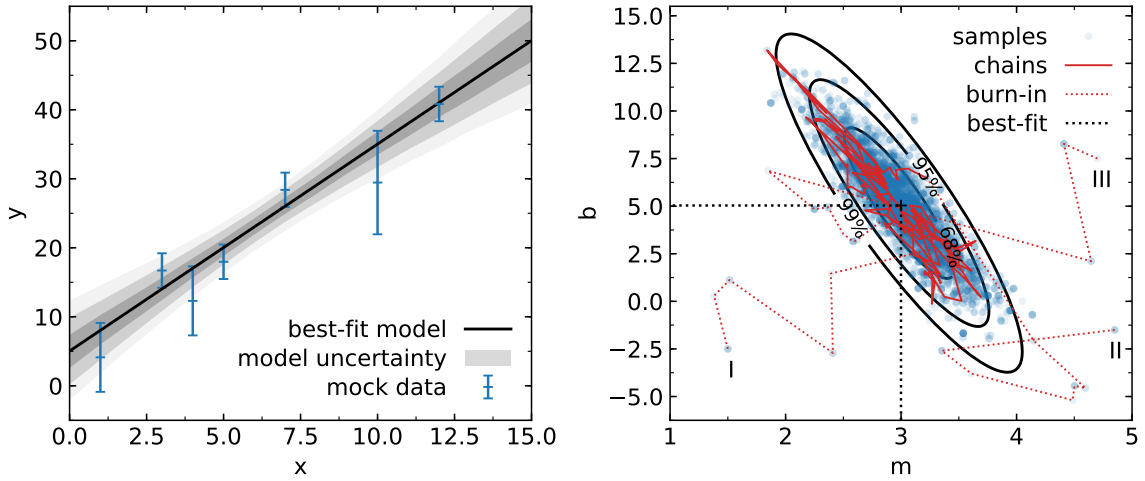


Figure 2.11: Linear regression of a mock data set using MCMC sampling. The left-hand panel shows a mock data set with uncorrelated data points. The solid black line indicates the best-fit model, while the grey shaded areas represent the most compact regions that contain 68.3%, 95.4% and 99.7% of all models. The red lines in the right-hand panel show the first 50 steps of three parallel MCMC chains in the plane of the model parameters m (slope) and b (offset). The dashed sections of the chains indicate their initial steps before converging. These initial samples are "burned" (excluded) in order to avoid biasing the results. The blue data points are the first 2000 samples of each chain and trace the posterior probability distribution, which is shown as black contours. The black dotted lines point towards the best-fit parameter values. The PDFs of the individual parameters are derived from the multi-dimensional posterior distribution by projecting it along a single axis, which is referred to as marginalization (see Fig 2.12).

a) Draw new set of $n$ parameter values $\mathbf{p}_i$ from an $n$-dimensional proposal distribution centred at $\boldsymbol{p_{i-1}}$

b) Compute $P_i(\boldsymbol{y}|\boldsymbol{p_i})$ for new parameters

c) Accept new parameters with probability min $\left(1, \frac{P_i(\boldsymbol{y}|\boldsymbol{p_i})}{P_{i-1}(\boldsymbol{y}|\boldsymbol{p_{i-1}})}\right)$

d) If new parameters are rejected, add $\boldsymbol{p_i} = \boldsymbol{p_{i-1}}$ to the chain

The algorithm above defines the behaviour of a single chain that performs a random walk and explores the parameter space. The resulting chain takes the form of a table with $n$ columns and $N$ lines. An example of Bayesian linear regression using the Metropolis algorithm is given in Fig. 2.11.

It can be shown that, if run for a sufficient period of time, the Metropolis- and similar algorithms like the generalised Metropolis Hastings algorithm (Hastings, 1970) and the Gibbs sampler (Geman & Geman, 1984), converge to a stationary distribution that is equal to the posterior probability distribution. As long as we can draw samples from a posterior, it can therefore always be estimated using MCMC techniques. A key challenge, however, is to ensure covergence of MCMC algorithm in a given period of time. The time required for a Markov-Chain to get close to its stationary distribution is called the mixing time. In case of the Metropolis algorithm, it depends on the choice of the proposal distribution. In this work, we adopt the common choice of a multivariate Gaussian for the proposal distributions. If the covariance matrix of the parameters is not known a prioi, they can assumed to be uncorrelated and the width of their respective Gaussian proposal distributions is chosen arbitrarily.

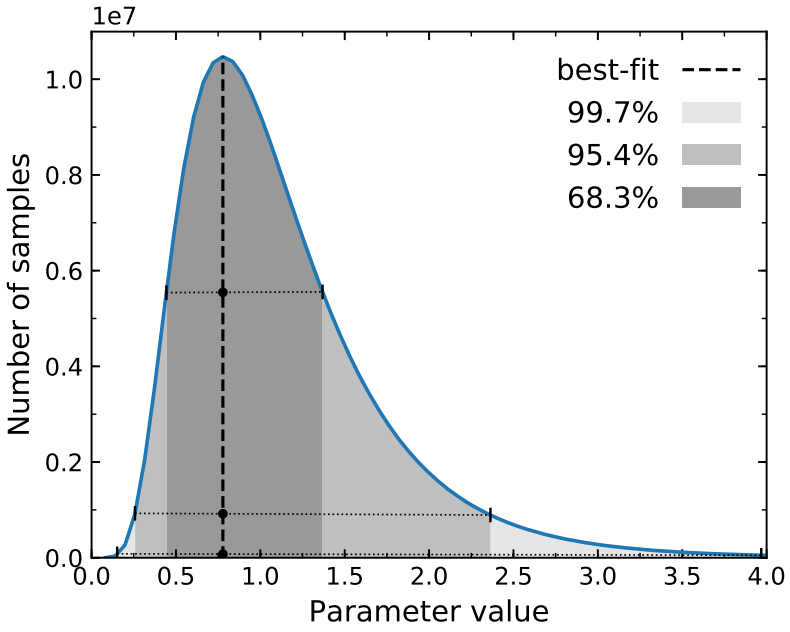


Figure 2.12: Example of an asymmetric 1D parameter value distribution obtained by marginalizing a sampled multi-dimensional posterior distribution along a single axis. If normalised to unit integral, this distribution provides an estimate of the PDF of the parameter. The grey shaded areas indicate the 68.3%, 95.4%, and 99.7% credible interval, which represent the most compact intervals containing the aforementioned percentages of samples. Note that the lower and upper bounds of a credible interval have the same probability density, as indicated by the black dotted lines, and probability densities within a credible interval are greater than outside of it. The black dashed line indicates the best-fit parameter value, which in this example coincides with the mode of the distribution.

If the proposal distributions are chosen too wide, a large fraction of the proposed parameter values is rejected. Similarly, the mixing time is prolonged by proposal distributions that are chosen too narrow, which result in the vast majority of proposed parameter values to be accepted. It is therefore recommended to monitor the acceptance rate of an MCMC chain and tune the widths of the proposal distribution accordingly. As a general rule of thumb, it is suggested to aim for an acceptance rate of 10%–30%.

In this work, convergence of MCMC chains is ensured by always running multiple parallel chains, each starting from a different set of randomly chosen initial parameters $\boldsymbol{p_0}$. The initial samples that are generated by each chain before they approach their stationary distribution are removed or "burned" in order not to bias parameter estimates. Afterwards the chains are merged and evaluated.

The results of an MCMC based data regression are presented as so-called cornerplots, which show the marginalized 1D and 2D posterior probability distributions of all free model parameters. Computing these marginalized distributions from an MCMC chain is straightforward and done by computing 1D and 2D histograms of the sampled data points. The provided best-fit values refer to the set of parameters that yields the highest recorded value of the likelihood and usually, but not necessarily, coincides with the mode of the marginalized 1D distributions. The uncertainty of the estimated parameter values is given by the 68.3% *credible interval*. For a Gaussian distribution, the

68.3% credible interval corresponds to the area that is contained within $\pm 1\sigma$ around the mean of the distribution. In general, the credible interval represents the most compact interval (in $p_i$) that contains a given percentage of the obtained samples. An example for an asymmetric distribution is given in Fig. 2.12. Note that occasionally, the credible interval is referred to as the confidence interval in this work, a term that is used for a related concept in Frequentist statistics. The computed values, however, always conform to the definition given previously.

CHAPTER 3

# Goals and structure of this work

Although observations of the SZ effect have seen tremendous technology-driven advances during the past two decades, all modern SZ instruments still lack the necessary sensitivity to perform detailed measurements of the spectrum of the SZ effect. Until recently, ground based instruments operated exclusively at frequencies of the SZ decrement. These observations allow for a very efficient detection of clusters out to high redshifts, which was done to great success using the SPT and ACT, but does not allow direct measurements of cluster masses, the temperature of the ICM, and their peculiar velocities. The current state of SZ observations can therefore be compared to observations of the X-ray surface brightness. Detailed measurements of the frequency spectrum of the SZ effect, on the other hand, would allow for the separation of the tSZ and kSZ, as well as their respective relativistic distortions, greatly enhancing the information that can be extracted from the scattered CMB photons.

The only instrument that offers the necessary frequency coverage for such observations is the *Planck* satellite. With *Planck* SZ data being largely unexplored and the first public release of *Planck* data taking place one year prior to the beginning of the thesis work presented here, my doctoral research began with a pilot study of the complete spectrum of the SZ effect to explore the feasibility of such observations with the most recent data. The results of this study are presented in Chapter 4 and were published in Erler et al. (2018).

Once a suitable data set is obtained, the main challenge in studying the spectrum of the SZ effect is the extraction of the microwave spectrum of clusters in the presence of much brighter Galactic foregrounds, extragalactic backgrounds, and a population of radio and far infrared point sources. After investigating several data reduction techniques, the most effective proofed to be so-called matched filtering, which uses the known spatial template of clusters to provide unbiased and precise photometry at each frequency, allowing for the successful conclusion of this research project. Afterwards, I explored a possible generalization of the matched filter concept that was inspired by my previous work with the similar ILC algorithm. The idea of this generalization was to modify matched filters to allow for the extraction of a known kind of signal, while suppressing other contaminating signals with a known spatial template.

The generalized matched filtering techniques developed in this work can be used to address a major problem in the study of clusters with SZ and X-ray data, which is contamination by point sources. Typically, these point sources are either AGN or star-forming galaxies. For SZ-data that is processed with conventional matched filters, the problem of point source contamination is analogous to that in ILC $y$-maps (see Fig. 2.7), which was addressed in the CILC technique by using additional spectral

information. For studies of the SZ spectrum, like the one presented in the first part of this work, this solution is not applicable and one has to use spatial information instead.

Since the spatial template of point sources will be given by the beam or PSF of the instrument, the application of the new matched filtering technique is straight forward. Chapter 5 presents the derivation of the new filters and their application to real and simulated data in order to highlight and understand the offered benefits as well as possible limitations imposed by the spatial resolution of the used instrument. This project was concluded with a demonstration of the application of the new generalized matched filters for the separation of clusters and point sources in X-ray data like those that will be obtained by the eROSITA space telescope, which started its multi-year mission recently. The results presented in Chapter 5 were published in Erler et al. (2019).

The year 2016 saw the birth of the CCAT-prime Collaboration, that aims to build a next generation mm/sub-mm survey telescope at the highest telescope site on the planet. Since its inception, CCAT-prime's crossed-Dragone optics were adopted by the SO and CMB-S4 collaborations for their large aperture telescopes. Additionally, the development of the main instruments for these facilities is now shared between collaborations. Of these future telescopes, CCAT-p will be the only one that observes at sub-mm wavelengths, offering unique advantages for SZ spectral studies similar to the one presented in the first part of this thesis. As a member of the CCAT-prime Collaboration, I investigated aspects of the galaxy cluster science case for CCAT-prime and contributed to several fund-raising proposals for its main instrument Prime-Cam. In particular, I investigated the achievable constraints on the SZ effect parameters with CCAT-prime, as well as the expected galaxy cluster sample size. This provided an opportunity to revist many of the spectral analysis tools that were used previously and apply the advanced matched filtering techniques that I developed as part of this work. The respective forecasts are presented in Chapter 6 and were partially published in Stacey et al. (2018) and Basu et al. (2019).

Finally, Chapter 7 summarizes the results of this work, describes its impact, and provides an outlook on the future of SZ observations of clusters.

Besides these main results, this work includes a series of appendices. Appendix A contains mostly technical remarks on unit conversions and numerical techniques. Appendix B presents additional, unpublished results related to the work presented in Chapter 5. Additional figures for Chapter 6 are shown in Appendix C.

Many of the codes written as part of this work are being released to the public in an ongoing effort under `https://github.com/j-erler`. This is done to ensure transparency and reproducibility of the results presented in this thesis and the related publications, as well as to encourage the usage of the developed methods (especially the new matched filters), spawn future collaborations, and provide a platform for the continued development of these codes under the inclusion of the wider astronomical community.

CHAPTER 4

# *Planck's* view on the spectrum of the Sunyaev–Zeldovich effect

This chapter is a reproduction of the article of the same title that has been published in Monthly Notices of the Royal Astronomical Society under the reference

- **Erler J.**, Basu K., Chluba J. and Bertoldi F., 2018, MNRAS, 476, 3360

The manuscript is reproduced under the non-exclusive right of re-publication granted by MNRAS to the authors of the article. To ensure open access to the article the peer-reviewed, published version has been uploaded to astro.ph (arXiv:1709.01187).

## 4.1 Abstract

We present a detailed analysis of the stacked frequency spectrum of a large sample of galaxy clusters using *Planck* data, together with auxiliary data from the *AKARI* and IRAS missions. Our primary goal is to search for the imprint of relativistic corrections to the thermal Sunyaev–Zeldovich effect (tSZ) spectrum, which allow to measure the temperature of the intracluster medium. We remove Galactic and extragalactic foregrounds with a matched filtering technique, which is validated using simulations with realistic mock data sets. The extracted spectra show the tSZ signal at high significance and reveal an additional far-infrared (FIR) excess, which we attribute to thermal emission from the galaxy clusters themselves. This excess FIR emission from clusters is accounted for in our spectral model. We are able to measure the tSZ relativistic corrections at $2.2\sigma$ by constraining the mean temperature of our cluster sample to $4.4^{+2.1}_{-2.0}$ keV. We repeat the same analysis on a subsample containing only the 100 hottest clusters, for which we measure the mean temperature to be $6.0^{+3.8}_{-2.9}$ keV, corresponding to $2.0\sigma$. The temperature of the emitting dust grains in our FIR model is constrained to $\simeq 20$ K, consistent with previous studies. Control for systematic biases is done by fitting mock clusters, from which we also show that using the non-relativistic spectrum for SZ signal extraction will lead to a bias in the integrated Compton parameter $Y$, which can be up to 14% for the most massive clusters. We conclude by providing an outlook for the upcoming CCAT-prime telescope, which will improve upon *Planck* with lower noise and better spatial resolution.

## 4.2 Introduction

The Sunyaev–Zeldovich (SZ) effect is a spectral distortion of the cosmic microwave background (CMB) due to inverse Compton scattering of CMB photons by free electrons by the hot plasma found in clusters of galaxies. The effect was first described by Sunyaev & Zeldovich (1970, 1972) and has been used extensively in the last two decades to detect and characterize galaxy clusters (e.g. Hasselfield et al. 2013; Planck Collaboration 2014d; Bleem et al. 2015; Bender et al. 2016).

The SZ signal is composed of two distinct parts, the thermal SZ (tSZ) caused by the scattering of CMB photons by thermal electrons and the kinetic SZ (kSZ), which is due to scattering of CMB photons by a population of electrons that moves with a line-of-sight peculiar velocity $v_{\rm pec}$ in the rest frame of the CMB. Detailed reviews of the SZ effect are provided by Birkinshaw (1999) and Carlstrom et al. (2002). Given the dimensionless frequency $x \equiv h\nu/(k_{\rm B}T_{\rm CMB})$, the SZ signal can be expressed as an intensity shift relative to the CMB

$$\frac{\Delta I_{\rm SZ}}{I_0} = h(x)\left[\underbrace{f(x,T_{\rm e})\,y}_{\rm tSZ} - \underbrace{\tau_{\rm e}\left(\frac{v_{\rm pec}}{c}\right)}_{\rm kSZ}\right], \tag{4.1}$$

where $y$ is the Compton $y$-parameter, a dimensionless measure of the line-of-sight integral of the electron pressure

$$y = \frac{\sigma_{\rm T}}{m_{\rm e}c^2}\int_{\rm l.o.s.} n_{\rm e}k_{\rm B}T_{\rm e}\,{\rm d}l. \tag{4.2}$$

Here, $k_{\rm B}$ is the Boltzmann constant, $\sigma_{\rm T}$ is the Thomson cross-section, $m_{\rm e}$ is the electron rest mass, $c$ is the speed of light, $T_{\rm CMB}$ is the CMB temperature, $I_0 = 2(k_{\rm B}T_{\rm CMB})^3/(hc)^2 \approx 270\,{\rm MJy\,sr^{-1}}$, $h(x) = x^4\exp(x)/(\exp(x)-1)^2$ and $\tau_{\rm e} = \sigma_{\rm T}\int n_{\rm e}(r)\,{\rm d}l$ is the optical depth of the plasma. The function $f(x)$ describes the spectral shape of the tSZ effect

$$f(x,T_{\rm e}) = \left(x\frac{\exp(x)+1}{\exp(x)-1} - 4\right) + \delta_{\rm rel}(x,T_{\rm e}), \tag{4.3}$$

where $\delta_{\rm rel}(x,T_{\rm e})$ denotes relativistic corrections to the frequency spectrum of the tSZ (e.g., Wright, 1979; Rephaeli, 1995; Itoh et al., 1998), which arise from the high electron temperature of a few keV found in the intracluster medium (ICM) of galaxy clusters. These corrections (sometimes referred to as the relativistic SZ effect or the rSZ effect) can be efficiently computed using SZPACK[1] (Chluba et al., 2012, 2013), which overcomes limitations of asymptotic expansions (Challinor & Lasenby, 1998; Itoh et al., 1998; Sazonov & Sunyaev, 1998) and explicit tabulation schemes (e.g., Nozawa et al., 2000). For the kSZ effect, we neglect relativistic corrections, which are well below the current sensitivity.

In its non-relativistic approximation, the tSZ effect has a characteristic spectral shape independent of the plasma temperature, causing a decrement in intensity at frequencies below the tSZ "null" at $\simeq 217.5\,{\rm GHz}$ and an increment above. Taking into account relativistic corrections, the frequency spectrum becomes a function of the electron temperature. With increasing temperature, the tSZ "null" shifts towards higher frequencies and the tSZ decrement and increment amplitudes decrease while the increment becomes wider (see Fig. 4.1). For a massive galaxy cluster with $k_{\rm B}T_{\rm e} = 10\,{\rm keV}$

[1] www.Chluba.de/SZpack

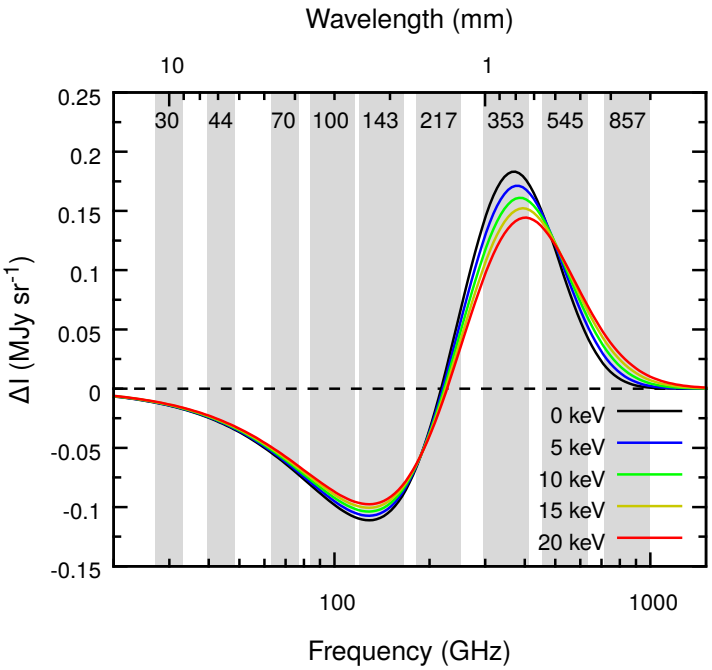


Figure 4.1: Spectrum of the thermal SZ effect with relativistic corrections for a range of electron temperatures at fixed $y = 10^{-4}$. The grey bands indicate the nine *Planck* frequency bands with $\Delta\nu/\nu = 0.2$ for the three low-frequency instrument and $\Delta\nu/\nu = 0.3$ for the six high-frequency instrument channels.

the tSZ intensity at 353 GHz, for example, reduces by 13%. Accurate measurements of the spectral shape of the SZ spectrum would thus allow us to measure the $y$-weighted line-of-sight averaged ICM temperature of galaxy clusters (e.g. Pointecouteau et al. 1998), allowing a more complete thermodynamic description without the need for additional density or temperature measurements from X-ray telescopes.

Since the SZ effect is a small distortion of the CMB, measuring weak changes in its spectrum at the level of a few per cent caused by relativistic effects or the similarly weak kSZ is very challenging and only recently have observations become sensitive enough. For example, Zemcov et al. (2012) reported a $3\sigma$ measurement of the shift of the SZ null using the $Z$-spec instrument. Under the assumption that the zero-shift is only caused by the relativistic distortions (i.e. no kSZ), the authors constrained the temperature of the cluster RX J 1347.5-1145 to $k_\mathrm{B}T_\mathrm{e} = (17.1 \pm 5.3)\,\mathrm{keV}$ . Prokhorov & Colafrancesco (2012) present a measurement of the line-of-sight temperature dispersion of the Bullet Cluster with observations of both the decrement and increment of the tSZ using data from ACBAR and *Herschel*-SPIRE. Their analysis was later refined by Chluba et al. (2013), showing that no significant temperature dispersion could be deduced. In an attempt to measure the evolution of the CMB temperature, Hurier et al. (2014) demonstrated that constraints on the electron temperature of a sample of clusters can be placed using data from the *Planck* satellite. More recently, Hurier (2016) claimed a high significance detection of the tSZ relativistic corrections based on a stacking analysis performed on large cluster samples using *Planck* data.

A major challenge for precision measurements of the electron temperature of galaxy clusters via the relativistic tSZ effect is far-infrared emission (FIR) that is spatially correlated with clusters and can

affect measurements of the tSZ increment. Galaxy clusters are populated with galaxies, some of which form stars, which then in turn heat up the dusty interstellar medium (ISM) of these galaxies, giving rise to thermal emission from warm dust grains. Although the star formation rates in most clusters are low, some are known to show exceptionally high star formation activity (e.g. McDonald et al. 2016). This dusty galaxy contribution corresponds to the halo–halo clustering term of the cosmic infrared background (CIB) that is correlated with cluster positions (e.g., Addison et al. 2012). Individual CIB sources are also magnified by clusters through gravitational lensing, leading to spatially correlated increases in the CIB flux (Blain, 1998). In addition to the unresolved galaxies, it has long been suspected that the ICM should contain large amounts of warm ($\simeq 20\,\mathrm{K}$) dust grains, which are thought to be stripped from infalling galaxies by ram pressure and supernova winds (e.g. Sarazin 1988). The dust grains are then stochastically heated by collisions with hot electrons from the ICM and re-emit the absorbed energy in the FIR (Ostriker & Silk, 1973; Dwek et al., 1990). In the ICM, dust grains can be destroyed by thermal sputtering (Draine & Salpeter, 1979), but the grain lifetimes are highly uncertain and depend on the ICM density and temperature, as well as the size of the dust grains, but can reach several billion years in the outskirts of clusters (Dwek & Arendt, 1992). The actual amounts of dust grains and their lifetime in the ICM is speculative and only recently have dust grains been included in hydrodynamical simulations of galaxies (McKinnon et al., 2016, 2017). All of the above contribute to an FIR excess observed at low resolution in stacked samples of clusters (Montier & Giard, 2005; Giard et al., 2008; Planck Collaboration, 2016e,i). Besides these spatially correlated sources of FIR emission, the spatially uncorrelated contribution of diffuse Galactic foregrounds like synchrotron, free–free and thermal dust emission, as well as the stochastic CIB from extragalactic sources, has to be subtracted or modelled carefully in order to allow for precise measurements of the SZ spectral shape.

In this work, we present a detailed analysis of the SZ spectrum of a stacked sample of galaxy clusters as seen by the *Planck* satellite. We remove Galactic and extragalactic foregrounds with a spatial matched filtering approach and include an FIR component in our model of the observed cluster spectrum. We provide an estimate of the sample mean electron temperature as well as the average FIR emission from clusters. A major aspect of our work is a realistic simulation set-up with mock clusters with which we test our method and demonstrate a potential $Y$-bias in the *Planck* SZ measurements, resulting from the use of the non-relativistic tSZ spectrum. As an outlook, we compare *Planck* to the upcoming CCAT-prime[2] telescope that will offer exciting observational possibilities like determining the SZ spectral shape for large number of clusters.

Our paper is structured as follows: Section 4.3 provides an overview over the maps and cluster catalogues used in this work. Section 4.4 describes our matched filtering and stacking methods that are tested on mock data in Section 4.5. Section 4.6 presents our results. In Section 4.7 we provide a discussion of our results as well as a comparison with some contemporary works and give an outlook to future experiments. Section 4.8 provides a summary and concludes our analysis.

Throughout this paper, we assume a flat ΛCDM cosmology with $\Omega_\Lambda = 0.7$, $\Omega_\mathrm{b} = 0.05$, $h = 0.7$ and $T_\mathrm{CMB} = 2.7255\,\mathrm{K}$, while $E(z) \equiv H(z)/H_0 = (\Omega_\mathrm{m}(1+z)^3 + \Omega_\Lambda)^{1/2}$ is the redshift-dependent Hubble ratio. Unless noted otherwise, the quoted parameter uncertainties refer to the 68% confidence interval. We made use of the IDL Astronomy Library (Landsman, 1993) and all-sky maps were processed with HEALPix (v3.30; Górski et al. 2005).

[2] http://www.ccatobservatory.org/

| $\nu$ (GHz) | $\lambda$ ($\mu$m) | FWHM (arcmin) | Calibration uncertainty (%) |
|---|---|---|---|
| | | ***Planck*** | |
| 70 | 4290 | 13.31 | 0.20 |
| 100 | 3000 | 9.68 | 0.09 |
| 143 | 2100 | 7.30 | 0.07 |
| 217 | 1380 | 5.02 | 0.16 |
| 353 | 850 | 4.94 | 0.78 |
| 545 | 550 | 4.83 | 6.10 |
| 857 | 350 | 4.64 | 6.40 |
| | | **IRAS/IRIS** | |
| 3000 | 100 | 4.30 | 13.5 |
| 5000 | 60 | 4.00 | 10.4 |
| | | ***AKARI*** | |
| 3330 | 90 | 1.3 | 15.1 |

Table 4.1: Characteristics of the *Planck*, IRAS and *AKARI* all-sky maps used in this work. We adopt a covariance estimation approach similar to Soergel et al. (2017) and assume that the calibration uncertainties between the *Planck* 70 GHz to 353 GHz and 545 GHz to 857 GHz channels are fully correlated.

## 4.3 Data sets

### 4.3.1 *Planck* all-sky maps

The main data used in our analysis are the all-sky microwave maps captured by the *Planck* satellite that were taken from the full data release in 2015 (R2.02; Planck Collaboration 2016a). *Planck* has observed the sky over a period of 4 yr and delivered maps in nine different frequency bands with two main instruments. The low frequency instrument (LFI) observed the sky in three bands ranging from 30 GHz to 70 GHz and completed a total of eight all-sky surveys. *Planck's* high frequency instrument (HFI; Planck Collaboration 2014b) observed in six bands between 100 GHz and 857 GHz and completed five all-sky surveys before the depletion of the necessary coolant. With its wide frequency coverage, *Planck* allows to probe the entire spectrum of the SZ (see Fig. 4.1), especially at the tSZ increment. For details on the time-ordered information (TOI) processing, the map-making process and calibration strategies we refer to the HFI and LFI papers. The main map characteristics are summarized in Table 4.1. All maps are provided in the HEALPix format with $N_{\rm side} = 2048$. Our analysis uses all six HFI channels as well as the LFI 70 GHz channel. The 30 GHz and 44 GHz LFI channels are not used due to their much lower angular resolution of 32 and 27 arcmin, respectively, and their sensitivity to low-frequency synchrotron and free–free emission from both Milky Way and bight radio galaxies along the line of sight. We convert all maps up to 353 GHz from units of $K_{\rm CMB}$ to MJy sr$^{-1}$ with the unit conversion factors given in the *Planck* 2015 release explanatory supplement[3].

We adopt a covariance estimation approach similar to Soergel et al. (2017), who assume that the calibration uncertainties of channels that were jointly calibrated are fully correlated. The *Planck* LFI and HFI channels up to 353 GHz where calibrated using the CMB dipole, while the two highest

[3] We use the band-average unit conversion factors that can be found here: https://wiki.cosmos.esa.int/planckpla2015/index.php/UC_CC_Tables

frequency maps were calibrated using planets (Planck Collaboration, 2016b). In accordance with Soergel et al. (2017), we assume a conservative 1% absolute calibration uncertainty for the channels up to 353 GHz and 6% for the two remaining channels.

### 4.3.2 IRAS and *AKARI* all-sky maps

In addition to the *Planck* all-sky maps, we use auxiliary maps from the *Infrared Astronomical Satellite* (IRAS, Neugebauer et al. 1984) and the *AKARI* satellite (Doi et al., 2015) to constrain our spectral model at high frequencies. The main characteristics of the used maps are summarized in Table 4.1.

IRAS performed the first all-sky survey in the mid-infrared and FIR in 1983 and delivered maps in four bands from 12 $\mu$m to 100 $\mu$m. We make use of the reprocessed IRIS maps (Miville-Deschênes & Lagache, 2005), which offer improved calibration, zero level and de-striping, as well as better zodiacal light subtraction. Our analysis uses the IRIS 60 $\mu$m and 100 $\mu$m maps in the HEALPix format with $N_{\mathrm{side}} = 2048$. Both maps have similar resolution like the *Planck* high frequency bands but suffer from larger calibration uncertainties.

The *AKARI* satellite, also known as ASTRO-F, performed an all-sky FIR survey in four bands, covering wavelengths between 65 $\mu$m and 160 $\mu$m. Compared to IRAS, *AKARI* offers a higher angular resolution of 1–1.5 arcmin at a similar noise level. We only use the 90 $\mu$m channel (WIDE-S) because it offers the lowest calibration uncertainties (Takita et al., 2015). As for the other data sets, we obtained the *AKARI* 90 $\mu$m map in the HEALPix format[4] with $N_{\mathrm{side}} = 4096$ to account for the higher angular resolution.

### 4.3.3 Galaxy cluster catalogues

At the core of our analysis lies a stacking approach, which requires a large number of massive clusters for which the relativistic distortions of the tSZ spectrum can be significant. For this reason, the main cluster catalogue used in this study is the second *Planck* Catalogue of Sunyaev–Zeldovich sources (PSZ2; Planck Collaboration 2016h), which provides the largest and deepest SZ-selected sample of galaxy clusters. The catalogue contains a total of 1653 detections, 1203 of which are confirmed galaxy clusters and 1094 have spectroscopic or photometric redshifts. The redshift range of the clusters is $0.01 \lesssim z \lesssim 0.97$ with a median redshift of $z_{\mathrm{m}} = 0.224$. We use the Union catalogue (R2.08), which combines the results of three distinct extraction algorithms. The MMF1 and MMF3 algorithms are based on matched multifiltering, a concept first proposed by Herranz et al. (2002), while the POWELLSNAKES (PwS) algorithm employs Bayesian inference. The provided estimates of the integrated Compton $y$-parameter within $5 \times R_{500}$ in the Union catalogue are taken from the algorithm that gave the highest signal-to-noise (S/N) detection for each individual cluster. Mass estimates are provided assuming the best-fit $Y$–$M$ scaling relation of Arnaud et al. (2010) as a prior. The mass range of the galaxy clusters with known redshifts is $7.8 \times 10^{13}\,\mathrm{M}_{\odot} \lesssim M_{500} \lesssim 1.6 \times 10^{15}\,\mathrm{M}_{\odot}$ with a median mass of $M_{500}^{\mathrm{m}} = 4.75 \times 10^{14}\,\mathrm{M}_{\odot}$.

[4] The *AKARI* maps can be downloaded in the HEALPix format from the Centre d'Analyse de Données Etendues (CADE, Paradis et al. 2012): `http://cade.irap.omp.eu/dokuwiki/doku.php?id=start`

## 4.4 Method

We search for the imprint of relativistic corrections to the tSZ by means of stacking multifrequency data for large samples of galaxy clusters. Since the relativistic corrections are expected to be weak ($\simeq 10\%$) even for massive and hot clusters, it is crucial to have high S/N data. Galactic foregrounds are reduced before the stacking of clusters by applying matched filters, tailored to the characteristic cuspy profile of galaxy clusters, to the all-sky maps. After filtering, the clusters are stacked within HEALPix to avoid possible biases introduced by approximate projections.

### 4.4.1 Matched filtering

Matched filtering is a technique that allows the construction of an optimal spatial filter to extract weak signals with a well-known spatial signature in the presence of much stronger foregrounds. Matched filtering was first proposed for the study of the kSZ by Haehnelt & Tegmark (1996) and was subsequently developed and generalized by Herranz et al. (2002) and Melin et al. (2006) for the extraction of the tSZ signal from multifrequency data sets like those delivered by the *Planck* mission. Matched filtering has since been adopted by the SPT, ACT and Planck Collaboration to extract the tSZ signal of clusters from their respective data sets (Hasselfield et al. 2013; Bleem et al. 2015; Planck Collaboration 2016h).

We apply our filter functions to the all-sky maps in spherical harmonic space to avoid using an approximate projection on to a flat-sky geometry. Assuming radial symmetry of the galaxy cluster profile (i.e. $m = 0$) and following the approach presented in Schäfer et al. (2006), a matched filter $\Psi_{l0}$ can be constructed by minimizing the variance of the filtered field

$$\sigma^2 = \sum_\ell C_\ell \Psi_{\ell 0}^2, \tag{4.4}$$

where $C_\ell$ is the power spectrum of the unfiltered map. At the same time, we demand the filtered field to be an unbiased estimator of the amplitude of the tSZ signal at the position of galaxy clusters. The latter condition can be rewritten as

$$\sum_\ell \tau_{\ell 0} \Psi_{\ell 0} = 1, \tag{4.5}$$

where $\tau_{\ell 0}$ are the $m = 0$ spherical harmonic coefficients of the cluster profile. A solution to this optimization problem is given by

$$\Psi_{\ell 0} = \left( \sum_\ell \frac{\tau_\ell^2}{C_\ell} \right)^{-1} \frac{\tau_\ell}{C_\ell}. \tag{4.6}$$

Using the convolution theorem on the sphere, the spherical harmonic coefficients of the filtered map $a_{\ell \mathrm{m}}^{\mathrm{filt}}$ can be related to the ones of the unfiltered map $a_{\ell \mathrm{m}}^{\mathrm{unfilt}}$ by

$$a_{\ell \mathrm{m}}^{\mathrm{filt}} = \sqrt{\frac{4\pi}{2\ell + 1}}\, \Psi_{\ell 0}\, a_{\ell \mathrm{m}}^{\mathrm{unfilt}} \equiv F_\ell\, a_{\ell \mathrm{m}}^{\mathrm{unfilt}}. \tag{4.7}$$

We approximate the spatial profile of the cluster tSZ signal by a projected spherical $\beta$-model (Cavaliere

& Fusco-Femiano, 1976):

$$y(\theta) = y_0 \left[1 + \left(\frac{\theta}{\theta_c}\right)^2\right]^{\frac{1-3\beta}{2}}, \tag{4.8}$$

where $\theta_c$ is the core radius. We set $y_0 = 1$ and adopt the commonly used value of $\beta = 1$, for which an analytic spherical harmonic transform can be found (e.g., Soergel et al., 2017)

$$y_{\ell 0} = 2\pi\theta_c^2 K_0(\ell\theta_c), \tag{4.9}$$

where $K_0$ is the modified Bessel function of the second kind. In order to account for the instrumental beam and the HEALPix pixelization, we multiply with the beam and pixel window functions $B_\ell$ and $w_\ell$:

$$\tau_\ell = \sqrt{\frac{2\ell+1}{4\pi}} \cdot \tilde{\tau}_{\ell 0} = \sqrt{\frac{2\ell+1}{4\pi}} \cdot y_{\ell 0} \cdot B_\ell \cdot w_\ell. \tag{4.10}$$

All instrumental beams are assumed to be Gaussian with FWHMs as summarized in Table 4.1. The final filters are therefore given by

$$F_\ell = \left[\sum_\ell \frac{(2\ell+1)\tilde{\tau}_\ell^2}{4\pi C_\ell}\right]^{-1} \frac{\tilde{\tau}_\ell}{C_\ell}. \tag{4.11}$$

Fig. 4.2 shows the filter kernels for *Planck* and IRAS data. A matched filter as the one defined here will provide an estimate of the deconvolved central $y$-parameter $y_0$.

The $C_\ell$ are computed directly from the all-sky maps. To mitigate the strong foregrounds along the Galactic disc, the maps are multiplied with a smoothed (2°) 40% Galactic mask. To prevent contamination of the results by large-scale residuals, an exponential taper is applied to the filters at scales $\ell < 300$. In order to stack the extracted tSZ signal amplitudes of different clusters, we bin them according to their apparent size and match the core radius used to compute the filter functions to each subsample. We find that good results can be obtained with 11 size-bins between $\theta_c^{\min} = 0.25'$ and $\theta_c^{\max} = 3'$ with $\theta_c = 0.2\,\theta_{500}^{\mathrm{m}}$, where $\theta_{500}^{\mathrm{m}}$ is the median $\theta_{500}$ for each subsample.

### 4.4.2 Sample selection

In order to avoid the strong Galactic foregrounds along the Galactic plane, we exclude galaxy clusters that fall within a 40% Galactic dust mask. Some galaxy clusters are also known to host bright radio galaxies that can bias measurements of the tSZ decrement (e.g. Lin & Mohr 2007). To avoid the brightest sources, we remove all clusters from our sample that have a known point source detected within a radius of 10 arcmin from the cluster centre. For this purpose, we use the *Planck* catalogue of compact sources in its second iteration (30 GHz to 217 GHz, Planck Collaboration 2016g) and include weak detections. These two steps reduce the size of our sample to 821 clusters. We furthermore exclude clusters with $\theta_{500} > 15$ arcmin in order to keep the number of size bins used in the matched filtering step low. By doing so, we exclude an additional 49 low-redshift clusters and are left with our final sample of 772 clusters, the positions of which are shown in Fig. 4.3. Our cluster sample has a median redshift of 0.23, the mean redshift is 0.27 and the mean cluster mass is $\langle M_{500}\rangle = 4.8 \times 10^{14}\,\mathrm{M}_\odot$ with a standard deviation of $\sigma_{M_{500}} = 1.9 \times 10^{14}\,\mathrm{M}_\odot$. The stacked cluster sample is shown in Fig. 4.4 both without and with foreground-removal at the *Planck* HFI frequencies, highlighting the effectiveness of

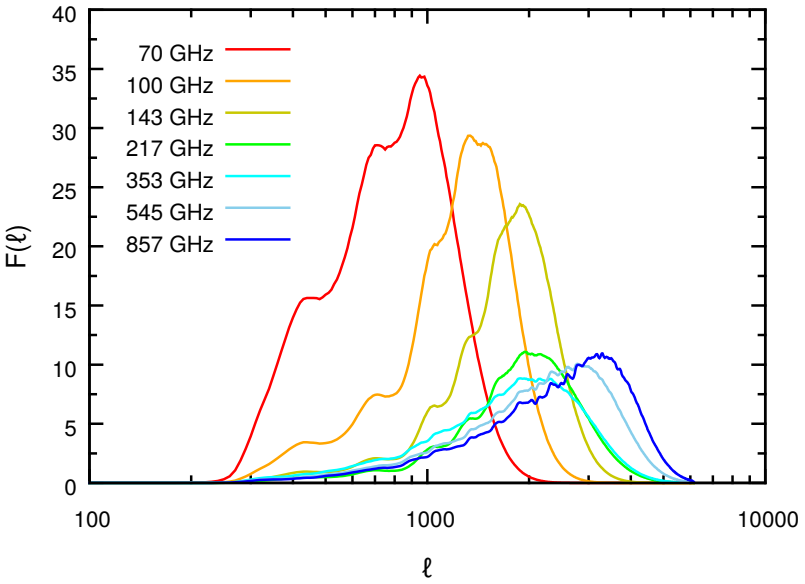


Figure 4.2: Filter kernels for galaxy clusters in the *Planck* data. The filters were constructed following equation (4.11) using a core radius of 1 arcmin and power spectra extracted from real data. For plotting purposes, the kernels were smoothed with a running average of $\Delta\ell = 50$. We use the unsmoothed filter kernels in our analysis.

our matched filtering technique.

We use the $M$–$T$ scaling relation given by Reichert et al. (2011) to obtain an estimate of the X-ray spectroscopic electron temperature of the clusters in our sample:

$$\frac{M_{500}}{10^{14}\,\mathrm{M}_\odot} = (0.291 \pm 0.031)\left(\frac{k_\mathrm{B}T_\mathrm{X}}{\mathrm{keV}}\right)^{1.62\pm0.08} E(z)^{-1.04\pm0.07}. \tag{4.12}$$

The error on the estimate of sample-average temperature is obtained via a Monte Carlo technique taking into account both the scaling relation uncertainties and the quoted mass errors in the *Planck* catalogue. This estimate of spectroscopic temperature is used to compare against the $\langle T_\mathrm{SZ}\rangle$ values as obtained from our tSZ spectral analysis. For example, we find a sample-average (mass-weighted) X-ray temperature $k_\mathrm{B}\langle T_\mathrm{X}\rangle = (6.91 \pm 0.08)\,\mathrm{keV}$ and sample standard deviation $k_\mathrm{B}\sigma_{T_\mathrm{X}} = 2.13\,\mathrm{keV}$ for the full sample of 772 clusters.

In addition to our full sample, we select a subsample containing the 100 hottest clusters by employing the same $M$–$T$ scaling relation. This subsample thus contains the most massive clusters from our original sample, with a mean mass of $\langle M_{500}\rangle = 7.9 \times 10^{14}\,\mathrm{M}_\odot$, and a higher mean redshift of 0.46 and a median of 0.45. The sample-average mass-weighted spectroscopic temperature is $k_\mathrm{B}\langle T_\mathrm{X}\rangle = (8.54 \pm 0.16)\,\mathrm{keV}$ with a sample dispersion of $k_\mathrm{B}\sigma_{T_\mathrm{X}} = 1.57\,\mathrm{keV}$. This sample allows us to test for a stronger relativistic tSZ signal with the drawback of a reduced sample size.

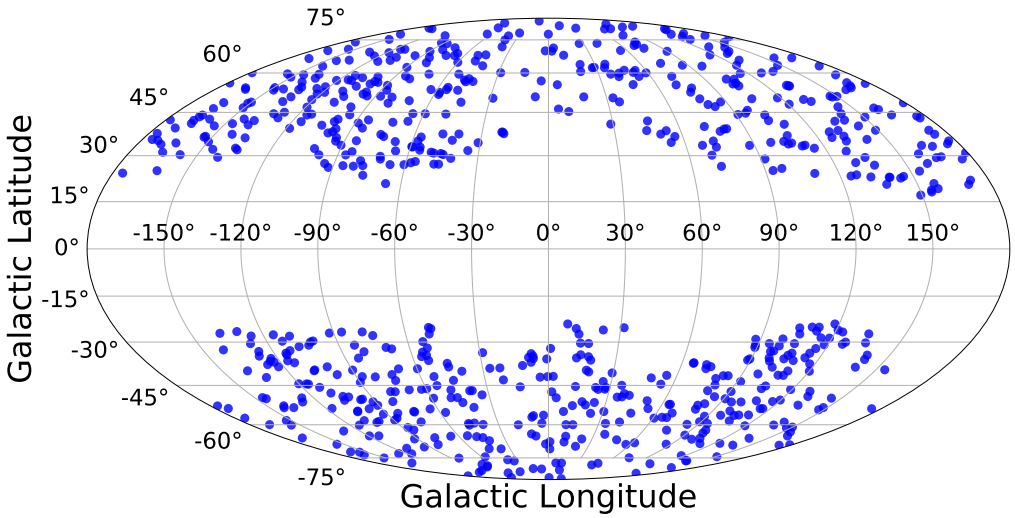


Figure 4.3: Mollweide projection of the sky in Galactic coordinates showing the subsample of the second *Planck* cluster catalogue used in this work. The cluster-free central part of the image traces the Galactic mask used for cluster selection. We also flag all clusters with a known low-frequency point sources within a radius of 10 arcmin from the cluster centre and exclude large low-redshift systems (see the main text).

### 4.4.3 Data modelling

After matched filtering, the extracted spectra will be free of spatially uncorrelated Galactic and extragalactic foregrounds, thus we only model the expected signal from the galaxy clusters. We fit a two-component model to the data that is the sum of a tSZ spectrum with relativistic corrections and a model for the expected FIR emission from galaxy clusters.

We compute the tSZ spectrum using the SZPACK code in its `'COMBO'` runmode, which delivers accurate results up to very high electron temperatures of 75 keV by combining asymptotic expansions and improved pre-computed basis functions (Chluba et al., 2012)[5]. The instrumental bandpass is accounted for by adopting the approach presented by the Planck Collaboration (2014b)

$$\Delta\tilde{I}_{\rm tSZ}(x,T_{\rm e}) = y\, I_0\, \frac{\int {\rm d}\nu\, \tau(\nu)\, h(x)\, f_{\rm rel}(x,T_{\rm e})}{\int {\rm d}\nu\, \tau(\nu)\, \left(\frac{\nu_{\rm c}}{\nu}\right)}, \tag{4.13}$$

where $\nu_{\rm c}$ denotes the band central frequency and $\tau(\nu)$ the bandpass transmission[6] at the frequency $\nu$. Table 4.4 provides the bandpass-corrected tSZ spectrum with relativistic corrections for a range of temperatures. At the given range of cluster temperatures in our sample, fitting the extracted spectrum of the stacked clusters with a tSZ spectrum will provide an estimate of the sample-average central

[5] Other fitting formulae (e.g. Nozawa et al. 2000) show noticeable artefacts in the spectrum that are avoided with SZPACK.

[6] The bandpass transmission tables can be found here: `http://irsa.ipac.caltech.edu/data/Planck/release_1/ancillary-data/`

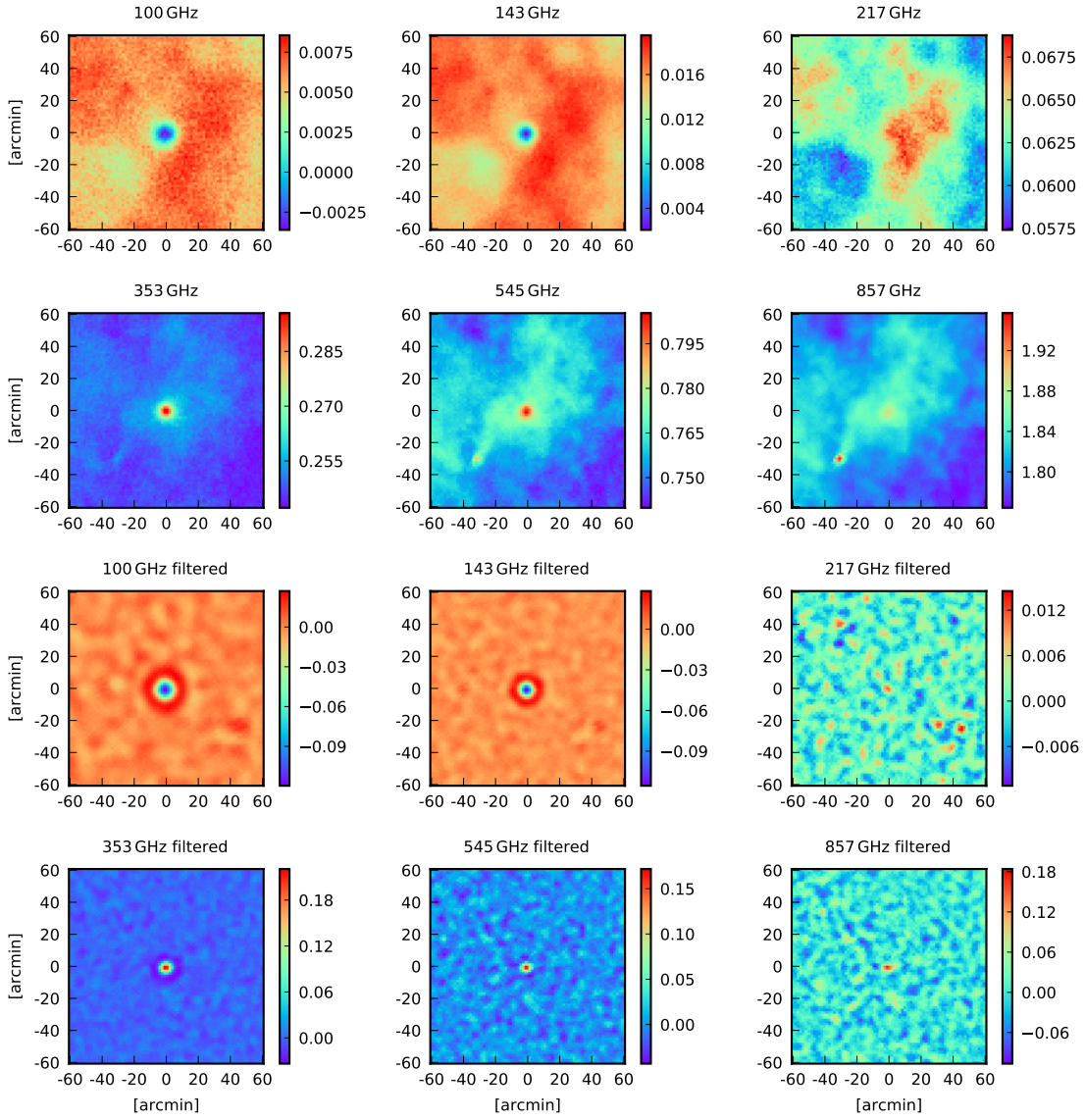


Figure 4.4: Stacked *Planck* HFI maps for our final sample of 772 clusters. All fields are $2^\circ \times 2^\circ$ and the units are MJy sr$^{-1}$. The panels in the upper two rows were created by smoothing all HFI channels to a common resolution of 9.66 arcmin and then stacking the cluster positions without further foreground or background removal. Although the stacking procedure averaged out most contaminants, there are still large inhomogeneities present in the maps. In contrast, the panels shown in the two lower rows were created by stacking the HFI data after matched filtering, which removed most contaminants with great efficiency. We note that we stack the maps directly in HEALPix for our spectral analysis and show these panels only for the purpose of illustration.

$y$-parameter $\langle y_0 \rangle$ and the pressure-weighted average electron temperature (e.g. Hansen 2004)

$$T_{\rm SZ} \approx \langle T_{\rm e} \rangle_{P_{\rm e}} = \frac{\int n_{\rm e} T_{\rm e}^2 \, {\rm d}l}{\int n_{\rm e} T_{\rm e} \, {\rm d}l}. \tag{4.14}$$

We choose to model the FIR emission from galaxy clusters with a modified blackbody

$$\tilde{I}_{\rm FIR}(\nu) = {\rm CC}(\beta_{\rm Dust}, T_{\rm Dust}) \, A_{\rm Dust} \left( \frac{\nu}{\nu_0} \right)^{\beta_{\rm Dust}} B_\nu(T_{\rm Dust}), \tag{4.15}$$

where $A_{\rm Dust}$, $T_{\rm Dust}$, and $\beta_{\rm Dust}$ are the dust amplitude, temperature, and spectral index, respectively, $\nu_0 = 857\,{\rm GHz}$, $B_\nu = 2\pi h \nu^3 / c^2 \, (\exp(h\nu / k_{\rm B} T_{\rm Dust}) - 1)^{-1}$ is Planck's law and CC denotes frequency-specific colour corrections

$${\rm CC}(\beta_{\rm Dust}, T_{\rm Dust}) = \frac{\int {\rm d}\nu \, \tau(\nu) \left( \frac{\nu^{\beta_{\rm Dust}} B_\nu(\nu, T)}{\nu_c^{\beta_{\rm Dust}} B_\nu(\nu_c, T)} \right)}{\int {\rm d}\nu \, \tau(\nu) \left( \frac{\nu_c}{\nu} \right)}. \tag{4.16}$$

For convenience, we recast equation (4.15) to

$$\tilde{I}_{\rm FIR}(\nu) = {\rm CC} \, A_{\rm Dust}^{857} \left( \frac{\nu}{\nu_0} \right)^{\beta_{\rm Dust}+3} \frac{\exp(h\nu_0 / (k_{\rm B} T_{\rm Dust})) - 1}{\exp(h\nu / (k_{\rm B} T_{\rm Dust})) - 1}, \tag{4.17}$$

and report the measured FIR intensity at 857 GHz as the amplitude $A_{\rm Dust}^{857}$. We account for the redshift distribution of our cluster sample by computing the FIR model at each specific cluster redshift and averaging the obtained values. The obtained parameter values are thus given in the rest frame of the source.

Finally, we fit our data in a Bayesian approach by constraining the posterior probability distribution of our model parameters $\boldsymbol{p}$ using Markov-Chain Monte Carlo (MCMC) sampling with

$$P(\boldsymbol{p}|\boldsymbol{I}_\nu) \propto P(\boldsymbol{I}_\nu|\boldsymbol{p}) \, P(\boldsymbol{p}), \tag{4.18}$$

where $\boldsymbol{I}_\nu$ is the measured sample-average of specific intensities after matched filtering, $P(\boldsymbol{I}_\nu|\boldsymbol{p})$ is the likelihood function and $P(\boldsymbol{p})$ is the prior. We restrict the electron temperature to values $0\,{\rm keV} < T_{\rm e} < 75\,{\rm keV}$ in accordance to SZPACK's `'COMBO'` runmode. Note that the sample-average temperature of the clusters should lie well within this range. We assume a flat positive prior on the remaining model parameters and a Gaussian likelihood that can be written as

$$\ln P(\boldsymbol{I}_\nu|\boldsymbol{p}) = -0.5 \, [\boldsymbol{I}_\nu(\boldsymbol{p}) - \langle \boldsymbol{I}_\nu \rangle]^{\rm T} \mathbf{C}^{-1} [\boldsymbol{I}_\nu(\boldsymbol{p}) - \langle \boldsymbol{I}_\nu \rangle]. \tag{4.19}$$

The frequency-to-frequency covariance matrix $\mathbf{C}$ is estimated by stacking 772 uniformly distributed random positions across the sky, excluding the area that falls into the Galactic mask used for sample selection. This step is repeated $10^4$ times, providing a large number of noise realizations for the covariance estimation. In this process, we account for the size binning of the clusters. This statistical component of the covariance matrix is then combined with the systematic part resulting from the instrumental calibration uncertainties. The corresponding correlation matrix is shown in Fig. 4.5.

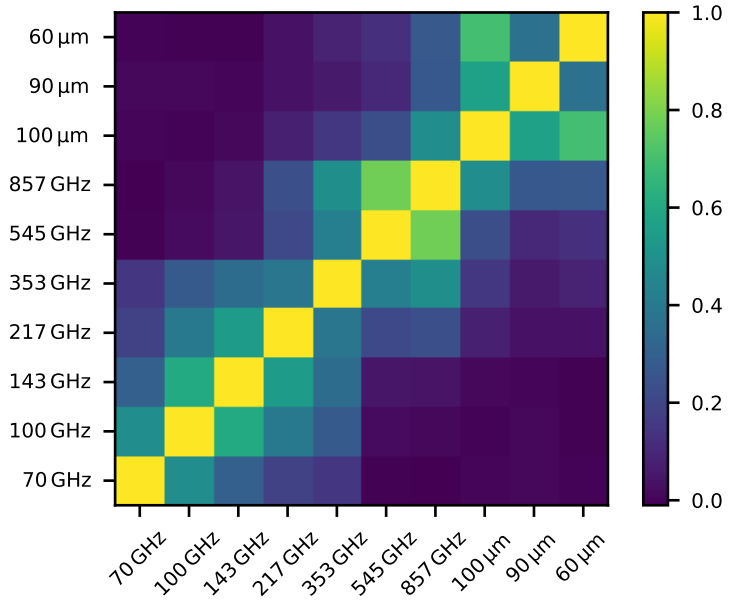


Figure 4.5: Channel-to-Channel correlation matrix used for the data modelling. It is composed of a statistical and a systematic component. The statistical component is constrained by stacking 772 random positions across the sky outside of the same Galactic mask used for sample selection and repeating this exercise 10,000 times. The systematic component contains the calibration uncertainties of the instruments.

We draw samples from the posterior probability distribution using an implementation of the Metropolis Hastings algorithm (Metropolis et al., 1953; Hastings, 1970) and report the marginalized two-dimensional (2D) and one-dimensional (1D) posterior distributions. We ensure convergence by comparing the results of multiple chains that start from random positions in the parameter space.

## 4.5 Simulations

### 4.5.1 Simulation set-up

In order to test our filtering pipeline and data modelling procedure before applying it to real data, we validate it using realistic all-sky mock data. We use the CMB and Galactic synchrotron, free–free and thermal dust maps provided by the Planck Collaboration (2016c) that were extracted with the Bayesian COMMANDER analysis framework. The COMMANDER synchrotron and free–free maps are provided at a low HEALPix resolution of $N_{\mathrm{side}} = 256$ and are upgraded to $N_{\mathrm{side}} = 2048$ in spherical harmonic space to avoid pixellation artefacts. Thermal dust maps are provided at both low- and high- HEALPix resolution. We use the $N_{\mathrm{side}} = 2048$ dust amplitude and $\beta_{\mathrm{Dust}}$ maps and upgrade the low-resolution dust temperature map to $N_{\mathrm{side}} = 2048$. Note that the same upgraded map was used as a prior during the creation of the $N_{\mathrm{side}} = 2048$ dust maps. The maps are scaled to *Planck* and IRAS frequencies from 70 GHz to 5 THz using the SEDs employed by the Planck Collaboration (2016c). We do not simulate *AKARI* data due to a lack of high-resolution templates. However, testing our pipeline on

*Planck* and IRAS mock data is sufficient for our purposes.

The tSZ signal from clusters of galaxies is simulated by line-of-sight projection of a generalized Navarro-Frenk-White (GNFW) pressure profile (Nagai et al., 2007) with the mass-dependent parametrization given by Arnaud et al. (2010):

$$\frac{P_\mathrm{e}(r)}{\mathrm{keV\,cm^{-3}}} = 1.65\times10^{-3}E(z)^{8/3}\left(\frac{M_{500}}{3\times10^{14}\,\mathrm{M_\odot}}\right)^{0.79} p\left(\frac{r}{r_{500}}\right), \tag{4.20}$$

where $p(r/r_{500})$ is the so-called "universal" shape of the cluster pressure profile:

$$p(r) = \frac{P_0}{\left(c_{500}\frac{r}{R_{500}}\right)^{\gamma}\left[1+\left(c_{500}\frac{r}{R_{500}}\right)^{\alpha}\right]^{(\beta-\gamma)/\alpha}}, \tag{4.21}$$

with $(P_0, c_{500}, \gamma, \alpha, \beta) = (8.403, 1.177, 0.3081, 1.0510, 5.4905)$ as the best-fit values reported by Arnaud et al. (2010). We project the model along a series of concentric isothermal shells with $0.01\,R_{500} < r < 3.5\,R_{500}$ and $\Delta r = 0.1\,R_{500}$, and assume the electron temperature to follow the profile given by Vikhlinin et al. (2006):

$$\frac{T(r)}{T_\mathrm{mg}} = 1.35\frac{\left(\frac{r}{0.045R_{500}}\right)^{1.9}+0.45}{\left(\frac{r}{0.045R_{500}}\right)^{1.9}+1}\frac{1}{\left[1+\left(\frac{r}{0.6R_{500}}\right)^{2}\right]^{0.45}}, \tag{4.22}$$

where $T_\mathrm{mg} = 0.9T_\mathrm{X}$ accounts for the lower temperature due to weighting with the gas mass. The tSZ signal is computed for each shell according to its temperature and $y$ parameter and the total signal for each cluster is given by the stack of all shells. Likewise, we also compute the optical depth $\tau_\mathrm{e}$ of each cluster shell by shell, as

$$\tau_{\mathrm{e},i} = \frac{y_i m_\mathrm{e} c^2}{k_\mathrm{B} T_{\mathrm{e},i}} \tag{4.23}$$

and then estimate the total $\tau_\mathrm{e}$ by stacking all the shells. The $\tau_\mathrm{e}$ values are used to estimate the residual kSZ signal after stacking (Section 4.5.3).

To ensure similar signal strength to the real data, we adopt the cluster masses and redshifts from the previously described cluster sample but assign new random sky coordinates outside of a Galactic mask to each cluster to avoid placing them on top of spatially correlated artefacts in the foreground maps. These artefacts result from a lack of an SZ model during the foreground modelling and can introduce a bias in our parameter constraints. Randomizing the sky coordinates of the clusters allows us to obtain multiple foreground realizations with only one set of foreground templates.

We simulate the FIR emission of galaxy clusters by assuming a constant dust-to-gas mass ratio $M_\mathrm{Dust}/M_\mathrm{Gas} = 10^{-4}$ for all clusters as well as a modified blackbody spectral energy distribution (SED) with $T_\mathrm{Dust} = 20\,\mathrm{K}$ and $\beta_\mathrm{Dust} = 1.5$, which are typical values found for the ISM of nearby galaxies and are consistent with the values reported by the Planck Collaboration (2016i). The amplitude of the

SED can be related to the dust mass following the approach of Hildebrand (1983)

$$A_{\mathrm{Dust}} = \frac{\kappa_\nu M_{\mathrm{Dust}}}{D_{\mathrm{L}}^2 \Omega}, \tag{4.24}$$

where $\kappa_\nu$ is the mass absorption coefficient, $D_{\mathrm{L}}$ is the angular diameter distance, and $\Omega = \pi(3\theta_{500})^2/D_{\mathrm{A}}^2$ is the solid angle of the emitting region. We adopt the mass absorption coefficient reported by Draine (2003), $\kappa_{850\mu\mathrm{m}} = 0.0383\,\mathrm{m}^2\,\mathrm{kg}^{-1}$, which was also used by the Planck Collaboration (2016i). Furthermore, the spatial profile of the FIR emission is assumed to follow a $\beta$-model with $\beta = 1$ and $r_{\mathrm{c}} = 0.2\,R_{500}$. The Planck Collaboration (2016e) found that the FIR emission follows a broader profile compared to the tSZ signal, but its exact radial profile remains unknown. Since we reject clusters with known low-frequency point sources, i.e. radio galaxies, during the sample selection process, we do not include a radio-source component in our cluster simulations.

The foreground and cluster maps are then convolved with the instrument beams, which we approximate as circular Gaussians with FWHM as listed in Table 4.1.

We add an estimate of the instrumental noise to each map, which is obtained by computing the half difference $(I_\nu^{\mathrm{ring1}} - I_\nu^{\mathrm{ring2}})/2$ of the two half-ring maps for every *Planck* channel, each of which only contains half of the stable pointing period data. Since no equivalent IRAS/IRIS maps are available, we use white noise maps for which we adopt the global noise level found in the IRIS maps of $\sigma_{60\,\mu\mathrm{m}} = 0.03\,\mathrm{MJy\,sr}^{-1}$ and $\sigma_{100\,\mu\mathrm{m}} = 0.06\,\mathrm{MJy\,sr}^{-1}$.

We have neglected the contribution from extragalactic dusty point sources in preparing our simulation set-up. These point sources constitute the CIB, with both one-halo (Poisson) and two-halo terms contributing to the relevant scales of tens of arcminutes (e.g., Béthermin et al. 2017). The one-halo or Poisson term of the CIB acts as an additional source of thermal noise affecting the high-frequency bands, but otherwise is uncorrelated with the cluster location and will be filtered away by the matched-filtering technique. Hence in our simulations we have an under-estimation of the noise at the IRAS frequencies as well as the highest frequency *Planck* channels, but this is not expected to result in any biases in the recovered model parameters. The contribution of the two-halo term in the CIB will be similar to the FIR component from the clusters already included in our analysis, barring a few extremely bright objects that will be flagged in a process similar to the cleaning of our real cluster sample.

Other foreground components excluded from our simulations are mainly the Galactic CO and anomalous microwave emission (AME), as well as the Galactic and extragalactic radio point sources. Their aggregate contribution is expected to be small given our use of HFI-only data plus sky masking and sample cleaning methods (the all-sky mock data are filtered with the same pipeline as the real data). Adding these subdominant foregrounds can only be expected to make the parameter uncertainties marginally worse, hence their exclusion is not a concern while testing the robustness of our filtering pipeline.

### 4.5.2 Method validation with mock data

Before applying our matched filtering pipeline to real data, it is important to assess if it allows an unbiased estimation of the cluster properties. In order to test our method, we simulate a total of 30 mock data sets and pass them through the same filtering and analysis pipeline as the real data. The obtained constraints on the tSZ parameters for all 30 data sets are shown in Fig. 4.6, while Fig. 4.7

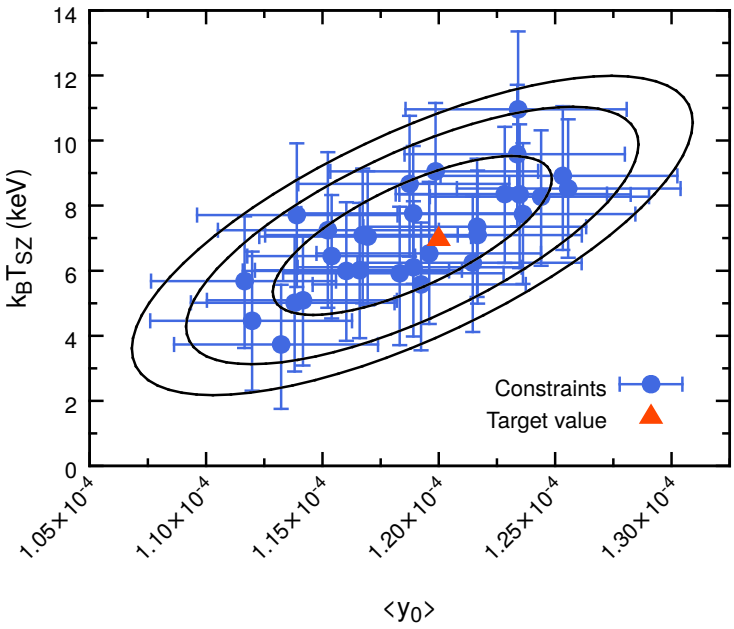


Figure 4.6: Constraints on the tSZ parameters obtained from simulations with 30 different foreground realizations, achieved by randomizing the cluster coordinates. The true sample-average $y$ and $T_{SZ}$ is indicated by the red triangle. The black contours indicate the 68, 95, and 99% confidence intervals. This result suggests that our matched filtering and spectral fitting pipeline allows an unbiased measurement of the tSZ parameters.

shows the extracted spectrum and model fitting as well as parameter constrains for one exemplary mock data set.

We find that the individual simulation constraints tightly scatter around the expected values that were derived directly from the simulated cluster data. This result demonstrates that an unbiased measurement of the sample-average $y_0$ and $T_{SZ}$ can be achieved in a matched filtering approach with size binning. Similar results are found for the three parameters of the cluster FIR model. Assuming a different pressure profile like the best-fit GNFW model presented by the Planck Collaboration (2013a) for our mock clusters while keeping our filter profile unchanged results in a bias in $y_0$ but not in $T_{SZ}$. This bias can be avoided by choosing a different core radius $\theta_c = 0.23\,\theta^m_{500}$ to construct our filters. The temperature $T_{SZ}$ is insensitive to small differences between the true cluster shape and the assumed model for filtering since the mismatch will be the same across all frequencies. Differences in spatial resolution across the frequency bands could introduce a bias to the SZ spectral shape, but our tests suggest such distortions to be insignificant.

We also filter the mock data with a lower number of size bins that leads to an under-estimation of $y_0$ and overestimation of $T_{SZ}$. Note that we do not test for potential biases due to cluster asphericity, which is a well-known problem in modelling individual objects (Piffaretti et al., 2003) but is not expected to cause a significant biases when stacking a large number of sources.

The analysis of our mock data sets suggests that for the given subsample of the *Planck* cluster catalogue with 772 clusters the sample-average temperature can be constrained with an statistical uncertainty of $k_B \Delta T_{SZ} \approx 2\,\mathrm{keV}$ suggesting a possible $\simeq 3\sigma$ detection, while the expected uncertainty

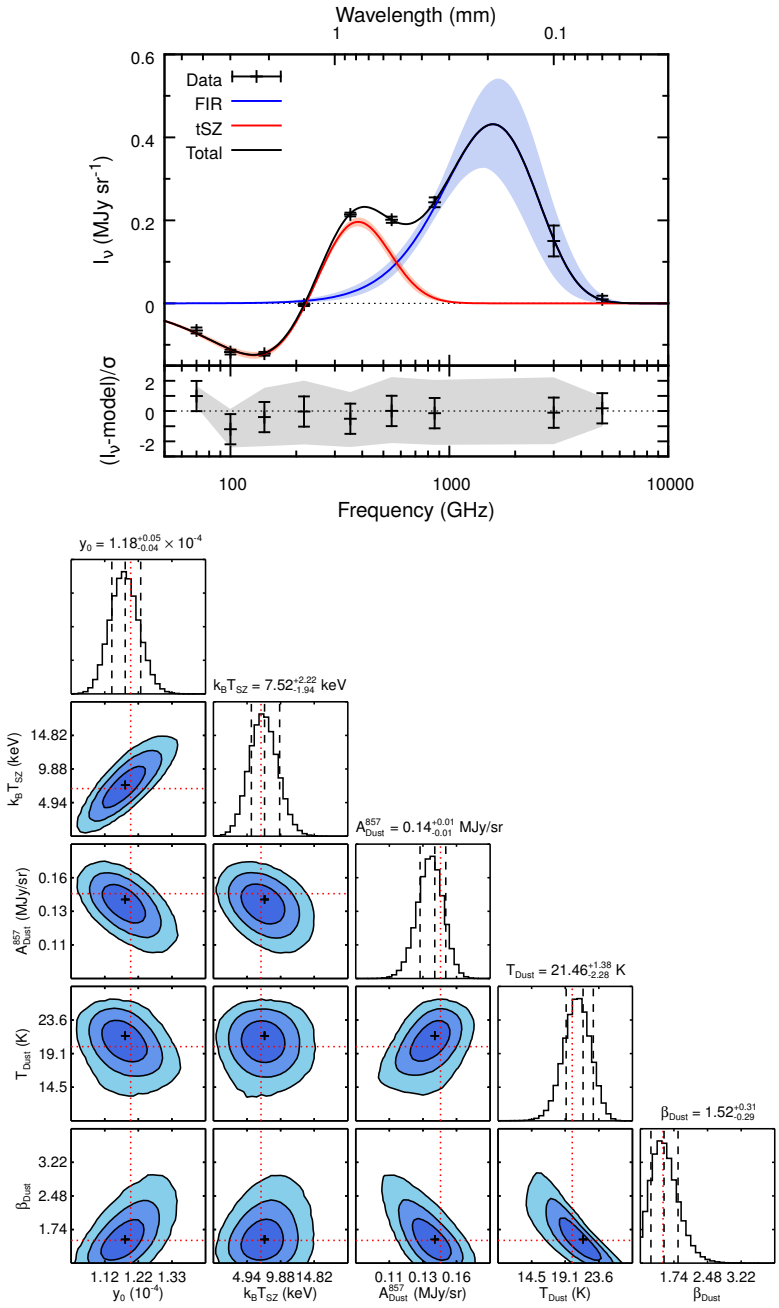


Figure 4.7: Spectral modelling results obtained from simulated all-sky mock data. These results represent a single foreground realization out of 30 that are shown in Fig. 4.6. **Top panel:** spectrum obtained after passing the mock data through our matched filtering pipeline and stacking of the positions of the simulated clusters. The red and blue solid lines show the best-fit tSZ and FIR models, while the shaded areas indicate the envelope derived from the 68% of models with the highest likelihood. The lower part of the panel shows the difference of the data and the best-fit model divided by the data error. As before, the shaded region corresponds to the 68% of models with the highest likelihood. **Bottom panel:** marginalized 2D and 1D constraints on our model parameters obtained through an MCMC approach. The colours in the 2D plots represent the 68, 95, and 99% confidence intervals. The dashed lines on top of the 1D constraints indicate the best-fit values and the 68% confidence interval, while the red dotted lines indicates the true values obtained directly from the simulated tSZ and FIR maps.

of the Comptonization parameter corresponds to $\Delta y_0 \approx 5\times10^{-6}$. We furthermore find tight constraints on the parameters of our FIR model with e.g. $A^{857}_{\rm Dust} = 0.14^{+0.01}_{-0.01}\,{\rm MJy\,sr^{-1}}$, $T_{\rm Dust} = 21.5^{+1.4}_{-2.3}\,{\rm K}$ and $\beta_{\rm Dust} = 1.5^{+0.3}_{-0.3}$. We note that these low uncertainties are primarily due to the lack of a CIB model at high frequencies and that the more complex real sky will not allow for such strong constraints on the properties of cluster FIR emission. The result of excluding the CIB component in our mock data tests therefore provides somewhat optimistic parameter constraints but no biases.

### 4.5.3 Simulation result: impact of the kSZ

One of the initial assumptions in our analysis is that stacking large samples of clusters will average out the kSZ signal due to the random directions of the clusters' peculiar velocities. To test this assumption, we assign a peculiar velocity component to each of our clusters by drawing from the distribution presented by Peel (2006), which is well approximated by a Gaussian with $\sigma = 311\,{\rm km\,s^{-1}}$ at $z = 0$. For simplicity, we neglect the weak redshift dependence of the halo peculiar velocity and note that it will drop by about 20% in the redshift range of $z \in [0,2]$ (Hernández-Monteagudo & Sunyaev, 2010), making our estimates of the kSZ signal contribution a conservative one.

Using this Gaussian approximation of the velocity distribution, we can expect that after stacking the residual sample-averaged velocity should be smaller than $311/\sqrt{772}\,{\rm km\,s^{-1}} \approx 11.2\,{\rm km\,s^{-1}}$ with 68% confidence. Using the optical depth of each cluster, we compute expected limits of the kSZ signal and find $I^{\rm kSZ}_{217} < 9.0\times10^{-4}\,{\rm MJy\,sr^{-1}}$ close to the peak of the kSZ spectrum, which corresponds to $0.27\sigma$ for our mock data. The situation is similar for our smaller subsample of 100 clusters with $I^{\rm kSZ}_{217} < 4.0\times10^{-3}\,{\rm MJy\,sr^{-1}}$, corresponding to $0.3\sigma$. This demonstrates that for the given sample sizes, the kSZ can be safely neglected. At smaller sample sizes however, the kSZ can potentially lower or raise the measured intensity at 143, 217, and 353 GHz whereas the other channels will stay mostly unaffected for all but the smallest samples.

### 4.5.4 Simulation result: potential $Y$-bias

It is often assumed that relativistic corrections to the tSZ effect can be neglected. Although detecting the relativistic distortions of the tSZ spectrum for individual clusters can be beyond the reach of current experiments, ignoring the relativistic corrections can lead to a bias of the Comptonization parameter that scales with cluster temperature and therefore cluster mass. This bias will depend on the observed frequency and can be written as

$$\frac{\Delta y}{y} = \frac{f(x,T_{\rm e})}{f(x,0\,{\rm keV})} - 1. \tag{4.25}$$

In multifrequency observations, this bias will depend on the weights assigned to each channel and thus has to be quantified through simulations. We investigate this bias using our mock data sets for two different scenarios. In the first scenario, we assume perfect foreground removal, in which case the weights for each channel will be given by the inverse squared thermal detector noise, providing the most optimistic estimate of the $y$-bias. In the second case, we clean our simulated cluster maps using an Internal Linear Combination (ILC) technique, the details of which are given in Appendix 4.11. ILC techniques are known for their robustness and simplicity and were used to produce some of the key SZ results published by the Planck Collaboration (e.g. Planck Collaboration 2013a,b, 2016d), but they require an accurate knowledge of the SZ spectral shape. In both cases, we compute the bias on

the measured cylindrically integrated Comptonization parameter within five times $R_{500}$, otherwise known as $Y_{5R500}$. Our results are summarized in Fig. 4.8.

Our simulations show that in both cases, the integrated Comptonization parameter is systematically biased low. Fitting the measured tSZ decrement/increment signal in absence of foregrounds with a non-relativistic tSZ spectrum yields a sample-average bias of $(3 \pm 1)\%$. The observed bias scales roughly linear with the cluster temperature and with $(M_{500})^{0.80\pm0.03}$. For high mass clusters, the bias can be as high as 7% in this approach. We find that our ILC technique produces a larger bias on average. Averaged over our entire cluster sample, the ILC estimate of the integrated $y$-parameter is biased low by $(7 \pm 2)\%$ and up to 14% for the hottest clusters. The bias again scales roughly linear with temperature and with $(M_{500})^{0.71\pm0.04}$ as is shown in Fig. 4.8. The reason for this strong bias is that the ILC technique assigns a high weight to the 143 GHz and 353 GHz channels (see Fig. 4.14) at which the difference between the relativistic and non-relativistic tSZ spectrum is particularly large. We point out that an unbiased estimation of the integrated $y$-parameter is possible by having a knowledge of the average $T_{\rm SZ}$ within the desired aperture while computing the ILC-weights. More recently, Hurier & Tchernin (2017) have introduced a modified version of the ILC algorithm that is tailored to observations of the relativistic tSZ effect.

Our results demonstrate that using the non-relativistic approximation of the tSZ spectrum will lead to a systematic underestimation of the Comptonization parameter that can be as high as 14% for the most massive clusters. The exact magnitude of the bias will depend on the details of the $y$-extraction method and has to be quantified and should be corrected for if possible. We further discuss this bias in Section 4.7.1.

## 4.6 Results from real data

The main results obtained from actual *Planck*, IRAS and *AKARI* data are summarized in Fig. 4.9. After matched filtering and stacking, we obtain a spectrum that clearly shows the characteristic tSZ decrement/increment plus an additional FIR excess, consistent with FIR emission from galaxy clusters. By fitting our two-component tSZ+FIR model to the extracted spectrum with $\beta_{\rm Dust} = 1.5$ kept fixed and marginalizing over the remaining free model parameters, we are able to constrain the average deconvolved central $y$-parameter of the sample to be $\langle y_0 \rangle = (1.24 \pm 0.04) \times 10^{-4}$, corresponding to a $31\sigma$-detection of the tSZ signal of 772 clusters.

By modelling the relativistic distortions of the tSZ spectrum we obtain a $2.2\sigma$ measurement of the sample-average cluster temperature, which we constrain to $k_{\rm B}\langle T_{\rm SZ} \rangle = 4.4^{+2.1}_{-2.0}\,$keV. Our model provides a good fit to the data with $\chi^2/{\rm df} = 0.98$. Furthermore, we obtain a $5\sigma$ detection of galaxy cluster-centric FIR emission with the FIR amplitude $A^{857}_{\rm Dust} = (0.10 \pm 0.2)\,{\rm MJy\,sr^{-1}}$. We constrain the temperature of the emitting dust grains to $T_{\rm Dust} = 18.4^{+3.9}_{-2.4}\,{\rm K}$, which is lower than the recent measurement of $(24.2 \pm 3.0)\,{\rm K}$[7] by the Planck Collaboration (2016i), who performed a stacking analysis on a similar cluster sample, but with a different foreground-removal technique (see Section 4.7.3).

Due to the high uncertainties in the IRAS and *AKARI* channels, most of the constraining power comes from the *Planck* data. Excluding the IRAS and *AKARI* data points from our fit leaves the constraints on the tSZ parameters virtually untouched, while the errors on the FIR component

[7] This value was obtained by converting the reported $(19.2 \pm 2.4)\,{\rm K}$ to the cluster rest frame using the mean redshift $\langle z \rangle = 0.26$ of the sample.

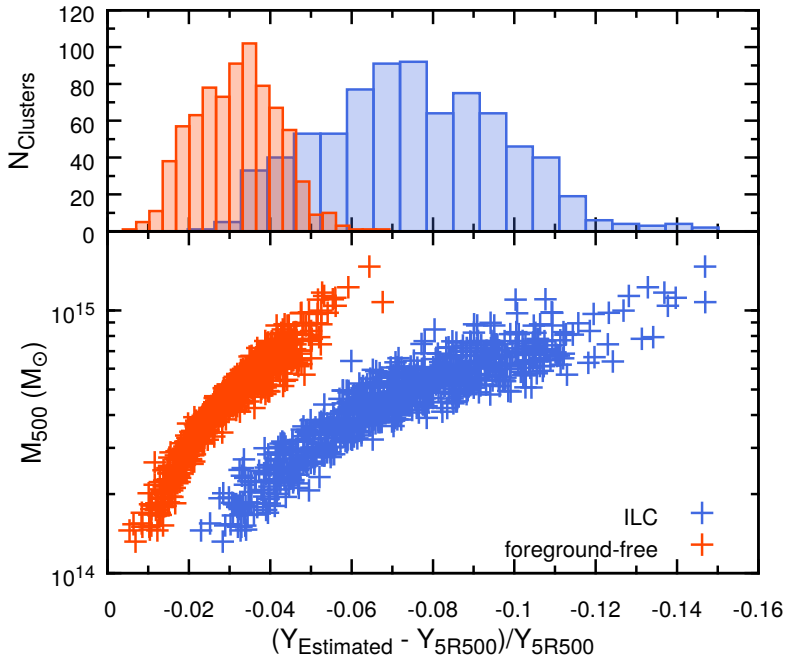


Figure 4.8: Mass-dependent bias of the Comptonization parameter introduced by using the non-relativistic approximation of the tSZ spectrum. We quantified the bias using our mock data sets including simulated relativistic spectra. The cylindrically integrated Comptonization parameter within $5\,\mathrm{R}_{500}$ was obtained from direct fitting of the simulated tSZ maps (red) and passing the maps though an ILC pipeline (blue, details in Appendix 4.11). In both cases, we find a mass-dependent bias of $Y_{5\mathrm{R}500}$. In the former case, the values for $Y_{5\mathrm{R}500}$ are biased low by 3% on average, whereas the ILC approach underestimates the true values on average by 7%.

parameters only inflate by a marginal amount to $A_{\mathrm{Dust}}^{857} = 0.11^{+0.02}_{-0.03}\,\mathrm{MJy\,sr^{-1}}$ and $T_{\mathrm{Dust}} = 18.8^{+4.0}_{-3.1}\,\mathrm{K}$ with $\chi^2/\mathrm{df} = 1.69$.

We also test for the impact of the choice of $\beta_{\mathrm{Dust}}$ by re-running our fit for a number of values ranging from 1.3 up to 2.0. We find that both $\langle T_{\mathrm{SZ}} \rangle$ and $T_{\mathrm{Dust}}$ are anticorrelated with $\beta_{\mathrm{Dust}}$. The results for spectral fitting with different fixed values for $\beta_{\mathrm{Dust}}$ are summarized in Table 4.2.

In case the SED of the cluster FIR emission varies strongly from cluster to cluster, choosing a modified blackbody as our model function can bias the tSZ parameters. We tried to account for this more complex spectrum by fitting our data with the second-order moment expansion of the modified blackbody that was introduced by Chluba et al. (2012) but find that our data are not able to constrain the additional parameters related to the distribution of $T_{\mathrm{Dust}}$ and $\beta_{\mathrm{Dust}}$. We note that the distortions of the dust SED will be strongest in the Wien part at THz frequencies, where we find large errors for the IRAS and *AKARI* intensities. At *Planck's* frequencies departures from the modified blackbody should be small.

In order to understand which channels have the biggest impact on the measurement of $T_{\mathrm{SZ}}$, we exclude individual channels one after another from the spectral fitting and record the changes of the $T_{\mathrm{SZ}}$ error. From this test we conclude that the *Planck* 217 GHz channel is the most important one for our analysis, followed by *Planck's* 545 GHz channel. Excluding one of these two channels increases the uncertainty of $T_{\mathrm{SZ}}$ by $\simeq 50\%$, highlighting the importance of the tSZ increment for measuring

temperatures via the relativistic tSZ spectrum.

In addition to our full sample of 772 clusters, we repeat our analysis for the subsample containing the 100 hottest clusters. The results of the spectral analysis of this subsample are shown in Fig. 4.10. Fitting the stacked spectrum of the clusters with the same two component tSZ+FIR model as before with $\beta_{\rm Dust} = 1.5$, we detect the tSZ signal at $23\sigma$ with $\langle y_0 \rangle = 2.58^{+0.16}_{-0.11} \times 10^{-4}$. We constrain the sample-average cluster temperature to $k_{\rm B}\langle T_{\rm SZ}\rangle = 6.0^{+3.8}_{-2.9}$ keV, which corresponds to a $2.0\sigma$ measurement of the tSZ relativistic corrections. As is the case for our full sample, we observe an FIR excess at $4.4\sigma$ that is well modelled by a modified blackbody SED. For the two free parameters of the FIR model we find $A^{857}_{\rm Dust} = 0.22^{+0.06}_{-0.05}$ MJy sr$^{-1}$ and $T_{\rm Dust} = 16.9^{+5.0}_{-2.3}$ K. As before, the model provides a good fit to the data with $\chi^2/{\rm df} = 0.69$, which changes to $\chi^2/{\rm df} = 1.28$ when the *AKARI* and IRAS data points are excluded from the fit. We note that, as for the full sample, most of the constraining power comes from the *Planck* data and excluding the additional FIR data points has little impact on our parameter constraints.

## 4.7 Discussion

### 4.7.1 Interpretation of the main results

After careful signal extraction and spectral fitting, we can confirm the signature of a relativistic tSZ (or rSZ) signal in *Planck* full-mission data at roughly 95% significance level. For our sample of 772 clusters, we find an average temperature of $k_{\rm B}\langle T_{\rm SZ}\rangle = 4.4^{+2.1}_{-2.0}$ keV, which is consistent with the mass-weighted average X-ray temperature $k_{\rm B}\langle T_{\rm X}\rangle = (6.91 \pm 0.07)$ keV. There is a tentative difference (at roughly $1.3\sigma$) between these two values, with $\langle T_{\rm SZ}\rangle$ being lower than the sample-averaged X-ray spectroscopic temperature $\langle T_{\rm X}\rangle$.

We find that, due to the sensitivity of *Planck*, a better constraint on the relativistic tSZ-derived temperature is not obtainable by simply selecting the hottest clusters from the cluster catalogue. While this approach increases the mean sample temperature, the noise also increases due to the smaller sample size. As a result, the detection significance of $\langle T_{\rm SZ}\rangle$ remains roughly constant. The best-fit value of $k_{\rm B}\langle T_{\rm SZ}\rangle = 6.0^{+3.8}_{-2.9}$ keV in this subsample is again lower but consistent with the expected mass-weighted X-ray temperature $k_{\rm B}\langle T_{\rm X}\rangle = (8.54 \pm 0.16)$ keV.

The lower $T_{\rm SZ}$ values can result from the different weighting schemes in tSZ and X-ray temperature measurements. While $T_{\rm SZ}$ is weighted linearly with the gas density, $T_{\rm X}$ is weighted with its square. Previous studies showed that the gas mass-weighted temperature $T_{\rm mg}$, which behaves similar to $T_{\rm SZ}$, measured within an aperture to be lower than the X-ray spectroscopic temperature (Vikhlinin et al., 2006; Nagai et al., 2007) and the ratio $Y_{\rm SZ}/Y_{\rm X}$ to be less than unity (Arnaud et al., 2010). We investigate the impact of the weighting schemes in Appendix 4.12 using analytical temperature and density profiles and find that $T_{\rm X}$ is higher than $T_{\rm SZ}$ by $\sim 20\%$ for non-cool-core clusters when averaged within $\theta_{500}$ and only lower then $T_{\rm SZ}$ for cool-core clusters when small apertures ($\lesssim 0.3\theta_{500}$) are used. We note that our cluster sample is a representative subset of the Planck PSZ2 clusters, since the sample selection is only affected by Galactic foregrounds and point sources. Recently, Rossetti et al. (2017) found the cool-core fraction of a representative subset of *Planck* clusters to be $\approx 30\%$. Therefore we do not expect the ratio $T_{\rm X}/T_{\rm SZ}$ observed within dense cool cores to significantly affect our results. On the other hand, hydrodynamic simulations frequently produce a large number of cold and dense clumps that are able to bias $T_{\rm X}$ low compared to $T_{\rm SZ}$ (or $T_{\rm mg}$) within the entire cluster volume (e.g. Kay et al. 2008; Biffi et al. 2014), yet more recent and improved simulation codes predict the dissociation

| $\beta_{\rm Dust}$ | $y_0$ | $k_{\rm B}T_{\rm SZ}$ (keV) | $A^{857}_{\rm Dust}$ (MJy sr$^{-1}$) | $T_{\rm Dust}$ (K) | $y_0$ | $k_{\rm B}T_{\rm SZ}$ (keV) | $A^{857}_{\rm Dust}$ (MJy sr$^{-1}$) | $T_{\rm Dust}$ (K) |
|---|---|---|---|---|---|---|---|---|
| | **Full sample ($n$ = 772)** | | | | **Hot sample ($n$ = 100)** | | | |
| 1.3 | $1.24^{+0.04}_{-0.04} \times 10^{-4}$ | $4.38^{+2.32}_{-1.79}$ | $0.10^{+0.02}_{-0.02}$ | $21.19^{+3.62}_{-2.91}$ | $2.58^{+0.16}_{-0.10} \times 10^{-4}$ | $6.35^{+3.87}_{-2.97}$ | $0.22^{+0.06}_{-0.05}$ | $19.21^{+5.07}_{-2.97}$ |
| 1.4 | $1.24^{+0.04}_{-0.04} \times 10^{-4}$ | $4.29^{+2.22}_{-1.90}$ | $0.10^{+0.02}_{-0.02}$ | $19.72^{+3.88}_{-2.57}$ | $2.58^{+0.17}_{-0.10} \times 10^{-4}$ | $6.39^{+3.53}_{-3.22}$ | $0.22^{+0.06}_{-0.05}$ | $18.39^{+4.62}_{-3.00}$ |
| **1.5** | $\mathbf{1.24^{+0.04}_{-0.04} \times 10^{-4}}$ | $\mathbf{4.36^{+2.13}_{-1.95}}$ | $\mathbf{0.10^{+0.02}_{-0.02}}$ | $\mathbf{18.44^{+3.94}_{-2.38}}$ | $\mathbf{2.58^{+0.16}_{-0.11} \times 10^{-4}}$ | $\mathbf{5.96^{+3.78}_{-2.93}}$ | $\mathbf{0.22^{+0.06}_{-0.05}}$ | $\mathbf{16.92^{+4.83}_{-2.26}}$ |
| 1.6 | $1.23^{+0.05}_{-0.03} \times 10^{-4}$ | $3.98^{+2.25}_{-1.77}$ | $0.10^{+0.02}_{-0.02}$ | $17.11^{+4.05}_{-2.07}$ | $2.58^{+0.15}_{-0.12} \times 10^{-4}$ | $6.24^{+3.19}_{-3.45}$ | $0.21^{+0.07}_{-0.04}$ | $16.14^{+4.33}_{-2.20}$ |
| 1.7 | $1.24^{+0.04}_{-0.04} \times 10^{-4}$ | $3.98^{+2.97}_{-1.67}$ | $0.10^{+0.02}_{-0.02}$ | $16.24^{+3.65}_{-2.02}$ | $2.59^{+0.14}_{-0.13} \times 10^{-4}$ | $5.68^{+3.64}_{-2.99}$ | $0.21^{+0.07}_{-0.05}$ | $15.23^{+4.36}_{-1.72}$ |
| 1.8 | $1.23^{+0.04}_{-0.03} \times 10^{-4}$ | $4.06^{+2.18}_{-1.84}$ | $0.10^{+0.02}_{-0.02}$ | $15.54^{+3.37}_{-1.94}$ | $2.57^{+0.16}_{-0.11} \times 10^{-4}$ | $5.22^{+3.92}_{-2.61}$ | $0.22^{+0.07}_{-0.06}$ | $15.19^{+3.38}_{-2.21}$ |
| 1.9 | $1.24^{+0.04}_{-0.04} \times 10^{-4}$ | $3.99^{+2.25}_{-1.77}$ | $0.10^{+0.02}_{-0.02}$ | $14.73^{+3.14}_{-1.73}$ | $2.56^{+0.16}_{-0.11} \times 10^{-4}$ | $4.94^{+3.98}_{-2.56}$ | $0.21^{+0.07}_{-0.05}$ | $14.61^{+3.13}_{-2.01}$ |
| 2.0 | $1.23^{+0.05}_{-0.03} \times 10^{-4}$ | $3.92^{+2.28}_{-1.70}$ | $0.10^{+0.02}_{-0.02}$ | $14.06^{+2.80}_{-1.56}$ | $2.55^{+0.17}_{-0.10} \times 10^{-4}$ | $4.68^{+3.95}_{-2.47}$ | $0.21^{+0.07}_{-0.05}$ | $13.89^{+3.04}_{-1.67}$ |

Table 4.2: Parameter constraints from spectral modelling for a range of different fixed values for the spectral index $\beta_{\rm Dust}$ of the modified blackbody for cluster FIR emission. The constraints for $\beta_{\rm Dust}$ = 1.5 that are highlighted in bold face are reported as our main results. We find that both $T_{\rm SZ}$ and $T_{\rm Dust}$ are anticorrelated with $\beta_{\rm Dust}$, whereas $\langle y_0 \rangle$ and $A^{857}_{\rm Dust}$ are independent of it.

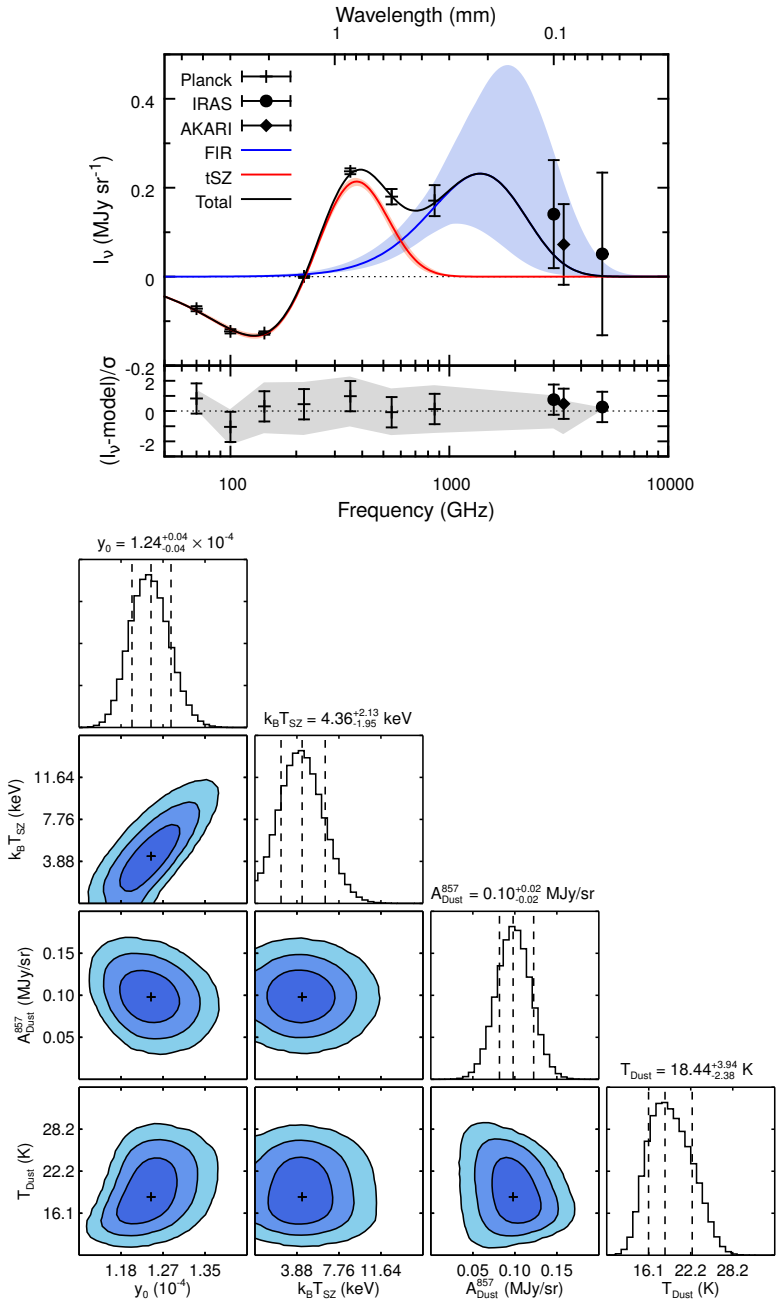


Figure 4.9: Spectral modelling results for our sample of 772 galaxy clusters selected from the second *Planck* cluster catalogue (PSZ2). **Top panel:** spectrum extracted after passing the *Planck*, IRAS and *AKARI* maps through our matched filtering pipeline and stacking the cluster positions. The red and blue solid lines indicate the best-fit tSZ and FIR models. Note that the data points have been corrected for the instrumental bandpasses using the best-fit model for illustrational purposes only in order to plot smooth curves. **Bottom panel:** marginalized 2D and 1D constraints on our model parameters obtained through an MCMC approach. The colours in the 2D plots represent the 68, 95, and 99% confidence intervals. The dashed lines on top of the 1D constraints indicate the best-fit values and the 68% confidence interval. The third parameter of the FIR model $\beta_{\rm Dust}$ was fixed to the common value 1.5 in order to obtain these results. We do not observe any strong correlation between the tSZ and FIR parameters. The tSZ signal of the sample is detected with high significance ($31\sigma$) and we obtain a $2.2\sigma$ measurement of the sample-average cluster temperature.

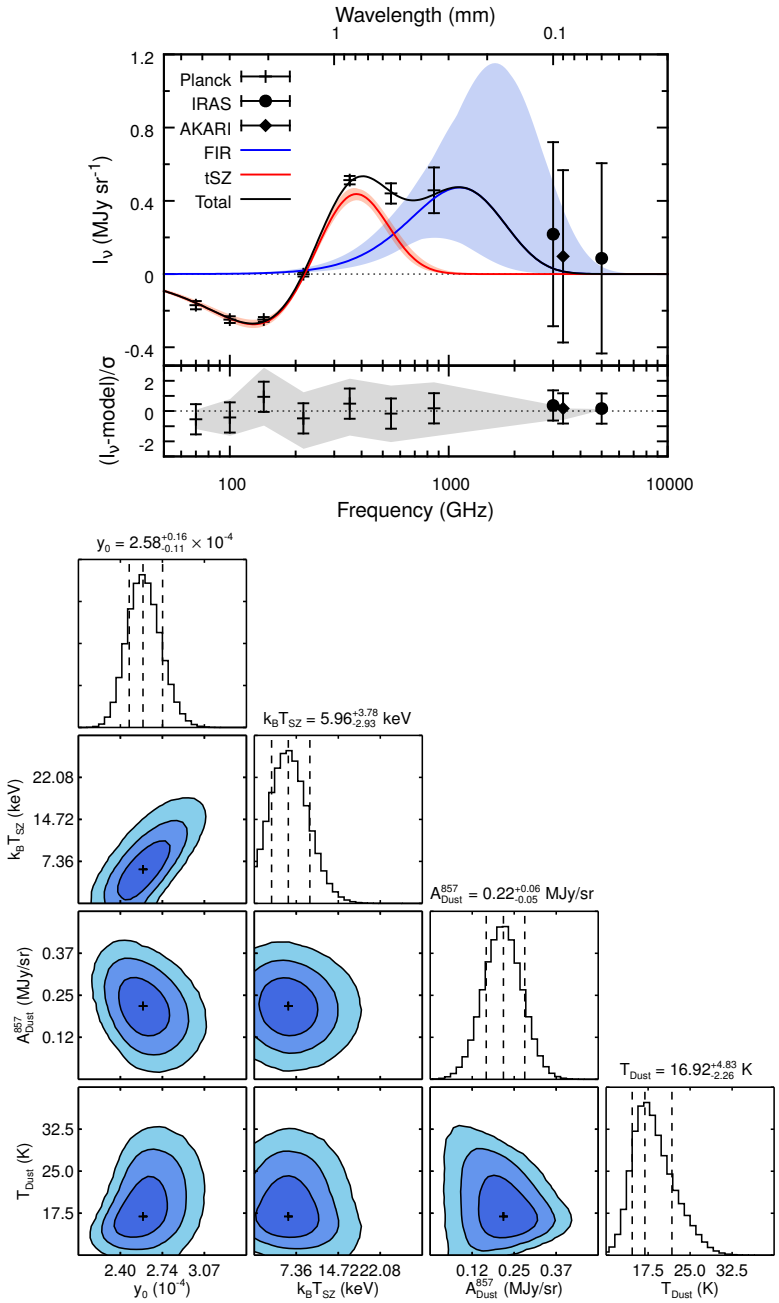


Figure 4.10: Spectral modelling results for a smaller subsample, containing just the 100 hottest clusters as determined through the $M$–$T$ scaling relation given by equation (4.12). **Top panel:** as before, we show the spectrum extracted after passing the *Planck*, IRAS and *AKARI* maps through our matched filtering pipeline and stacking the cluster positions. The red and blue solid lines indicate the best-fit tSZ and FIR models. **Bottom panel:** marginalized 2D and 1D constraints on our model parameters obtained through an MCMC approach for the 100 hottest clusters. As for the full sample, the third parameter of the FIR model $\beta_{\rm Dust}$ was fixed to 1.5. We again do not observe a strong correlation of the tSZ and FIR model parameters. Although the average $y$-parameter of the clusters is roughly twice as high as for the full sample, the significance of the tSZ signal detection reduces to $23\sigma$. We are able to measure a higher sample-average cluster temperature, consistent with our expectation, but at a slightly reduced significance of $2.0\sigma$.

of such clumps (Beck et al., 2016). It is beyond the scope of the current paper to make a detailed analysis of this ratio that will require a systematic evaluation of the $T_X$ measurements in the parent samples of Reichert et al. (2011) from which our $T_X$ scaling is taken, for example whether spectral fits were obtained after masking dense substructures within the clusters or not.

Even though *Planck* data do not provide evidence for the relativistic distortions in the tSZ spectrum with high significance, the presence of these distortions can nevertheless cause a bias in the measured SZ signals when non-relativistic spectra are used to extract Comptonization $y$-maps or fit data in a matched multifiltering approach. We demonstrated this bias in Section 4.5.4 through our simulated mock cluster sample with realistic noise and foregrounds. A similar analysis based on the application of ILC algorithms on simulated maps for the Cosmic ORigins Explorer (COrE) mission has been presented by Hurier & Tchernin (2017), who find bias up to 20% in the $Y$-value of the hottest clusters.

The bias lowers the measured $Y$-value and is mass-dependent. A mass dependence is expected since the relativistic corrections to the spectrum would only be significant for high-mass clusters. It is interesting to note that the direction and mass dependence of this bias are both similar to the so-called hydrostatic mass bias that is assumed in the cosmological analysis of *Planck* clusters. This bias term, parameterized by a $(1-b)$ factor in $Y$–$M$ scaling relations (e.g., Planck Collaboration 2014c), accounts for all possible biases in the mass measurement and the use of the non-relativistic spectrum for the tSZ signal extraction will certainly be a part of it. As we do not follow the exact SZ signal extraction methods (matched multifiltering and POWELLSNAKES) that are used by the Planck Collaboration and also do not carry out the steps necessary to connect $Y_{500}$ to $M_{500}$ via X-ray mass proxies, we are unable to comment on the exact bias on the $Y_{500}$–$M_{500}$ scaling relation used in the *Planck* analysis.

We instead focus on quantifying the $Y$-measurement bias based on our mock data, finding it to be around 5% (optimistic case with no foregrounds) up to about 14% (extreme case based on the ILC method) for the most massive clusters. The mass dependence of the $Y$-bias is also of interest, which we found to be approximately $(M_{500})^{0.71\pm0.04}$ when using the ILC approach. This is very similar to the slope of the hydrostatic mass bias found in weak-lensing mass calibration of subsets of *Planck* clusters, for example by von der Linden et al. (2014b), who found a mass scaling between the *Planck* SZ and weak-lensing mass estimates having a power law index of $0.68^{+0.15}_{-0.11}$. Even though it is expected that more massive systems would show stronger deviations from hydrostatic equilibrium due to their enhanced mass accretion rate (e.g., Shi & Komatsu 2014), the similar mass dependence of both these biases suggests that the observed effect can be a combination of the two.

We also consider the effect of electron temperature variance within our mock cluster sample. As explained in Chluba et al. (2013), the second moment of the temperature field causes another correction to the average SZ signal. Using our mock data, we find the $y$-weighted temperature moments, $k_B\langle T_e\rangle_y \simeq 7.7\,\mathrm{keV}$ and $k_B\langle T_e^2\rangle_y \simeq 64\,\mathrm{keV}^2$, implying $\sigma_{T_e} \simeq 2.1\,\mathrm{keV}$. At the current level of sensitivity, this leads to a negligible correction to the sample-averaged relativistic SZ signal and can be ignored. However, future precision measurements of $T_{SZ}$ in multiple mass bins might offer a possibility to constrain the slope of the cluster mass function using higher-order moments of $T_e$.

### 4.7.2 Comparison with other works

Recently, Hurier (2016) claimed the first high significance detection of the tSZ relativistic corrections by stacking *Planck* maps of clusters taken from the X-ray-selected MCXC cluster catalogue (Piffaretti et al., 2011), as well as several smaller cluster catalogues with X-ray spectroscopic temperatures. Hurier (2016) binned clusters from both the MCXC cluster catalogue and the combined spectroscopic

catalogue according to their temperature. A comparison of the obtained tSZ inferred ICM temperatures $T_{\rm SZ}$ with $T_{\rm X}$ revealed a linear trend with a significance of $3.7\sigma$ for the MCXC clusters and $5.3\sigma$ for the spectroscopic ones, which is the main result reported by the author. In addition Hurier (2016) finds that the $T_{\rm SZ}$ values are higher than $T_{\rm X}$ with a ratio $T_{\rm SZ}/T_{\rm X}$ of $1.65 \pm 0.45$ and $1.38 \pm 0.26$, respectively.

The approach presented in this work differs from the one used by Hurier (2016) mostly in the foreground removal and spectral modelling techniques. Hurier (2016) adopted the foreground removal approach presented by Hurier et al. (2014), in which Galactic and extragalactic thermal dust emission is subtracted by using the *Planck* 857 GHz channel as a template that is extrapolated to lower frequencies using a scale factor. This scale factor is computed for each channel under the assumption that the SED is constant in a $2^\circ \times 2^\circ$ field around each cluster, excluding the central 30 arcmin. The *Planck* 217 GHz channel is used analogously to remove the contribution of the CMB from the remaining maps, making use of its well-known frequency spectrum.

We note that subtracting the 217 GHz and 857 GHz maps to remove the CMB and Galactic dust can lead to a distortion of the tSZ spectrum of the clusters due to the non-negligible tSZ signal within these two *Planck* bands. This can be understood using the tabulated, band-integrated spectra provided in Table 4.4. Assuming a typical dust SED with $T_{\rm Dust} = 20\,{\rm K}$ and $\beta = 1.5$, the intensity at 545 GHz is approximately 33% of the intensity at 857 GHz and 9% in case of 353 GHz. For a 10 keV cluster subtracting the 857 GHz map thus reduces the tSZ signal at 545 GHz by about $47\,{\rm MJy\,sr^{-1}}$ to $907\,{\rm MJy\,sr^{-1}}$, corresponding to $T_{\rm e} \approx 5\,{\rm keV}$. Analogous calculations can be done to estimate the impact of subtracting the 217 GHz map and show that the bias will be largest for low- temperature systems. In addition to the partial subtraction of the tSZ signal, the assumption of a constant dust SED across the field neglects the redshift-induced $K$-correction needed for the cluster FIR emission.

Our work relies on a matched filtering approach to reduce the Galactic and extragalactic foregrounds, which only assumes that these are spatially uncorrelated with the cluster signal. The correlated cluster FIR component is accounted for later in our spectral modelling. The validity of our approach is tested with mock data. Clusters with known low-frequency point sources are removed from our sample and we therefore do not include a dedicated low-frequency component in our spectral model.

Our attempts at constraining the $T_{\rm X}$ versus $T_{\rm SZ}$ linear slope using a cluster sample similar to the one used by Hurier (2016) with direct X-ray spectroscopic temperatures produce inconclusive results. Starting from the same cluster catalogues with spectroscopic $T_{\rm X}$ information, we obtain a total of 313 clusters after removal of duplicates and applying our Galactic mask and point source flagging. This sample, when split into three temperature bins, yields large errors that leave $T_{\rm SZ}$ unconstrained. We repeat this analysis with our full sample of 772 clusters, with $T_{\rm X}$ values estimated using equation (4.12) and grouped into four temperature bins. Fixing the line intercept at $[0\,{\rm keV}, 0\,{\rm keV}]$, we find the normalization of the ratio $T_{\rm SZ}/T_{\rm X}$ to be smaller than unity at roughly $2\sigma$ significance. This result and its errors are similar to the values derived earlier for our full sample and the subsample containing the 100 hottest clusters.

### 4.7.3 FIR emission from galaxy clusters

In recent years, it has been shown that clusters are sources of FIR emission. Although the exact nature of this emission remains uncertain, current observations point towards both dusty cluster members, as well as stripped warm dust in the ICM. Furthermore, clusters act as powerful gravitational lenses of the CIB, the magnified emission of which further adds to the observed emission. This spatially correlated FIR emission makes accurate measurements of the relativistic tSZ more challenging and requires joint

spectral modelling of both components. Matched filtering techniques like the one employed by us are particularly suited to separate the FIR emission from clusters from Galactic and uncorrelated CIB emission with similar SED based on their spatial distribution.

To demonstrate this, we compare our method against the frequently used 'aperture photometry' method of foreground removal, and the results are shown in Fig. 4.11. The matched filters are constructed and applied in the same way as described in Section 4.4.1, with the exception that we compute the signal integrated within 15 arcmin, which is achieved by multiplying the deconvolved amplitude that is returned by the filter with the integral of the cluster profile:

$$S_\nu(< r) = I_\nu^{\mathrm{filt}} 2\pi \int_0^{\theta'} \theta y(\theta)\, \mathrm{d}\theta, \tag{4.26}$$

where $I_\nu^{\mathrm{filt}}$ is the stacked flux after filtering. In case of the aperture photometry technique, we integrate the signal in the stacked maps within the same 15 arcmin aperture and subtract the background that is constrained from an annulus with $15' < r < 60'$. The errorbars are derived by performing the same steps on 1000 randomly positioned stacked fields. Our comparison shows that matched filtering allows for less Galactic foreground residuals resulting in smaller errorbars and reduces the contribution of cluster FIR emission to the observed signal significantly. Spectral fitting of the spectrum obtained through aperture photometry delivers a higher dust temperature $T_{\mathrm{Dust}} = 22.6^{+0.9}_{-1.3}$ K compared to matched filtering. This is closer to the value reported by the Planck Collaboration (2016i). Even though we measure the dust temperature at higher significance compared to the values reported in Section 4.6 due to the increased FIR amplitude, the larger errors at low frequencies do not allow to constrain the average electron temperature of the clusters.

Although *Planck's* resolution does not allow us to determine the exact nature of the FIR emission from clusters, we can explore its scaling with cluster mass and redshift. Due to the redshift-dependent selection of the *Planck* clusters, splitting the entire sample into two mass or redshift bins will produce correlated results; hence, we restrict these variables for the following analysis. We find that half of our sample (i.e. 386 clusters) lies within a relatively narrow redshift interval $0.072 < z < 0.257$, allowing us to minimize a potential redshift evolution of the dust luminosity. We split this sample into a low-mass and a high-mass subsample with 193 clusters each ($\langle M_{500}^{\mathrm{high}} \rangle = 5.1 \times 10^{14}\,\mathrm{M}_\odot$, $\langle M_{500}^{\mathrm{low}} \rangle = 3.0 \times 10^{14}\,\mathrm{M}_\odot$, $\langle z^{\mathrm{high}} \rangle = 0.192$, $\langle z^{\mathrm{low}} \rangle = 0.132$). After fixing the SED of the FIR component by assuming $T_{\mathrm{Dust}} = 20$ K for both samples, the observed dust amplitudes and average sample masses are assumed to be related via a power law:

$$\frac{A_{\mathrm{Dust}}^{\mathrm{high}}}{A_{\mathrm{Dust}}^{\mathrm{low}}} = \left( \frac{1 + \langle z^{\mathrm{low}} \rangle}{1 + \langle z^{\mathrm{high}} \rangle} \right)^4 \left( \frac{\langle M_{500}^{\mathrm{high}} \rangle}{\langle M_{500}^{\mathrm{low}} \rangle} \right)^\epsilon . \tag{4.27}$$

We find that the observed dust amplitude scales with the cluster mass to the power of $\epsilon = 0.8^{+1.7}_{-1.3}$. This value is consistent with the value of 1.0 that is assumed by the Planck Collaboration (2016e), but is significantly smaller than the value of $4.4 \pm 1.0$ that can be derived from the dust masses reported by the Planck Collaboration (2016i) for two different cluster mass bins. Our analysis is limited by the large uncertainties on $A_{\mathrm{Dust}}$ ($A_{\mathrm{Dust}}^{\mathrm{high}} = (0.07 \pm 0.03)\,\mathrm{MJy\,sr^{-1}}$, $A_{\mathrm{Dust}}^{\mathrm{low}} = 0.04^{+0.03}_{-0.02}\,\mathrm{MJy\,sr^{-1}}$).

We investigate the redshift evolution of the FIR emission by repeating this test analogously for a low-$z$ and a high-$z$ subsample. We find that half of our sample lies within the cluster mass interval $3.7 \times 10^{14}\,\mathrm{M}_\odot < M_{500} < 6.0 \times 10^{14}\,\mathrm{M}_\odot$, which we than split into a low-redshift subsample with

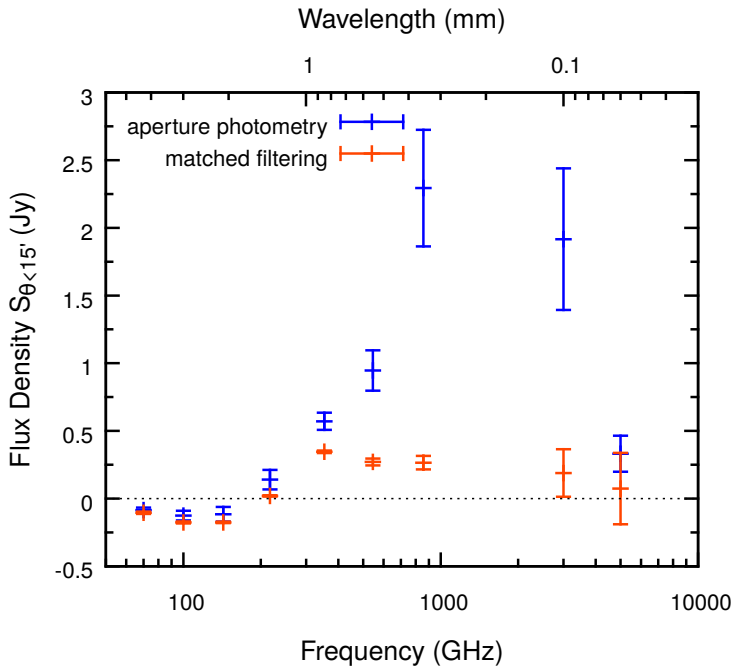


Figure 4.11: Comparison of the fluxes extracted with our matched filtering technique (red) and the aperture photometry method (blue). The latter has been used in previous studies conducted by the Planck Collaboration (2016e; 2016i). We use both techniques to extract the stacked spectrum of our sample of 772 clusters integrated within 15 arcmin. We find that matched filtering offers much cleaner maps with less Galactic residuals, as reflected by the smaller errorbars, and reduces the contribution from cluster FIR emission to the extracted spectrum significantly.

$\langle z^{\mathrm{low}} \rangle = 0.191$ and a high redshift subsample with $\langle z^{\mathrm{high}} \rangle = 0.387$. We again use a power law to relate the observed FIR amplitudes to the redshifts of the subsamples

$$\frac{A_{\mathrm{Dust}}^{\mathrm{high}}}{A_{\mathrm{Dust}}^{\mathrm{low}}} = \left( \frac{1 + \langle z^{\mathrm{high}} \rangle}{1 + \langle z^{\mathrm{low}} \rangle} \right)^{\delta - 4} , \tag{4.28}$$

and constrain the power law slope of the redshift dependence to be $\delta = 6 \pm 3$ with $A_{\mathrm{Dust}}^{\mathrm{high}} = 0.13^{+0.05}_{-0.04}\,\mathrm{MJy\,sr^{-1}}$ and $A_{\mathrm{Dust}}^{\mathrm{low}} = 0.09^{+0.04}_{-0.03}\,\mathrm{MJy\,sr^{-1}}$.

Detailed studies of the mass and redshift dependence of the infrared luminosity and the related dust content of clusters will be exciting goals for the next generation of sub-mm/FIR observatories. With the increased sensitivities that will be provided by future observatories, the assumption of a single temperature modified blackbody is likely to break down. As a consequence, more complex models that account for a temperature variance along the line of sight like the one presented by Chluba et al. (2017) might be needed.

### 4.7.4 Outlook: CCAT-prime

In the final section, we discuss what future SZ experiments might be able to improve upon the constraints on the relativistic tSZ-derived temperature. Currently, *Planck* is the only experiment with the necessary spectral coverage to model the entire tSZ/relativistic tSZ spectrum and separate its contribution from cluster FIR emission. Future space-based experiments, similar to the COrE mission (Delabrouille et al., 2018), will have the same spectral coverage as *Planck*, but with many more spectral channels and far better sensitivity making them ideally suited for this kind of measurements. In addition, future CMB spectrometers, similar to the Primordial Inflation Explorer (PIXIE; Kogut et al. 2011), would improve upon the sensitivity of COBE FIRAS experiment by several orders of magnitude and are expected to detect the average relativistic thermal SZ at very high significance ($\simeq 10-20\sigma$, Hill et al. 2015; Abitbol et al. 2017), although their angular resolution may not allow for a study of individual clusters. Ground-based experiments proposed under the CMB-S4 concept[8] will have a restricted frequency range, capped at around 270 GHz, but more than two orders of magnitude better sensitivity than *Planck* that will also enable a detailed modelling of the SZ spectrum. Here we present result predictions for a new telescope, named CCAT-prime, that is expected to start its observation well ahead of these two other classes of experiments and can provide relativistic tSZ-based temperature measurements of individual clusters.

CCAT-prime (CCAT-p for short) will be a 6 m diameter submillimetre telescope operating at 5600 m altitude in the Chilean Atacama desert. The high and dry site on a mountaintop in the Chajnantor plateau will offer excellent atmospheric conditions for submillimetre continuum surveys up to 350 $\mu$m wavelength (Bustos et al., 2014), and the high-throughput optical design will allow for large focal-plane arrays similar to the future CMB-S4 experiments (Niemack, 2016). Beginning its first-light observations in 2021, CCAT-p will perform large area multiband surveys for the SZ effect. We consider the sensitivities for a fiducial 4000 h, 1000 deg$^2$ survey in seven frequency bands with an instrument based on the design presented by Stacey (2014). The expected survey sensitivities are quoted in Table 4.3 in comparison to the *Planck* full-mission data. It is seen that the individual channel sensitivities for CCAT-p are about a factor of $\simeq 5-15$ better, except for the highest frequency band, for which the sky emissivity is roughly 40% from the ground even in the best quartile of weather.

We carry out a simplified comparison between *Planck* and CCAT-p for constraining the cluster SZ and dust parameters that ignores all Galactic and extragalactic foregrounds (thus also not taking advantage of the roughly six times better angular resolution compared to *Planck* for matched filtering). We consider a high mass ($M_{500} = 10^{15}$ M$_\odot$) cluster at $z = 0.23$ with a dust mass of $5 \times 10^{10}$ M$_\odot$ and $T_{\rm Dust} = 20$ K, which we simulate using the same model that was introduced in Section 4.5.1. The results of our analysis are summarized in Fig. 4.12. Thanks to the roughly one order of magnitude better sensitivity in the 95–405 GHz frequency range, the CCAT-p survey will be able to determine the temperature of this single high-mass cluster with high precision from the survey data (CCAT-p: $Y_{500}^{\rm cyl} = 1.93^{+0.02}_{-0.01} \times 10^{-4}$ Mpc$^2$, $k_{\rm B}T_{\rm SZ} = 9.1^{+1.5}_{-1.0}$ keV; *Planck*: $Y_{500}^{\rm cyl} = 1.92^{+0.15}_{-0.10} \times 10^{-4}$ Mpc$^2$, $k_{\rm B}T_{\rm SZ} = 9.3^{+10.6}_{-4.5}$ keV). The cluster FIR emission is constrained roughly at the same level of precision as with *Planck* data, although the better angular resolution (0.2 arcmin at 862 GHz) will help for more accurate point source removal (CCAT-p: $A_{\rm Dust}^{857} = (88 \pm 4)$ kJy sr$^{-1}$, $T_{\rm Dust} = 20.0^{+2.2}_{-1.4}$ K; *Planck*: $A_{\rm Dust}^{857} = (88 \pm 6)$ kJy sr$^{-1}$, $T_{\rm Dust} = 20.0^{+5.5}_{-2.6}$ K). By excluding individual channels from the spectral fitting, we infer that the 405 GHz has the biggest impact on the constrain on $T_{\rm SZ}$ for the CCAT-p survey, while the 862 GHz channel is crucial for

[8] https://cmb-s4.org

| $\nu$ (GHz) | FWHM (arcmin) | $\Delta T$ ($\mu K_{RJ}$-arcmin) | $\Delta T$ ($\mu K_{CMB}$-arcmin) | $\Delta I$ (kJy/sr-arcmin) |
|---|---|---|---|---|
| ***Planck* (all-sky-average full mission data)** | | | | |
| 100 | 9.68 | 61.4 | 77.3 | 18.9 |
| 143 | 7.30 | 19.8 | 33.4 | 12.4 |
| 217 | 5.02 | 15.5 | 46.5 | 22.5 |
| 353 | 4.94 | 11.7 | 156 | 44.9 |
| 545 | 4.83 | 5.1 | 806 | 46.8 |
| 857 | 4.64 | 1.90 | $1.92 \times 10^4$ | 43.5 |
| **CCAT-p (4000 h, 1000 deg$^2$ survey)** | | | | |
| 95 | 2.2 | 3.9 | 4.9 | 1.1 |
| 150 | 1.4 | 3.7 | 6.4 | 2.6 |
| 226 | 1.0 | 1.5 | 4.9 | 2.4 |
| 273 | 0.8 | 1.2 | 6.2 | 2.7 |
| 350 | 0.6 | 2.0 | 25 | 7.6 |
| 405 | 0.5 | 2.9 | 72 | 15 |
| 862 | 0.3 | 3.9 | $6.6 \times 10^4$ | 89 |

Table 4.3: Comparison of the noise characteristics and spatial resolution of CCAT-p and *Planck*. The values for *Planck* represent all-sky averages (Planck Collaboration, 2016a) that were scaled to arcmin scale under the assumption of white noise. The values for CCAT-p are representative of a 4000 h, 1000 deg$^2$ survey performed under average weather condition. The intrinsic beam sensitivities are again given at arcmin scale.

measuring the properties of the FIR component.

We find that when including a cluster velocity component ($v_{pec} = 500\,km\,s^{-1}$) and fitting simultaneously for the kSZ signal, the uncertainty of the tSZ parameters $Y_{500}^{cyl}$ and $T_{SZ}$ increases by roughly 50%, while the peculiar velocity is constraint to $v_{pec} = 521^{+76}_{-62}\,km\,s^{-1}$. The SZ and dust parameters show very little correlation, resulting in almost unchanged constraints on the dust amplitude and temperature. In contrast, when adding a kSZ component we are neither able to constrain the peculiar velocity nor the dust temperature from our simulated *Planck* data without assigning strong priors. Further predictions for kSZ observations of clusters with CCAT-p are given by Mittal et al. (2018).

We note again that the limits quoted here are only for an idealized comparison between the two instruments when foregrounds are neglected. Our results nevertheless highlight the potential of the upcoming CCAT-p telescope to radically improve on *Planck* and push the limits of ground based observations. The performance of CCAT-p will be explored under more realistic circumstances in forthcoming papers.

## 4.8 Conclusions

The tSZ effect has become a widely used tool for finding mass-selected cluster samples, since its signal is proportional to the thermal energy of the intracluster medium and thus to the total cluster mass. In addition to the integrated pressure, the spectrum of the tSZ effect also contains information on the ICM temperature as the thermal electrons with keV energies inside massive galaxy clusters

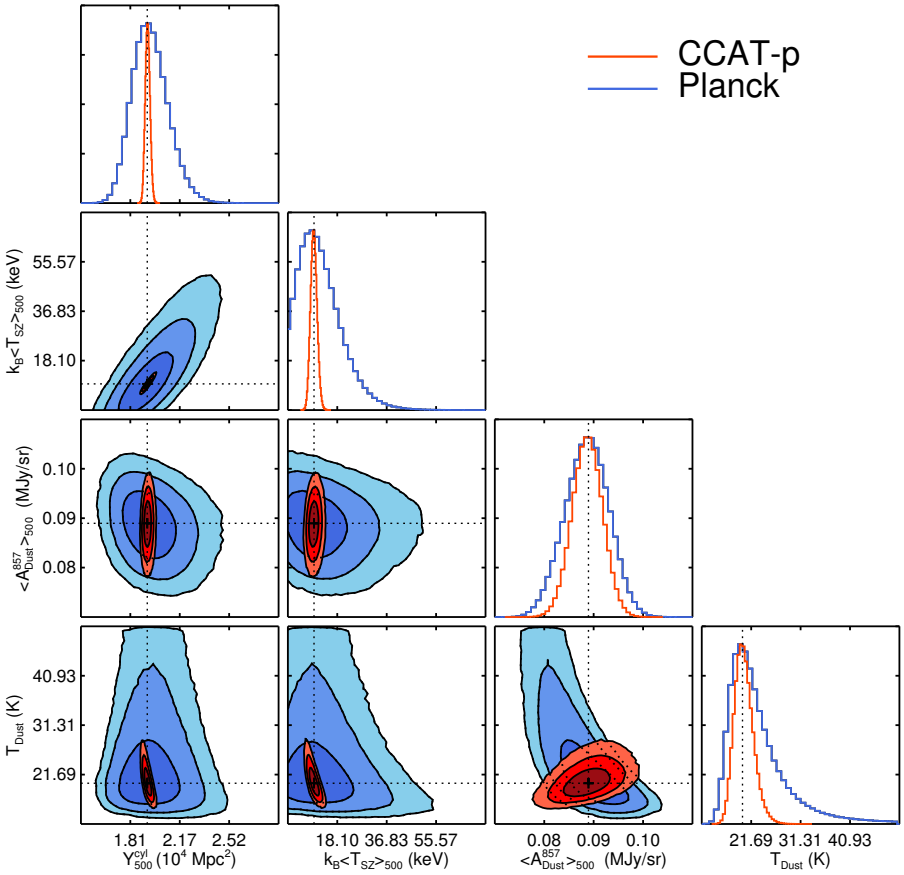


Figure 4.12: Spectral modelling comparison between the *Planck* and CCAT-prime sensitivities. The blue contours correspond to *Planck* and the red ones to CCAT-p, while the dotted lines indicate the input values. We neglect the foreground emissions and the kSZ signal arising from the cluster peculiar motion, considering only the thermal noise as listed in Table 4.3. The modelling results are for a single $M_{500} = 10^{15}\,\mathrm{M}_{\odot}$ cluster at $z = 0.23$ with dust mass $M_{\mathrm{Dust}} = 5 \times 10^{10}\,\mathrm{M}_{\odot}$. The improved sensitivity of the CCAT-p in the 95–405 GHz range helps to place far better constraints on the cluster SZ parameters than *Planck*, while having roughly the same constraining power on the cluster dust temperature and amplitude as in *Planck* due to the lower sensitivity in the 862 GHz channel. The temperature in this single high-mass cluster is constrained at $9\sigma$ for the CCAT-p survey sensitivity.

will distort the tSZ spectrum towards higher frequencies, resulting in an effect that is second-order in cluster temperature. These relativistic corrections to the tSZ effect are commonly accounted for when modelling the tSZ signal from massive clusters, but only recently have direct measurements become feasible. In this paper, we present the first attempt to constrain the relativistic signal in the tSZ spectrum by directly modelling it together with cluster FIR emission within a wide frequency range.

The detection of the relativistic tSZ effect requires to measure both the decrement and increment of the tSZ spectrum using a set of massive galaxy clusters. Both these requirements are satisfied by the data from the *Planck* mission, which is the only current data set that has the necessary spectral coverage and sensitivity and also provides an almost complete catalogue of the most massive clusters in the observable universe. We set out to stack the multifrequency data of a well-selected sample of 772 galaxy clusters. Our modelling includes an FIR component associated with galaxy clusters, which has been established by several recent measurements, and we employ data from the IRAS and *AKARI* missions in addition to the *Planck* HFI channels to augment the stacked tSZ+FIR spectrum at THz frequencies.

One important aspect of our analysis is realistic simulations with mock clusters that are used for the validation of our approach. We show that the cluster model parameters recovered through our spectral fitting method are free from any significant biases and that the kSZ signal from the cluster peculiar motions are effectively averaged out by stacking a large number of clusters. With these simulated data sets, we also show that measuring the integrated Compton $y$-parameter by using a non-relativistic spectrum, as is done for *Planck* and other SZ survey data, can result in a non-negligible bias towards lower $Y$-values. For the most massive clusters in the *Planck* catalogue, we compute this bias to be around 5–14%, depending on the method. This bias also carries a moderate mass dependence that scales (in the units of $Y_{5R500}$) approximately as $(M_{500})^{0.7-0.8}$.

Results from stacking the all-sky data from *Planck* provide significant, but not fully conclusive evidence for the relativistic tSZ signal. When stacking our full sample of 772 clusters, we are able to measure the tSZ relativistic corrections at $2.2\sigma$, constraining the mean temperature of this sample to be $4.4^{+2.1}_{-2.0}$ keV. We repeat the same analysis on a subsample containing only the 100 hottest clusters, for which we measure the mean temperature to be $6.0^{+3.8}_{-2.9}$ keV, corresponding to $2.0\sigma$. In contrast to some recently published results, we find that these average $T_{\rm SZ}$ values appear to be lower than the corresponding $\langle T_{\rm X}\rangle$ values. This might be a systematic trend due to the different weighting schemes of SZ and X-ray temperature measurements, which lead to $T_{\rm X} > T_{\rm SZ}$ averaged within $\theta_{500}$ and beyond if gas clumping is moderate. However, the large uncertainties of our $T_{\rm SZ}$ measurements do not permit a more detailed analysis.

In our analysis, the temperature of the emitting dust grains that cause the observed cluster FIR emission is constrained to $\simeq 20$ K, consistent with previous studies. The measured amplitude of our FIR model is roughly one order of magnitude lower than those reported in earlier works, which used aperture photometry for signal extraction. This demonstrates the superiority of the matched filtering technique in removing all spatially uncorrelated foregrounds as well as reducing any cluster specific emission with a spatial distribution that differs from the SZ signal. We probe the mass and redshift dependence of the cluster FIR signal amplitude and find that with the current data we cannot constrain a power law mass dependence, although there is some evidence for strong scaling of the cluster FIR emission with redshift.

As a final outlook we provide predictions for a future ground-based submillimetre survey experiment called CCAT-prime. Using the sensitivity estimates of a fiducial CCAT-prime survey of 4000 h, we find that this experiment will be able to constrain the cluster SZ parameters with roughly 5–10 times higher

precision than *Planck*, therefore being able to determine the temperature of individual high-mass systems using the relativistic tSZ signal. Similarly improved constraints (compared to *Planck* data) are obtained when a kSZ signal due to the peculiar motion of clusters is added to the model. Such high-precision data will bring a new era of SZ measurements of galaxy clusters in which the relativistic tSZ effect can be used to obtain an independent measurement of the ICM temperature, thereby breaking the degeneracy between the density and temperature from tSZ measurements, providing a more complete thermodynamical description of the intracluster medium from SZ data alone.

## 4.9 APPENDIX A: Tabulated SZ spectra

Table 4.4 provides the tSZ spectrum including relativistic corrections from 0 keV to 20 keV computed with SZPACK (Chluba et al., 2012) for the *Planck* 70–857 GHz channels. The spectra include corrections for the *Planck* instrumental bandpass that were computed as presented by the Planck Collaboration (2014b). Assuming $y = 1$, we provide the spectra both in units of specific intensity (MJy sr$^{-1}$) as well as $\mathrm{K_{CMB}}$. In the former case, we provide the intensity decrement/increment $\Delta I_{\mathrm{tSZ}}(x, T_{\mathrm{e}}) = y I_0\, h(x)\, f(x, T_{\mathrm{e}})$ as given by equation (4.13). In units of $\mathrm{K_{CMB}}$, we provide $\Delta T_{\mathrm{tSZ}}(x, T_{\mathrm{e}}) = y\, T_{\mathrm{CMB}}\, f(x, T_{\mathrm{e}})$ for which we find

$$\Delta\tilde{T}_{\mathrm{tSZ}}(x, T_{\mathrm{e}}) = y\, T_{\mathrm{CMB}}\, \frac{\int \mathrm{d}\nu\, \tau(\nu)\, h(x)\, f_{\mathrm{rel}}(x, T_{\mathrm{e}})}{\int \mathrm{d}\nu\, \tau(\nu)\, h(x)}. \tag{4.29}$$

## 4.10 APPENDIX B: Null tests

Our analysis follows the approach of Soergel et al. (2017) who use a similar stacking approach of *Planck*, IRAS, and *AKARI* data to search for active galactic nucleus feedback in quasi-stellar objects (QSOs) with the tSZ effect. As part of their results, the authors reported a statistically significant offset of −1.5 mJy in their matched-filtered IRIS 100 $\mu$m map after stacking random positions as part of a null test. This result is obtained by employing a similar matched filtering approach to the one used in this work. As possible reasons for this offset, Soergel et al. (2017) name striping errors or calibration uncertainties and excluded the 100 $\mu$m channel from their main analysis.

We conduct a similar test by stacking 772 random positions uniformly sampled across the sphere outside the same 40% Galactic mask used for sample selection. This step is repeated 10 000 times to produce a sufficiently high number of realizations to obtain an estimate of the channel-to-channel covariance matrix used in our main analysis and double as the data for our null test. The result of this test is shown in Fig. 4.13.

Our results demonstrate that none of the instruments shows a significant offset in any of the used channels. We find that the average signal at 100 $\mu$m is consistent with 0 and we are unable to reach the precision necessary to test the findings reported by Soergel et al. (2017). The different results of the null tests are likely due to the non-uniform sampling of the random positions mimicking the distribution of QSOs based on Sloan Digital Sky Survey data as adopted by Soergel et al. (2017). The authors also employ a much larger sample size of 377 136 QSOs and optimize their filters to recover point-like sources, whereas we optimize our filters for galaxy clusters. To test whether a larger sample

| $k_B T_e$ | 70 GHz | | 100 GHz | | 143 GHz | | 217 GHz | | 353 GHz | | 545 GHz | | 857 GHz | |
|---|---|---|---|---|---|---|---|---|---|---|---|---|---|---|
| (keV) | (MJy/sr) | ($K_{CMB}$) | (MJy/sr) | ($K_{CMB}$) | (MJy/sr) | ($K_{CMB}$) | (MJy/sr) | ($K_{CMB}$) | (MJy/sr) | ($K_{CMB}$) | (MJy/sr) | ($K_{CMB}$) | (MJy/sr) | ($K_{CMB}$) |
| 0 | -637.9 | -4.938 | -981.6 | -4.021 | -1034.7 | -2.784 | 93.5 | 0.193 | 1784.4 | 6.207 | 838.7 | 14.451 | 59.7 | 26.323 |
| 1 | -634.9 | -4.915 | -969.7 | -3.973 | -1027.9 | -2.765 | 83.9 | 0.173 | 1758.4 | 6.117 | 855.8 | 14.746 | 66.9 | 29.502 |
| 2 | -631.7 | -4.889 | -963.5 | -3.947 | -1020.7 | -2.746 | 72.9 | 0.151 | 1732.4 | 6.027 | 870.9 | 15.007 | 74.5 | 32.836 |
| 3 | -628.4 | -4.864 | -957.3 | -3.922 | -1013.7 | -2.727 | 62.3 | 0.129 | 1707.0 | 5.938 | 884.9 | 15.247 | 82.4 | 36.318 |
| 4 | -625.2 | -4.839 | -951.2 | -3.897 | -1006.8 | -2.708 | 52.0 | 0.107 | 1682.2 | 5.852 | 897.7 | 15.468 | 90.6 | 39.925 |
| 5 | -622.0 | -4.815 | -945.2 | -3.872 | -1000.2 | -2.691 | 42.0 | 0.087 | 1658.0 | 5.768 | 909.4 | 15.670 | 99.0 | 43.636 |
| 6 | -618.9 | -4.790 | -939.3 | -3.848 | -993.6 | -2.673 | 32.3 | 0.067 | 1634.4 | 5.686 | 920.2 | 15.856 | 107.6 | 47.428 |
| 7 | -615.7 | -4.766 | -933.5 | -3.824 | -987.3 | -2.656 | 22.9 | 0.047 | 1611.3 | 5.605 | 930.0 | 16.025 | 116.3 | 51.283 |
| 8 | -612.6 | -4.742 | -927.8 | -3.801 | -981.0 | -2.639 | 13.9 | 0.029 | 1588.6 | 5.527 | 939.0 | 16.179 | 125.2 | 55.186 |
| 9 | -609.5 | -4.718 | -922.1 | -3.778 | -975.0 | -2.623 | 5.1 | 0.010 | 1566.5 | 5.450 | 947.1 | 16.320 | 134.1 | 59.120 |
| 10 | -606.5 | -4.695 | -916.6 | -3.755 | -969.0 | -2.607 | -3.4 | -0.007 | 1544.9 | 5.374 | 954.5 | 16.447 | 143.1 | 63.070 |
| 11 | -603.5 | -4.671 | -911.1 | -3.732 | -963.2 | -2.591 | -11.7 | -0.024 | 1523.7 | 5.301 | 961.2 | 16.562 | 152.0 | 67.027 |
| 12 | -600.5 | -4.648 | -905.7 | -3.710 | -957.5 | -2.576 | -19.7 | -0.041 | 1502.9 | 5.228 | 967.2 | 16.665 | 161.0 | 70.977 |
| 13 | -597.5 | -4.625 | -900.3 | -3.688 | -951.9 | -2.561 | -27.5 | -0.057 | 1482.6 | 5.158 | 972.6 | 16.758 | 169.9 | 74.912 |
| 14 | -594.6 | -4.603 | -895.1 | -3.667 | -946.5 | -2.546 | -35.0 | -0.072 | 1462.7 | 5.089 | 977.3 | 16.840 | 178.8 | 78.822 |
| 15 | -591.7 | -4.580 | -889.9 | -3.646 | -941.1 | -2.532 | -42.3 | -0.088 | 1443.2 | 5.021 | 981.6 | 16.913 | 187.6 | 82.701 |
| 16 | -588.8 | -4.558 | -884.8 | -3.625 | -935.8 | -2.517 | -49.4 | -0.102 | 1424.1 | 4.954 | 985.3 | 16.977 | 196.3 | 86.542 |
| 17 | -585.9 | -4.536 | -879.7 | -3.604 | -930.7 | -2.504 | -56.3 | -0.116 | 1405.4 | 4.889 | 988.5 | 17.033 | 204.9 | 90.337 |
| 18 | -583.1 | -4.514 | -874.7 | -3.584 | -925.6 | -2.490 | -63.0 | -0.130 | 1387.0 | 4.825 | 991.3 | 17.080 | 213.4 | 94.084 |
| 19 | -580.3 | -4.492 | -869.8 | -3.563 | -920.6 | -2.477 | -69.5 | -0.144 | 1369.0 | 4.763 | 993.6 | 17.121 | 221.8 | 97.777 |
| 20 | -577.5 | -4.471 | -865.0 | -3.544 | -915.7 | -2.463 | -75.8 | -0.157 | 1351.4 | 4.701 | 995.5 | 17.154 | 230.0 | 101.412 |

Table 4.4: Tabulated, bandpass integrated tSZ spectra with relativistic corrections computed with SZPACK for $y = 1$. The spectra are provided for all *Planck* channels used in the main analysis and for electron temperatures ranging from 0 keV (non-relativistic) up to 20 keV. The tSZ is negligible in the IRAS and *AKARI* bands at thermal temperatures. We provide the spectra in units of both $K_{CMB}$ and specific intensity. Please note that we compute the tSZ spectrum on a much finer temperature grid for the main analysis and allow temperatures up to 75 keV.

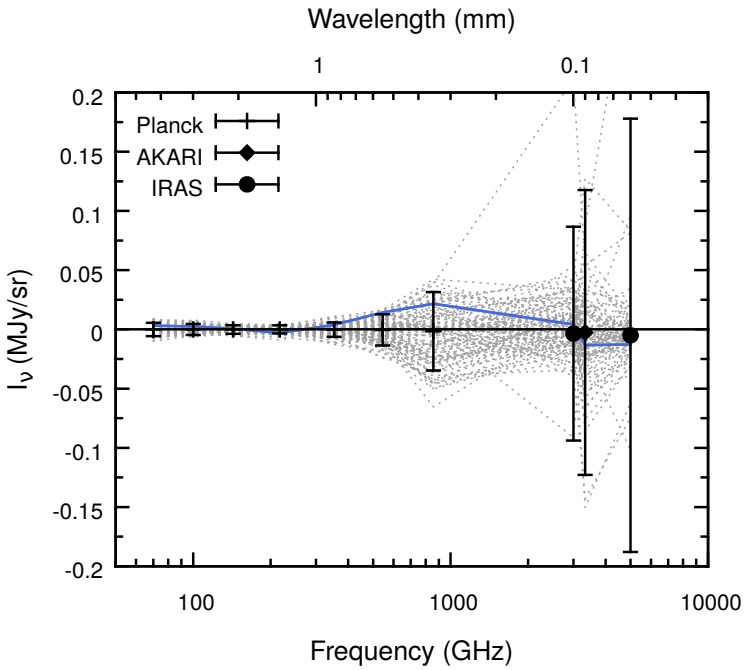


Figure 4.13: Results of a null test performed by stacking random positions after matched filtering of each map. Each realization, shown as grey dotted lines, was produced by stacking 772 positions, equal to the number of cluster in our sample. The black data points indicate the average of all realizations, while the blue solid line highlights a single representative realization.

size reveals a weak bias, we stack $\sim 300\,000$ random positions to roughly match the QSO sample size and find an average intensity of $(-0.0001 \pm 0.0036)$ MJy sr$^{-1}$ in the stacked 100 $\mu$m map. Our results thus indicate that, after matched filtering, the *Planck* 70–857 GHz, IRAS 100 and 60 $\mu$m as well as the *AKARI* 90 $\mu$m channel do not show a statistically significant bias within the boundary of our method.

## 4.11 APPENDIX C: The ILC technique

The ILC algorithm (Bennett et al., 2003) is a popular technique for the removal of foregrounds in multifrequency CMB observations. It is a so-called semiblind approach to foreground removal; that is, it only requires precise knowledge of the frequency spectrum of the desired astrophysical signal making it an ideal tool for the extraction of CMB maps. While doing so, no prior information or auxiliary data from other observations is needed, which is the reason for the term 'internal'. The method makes two key assumptions:

1. The observed maps are a linear mixture of astrophysical components and instrumental noise.
2. The individual components are uncorrelated.

Using the first assumption and following the approach presented by Hurier et al. (2013), the $N_\nu$ observed maps $\boldsymbol{I}(p)$ can be written as

$$\boldsymbol{I}(p) = \mathbf{A}\boldsymbol{S}(p) + \boldsymbol{N}(p), \tag{4.30}$$

where $p$ denotes the map pixels, $\mathbf{A}$ is the mixing matrix that contains the spectral information of the $N_s$ astrophysical components and has the dimensions $N_\nu \times N_s$, $\boldsymbol{S}(p)$ is a vector that contains the $N_s$ astrophysical components and $\boldsymbol{N}(p)$ is the vector containing the instrumental noise of the $N_\nu$ channels.

The ILC technique assumes that an estimate of an astrophysical component of interest can be obtained by forming a linear combination of the observed maps

$$\hat{S}_{\mathrm{ILC}}(p) = \boldsymbol{\omega}^{\mathrm{T}}\boldsymbol{I}(p) = \sum_{i=1}^{N_\nu} = \omega_i I_i(p). \tag{4.31}$$

Following Eriksen et al. (2004), the variance of the map $\hat{\mathbf{S}}_{\mathrm{ILC}}$ can be written as

$$Var(\hat{\mathbf{S}}_{\mathrm{ILC}}) = \boldsymbol{\omega}^{\mathrm{T}}\hat{\mathbf{C}}\boldsymbol{\omega}, \tag{4.32}$$

where $\hat{\mathbf{C}}$ is the empirical covariance matrix of the observed maps

$$\hat{C}_{ij} = COV(I_i, I_j) \equiv \frac{1}{N_{\mathrm{pix}}} \sum_{p=1}^{N_{\mathrm{pix}}} (I_i(p) - \langle I_i \rangle)(I_j(p) - \langle I_j \rangle). \tag{4.33}$$

The ILC-weights $\boldsymbol{\omega}^{\mathrm{T}}$ are determined by minimizing the variance of $\hat{\mathbf{S}}_{\mathrm{ILC}}$

$$\frac{\partial}{\partial\, \omega_{\mathrm{i}}} \left[\boldsymbol{\omega}^{\mathrm{T}}\hat{\mathbf{C}}\boldsymbol{\omega}\right] = 0. \tag{4.34}$$

In addition, the weights $\boldsymbol{\omega}$ are required to have unit response to the component of interest in order to preserve its signal, i.e.

$$\boldsymbol{\omega}^{\mathrm{T}}\boldsymbol{a} = 1, \tag{4.35}$$

where $\boldsymbol{a}$ is the mixing vector of the component of interest. In case of the tSZ, the mixing vector will be $\boldsymbol{a} = \Delta I_{\mathrm{tSZ}}/y = I_0 h(\boldsymbol{x}) f(\boldsymbol{x}, T_{\mathrm{e}})$. We note that instrument-specific bandpass corrections like presented in equation (4.13) will have to be applied. Furthermore, Remazeilles et al. (2011a) showed that additional astrophysical components with well-known frequency spectra $\boldsymbol{b_i}$ can be removed in a constrained ILC approach by demanding

$$\boldsymbol{\omega}^{\mathrm{T}}\boldsymbol{b}_i = 0. \tag{4.36}$$

We combine the mixing vector of the component of interest together with the mixing vectors of all $N$ constrained unwanted components into the matrix $\mathbf{F}$ of dimensions $N_\nu \times (1 + N)$

$$\mathbf{F} = \begin{pmatrix} a[1] & b_1[1] & \dots & b_N[1] \\ \vdots & \vdots & \ddots & \vdots \\ a[N_\nu] & b_1[N_\nu] & \dots & b_N[N_\nu] \end{pmatrix}. \tag{4.37}$$

A solution to this optimization problem can be found by solving a linear system using Lagrange multipliers $\boldsymbol{\lambda}$

$$\begin{pmatrix} 2 \cdot \hat{\mathbf{C}} & -\mathbf{F} \\ \mathbf{F}^{\mathrm{T}} & 0 \end{pmatrix} \begin{pmatrix} \boldsymbol{\omega} \\ \boldsymbol{\lambda} \end{pmatrix} = \begin{pmatrix} 0 \\ \boldsymbol{e} \end{pmatrix}, \tag{4.38}$$

where $\boldsymbol{e} = (1, 0, ..., 0)^{\rm T}$ is the $(1 + N)$ vector containing the response of the constrained astrophysical components to the ILC-weights. The solution to this problem is given by

$$\boldsymbol{\omega}^{\rm T} = \boldsymbol{e}^{\rm T} \left( \mathbf{F}^{\rm T} \hat{\mathbf{C}}^{-1} \mathbf{F} \right)^{-1} \mathbf{F}^{\rm T} \hat{\mathbf{C}}^{-1}. \tag{4.39}$$

Since the ILC technique requires precise knowledge of the frequency spectrum of the component of interest, any deviation from the correct spectral shape will lead to a bias in the estimate of the component map $\hat{\mathbf{S}}_{\rm ILC}$. This is particularly problematic because the covariance matrix of the observed maps and thus the ILC-weights are usually computed over a large field of several square degree. Therefore, even when relativistic corrections are included, a bias will be present in most pixels of the map because galaxy clusters are not isothermal and a single large field will contain multiple clusters. If a non-relativistic tSZ spectrum is used to compute the ILC-weights, the $y$-bias will be given by

$$\frac{\Delta y}{y} = \boldsymbol{\omega}^{\rm T} \boldsymbol{a}_{\rm tSZ}^{\rm rel} - 1, \tag{4.40}$$

where $\boldsymbol{a}_{\rm tSZ}^{\rm rel}$ is the relativistic tSZ mixing vector for a given temperature.

In order to investigate the bias caused by using the non-relativistic tSZ spectrum, we use mock data sets created using the steps presented in Section 4.5. We compute the covariance matrix of the simulated maps from $10^\circ \times 10^\circ$ cut-outs around our simulated clusters and constrain the CMB spectrum, which in units of specific intensity will have the mixing vector $\boldsymbol{b}_{\rm CMB} = h(\boldsymbol{x})$. For simplicity, we do not employ spatial decomposition techniques like the ones that are used by the NILC (Remazeilles et al., 2011b) and MILCA (Hurier et al., 2013) algorithms. We then apply the obtained ILC-weights directly to the simulated SZ decrement/increment maps in order to obtain estimates of the $y$-maps that are unaffected by foreground residuals and instrumental noise, but are determined using realistic data. The results are shown in the main text. We verify our algorithm by also simulating mock data sets featuring non-relativistic clusters, in which case, as expected, we do not observe any bias in $y$.

The large $y$-bias found in ILC $y$-maps can be understood by computing the contribution of each channel in the linear combination. The contribution is given by the product of the weights $\boldsymbol{\omega}$ and the mixing vector $\boldsymbol{a}_{\rm tSZ}$ for the tSZ, which is shown in Fig. 4.14 and compared against the difference of the relativistic and non-relativistic tSZ spectrum for different temperatures. It can be seen that the ILC algorithm assigns particularly high weight to the 143 GHz and 353 GHz channels where the difference between the spectra is particularly high, resulting in the large bias observed in our simulations. We stress that this result is not limited to our simulations and that similar ILC-weights are also found in the official maps made public by the Planck Collaboration (2016d) that were created using the more sophisticated MILCA and NILC algorithms.

## 4.12 APPENDIX D: Comparison of $T_{\rm SZ}$ and $T_{\rm X}$

We compare the expected aperture-average values for $T_{\rm X}$ and $T_{\rm SZ}$ using electron pressure and temperature profiles from Arnaud et al. (2010) and Vikhlinin et al. (2006) that were used to create our mock data sets. The aperture average temperatures are given by

$$T_{\rm obs.}(< \theta) = \frac{\int w\, T_{\rm e}(r)\, {\rm d}V}{\int w\, {\rm d}V}, \tag{4.41}$$

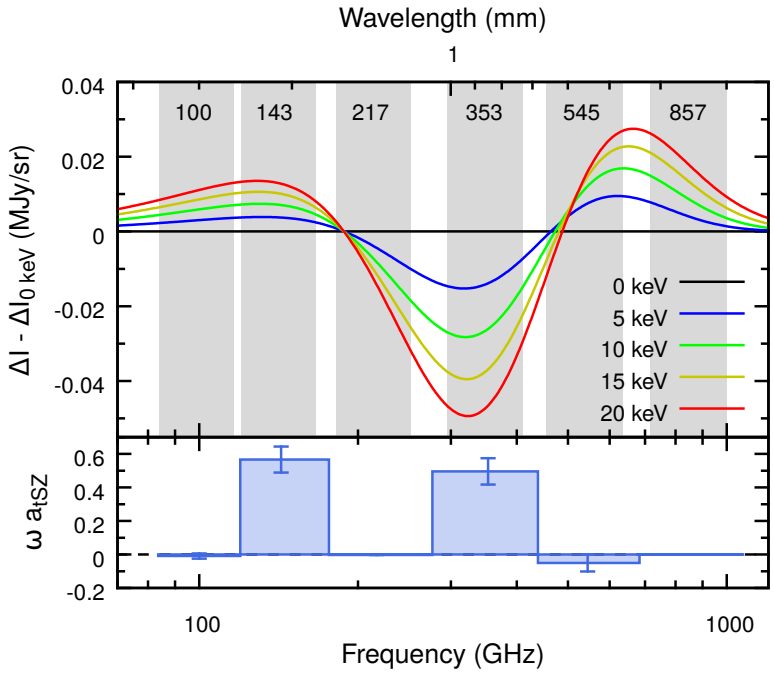


Figure 4.14: Explanation of the high $y$-bias found in ILC y-maps. The upper panel shows the difference of the tSZ spectrum computed for different temperatures to the tSZ spectrum at 0 keV for $y = 10^{-4}$. The lower panel shows the product of the ILC-weights $\boldsymbol{\omega}$ and the mixing vector of the non-relativistic tSZ spectrum $\boldsymbol{a}_{\mathrm{tSZ}} = \Delta I_{\mathrm{tSZ}}(0\,\mathrm{keV})/y$, i.e. the fraction that each channel contributes to the estimated $y$. Summing the product up over all channels will yield 1. The ILC algorithm produces a high $y$-bias because of the high weights that are assigned to the 143 GHz and 353 GHz channel at which the difference between the relativistic and non-relativistic tSZ spectra is particularly large.

where $w$ is a method-dependent weight and the volume integrals are carried out for a cylindrical volume that relates directly to the average signal within the aperture $\theta = R/D_{\mathrm{A}}$. The X-ray spectroscopic temperature $T_{\mathrm{X}}$ can be obtained using the spectroscopic-like weight $w_{\mathrm{X}} = n_{\mathrm{e}}^2 T_{\mathrm{e}}^{-\frac{3}{4}}$ (Mazzotta et al. 2004), while $T_{\mathrm{SZ}}$ is well approximated by using $w_{\mathrm{SZ}} = n_{\mathrm{e}} T_{\mathrm{e}}$ (Hansen 2004). We compute the ratio $T_{\mathrm{X}}/T_{\mathrm{SZ}}$ using analytical temperature and density profiles and without taking into consideration the effect of gas clumping. The temperature model is taken from Vikhlinin et al. (2006), which we consider as the temperature profile of a typical cool-core cluster. We also construct a non-cool-core variant by reducing the size of the cooling radius in the original Vikhlinin et al. model to an arbitrarily small value. These two input temperature profiles are shown in Fig. 4.15. The corresponding density profiles are obtained by dividing our adopted pressure model by these two temperature profiles. Fig. 4.16 then shows the ratio $T_{\mathrm{X}}/T_{\mathrm{SZ}}$ as a function of aperture size for these two types of clusters.

Assuming the aforementioned radial profiles, we find that for clusters without a cool-core the ratio $T_{\mathrm{X}}/T_{\mathrm{SZ}}$ will always be larger than unity due to the density-square weighting of the X-ray spectroscopic temperature. The same density-square weighting will result in $T_{\mathrm{X}}/T_{\mathrm{SZ}} < 1$ at very small aperture radii ($\theta \lesssim 0.3\,\theta_{500}$) for cool-core clusters. At the characteristic aperture $\theta_{500}$, we expect $T_{\mathrm{X}}/T_{\mathrm{SZ}} \approx 1.1$ for cool-core and $T_{\mathrm{X}}/T_{\mathrm{SZ}} \approx 1.2$ for non-cool-core clusters. However, $T_{\mathrm{SZ}}$ can be larger than $T_{\mathrm{X}}$ at all radii in case clusters show significant gas clumping as suggested by hydrodynamical simulations (Kay

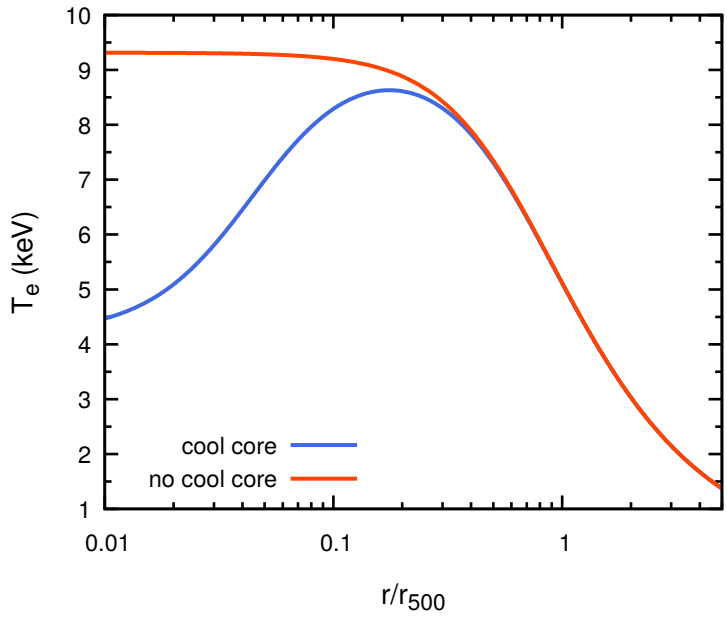


Figure 4.15: Example cool-core (blue) and non-cool-core (red) radial electron temperature profiles for a cluster with $M_{500} = 6 \times 10^{14}\,M_{\odot}$. The cool core profile is taken from Vikhlinin et al. (2006) and the non-cool-core one is obtained by slightly modifying it by choosing an infinitesimally small cooling radius.

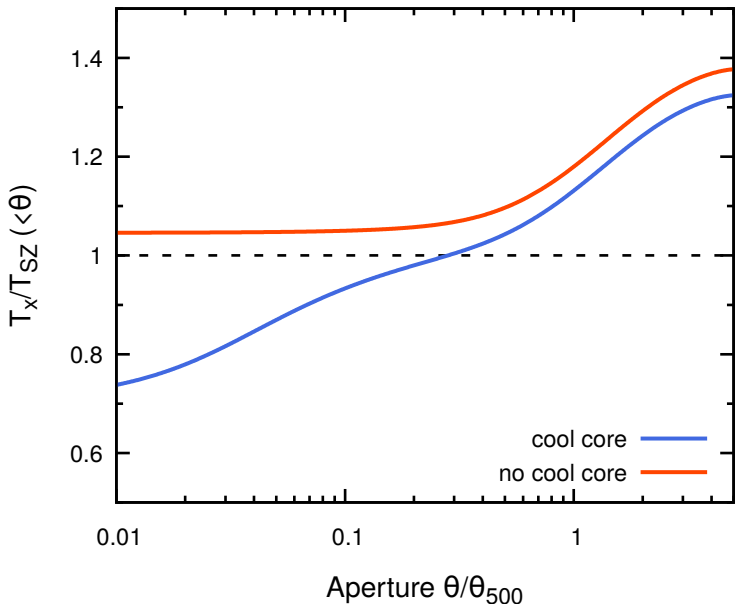


Figure 4.16: Comparison of the expected X-ray spectroscopic and SZ measured ICM temperatures within different apertures. The temperature ratio $T_X/T_{SZ}$ is shown as a function of aperture size $\theta$ assuming a cool-core (blue) and a non-cool-core (blue) $T_e$-profile. We find that the ratio is always unity for non-cool-core clusters and only smaller then unity for cool-core clusters when $\theta \lessapprox 0.3\theta_{500}$.

et al., 2008; Biffi et al., 2014). On the other hand, clusters simulated with more recent, improved smooth particle hydrodynamical (SPH) codes show less clumps and smoother gas and temperature distributions (Beck et al., 2016).

CHAPTER 5

# Introducing constrained matched filters for improved separation of point sources from galaxy clusters

This chapter is a reproduction of the article of the same title that has been published in Monthly Notices of the Royal Astronomical Society under the reference

- **Erler J.**, Ramos-Ceja M. E., Basu K., and Bertoldi F., 2019, MNRAS, 484, 1988

The manuscript is reproduced under the non-exclusive right of re-publication granted by MNRAS to the authors of the article. To ensure open access to the article the peer-reviewed, published version has been uploaded to astro.ph (arXiv:1809.06446). Furthermore, a python implementation of the MF-techniques introduced in this work has been published at `https://github.com/j-erler/pymf` under the MIT license for open source software. Additional, unpublished results are presented in Appendix B.

## 5.1 Abstract

Matched filters (MFs) are elegant and widely used tools to detect and measure signals that resemble a known template in noisy data. However, they can perform poorly in the presence of contaminating sources of similar or smaller spatial scale than the desired signal, especially if signal and contaminants are spatially correlated. We introduce new multicomponent MF and matched multifilter (MMF) techniques that allow for optimal reduction of the contamination introduced by sources that can be approximated by templates. The application of these new filters is demonstrated by applying them to microwave and X-ray mock data of galaxy clusters with the aim of reducing contamination by point-like sources, which are well approximated by the instrument beam. Using microwave mock data, we show that our method allows for unbiased photometry of clusters with a central point source but requires sufficient spatial resolution to reach a competitive noise level after filtering. A comparison of various MF and MMF techniques is given by applying them to *Planck* multifrequency data of the Perseus galaxy cluster, whose brightest cluster galaxy hosts a powerful radio source known as Perseus

A. We also give a brief outline how the constrained MF (CMF) introduced in this work can be used to reduce the number of point sources misidentified as clusters in X-ray surveys like the upcoming eROSITA all-sky survey. A PYTHON implementation of the filters is provided by the authors of this manuscript at `https://github.com/j-erler/pymf`.

## 5.2 Introduction

Matched filtering (MF) is a technique for the extraction of the flux of sources with a well-known spatial template at optimal signal-to-noise ratio (SNR). MF was first proposed for the study of the kinetic Sunyaev–Zeldovich (kSZ) signal from clusters of galaxies by Haehnelt & Tegmark (1996) and subsequently developed and generalized by Herranz et al. (2002) and Melin et al. (2006) for the extraction of the thermal Sunyaev–Zeldovich (tSZ) signal from multifrequency data sets like those delivered by the *Planck* mission, giving rise to what is now known as the matched multifilter (MMF). These filters have since been adopted with great success by the SPT, ACT and Planck Collaborations to extract the tSZ signal of clusters from their respective multifrequency data sets (Hasselfield et al. 2013; Bleem et al. 2015; Planck Collaboration 2016h).

While MFs perform admirably in separating diffuse Galactic foregrounds and primary cosmic microwave background (CMB) anisotropies from the SZ signal of clusters, contamination by point sources remains an issue (e.g. Bartlett & Melin 2006; Melin et al. 2006) and can lead to significant biases in the measured cluster parameters (Knox et al., 2004; Aghanim et al., 2005; Lin & Mohr, 2007; Sehgal et al., 2010). This problem is mitigated to a degree by MMFs due to the prior knowledge of the tSZ spectrum that is used to construct these multifilters, but accurate photometry of clusters that contain a central radio source remains challenging. Point source confusion is also a central concern for the detection of clusters in X-ray observations (e.g. Biffi et al. 2018; Koulouridis et al. 2018). Tarrío et al. (2016) and Tarrio18 recently demonstrated that point source confusion can be reduced by a joint SZ and X-ray MMF analysis, using their very different spectral characteristics at microwave frequencies compared to the X-ray regime.

In this work, we present a multicomponent extension of the MF concept that can improve the separation of contaminants that can be approximated by well-known templates (e.g. point sources) based purely on their spatial characteristics. This approach is mathematically identical to the generalized multicomponent internal linear combination (ILC) algorithms introduced by Remazeilles et al. (2011a,b) and Hurier et al. (2013), which can be thought of as MFs in frequency space, and allows for an unbiased photometry of clusters with a central point source. Generalizing our method to multifrequency data gives rise to a new matched multifiltering technique that combines spatial and spectral constraints to provide an optimal separation. A similar but less general approach was presented by Herranz et al. (2005), who showed that the tSZ and kSZ signals of clusters can be separated with MMFs that use the different spectra of the two effects but take the same spatial template for the two components, which restricts the method from being applied to other contaminating sources. In this work, we derive our new filters and demonstrate their application using mock microwave and X-ray data of clusters, as well as *Planck* data of the Perseus galaxy cluster.

This article is structured as follows: Section 5.3 introduces MFs and MMFs for galaxy clusters and our proposed constrained filters in detail. Section 5.4 describes our simulation pipeline for the creation of mock data that are used to test the performance of the constrained MFs. The results obtained on both simulations and on data from the *Planck* mission are presented in Section 5.5. In Section 5.6, we

provide a discussion of our new technique and give an outlook to its application in future experiments. Section 5.7 provides a summary and concludes our analysis.

Throughout this paper we assume a flat Lambda cold dark matter cosmology with $\Omega_\Lambda = 0.7$, $\Omega_\mathrm{b} = 0.05$, $h = 0.7$, and $T_\mathrm{CMB} = 2.7255\,\mathrm{K}$. $E(z) \equiv H(z)/H_0 = (\Omega_\mathrm{m}(1+z)^3 + \Omega_\Lambda)^{1/2}$ denotes the redshift-dependent Hubble ratio and $\rho_\mathrm{crit}(z) = 3H(z)^2/(8\pi G)$ the critical density of the Universe at redshift $z$. Unless noted otherwise, the quoted parameter uncertainties refer to the 68 per cent credible interval. All-sky maps were processed with HEALPix (v3.31; Górski et al. 2005).

## 5.3 Matched filtering

Setting up an MF requires only very limited knowledge about the astrophysical content of a data set. We assume that an observed map $\mathbf{I}_\nu$ at frequency $\nu$ represents a linear combination of the desired signal, e.g. the SZ signal from galaxy clusters with the spectrum $f(\nu)$, plus a noise map $\mathbf{N}_\nu$ that contains both instrumental noise and astrophysical emission:

$$\mathbf{I}_\nu = f(\nu) \cdot A\,\mathbf{y} + \mathbf{N}_\nu. \tag{5.1}$$

The signal must be well approximated by a known spatial template $\mathbf{y}$ like the projected pressure profile of clusters. We now would like to construct a filter $\mathbf{\Psi}$ that returns the signal (i.e. the amplitude $A$ of the source template if $\mathbf{y}$ is normalized to unity) at maximum significance. Using the flat sky approximation and changing to Fourier space, an MF $\mathbf{\Psi}$ can be constructed by minimizing the variance of the filtered map (e.g. Schäfer et al. 2006)

$$\sigma^2 = \mathbf{\Psi}^\mathrm{T}\mathbf{C}\mathbf{\Psi}, \tag{5.2}$$

where $\mathbf{C}$ is the azimuthally averaged noise power spectrum of the unfiltered map expressed as a diagonal matrix $\mathbf{C} = \mathrm{diag}(|\mathbf{N}(\boldsymbol{k})|^2)$. Here $\boldsymbol{k}$ denotes the two-dimensional spatial frequency that corresponds to the two-dimensional sky position $\boldsymbol{x}$ in Fourier space. At the same time, we demand the filtered field to be an unbiased estimator of the deconvolved amplitude of the signal template at the position of sources. This condition can be written as

$$\mathbf{\Psi}^T\boldsymbol{\tau} = 1, \tag{5.3}$$

where $\boldsymbol{\tau}$ is the Fourier transform of the source template $\mathbf{y}$ convolved with the instrument beam. A solution to this optimization problem is found by introducing a Lagrange multiplier $\lambda$, which leads to a system of linear equations

$$\begin{pmatrix} 2\cdot\mathbf{C} & -\boldsymbol{\tau} \\ \boldsymbol{\tau}^\mathrm{T} & 0 \end{pmatrix} \begin{pmatrix} \mathbf{\Psi} \\ \lambda \end{pmatrix} = \begin{pmatrix} 0 \\ 1 \end{pmatrix}, \tag{5.4}$$

the solution to which is:

$$\mathbf{\Psi} = \left[\boldsymbol{\tau}^\mathrm{T}\mathbf{C}^{-1}\boldsymbol{\tau}\right]^{-1}\boldsymbol{\tau}\mathbf{C}^{-1}. \tag{5.5}$$

The MF derived here is optimal in the least square sense and was first proposed for the study of galaxy clusters by Haehnelt & Tegmark (1996). Although it is most commonly applied to data sets with Gaussian noise, Gaussianity is not a strict requirement. Non-Gaussian noise will not cause a bias but the solution might no longer be optimal (Melin et al., 2006). However, optimal MFs were

recently derived for the low-number count Poisson noise regime that is relevant for X-ray and $\gamma$-ray observations (Ofek & Zackay, 2018; Vio & Andreani, 2018).

### 5.3.1 Constrained matched filters (CMF)

We now show that the MF concept can be generalized to multiple sources with known spatial templates. For this we assume that the observed sky is a linear combination of $n$ sources with known templates $\mathbf{y}_i$ plus noise:

$$\mathbf{I}_\nu = f_1(\nu) \cdot A_1 \, \mathbf{y}_1 + \cdots + f_n(\nu) \cdot A_n \, \mathbf{y}_n + \mathbf{N}. \tag{5.6}$$

Our goal is to construct a filter that minimizes the variance of the filtered map as defined in equation (5.2) and at the same time has an unbiased response to the chosen source template. We now place additional constraints by e.g. demanding the filter to have zero response to contaminating sources with well-known spatial templates:

$$\begin{aligned} \boldsymbol{\Psi}^T \boldsymbol{\tau}_1 &= 1 \\ \boldsymbol{\Psi}^T \boldsymbol{\tau}_2 &= 0 \\ &\vdots \\ \boldsymbol{\Psi}^T \boldsymbol{\tau}_n &= 0. \end{aligned} \tag{5.7}$$

In the following it is convenient to construct a matrix $\mathbf{T}$ of dimensions $n_k \times n$ from the $n$ spatial templates $\boldsymbol{\tau}_i$:

$$\mathbf{T} = \begin{pmatrix} \tau_1[1] & \tau_2[1] & \dots & \tau_n[1] \\ \vdots & \vdots & \ddots & \vdots \\ \tau_1[n_k] & \tau_2[n_k] & \dots & \tau_n[n_k] \end{pmatrix}. \tag{5.8}$$

We can derive the form of the new filter by solving a system of linear equations analogous to equation (5.4)

$$\begin{pmatrix} 2 \cdot \mathbf{C} & -\mathbf{T} \\ \mathbf{T}^{\mathrm{T}} & 0 \end{pmatrix} \begin{pmatrix} \boldsymbol{\Psi} \\ \boldsymbol{\lambda} \end{pmatrix} = \begin{pmatrix} 0 \\ \boldsymbol{e} \end{pmatrix}, \tag{5.9}$$

where $\boldsymbol{e} = (1, 0, \dots)^{\mathrm{T}}$ is a vector that contains the response of the filter to the $n$ constraints defined in equation (5.7) and $\boldsymbol{\lambda}$ are the $n$ Lagrange multipliers. The solution for the CMF is

$$\boldsymbol{\Psi} = \boldsymbol{e}^{\mathrm{T}} \left[ \mathbf{T}^{\mathrm{T}} \mathbf{C}^{-1} \mathbf{T} \right]^{-1} \mathbf{T} \mathbf{C}^{-1}, \tag{5.10}$$

which is similar to the one of the traditional MF in equation (5.5). A possible application of this new filter is the reduction of point source contamination in observations of galaxy clusters, which will be explored in Section 5.5. However any other contaminating source with a well-known template or even multiple sources could be set to zero using this approach. This benefit will come at the cost of a reduced SNR, which will be discussed in Section 5.5. A comparison of the two filters using simulated microwave data of galaxy clusters and point sources is shown in Fig. 5.1.

A mathematically identical multicomponent generalization to the CMF has been derived and successfully applied for ILC algorithms (Remazeilles et al., 2011a,b; Hurier et al., 2013), which are commonly used to extract Comptonization maps from *Planck* data using the spectrum of the tSZ signal

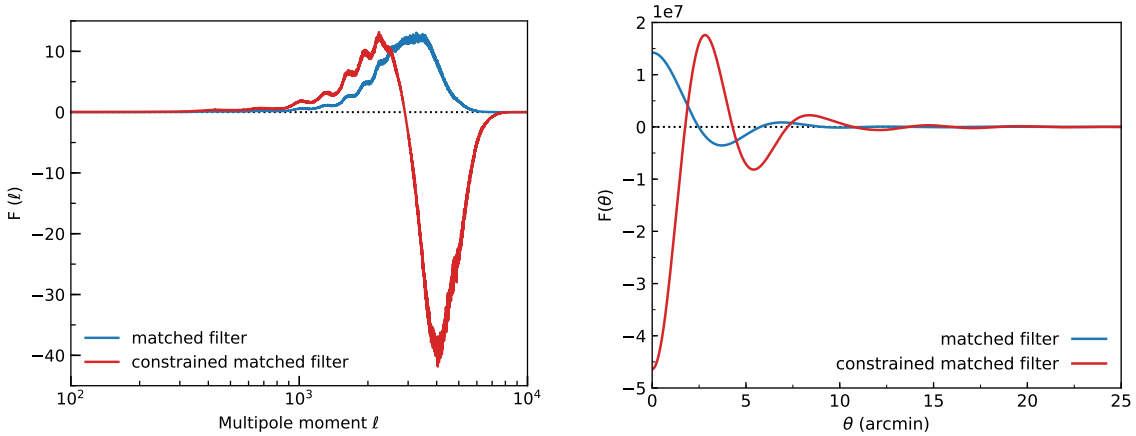


Figure 5.1: Comparison of the traditional MF and the CMF presented in this work. The filters are computed using the all-sky formalism given in appendix 5.8 on the simulated 150 GHz sky presented in Section 5.4 assuming a $\beta$-model (Cavaliere & Fusco-Femiano, 1976) with core radius $\theta_c = 2$ arcmin and $\beta = 1$ convolved with a Gaussian beam with an FWHM of 5 arcmin as the source template. A point source template has been used as an additional constraint for the CMF. **Left-hand panel:** Filter window functions in spherical harmonic space. **Right-hand panel:** Filter kernel profiles in real space.

while zeroing out the primary CMB anisotropies by constraining their well understood blackbody spectrum.

### 5.3.2 Constrained matched multifilters (CMMF)

Both the MF and CMF presented previously were built to be applied to a single-frequency map. However, the MF concept can be generalized to multifrequency data sets like the ones delivered by *Planck*. These generalized techniques are known as matched multifilters (MMF; Herranz et al. 2002; Melin et al. 2006; Lanz et al. 2010; Melin et al. 2012; Tarrío et al. 2016, 2018) and are designed to use prior spatial and spectral information about a source to return an optimally filtered map of A in the least-square sense. We will show here that the MMF concept can be generalized to separate multiple components with known spatial and spectral templates in an analogous way to the single-frequency filter. We start again by constructing a simple model of the observed sky. As before, we can represent observations of the sky as a linear mixture of astrophysical emission and noise:

$$\boldsymbol{I}(\boldsymbol{x}) = \boldsymbol{f}_\nu \cdot A\, y(\boldsymbol{x}) + \boldsymbol{N}(\boldsymbol{x}). \tag{5.11}$$

Different from equation (5.1) we now describe the observed maps as vectors in frequency space with $n_\nu$ components at each sky position $\boldsymbol{x}$ in order to simplify the notation. Using this formalism and changing to Fourier space, the multifrequency source template will be given at each $\boldsymbol{k}$ as a vector $\boldsymbol{F}$ in frequency space

$$\boldsymbol{F}(\boldsymbol{k}) = \boldsymbol{f}_\nu\, y(\boldsymbol{k})\, B_\nu(\boldsymbol{k}), \tag{5.12}$$

where $B_\nu(\boldsymbol{k})$ denotes the Fourier transform of the beam, which in general will be frequency dependent. We now aim to find a filter $\boldsymbol{\Psi}(\boldsymbol{k})$ that, as before, has unit response to the multifrequency source

template:

$$\int \mathrm{d}^2k\ \boldsymbol{\Psi}^T(\boldsymbol{k})\boldsymbol{F}(\boldsymbol{k}) = 1. \tag{5.13}$$

We therefore construct a series of $n_\nu$ filters $\Psi(\boldsymbol{k})$ that are the components of $\boldsymbol{\Psi}(\boldsymbol{k})$. The final result will be a single map that is the linear combination of the observed maps, each convolved with their respective frequency-dependent filter. The MMF is derived analogously to the single-frequency case by demanding minimum variance of the filtered map at each spatial scale

$$\sigma^2 = \boldsymbol{\Psi}^{\mathrm{T}}(\boldsymbol{k})\mathbf{P}(\boldsymbol{k})\boldsymbol{\Psi}(\boldsymbol{k}), \tag{5.14}$$

where $\mathbf{P}$ is the noise power spectrum, a matrix in frequency space with $n_\nu \times n_\nu$ components for each $\boldsymbol{k}$ that are defined as $P_{ij}(\boldsymbol{k})\delta(\boldsymbol{k}-\boldsymbol{k}') = \langle N_{\nu_i}(\boldsymbol{k})N^*_{\nu_j}(\boldsymbol{k})\rangle$. The asterisk denotes the complex conjugate. The MMF is then given by

$$\boldsymbol{\Psi}(\boldsymbol{k}) = \sigma^2_{\mathrm{MMF}}\mathbf{P}^{-1}(\boldsymbol{k})\boldsymbol{F}(\boldsymbol{k}), \tag{5.15}$$

with the variance of the filtered map:

$$\sigma^2_{\mathrm{MMF}} = \left[\int \mathrm{d}^2k\ \boldsymbol{F}^{\mathrm{T}}(\boldsymbol{k})\mathbf{P}^{-1}(\boldsymbol{k})\boldsymbol{F}(\boldsymbol{k})\right]^{-1}. \tag{5.16}$$

The MMF derived here was employed with great success for the detection and photometry of galaxy clusters by the ACT, SPT, and Planck collaborations (Hasselfield et al. 2013; Bleem et al. 2015; Planck Collaboration 2016h).

We now show that a CMMF can be constructed in similar fashion as before. The aim is to find a filter that allows us to constrain multiple well-known multifrequency source templates to reduce the impact of well-characterized contaminants on the filtered map. We begin by assuming that the observed sky is a linear mixture of known sources plus noise:

$$\boldsymbol{I}(\boldsymbol{x}) = \boldsymbol{f}_{\nu,1}\cdot A_1\, y_1(\boldsymbol{x}) + \cdots + \boldsymbol{f}_{\nu,n}\cdot A_n\, y_n(\boldsymbol{x}) + \boldsymbol{N}(\boldsymbol{x}). \tag{5.17}$$

Next, we define the desired response of the filter to our known source templates:

$$\begin{aligned}
\int \mathrm{d}^2k\ \boldsymbol{\Psi}^T(\boldsymbol{k})\boldsymbol{F}_1(\boldsymbol{k}) &= 1\\
\int \mathrm{d}^2k\ \boldsymbol{\Psi}^T(\boldsymbol{k})\boldsymbol{F}_2(\boldsymbol{k}) &= 0\\
&\vdots\\
\int \mathrm{d}^2k\ \boldsymbol{\Psi}^T(\boldsymbol{k})\boldsymbol{F}_n(\boldsymbol{k}) &= 0.
\end{aligned} \tag{5.18}$$

For each $\boldsymbol{k}$ the constraints can be written as a matrix $\mathbf{U}$ with dimensions $n_\nu \times n$:

$$\mathbf{U}(\boldsymbol{k}) = \begin{pmatrix} F_1[1](\boldsymbol{k}) & F_2[1](\boldsymbol{k}) & \dots & F_n[1](\boldsymbol{k}) \\ \vdots & \vdots & \ddots & \vdots \\ F_1[n_\nu](\boldsymbol{k}) & F_2[n_\nu](\boldsymbol{k}) & \dots & F_n[n_\nu](\boldsymbol{k}) \end{pmatrix}. \tag{5.19}$$

By minimizing the variance of the filtered map, we find that the CMMF is

$$\boldsymbol{\Psi}(\boldsymbol{k}) = \boldsymbol{e}^{\mathrm{T}}\mathbf{S}^{-1}\mathbf{P}^{-1}(\boldsymbol{k})\mathbf{U}(\boldsymbol{k}), \tag{5.20}$$

with the $n \times n$ matrix $\mathbf{S}$ defined as:

$$\mathbf{S} = \int \mathrm{d}^2k\ \mathbf{U}^{\mathrm{T}}(\boldsymbol{k})\mathbf{P}^{-1}(\boldsymbol{k})\mathbf{U}(\boldsymbol{k}). \tag{5.21}$$

The variance of the filtered map can be computed as:

$$\sigma^2_{\mathrm{CMMF}} = \int \mathrm{d}^2k \boldsymbol{\Psi}^{\mathrm{T}}(\boldsymbol{k})\mathbf{P}(\boldsymbol{k})\boldsymbol{\Psi}(\boldsymbol{k}). \tag{5.22}$$

The CMMF defined this way can be used to separate sources in a similar fashion as the single frequency CMF, but for multifrequency data sets. This will require both a spatial and a spectral template for each constrained source, e.g. if we want to extract galaxy clusters from multifrequency microwave data while minimizing point source contamination we need to know the beam as well as the spectral energy distribution (SED) of the point sources. This makes the method very efficient in cleaning the data, but it will be limited to a specific type of source. Reducing the contamination of radio and far-infrared point sources at the same time can be achived by placing two additional constraints using the same spatial template (i.e. the beam) but two different SEDs. We will compare the performance of the different filters presented here by applying them to *Planck* High Frequency Instrument (HFI) data of the Perseus galaxy cluster in Section 5.5.

## 5.4 Simulations

### 5.4.1 The SZ effect of galaxy clusters

In order to test the performance of the CMF and compare it to the traditional MF we prepared a pipeline for the creation of mock images of the microwave sky. We use the tSZ effect signal (Sunyaev & Zeldovich, 1970, 1972; Birkinshaw, 1999; Carlstrom et al., 2002) of galaxy clusters as our sources of interest.

The tSZ effect is a secondary anisotropy of the CMB that is caused by inverse Compton scattering of CMB photons by free electrons in the intracluster medium (ICM). The tSZ effect causes a characteristic distortion of the CMB spectrum with a temperature decrement at low ($\lesssim 217\,\mathrm{GHz}$) and a temperature increment at high ($\gtrsim 217\,\mathrm{GHz}$) frequencies. Peculiar motion of clusters will cause a red/blue-shift of the CMB in their rest frame, which gives rise to the kSZ effect. The spectra of the SZ signals are commonly expressed as a temperature shift relative to the CMB monopole, which can be written as

$$\frac{\Delta T_{\mathrm{SZ}}}{T_{\mathrm{CMB}}} = \underbrace{f(x, T_{\mathrm{e}})\, y}_{\mathrm{tSZ}} - \underbrace{\tau_{\mathrm{e}} \left(\frac{v_{\mathrm{pec}}}{c}\right)}_{\mathrm{kSZ}}, \tag{5.23}$$

where $T_{\mathrm{CMB}}$ is the CMB temperature, $c$ is the speed of light, $v_{\mathrm{pec}}$ is the peculiar velocity along the line of sight, $f(x, T_{\mathrm{e}})$ is the relativistic tSZ (rSZ) spectrum (e.g., Wright, 1979; Itoh et al., 1998; Chluba et al., 2012), $x \equiv h\nu/(k_{\mathrm{B}}T_{\mathrm{CMB}})$ is the dimensionless frequency, $\tau_{\mathrm{e}}(r) = \sigma_{\mathrm{T}} \int n_{\mathrm{e}}(r)\,\mathrm{d}l$ is the optical

depth of the plasma and $y$ is the Comptonization parameter:

$$y(r) = \frac{\sigma_\mathrm{T}}{m_\mathrm{e} c^2} \int_\mathrm{l.o.s.} \mathrm{d}l \underbrace{n_\mathrm{e}(r) k_\mathrm{B} T_\mathrm{e}(r)}_{P_\mathrm{e}(r)} . \tag{5.24}$$

Here, $k_\mathrm{B}$ is the Boltzmann constant, $\sigma_\mathrm{T}$ is the Thomson cross-section, $m_\mathrm{e}$ is the electron rest mass and $n_\mathrm{e}$ and $T_\mathrm{e}$ are the number density and temperature of the electrons in the ICM.

The Comptonization parameter is a measure of the gas pressure integrated along the line of sight (l.o.s.) and is computed by projection of the Generalized Navarro–Frenk–White (GNFW) pressure profile (Nagai et al., 2007) using the parametrization presented by Arnaud et al. (2010)

$$\frac{P_\mathrm{e}(r)}{\mathrm{keV\,cm^{-3}}} = 1.65 \times 10^{-3} E(z)^{8/3} \left( \frac{M_{500}}{3 \times 10^{14}\,\mathrm{M_\odot}} \right)^{0.79} p\left( \frac{r}{r_{500}} \right), \tag{5.25}$$

where $p(r/r_{500})$ is the so-called 'universal' shape of the cluster pressure profile

$$p(r) = \frac{P_0}{\left(c_{500} \frac{r}{r_{500}}\right)^\gamma \left[1 + \left(c_{500} \frac{r}{r_{500}}\right)^\alpha\right]^{(\beta-\gamma)/\alpha}}, \tag{5.26}$$

for which we adopt the best-fit values for the profile parameters $P_0, c_{500}, \gamma, \alpha$, and $\beta$ presented by Arnaud et al. (2010). In the following we refer to this profile as the GNFW profile. The characteristic cluster size $r_{500}$ marks the radius of the sphere within which the average matter density is 500 times the critical density, while $M_{500}$ is the total mass enclosed within $r_{500}$. The temperature profile of the clusters is computed assuming a polytropic relation $n_\mathrm{e} T_\mathrm{e} = n_\mathrm{e}^\delta$ between electron density and temperature, with $\delta = 1.2$ (Ostriker et al., 2005).

### 5.4.2 Simulating the microwave sky

The simulated clusters are added to an artificial CMB map computed from a synthetic power spectrum that was generated using CAMB (Lewis et al., 2000). We account for emission from the cosmic infrared background (CIB) by adding maps of the resolved and the clustered CIB provided by the WebSky Extragalactic CMB Mocks team[1] to our simulation pipeline. We use the PYTHON sky model (PySM; Thorne et al. 2017) to obtain maps of Galactic synchrotron, free–free, spinning dust, and thermal dust components. The PySM uses the most recent foreground maps published by the Planck Collaboration (2016c) for the latter three components and adds small-scale fluctuations to all maps following an approach similar to the one presented by Miville-Deschênes et al. (2007).

Compact radio sources are modelled by including all sources from the NVSS point source catalogue (Condon et al., 1998). The measured fluxes densities at 1.4 GHz are extrapolated to microwave frequencies assuming a power-law SED, $I(\nu) \propto \nu^{-\alpha}$ with a spectral index $\alpha$ randomly drawn for each source from a Gaussian distribution with a mean of 0.5 and a standard deviation of 0.1. Galactic and extragalactic near-infrared point sources are included by adding the sources listed in the IRAS point

[1] The mocks are provided at `https://mocks.cita.utoronto.ca`

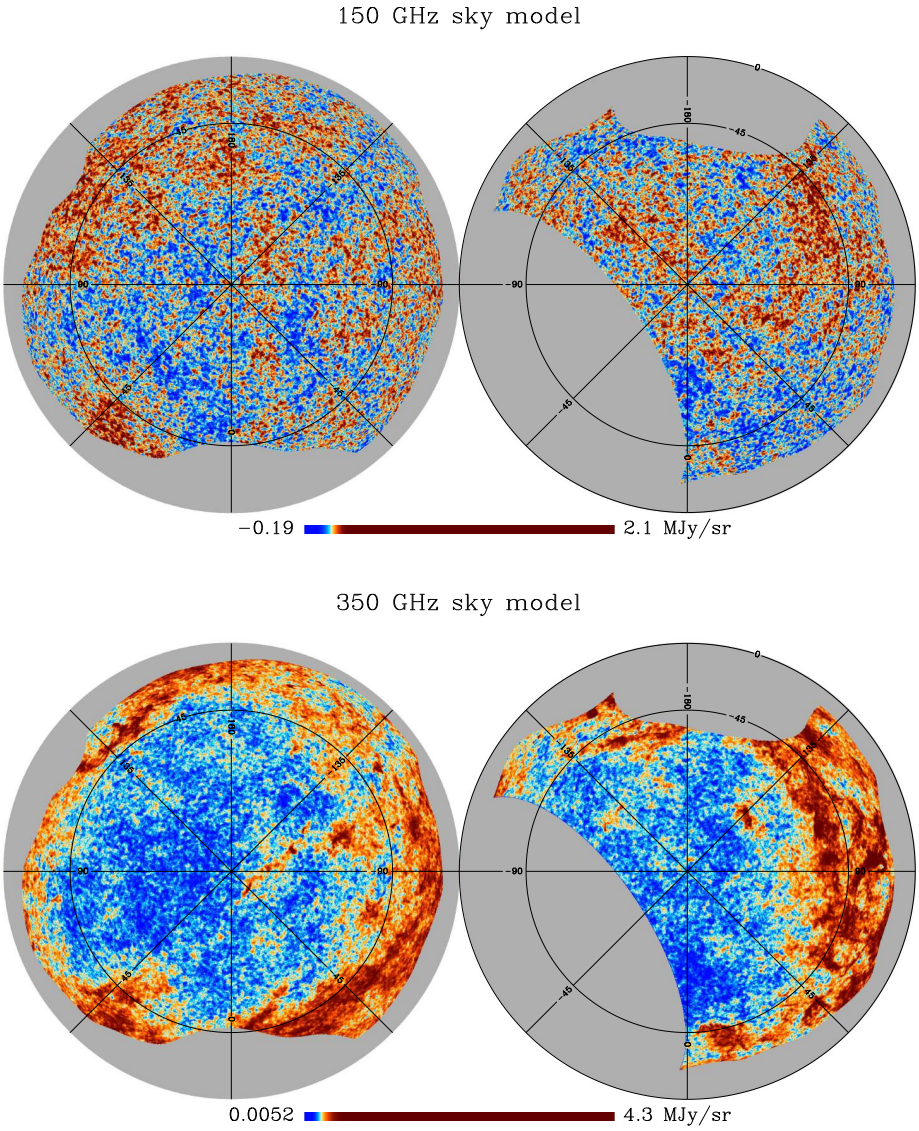


Figure 5.2: Orthographic view of the simulated microwave sky at 150 and 350 GHz that was used to test the different filtering techniques. The projection is centred on the Galactic north and south pole. The maps are shown in histogram equalized scale to enhance the dynamic range. The composition of the maps is described in Section 5.4. We remove the brightest parts of the Galactic disc by applying a 40 per cent Galactic mask and exclude the part of the sky that has not been observed by the NVSS.

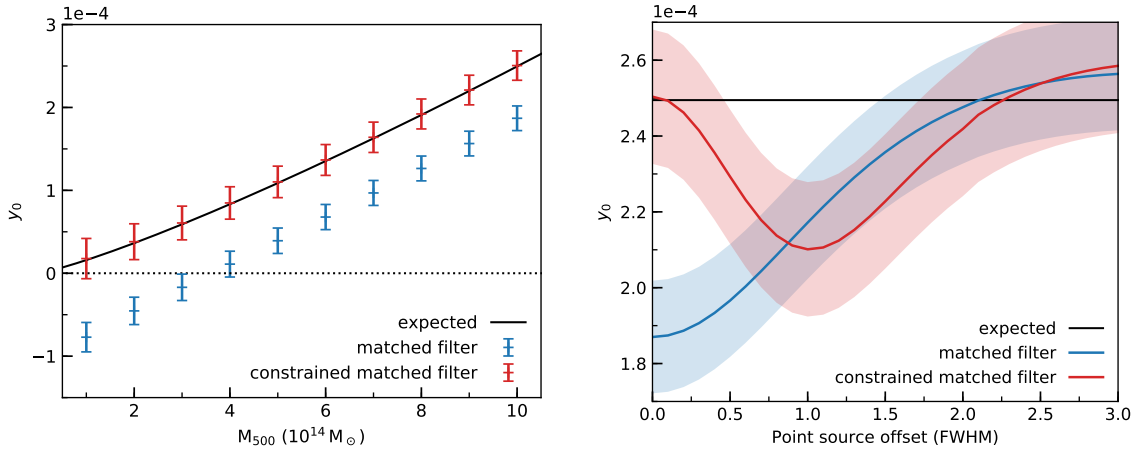


Figure 5.3: **Left-hand panel:** Impact of (radio) point source contamination on the measured Comptonization parameter. We simulate the tSZ decrement at 150 GHz for a range of clusters with different masses at a constant redshift of $z = 0.2$ using the GNFW profile and add a central point source with a fixed flux density of 10 mJy to each of them. The blue data points show the estimates of the central Componization parameter $y_0$ obtained using MFs, while the data shown in red were obtained using CMFs. The solid black line indicates the expected relation. CMFs allows an unbiased measurement of a cluster's flux in the presence of a central point source, while MFs will return a biased value. **Right-hand panel:** Impact of an offset in the point source location on the previous results. The $x$-axis gives the positional offset relative to the cluster centre. For this test we assume the same resolution, frequency, point source flux, and source redshift, but only consider a single cluster of mass $M_{500} = 10^{15}\,M_\odot$. The shaded regions indicate the uncertainty of the flux estimates. We find that CMFs perform better than MFs up to an offset of $\sim 0.75$ FWHM. For higher values, both methods provide a similar bias.

source catalogue (Beichman et al., 1988) by following the approach presented by Delabrouille et al. (2013) to extrapolate the reported flux densities to lower frequencies.

We restrict our analysis to the extragalactic sky that is relevant for studies of galaxy clusters and cosmological studies by applying a 40 per cent Galactic dust mask to our mock maps. We furthermore exclude the region of the sky that has not been observed by the NVSS in order to keep the properties of our sky model homogeneous.

All maps are processed at HEALPix $n_{\mathrm{side}} = 8192$, which allows to generate mock data with a minimum full width at half-maximum (FWHM) of 1 arcmin. Maps that come at a lower native resolution are oversampled and smoothed with a narrow Gaussian beam to avoid pixellation artefacts. The microwave sky is simulated at 150 GHz and 350 GHz with different spatial resolutions ranging from 1 arcmin to 20 arcmin, assuming circular Gaussian beams and white instrumental noise with $\sigma^{\mathrm{noise}}_{150\,\mathrm{GHz}} = 6.4\,\mu\mathrm{K_{CMB}}$-arcmin and $\sigma^{\mathrm{noise}}_{350\,\mathrm{GHz}} = 25\,\mu\mathrm{K_{CMB}}$-arcmin. The wide range of simulated spatial resolutions allows us to test our filtering techniques for instruments ranging from *Planck* to current and future ground-based experiments. The resulting maps are shown in Fig. 5.2.

### 5.4.3 Simulating X-ray data

In addition to tests using the simulated microwave data that were previously introduced, we apply the single-frequency filters presented in Section 5.3 to simulated X-ray data. We chose to create mock images of the upcoming extended ROentgen Survey with an Imaging Telescope Array (eROSITA,

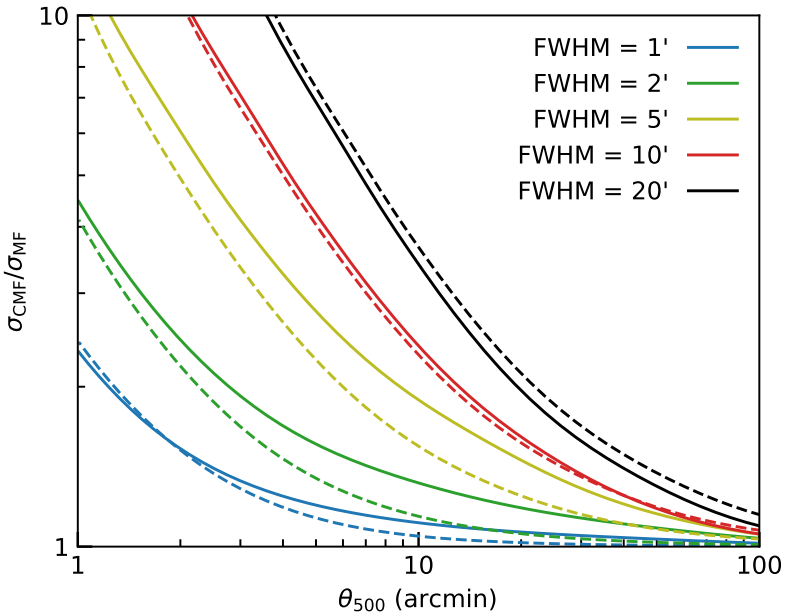


Figure 5.4: Ratio of the noise level in the CMF and MF filtered maps defined in equation (5.2) as a function of cluster size. The different colors correspond to different beam FWHMs. The solid lines correspond to results obtained from the 150 GHz mock data while the results shown with dashed lines where obtained using the 350 GHz mock data.

Merloni et al. 2012; Predehl 2017), which will explore the high-redshift Universe with unprecedented sensitivity combined with all-sky coverage. This makes eROSITA an ideal case to explore our new filtering techniques, since active galactic nuclei (AGNs) activity is expected to increase with redshift and might dominate the X-ray observed flux around cluster positions (e.g. Biffi et al. 2018; Koulouridis et al. 2018).

Following Clerc et al. (2018), the images are simulated in the 0.5 – 2 keV energy band. Each image has a size of $3.6^\circ \times 3.6^\circ$, with a pixel size of 4 arcsec and a simulated exposure time of 1.6 ks. We include the X-ray and instrumental background model presented in Table 1 of Borm et al. (2014). A randomly distributed population of point sources, which is described by the Moretti et al. (2013) $\log N$ – $\log S$ relation, is added. For simplicity, the images only contain a single type of isothermal cluster, simulated using a projected $\beta$–model (Cavaliere & Fusco-Femiano, 1976)

$$S_X(\theta) \propto \int_{l.o.s} \mathrm{d}l\, n_e(r)^2 \propto \left[1 + \left(\frac{\theta}{\theta_c}\right)\right]^{\frac{1}{2}-3\beta}, \tag{5.27}$$

with a fixed flux of $5 \times 10^{-13}$ erg s$^{-1}$ cm$^{-2}$, core radius $\theta_c$ of 20 arcsec, and $\beta$ of 2/3. All sources are convolved with a Gaussian PSF with an FWHM of 28 arcsec, which is the expected value in survey mode for eROSITA (Merloni et al., 2012). We derived the count rates of the sources from the physical fluxes for a given spectral emission model and using the instrumental response file `erosita_iv_7telfov_ff.rsp`[2]. In this work, we assume an APEC thermal plasma model (Smith

[2] The eROSITA response file is available at

et al., 2001) having a metal abundance of $0.3\,Z_{\odot}$ along with a Galactic hydrogen column density corresponding to $1.7 \times 10^{20}\,\mathrm{cm}^{-2}$ (Kalberla et al., 2005; Borm et al., 2014). The simulated X-ray images will be used in Section 5.5.3 to demonstrate how CMFs can aid the separation of galaxy clusters and point sources in X-ray surveys.

## 5.5 Results

### 5.5.1 Photometry of clusters with a central point source

Using the simulation pipeline introduced in the previous section, we first investigate how the new filtering technique presented in this work can improve the photometry of clusters that harbour a bright central point source. We do so by creating 150 GHz mock observations of clusters with masses ranging from $10^{14}\,\mathrm{M}_{\odot}$ to $10^{15}\,\mathrm{M}_{\odot}$ at a constant redshift of 0.2. Each simulated cluster features a central radio source with a fixed flux density of 10 mJy at 150 GHz. The beam is assumed to have an FWHM of 1 arcmin. The values of the central Comptonization parameter computed from the measured cluster flux after filtering are shown in the left-hand panel of Fig. 5.3. By construction, a CMF always returns an unbiased result, while the values obtained through MF are biased low with a linear dependence on the brightness of the point source. For the given flux density this bias has a significance of $\sim 4\sigma$ and increases to $\sim 5\sigma$ for lower cluster masses due to the decreasing cluster size. The biased fluxes can therefore lead to a non-detection of low-mass clusters and biased inferred cluster properties for high-mass systems.

We also consider a potential offset of a bright central point source relative to the cluster centre. If a central point source is not aligned with the cluster, both methods will find a bias due to ringing artefacts around the filtered point source. We find that for small angular separations up to $\sim 0.75$ FWHM CMFs return a value with a bias that is smaller than the one observed in the values returned by MFs, while both methods find similar values for larger offsets.

The comparison above highlights a clear advantage of the CMF, which however is bought with an increase in the noise level in the filtered map that limits the usefulness of the method in some cases. This noise increase results from placing additional constraints that inevitably lower the degrees of freedom available for the optimization of the variance of the filtered map. Figure 5.4 shows the ratio of the noise in the filtered maps as a function of apparent cluster size and instrument beam. This ratio scales linearly with the cluster-size-to-beam ratio if the map noise is Gaussian. The differences between the results obtained at 150 GHz and 350 GHz are due to the different foreground properties. We find that the CMF provides maps with a marginally increased noise level for most modern ground-based mm telescopes that offer a typical resolution of $\sim 1$ arcmin. The use case for low-resolution instruments like *Planck* is however restricted to large, mostly nearby clusters with radii of several tens of arcminutes.

### 5.5.2 Application to *Planck* data

In addition to tests on simulated microwave images we apply all filters presented in Section 5.3 to *Planck* HFI data of the Perseus galaxy cluster at $z = 0.0179$. The brightest cluster galaxy (BCG) of the Perseus cluster (NGC 1275) is a powerful radio source known as Perseus A that is unresolved

http://www2011.mpe.mpg.de/erosita/response/

| $\nu$ (GHz) | FWHM (arcmin) | $S_\nu$ (Jy) |
|---|---|---|
| 100 | 9.68 | 10.36 ± 0.15 |
| 143 | 7.30 | 7.80 ± 0.13 |
| 217 | 5.02 | 5.74 ± 0.25 |
| 353 | 4.94 | 4.12 ± 0.87 |
| 545 | 4.83 | 2.82 ± 2.81 |
| 857 | 4.64 | 2.12 ± 7.90 |

Table 5.1: SED of Perseus A extracted from *Planck* HFI data using CMFs that remove the tSZ signal of the cluster. It is well approximated by a power-law with a spectral index of 0.78 ± 0.05. In turn this SED is used to clean tSZ maps of the Perseus cluster in various ILC and MMF approaches.

in all *Planck* bands. While the MMF and CMMF are applied directly to the HFI data without any pre-processing other than converting the 545 and 857 GHz maps to units of $K_{CMB}$, the HFI maps are combined into a single map before applying the single-frequency filers. This is achieved by smoothing the maps to a common resolution of 9.68 arcmin after which they are combined into a $y$-map with ILC or constrained ILC (CILC) algorithms (Remazeilles et al. 2011a; see Appendix C of Erler et al. 2018 for details). The radio galaxy Perseus A appears as a bright source with negative amplitude in the ILC $y$-map due to its diminishing brightness with increasing frequency, which is also seen in the MILCA and NILC $y$-maps published by the Planck Collaboration (2016d). In contrast, the CILC algorithm allows to constrain the Perseus A SED and thus remove its contamination to the $y$-map. The Perseus A SED used for the CILC and CMMF algorithms is extracted directly from the *Planck* HFI data using CMFs that remove the tSZ contamination by the ICM of the cluster and found to be well approximated by a power-law with spectral index $\alpha = 0.78 \pm 0.05$ (see Table 5.1). We model the tSZ signal of the Perseus cluster with a GNFW pressure profile with $\theta_{500} = 59.7$ arcmin (Urban et al., 2014) and use a non-relativistic approximation of the tSZ spectrum. All maps are $10^\circ \times 10^\circ$ fields centred on (RA, Dec.) = (03h19m47.2s, +41°30′47″).

We summarize our results by providing the extracted values for the central Comptonization parameter $y_0$ and the derived integrated value $Y_{500}$ in Table 5.2. The latter is integrated in a cylindrical aperture with the radius $\theta_{500}$

$$Y_{500}^{\mathrm{cyl}} = y_0 \frac{2\pi}{(10^6\, pc)^2} \int_0^{D_\mathrm{A}\theta_{500}} \mathrm{d}r\; y(r)\, r, \tag{5.28}$$

where $y(r)$ is the cluster template that has been normalized to unit amplitude and $D_\mathrm{A}$ is the angular diameter distance of the cluster. The processed maps are shown in Fig. 5.5.

If neither a spatial nor a spectral constraint for Perseus A is used, as in the MMF and ILC + MF scenarios, we extract a strongly biased negative value for $y_0$ and thus $Y_{500}$. This provides a plausible explanation for the necessity of point source masks that are the reason why the Perseus cluster is not listed in the *Planck* SZ cluster catalogues (PSZ and PSZ2, Planck Collaboration 2014d, 2016h), which were built using two MMF pipelines (MMF1 and MMF3) and the Bayesian PowellSnakes (PwS) algorithm.

The bias introduced by Perseus A is removed by applying a CMF to the same $y$-map, which yields $y_0 = (9.4 \pm 0.7) \times 10^{-5}$. For the application of a CMF to an ILC $y$-map it is critical to smooth all

| Technique | $y_0$ $10^{-5}$ | $Y_{500}$ $10^{-5}$ Mpc$^2$ | SNR |
|---|---|---|---|
| ILC + MF | -0.74 ± 0.66 | -0.50 ± 0.44 | -1.1 |
| ILC + CMF | 9.35 ± 0.70 | 6.31 ± 0.47 | 13.4 |
| CILC + MF | 9.44 ± 0.77 | 6.37 ± 0.52 | 12.3 |
| CILC + CMF | 9.77 ± 0.82 | 6.59 ± 0.55 | 12.0 |
| MMF | -2.64 ± 0.39 | -1.77 ± 0.27 | -6.8 |
| CMMF | 10.0 ± 0.42 | 6.76 ± 0.28 | 24.0 |

Table 5.2: Comparison of the extracted tSZ signal of the Perseus galaxy cluster extracted from *Planck* HFI data with various ILC and MMF techniques. The corresponding maps are shown in Fig. 5.5. The ILC-based techniques first combine the six HFI maps in an optimal linear combination, after which we apply either an MF or a CMF. The MMF techniques are directly applied to the HFI maps. The CILC and CMMF techniques use the Perseus A SED given in Table 5.1. Radio sources like Perseus A will appear as sources with negative $y$ in ILC $y$-maps and MMF maps, leading to biased photometry if not accounted for.

maps to a common resolution before combining them. Combining the maps in Fourier space at their native resolution will distort the beam in the $y$-map, which increases the complexity of constraining the spatial template of the beam for point source removal.

Using the Perseus A SED to construct a CILC $y$-map before filtering is an alternative way to remove the bias introduced by the radio source. In that case, both the MF and the CMF yield similar values for $y_0$, both of which are consistent with the previous result. Placing a spectral constraint in the CILC step however results in a noisier $y$-map and thus a slightly lower SNR in both cases.

Finally, applying a CMMF that uses both the SED of Perseus A and our knowledge of the *Planck* beams yields $y_0 = (10.0 \pm 0.42) \times 10^{-5}$, which is in agreement with the previous values and with an SNR of 24 offers the clearest signal of all methods compared here. This SNR is comparable to the SNR of 22 we obtain by applying an MMF to *Planck* HFI maps of the Coma cluster, a system of similar mass at z= 0.0231. Using the $M_{500} - Y_{500}$ scaling relation from the Planck Collaboration (2014c, 2016f) and converting to $Y_{500}^{\rm sph}$ we find a mass of $(6.97 \pm 0.24) \times 10^{14}$ M$_\odot$ for the Perseus cluster, which is consistent with the value obtained by Urban et al. (2014)[3].

For Coma, all six methods yield similar values for $y_0$ due to the lack of a bright central radio or FIR source. We find however that the two multifilters deliver an almost identical SNR as the ILC plus MF techniques, while the CILC approach gives a slightly lower SNR of 17. This indicates that the additional constraints are 'cheaper' for multifilters but come at the drawback that multiple constraints have to be placed for sources with identical spatial template but different SEDs. Combining an ILC map and CMFs will remove sources just based on their spatial signature with no need to have constraints on their SED.

This example illustrates that there are multiple ways of dealing with point source contamination in clusters. The advantage of the CMF over using spectral constraints is that it is often easier to characterize the instrument beam than measuring the SED of a source. Radio sources like Perseus A can show variability and extrapolating their fluxes to microwave frequencies based on radio measurements

[3] The error on the mass includes the uncertainties of the scaling relation parameters given by Planck Collaboration (2016f), which we assume to be uncorrelated.

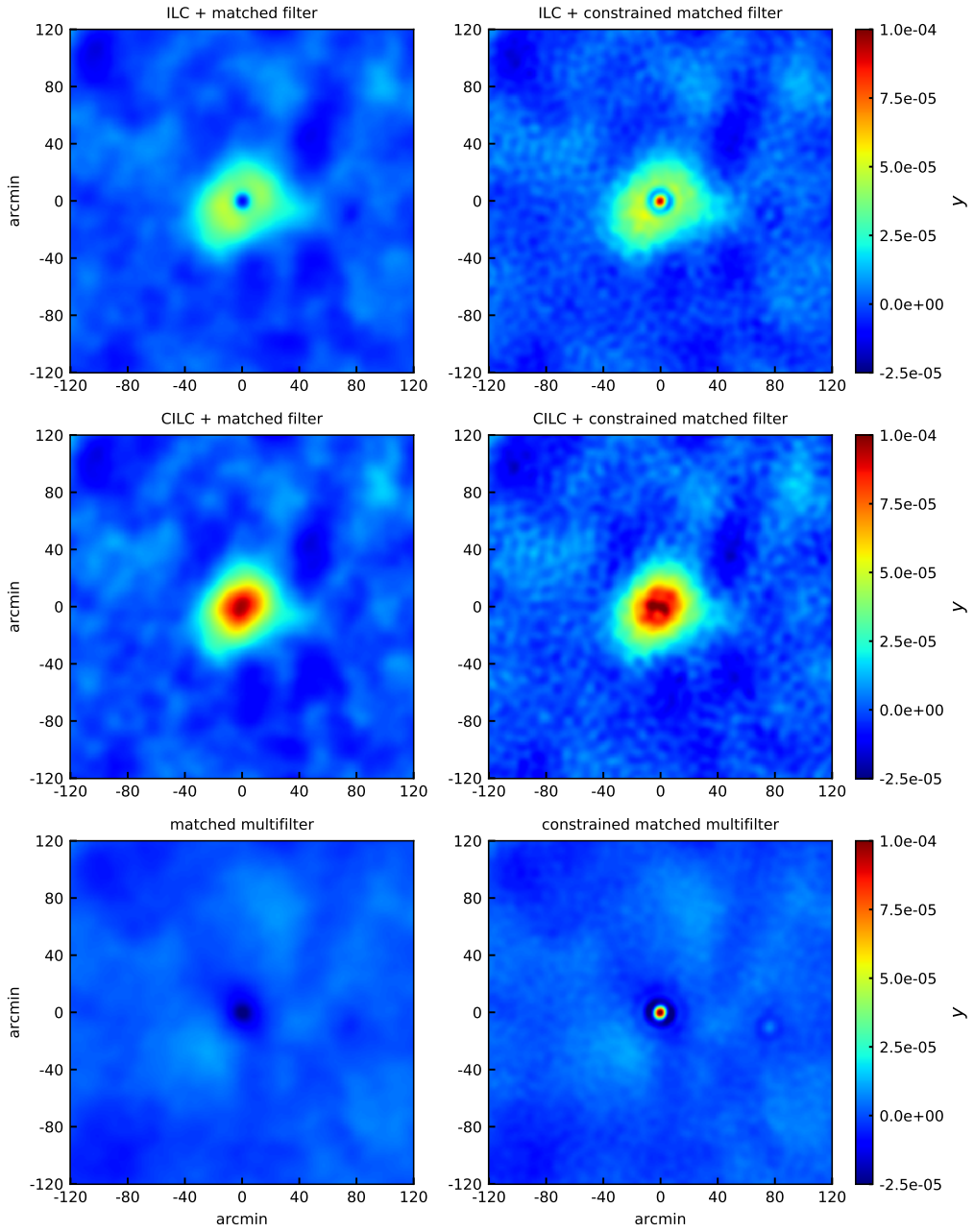


Figure 5.5: Filtered maps of the Perseus galaxy cluster processed with the filtering techniques presented in Section 5.3. The BCG of Perseus hosts a bright radio source called Perseus A that is known to contaminate tSZ observations of the cluster, leading to biased fluxes. We applied all algorithms to $10^\circ \times 10^\circ$ *Planck* HFI maps centred on (RA, Dec.) = (03h19m47.2s, +41°30′47″). The maps above show the inner $4^\circ \times 4^\circ$ of the field. In order to apply the single-frequency filters, the six HFI maps were combined into a $y$-map using ILC and CILC algorithms, the latter of which allows to remove the contamination caused by Perseus A by constraining its SED. Our comparison shows that there are various ways of removing point sources from clusters using either spectral or spatial constraints or a combination of both, all of which find consistent values for the central Comptonization parameter $y_0$ and thus $Y_{500}$. The best SNR is delivered by the CMMF, which yields a value of 24. This is comparable to the SNR of clusters with similar mass and redshift to Perseus that do not suffer from point source contamination, like the Coma cluster.

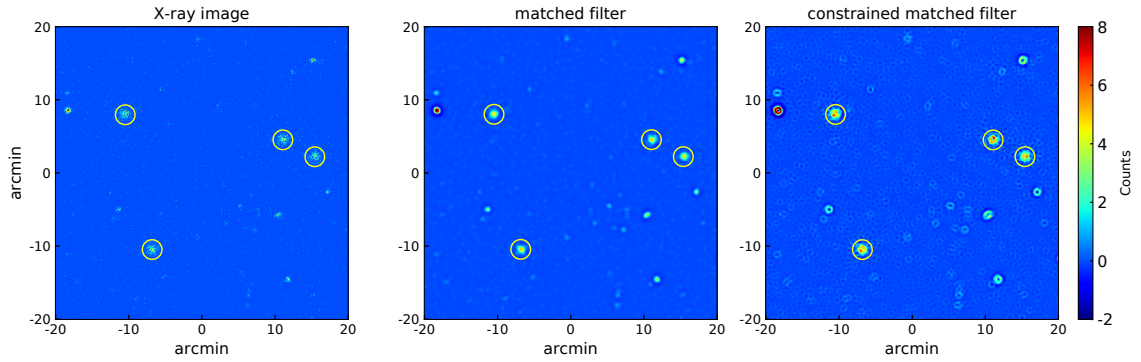


Figure 5.6: Zoom-in on a simulated X-ray photon image (left) and the same image convolved with an MF (centre) and CMF (right). The colour bar to the right has been cropped at eight counts to highlight faint structures in the filtered maps. The mock data features realistic X-ray and instrumental backgrounds as well as a realistic point source population, but for simplicity only contains multiple realizations of a single simulated cluster (highlighted with yellow circles). A detailed description of the data can be found in Section 5.4.3. The MF yields an SNR amplification of the clusters but its response to point sources is similar to that of clusters, which makes the separation of the two source populations challenging in some cases. In contrast, the CMF nullifies point sources and leaves behind 'doughnuts' at their positions in the map. Since both filters have an identical response to clusters, combining their results allows for a quick and simple separation of the two source populations, which is shown in Fig. 5.7.

often relies on the assumption of a perfect power-law SED, which can be prone to mistakes since many sources are known to have SEDs that deviate from a power-law (Herbig & Readhead, 1992). Furthermore, using spectral information will require individual measurements for each source, while a spatial technique can be applied blindly to a large number of objects.

### 5.5.3 Blind cluster detection and X-ray application

We also investigate the potential application of the CMF to reduce point source contamination for blind cluster detection. In tSZ surveys below 217 GHz point sources will not be misclassified as galaxy clusters due to the tSZ effect's characteristic decrement. They can however lower the decrement or even overpower it, which can lead to a biased flux or a non-detection as has been illustrated previously in Section 5.5.1. At higher frequencies, in the tSZ increment, point sources can bias the flux and might be misclassified as clusters. For instruments like *Planck* the situation has been mitigated by multifrequency coverage (e.g. Bartlett & Melin 2006), but prominent examples like the Perseus cluster remain.

Point source contamination is an even greater issue in X-ray surveys due to the stochastic nature of the observed signal. The upcoming eROSITA survey is expected to detect about 100 000 galaxy clusters (Pillepich et al., 2012; Clerc et al., 2018) as well as millions of AGNs. Separating both source populations presents a major challenge for cluster detection algorithms. The CMF introduced here presents an additional tool for this task that has the benefit of using reasonable assumptions, like well-known cluster profiles and the PSF of the instrument, to deliver an optimal result. In the remaining part of this section we will provide a brief outline how the traditional and CMFs can be combined to detect clusters in X-ray surveys and reduce the number of misclassified point sources.

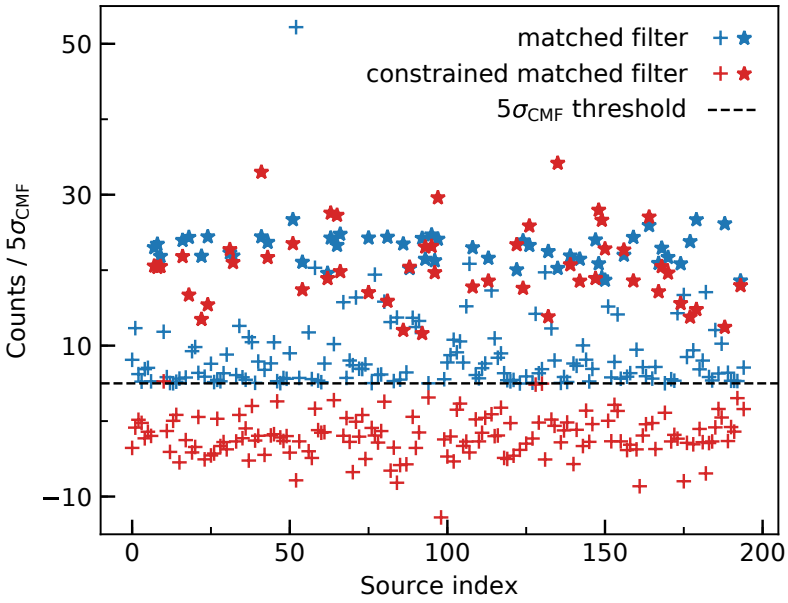


Figure 5.7: A simplified demonstration of the application of the CMF to eROSITA mock data. Simulated clusters are shown as stars while point sources are shown as crosses. Applying an MF to a map with 1.6 ks exposure time will typically result in 200 sources with centroid values above $5\sigma_{CMF}$. When measuring the corresponding values in a map processed with a CMF, the vast majority of previously detected point sources (blue crosses) will drop below the threshold (red crosses), leaving us with a cleaner sample of cluster candidates.

We perform our tests on the eROSITA mock data that was introduced in Section 5.4.3. Each field is filtered with both an MF and a CMF. We then apply a simple source finder[4] to the former map to identify bright sources above a fixed threshold, e.g. $5\sigma_{CMF}$ as defined by equation (5.2), and determine their centroids. This typically leaves us with around 200 source candidates, the majority of which are point sources. We then determine the values of the map processed with the CMF at the position of the previously measured centroids and only classify objects for which both values lie above the former threshold as cluster candidates. This procedure is illustrated for a single field in Figs. 5.6 and 5.7 .

We find that using both filters in conjunction will strongly reduce the number of misclassified point sources. As demonstrated clearly in Fig. 5.7, the CMF yields a better segregation of point sources in terms of their SNR but also raises the scatter of the filtered cluster photon counts due to the increased map noise.

## 5.6 Discussion

The new CMF and CMMF techniques presented in this work are straightforward extensions of the MF concept that enable optimal extraction of sources with known templates while at the same time allowing for an optimal reduction of known contaminating sources. The results presented in Section 5.5 focused on the reduction of point source contamination to SZ and X-ray observations of galaxy clusters, but it is important to stress that the methods presented here are applicable to any contaminating source that

[4] We use the `find_peaks()` function of the python PHOTUTILS package.

can be approximated through a known template. It is also possible to place more than one constraint, yet care has to be taken since every additional constraint will result in a noisier map. As with any MF, the values found in the filtered map will be biased if the source template does not match the true shape of a resolved source. We note however that the CMFs can provide a slightly larger bias than the traditional MF if the desired source is more compact than its template and other compact sources are supposed to be removed.

A technique similar to the CMMF presented in this work was explored by Herranz et al. (2005), who derived an unbiased MMF to minimize the contamination of the tSZ to kSZ maps and vice versa. These authors derived a two-component version of the filter presented here and then use the same spatial but different spectral templates for the two different SZ components to separate them. However, a potential drawback of this method is that the spatial templates of the tSZ and kSZ signals should in general be different, especially for merging systems.

An important detail of the new methods is their dependence on the spatial resolution of the instrument, which has a crucial impact on the noise level of the filtered map. Compact clusters will thus remain spatially indistinguishable from point sources if the instrument beam is large. This also restricts the application of the constrained filters on *Planck* data to nearby clusters with large apparent radii. The situation improves when the instrument beam has an FWHM of $\sim 1$ arcmin or less, at which point the noise will only increase by a few percent compared to a matched filtered map for most cluster sizes. Such resolution is quite common for ground-based cluster surveys like the ones performed by the SPT and ACT. However, additional filtering will be applied for ground-based instruments to reduce atmospheric contamination. The impact of these filtering steps on the astrophysical signal has to be understood and characterized before MFs are applied (e.g. Bleem et al. 2015).

The new filtering techniques are especially interesting for studies of the kSZ and relativistic tSZ at sub-mm wavelengths with upcoming instruments like CCAT-prime[5]. CCAT-prime will be a 6 m diameter submillimetre survey telescope that is going to operate at 5600 m altitude on the summit of the Cerro Chajnantor in the Chilean Atacama Desert (Parshley et al., 2018b,a). The high and dry site offers superb conditions for observations at frequencies ranging from 270 GHz to 860 GHz (Vavagiakis et al., 2018) at up to one order of magnitude better sensitivity than *Planck* (Erler et al., 2018; Mittal et al., 2018). Combined with mm-data of the advanced ACT-pol survey, CCAT-prime will offer full coverage of the SZ spectrum and allow significant improvements over *Planck* in measuring cluster parameters (Erler et al., 2018; Stacey et al., 2018). In order to constrain key properties of clusters via the SZ effects, accurate mm and sub-mm photometry will be required and MF techniques including the ones introduced here are an excellent tool for this (Soergel et al., 2017; Erler et al., 2018).

One of the most important applications of the CMF will be next-generation wide-area X-ray surveys, such as eROSITA, that aim to detect the diffuse emission of many thousands of galaxy clusters out to high redshift in the presence of millions of AGNs. The need for new techniques for better point source separation was recently highlighted by Biffi et al. (2018), who used X-ray mocks derived from the hydrodynamical *Magneticum Pathfinder Simulation* to investigate the contribution of AGNs inside clusters to the X-ray luminosity of the ICM. The methods presented in this work are especially tailored to this application, since they only require a spatial template and provide an optimal and unbiased result. An important benefit of the filters presented here is their ability to separate clusters and point sources even if they are aligned. On one hand, this can lead to biased photometry of clusters with compact cool cores if the template does not account for it, but on the other hand such a bias can

[5] http://www.ccatobservatory.org/

actually be useful to mitigate the so-called cool-core selection bias in X-ray cluster surveys.

We note however that the CMF should not be considered as a replacement for well-proven and tested methods but rather presents an additional tool that will work best in conjunction with other methods such as the traditional MF or e.g. the well-known sliding cell (Harnden et al., 1984) and wavelet (Freeman et al., 2002) algorithms, since significant discrepancies between their extracted signals hint at potential point source contamination.

The X-ray analysis presented here was deliberately chosen to be qualitative and focuses on the conceptual application of the new methods, since we do not account for the Poissonian statistics that govern X-ray observations and do not tune the detection threshold to maximize the number of detected clusters while staying below a fixed rate of spurious detections. In addition to a robust X-ray implementation of the filters, future, more quantitative studies of the X-ray application of the CMF should include a realistic energy and line-of-sight dependent PSF and tests using archival X-ray data.

Other recent attempts on improving the separation of point sources and galaxy clusters in X-ray data sets include the combination with optical data (Green et al., 2017) and a new MMF technique introduced by Tarrío et al. (2016, 2018) who used ROSAT data as an additional *Planck* channel to use the different point source populations in the two data sets.

## 5.7 Conclusions

This work introduced a new way to generalize MFs and MMFs to separate desired and undesired sources based on just their spatial (CMF) or their spatial and spectral (CMMF) characteristics. Adding additional constraints will reduce the SNR of the sources, but if both source and contaminant are well approximated by given templates the methods introduced here will allow for unbiased photometry and reduced confusion. When applied to Gaussian data, MFs are optimal in the least-square sense, making them ideal tools for the extraction of the SZ signal of galaxy clusters from microwave data. However, traditional MF techniques can perform poorly if microwave data of galaxy clusters are contaminated by point sources.

At microwave frequencies, there are two distinct populations of point-like sources that are spatially correlated with galaxy clusters. The first consists of radio-bright AGNs that are found at the centres of many BCGs, and the second being composed of dusty star-forming galaxies. Using realistic microwave mock data we showed that the CMF introduced in this work allows for unbiased photometry of clusters that harbour a central point source. If applied at multiple frequencies it enables studies of the SZ spectrum of clusters with no need to account for the SED of the point source. We showed that our method requires sufficient spatial resolution to be competitive and otherwise will yield an unbiased but noisy result. Applying constrained and unconstrained MFs and MMFs to *Planck* HFI data of the Perseus cluster, which features a bright central radio source, demonstrated that there are multiple ways to remove a central source from actual data, requiring only spatial or spectral constraints, or the combination of both. In the latter case we showed that Perseus can be detected with an SNR typical for a cluster of its mass and redshift. However using only spatial constraints will reduce contamination by point sources regardless of their SED.

The application of the methods presented here is especially interesting to the upcoming CCAT-prime and eROSITA cluster surveys. While CCAT-prime will benefit from unbiased photometry of clusters with central point sources for detailed measurements of the rSZ and kSZ effects, point source confusion during cluster detection is a major concern for X-ray surveys. We illustrated how the CMF can provide

an optimal way to distinguish between clusters and point sources and showed that the new method has the potential to be developed into a competitive cluster finding algorithm.

## 5.8 APPENDIX A: all-sky formalism

The MF formalism presented in Section 5.3 used the flat sky approximation but can be adopted to the full sphere with little effort. Implementing MFs on the full sphere can have advantages in certain situations, because we can avoid using an approximate projection to a flat-sky geometry. Schäfer et al. (2006) provide an excellent overview on the details. This section is intended to give a summary of the most important points.

Assuming radial symmetry of the sources that we are interested in (i.e. $m = 0$) and using the convolution theorem on the sphere we can relate the spherical harmonic coefficients of the unfiltered map $a_{\ell\mathrm{m}}^{\mathrm{unfilt}}$ to the ones of the filtered map $a_{\ell\mathrm{m}}^{\mathrm{filt}}$ by:

$$a_{\ell\mathrm{m}}^{\mathrm{filt}} = \sqrt{\frac{4\pi}{2\ell+1}}\,\Psi_{\ell 0}\,a_{\ell\mathrm{m}}^{\mathrm{unfilt}} \equiv F_\ell\,a_{\ell\mathrm{m}}^{\mathrm{unfilt}}. \tag{5.29}$$

The new all-sky MF $\boldsymbol{F}$ will thus be

$$\boldsymbol{F} = (\boldsymbol{\tau}^{\mathrm{T}}\mathbf{C}^{-1}\boldsymbol{\tau})^{-1}\tilde{\boldsymbol{\tau}}\mathbf{C}^{-1}, \tag{5.30}$$

where $\mathbf{C}$ is the power spectrum of the all-sky map recast as a diagonal matrix as was done in Section 5.3 and the elements of $\boldsymbol{\tau}$ and $\tilde{\boldsymbol{\tau}}$ are defined as:

$$\tau_\ell = \sqrt{\frac{2\ell+1}{4\pi}}\cdot\tilde{\tau}_{\ell 0} = \sqrt{\frac{2\ell+1}{4\pi}}\cdot y_{\ell 0}\cdot B_\ell\cdot w_\ell. \tag{5.31}$$

Here, $y_{\ell 0}$ denotes the spherical harmonic transform of the source template profile, while $B_\ell$ and $w_\ell$ are the beam and pixel window functions. When computing the $C_\ell$ it is often useful to mask the brightest regions of the Galaxy to reduce contamination from bright ringing artefacts and ensure that the data are Gaussian.

The CMF can be applied to the full sphere analogously. Using equation (5.29) the all-sky filter can be written as:

$$\boldsymbol{F} = \boldsymbol{e}^{\mathrm{T}}\left(\mathbf{T}^{\mathrm{T}}\mathbf{C}^{-1}\mathbf{T}\right)^{-1}\tilde{\mathbf{T}}\mathbf{C}^{-1}. \tag{5.32}$$

As defined in Section 5.3, $\mathbf{T}$ and $\tilde{\mathbf{T}}$ are matrices build from the $n$ spatial constraints

$$\mathbf{T} = \begin{pmatrix} \tau_1[1] & \tau_2[1] & \dots & \tau_n[1] \\ \vdots & \vdots & \ddots & \vdots \\ \tau_1[n_\ell] & \tau_2[n_\ell] & \dots & \tau_n[n_\ell] \end{pmatrix}, \tag{5.33}$$

$$\tilde{\mathbf{T}} = \begin{pmatrix} \tilde{\tau}_1[1] & \tilde{\tau}_2[1] & \dots & \tilde{\tau}_n[1] \\ \vdots & \vdots & \ddots & \vdots \\ \tilde{\tau}_1[n_\ell] & \tilde{\tau}_2[n_\ell] & \dots & \tilde{\tau}_n[n_\ell] \end{pmatrix}, \tag{5.34}$$

where the components $\tau_i$ and $\tilde{\tau}_i$ are defined for each template $i$ as done in equation (5.31).

CHAPTER 6

# Galaxy cluster sample size and SZ-spectroscopy forecasts for CCAT-prime

Some results created with the CCAT-prime galaxy cluster forecast pipeline presented in this chapter have been used for a recent Astro2020 white paper on "SZ-spectroscopy" in the coming decade:

- Basu K., **Erler J.**, Chluba J. et al., 2019, arXiv:1809.06446,

as well as in two publications by the CCAT-prime collaboration that present the science case for the experiment:

- Stacey G. J., Aravena M., Basu K., Battaglia N., Beringue B., Bertoldi F., ... , **Erler J.** et al., 2018, Proc. SPIE, 10700, 107001M.
- Aravena M., Austermann J., Basu K., Battaglia N., Beringue B., Bertoldi F., ... , **Erler J.** et al., 2019, arXiv:1909.02587.

Furthermore, the forecasts presented here have been used in several unpublished fundraising proposals for CCAT-prime's main instrument Prime-Cam. Additional plots for this chapter are shown in Appendix C.

## 6.1 Abstract

CCAT-prime is a next-generation multifrequency survey telescope that will observe a large fraction of the sky at submillimetre wavelengths and promises novel scientific discoveries across many relevant areas of modern astrophysics, ranging from star formation in the Milky Way over Galactic and extragalactic transients to the first galaxies and cosmology with galaxy clusters. This work presents the development of a pipeline for the generation of mock observations for CCAT-prime and similar instruments, which is used to produce forecasts for the envisioned galaxy cluster science case for CCAT-prime. Specifically, the pipeline is used to estimate the expected galaxy cluster sample size that will be obtained with CCAT-prime and investigate the constraints on the parameters of the

Sunyaev-Zeldovich effect. The predictive power of the pipeline is verified by reproducing the *Planck* and SPT-SZ cluster samples, for which we reach excellent agreement, besides previously known incompatibilities between *Planck* and SPT cluster masses. Multiple variations of CCAT-prime are investigated and our results indicate that CCAT-p will be able to observe between 2000 and 10 000 clusters, depending on the exact details of the survey. With its unique access to high frequencies, CCAT-prime is found to be able to double the sample size of near-future instruments like AdvACT if the data sets are combined. Although superior to other upcoming surveys, the constraints on the temperature of the intracluster medium and peculiar velocity of clusters that can be obtained via the thermal and kinetic SZ effects will not be sufficient for direct measurements of the two quantities. Besides the use of statistical techniques like stacking, we demonstrate that strong spectral constraints can be achieved through the introduction of an X-ray-derived prior on the cluster optical depth $\tau_e$, which opens up interesting synergies of CCAT-prime with the upcoming eROSITA X-ray all-sky survey.

## 6.2 Introduction

The *Planck*, ACT and SPT surveys (Hasselfield et al., 2013; Bleem et al., 2015; Planck Collaboration, 2016a) have revolutionised the observations of the SZ effects of clusters over the last decade. The three facilities delivered the first SZ-selected cluster samples containing many hundreds of clusters, a large number of them being previously unknown disturbed systems at high redshift. These successful surveys however represent only the fist generation of SZ cluster surveys and the next generation is already collecting data (e.g. SPT-3G; Benson et al., 2014). These upcoming experiments are expected to increase the sample size to many thousands of objects (Abazajian et al., 2016; Melin et al., 2018b; Ade et al., 2019). The increased sensitivities will be achieved by large bolometer arrays that already deploy $\sim 10^4$ multichroic TES detectors (Anderson et al., 2018) and fill the full focal plane of current-generation telescopes.

A fundamental limitation of past and current generation galaxy cluster surveys is their limited frequency coverage. Except for the *Planck* satellite, which itself is limited by its comparatively poor spatial resolution and sensitivity, today's ground based surveys typically observe in the millimetre-regime from about 30 GHz, or 1 cm, to 270 GHz, or 1.1 mm, with a small number of frequency channels. Observing at submillimetre frequencies using ground-based facilities is challenging since water vapour in the atmosphere absorbs and attenuates submillimetre radiation and even high and dry sites like the Chajnantor plateau in the Atacama desert only allow efficient observations during a small fraction of the available observing time when the PWV is sufficiently low. However, such observations would be extremely valuable for multiple reasons. First, they would allow a better modelling of high-frequency galactic foregrounds, mostly thermal dust emission, as well as the CIB. Second, high-frequency observations can provide powerful constraints on the shape of the spectrum of the SZ effects of clusters, especially the distortions of the tSZ spectrum caused by relativistic effects. This is illustrated in Fig. 6.1.

The CCAT-prime telescope, which was introduced in Section 2.2, will address these shortcomings by observing the sky from the summit of the Cerro Chajnantor. This exceptional site lies $\sim 500$ m above the ALMA site and offers the lowest PWV values of all telescope sites in the Atacama desert. These conditions will allow CCAT-prime to observe at submillimetre frequencies for most of the year and occasionally even permit observations in the terahertz regime. CCAT-prime is expected to

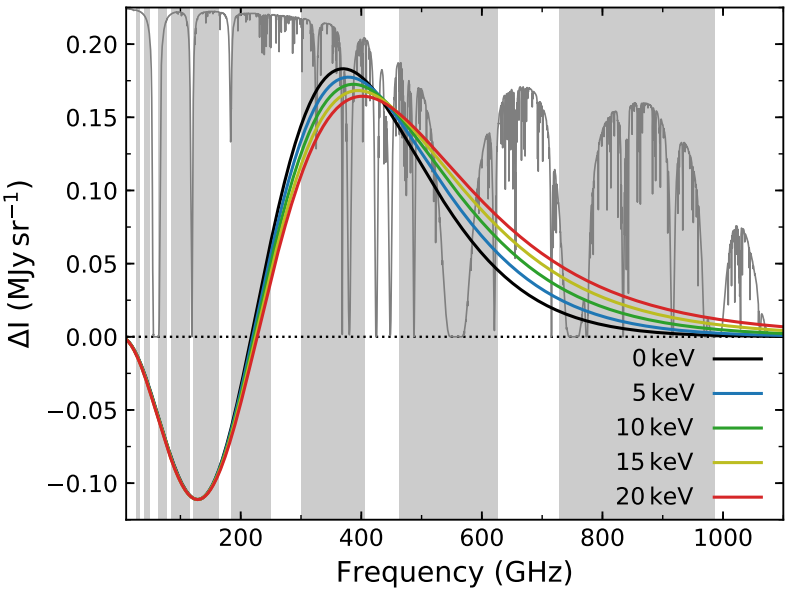


Figure 6.1: Illustration of the degeneracy of relativistic tSZ spectra at low frequency. The grey areas indicate the *Planck* LFI and HFI bands while the grey curves are the atmospheric transmission at the CCAT-prime site computed using the ATM model (Pardo et al., 2001) for PWV = 0.21 mm. The black line shows the widely used non-relativistic approximation of the tSZ effect for $y = 10^{-4}$. The coloured curves show the tSZ spectrum computed with relativistic corrections for a range of temperatures. For these curves, the Compton-$y$ values have been chosen such that the lowest point of the tSZ decrement matches the one of the non-relativistic tSZ spectrum shown here. This demonstrates that observations at high frequencies are needed in order to measure ICM temperatures via the tSZ effect and avoid biased estimates of $y$.

perform a wide area survey of the microwave sky in several bands above 220 GHz, which will be complementary to the surveys that are going to be conducted by the Advanced ACT and the SO. The cluster survey will be conducted using Prime-Cam, a first-light instrument that uses a large cryostat that can hold up to seven instrument modules. In its original configuration, Prime-Cam was supposed to observe the sky in seven frequency bands raging from 95 GHz to 862 GHz (Mittal et al., 2018; Erler et al., 2018), providing a frequency coverage that is similar to that of the *Planck* HFI, but with an increase in sensitivity by roughly an order of magnitude and improved, diffraction-limited, angular resolution. At the current point in time, Prime-Cam is not funded however and the exact number of channels and their band centres therefore remain uncertain.

A crucial step in the preparation of a survey, like the one that will be conducted by CCAT-prime, are detailed forecasts, which help to identify the optimal frequency coverage, number of channels and sky area that will be needed in order to meet the scientific goals of a project. A first set of forecasts of the constraints on the properties of a single massive cluster were presented by Erler et al. (2018) and reproduced in Chapter 4 of this work. Additional forecasts for CCAT-prime have been presented by Mittal et al. (2018) using a Fisher matrix approach, which is prone to underestimate the uncertainties of the recovered SZ signal and model parameters.

In this work, we present the development of a realistic sky model for CCAT-prime based on the best available templates for the most important Galactic foregrounds and extragalactic backgrounds. This

sky model is then used to predict the number of clusters that CCAT-prime and other observatories are expected to detect and what constraints we can achieve on the fundamental SZ parameters. These performance metrics are used to compare several proposed layouts of Prime-Cam in order to find the optimal number of channels and their band centres. Such map-based forecasts allow to apply the same analysis techniques that are used for real data and have been called the "gold standard" for predicting the performance of future facilities (Hanany et al., 2019).

This chapter is structured as follows. The model of the microwave sky is introduced in detail in Section 6.3, providing information on all of its components. Afterwards, it is explained how clusters are simulated, how their expected SNR in a survey is estimated using MMFs, and how mock cluster spectra are generated. Section 6.4 summarises the results that were obtained, starting with a reproduction of the *Planck* and SPT-SZ cluster sample sizes followed by predictions for the sample size and property of surveys with CCAT-prime. The second part of this section provides updated detailed forecasts on the spectral constraints for individual massive clusters, as well as the average constraints expected for the full expected cluster sample. Section 6.5 puts the results we obtain into perspective by comparing with forecasts for other future surveys and provides a discussion of the most relevant findings and their implications. Finally, Section 6.6 concludes the analysis.

## 6.3 Methods

The aim of this work is to investigate and compare the obtainable constraints on the SZ cluster parameters $y$, $\tau_e$, $v_{pec}$, and $T_e$ across different instruments, including several proposed layouts of CCAT-prime's first light instrument Prime-Cam. As an additional performance metric that can be used to optimise the layout of Prime-Cam, we compute the expected number of clusters that a survey, or a combination of surveys, are expected to detect based on their frequency coverage, sensitivities, spatial resolution and fraction of surveyed sky. As has been shown by Erler et al. (2018), contamination of the galaxy cluster SZ signal by spatially correlated FIR emission will likely be a major concern for the next generation of SZ surveys, especially for those that extend into the submillimetre regime. To investigate the degree to which future observations will be influenced/limited by FIR emission, a galaxy cluster FIR component is included in some tests. The following sections provide a detailed overview over the sky and cluster models as well as the image processing and data modelling techniques that are deployed to produce the forecasts.

### 6.3.1 Modelling the microwave sky

We largely follow the steps that were laid out by Erler et al. (2019) to set up a model of the microwave sky. Since CCAT-prime is expected to provide a spatial resolution of $\lesssim 1$ arcmin at $\nu \gtrsim 220$ GHz we, set up our sky model to reach a minimum FWHM of 1 arcmin. The model comes as a series of all-sky component maps at HEALPix $N_{side} = 8192$ with an effective pixel size of 0.43 arcmin to ensure the sampling rate satisfies the Nyquist theorem. At the current point in time, a sky model with a higher spatial resolution is unfortunately not feasible due to the lack of high-resolution component templates and the rapidly increasing computational demands that would come along with them. All components of the sky model are summarised in Table 6.1.

We use a high-resolution CMB map that was generated using the SYNFAST algorithm at $N_{side} = 8192$ and smoothed to a resolution of 1 arcmin. The CMB map was generated from a power spectrum that

| component | template | effective resolution | limitations |
|---|---|---|---|
| | | **diffuse high-$z$ backgrounds** | |
| CMB | synthetic power spectrum | arbitrary | |
| CIB | CITA CIB map | $N_{\mathrm{side}} = 2048$, $1.7'$ p. pix. | |
| | | **Galactic foregrounds** | |
| synchrotron | PySM, model 's1' | $N_{\mathrm{side}} = 512$, $6.9'$ p. pix. | low res. |
| free–free | PySM, model 'f1' | $N_{\mathrm{side}} = 512$, $6.9'$ p. pix. | low res. |
| thermal dust | PySM, model 'd1' | $N_{\mathrm{side}} = 512$, $6.9'$ p. pix. | low res. |
| AME | PySM, model 'a1' | $N_{\mathrm{side}} = 512$, $6.9'$ p. pix. | low res. |
| | | **point sources** | |
| radio PS | NVSS catalogue<br>1 773 484 sources | arbitrary | extrapolated SEDs ($\alpha = 0.5^{+0.1}_{-0.1}$)<br>complete to 2.3 mJy at 1.4 GHz<br>$f_{\mathrm{sky}} = 0.83$ (Dec. $> -40^{\circ}$) |
| FIR PS | IRAS PS catalogue<br>245 589 sources | arbitrary | extrapolated SEDs (MBB)<br>complete to 1 Jy at 100 $\mu$m |
| | | **galaxy clusters** | |
| tSZ + kSZ | CITA | $N_{\mathrm{side}} = 2048$, $1.7'$ p. pix. | |

Table 6.1: Components of the microwave sky model that is used in this work. Apart from minor changes, the sky model is based on the one presented by Erler et al. (2019) and uses high-resolution templates for most components besides the diffuse Galactic foregrounds, which are simulated using the PySM (Thorne et al., 2017). All components are processed as HEALPix all-sky maps.

was computed with CAMB (Lewis et al., 2000) to $\ell_{\mathrm{max}} = 2 \times 10^4$, assuming the same flat ΛCDM cosmology with $h = 0.7$, $\Omega_\Lambda = 0.7$, $\Omega_{\mathrm{m}} = 0.3$, and $\Omega_{\mathrm{b}} = 0.05$. We model the expected contribution from the CIB by adopting the synthetic all-sky CIB maps provided by the WebSky extragalactic CMB mocks team that have been build from a peak-patch simulation that included $8192^3$ particles in a cube with a co-moving side length of 16 Gpc. The provided maps come at the *Planck* HFI frequencies and and are split into two parts: The flux of resolved halos with $M_{200m} > 2.6 \times 10^{13} \mathrm{M}_\odot$ and the unresolved galaxy "field". The latter is an isotropic component that follows a predicted two-point correlation function. The total CIB emission is given by the sum of these two components. We extrapolate the CIB model to arbitrary frequencies by fitting each pixel with a modified blackbody in order to derive three all-sky parameter value maps for the variables $A_{\mathrm{CIB}}$, $T$, and $\beta$. The flux density in each pixel is than given by

$$I_{\mathrm{CIB}}(\nu) = A_{\mathrm{CIB}} \left(\frac{\nu}{\nu_0}\right)^{\beta+3} \frac{\exp(h\nu_0/(k_{\mathrm{B}}T)) - 1}{\exp(h\nu/(k_{\mathrm{B}}T)) - 1}, \tag{6.1}$$

where $\nu_0 = 857$ GHz. Finally, the obtained maps are upgraded to $N_{\mathrm{side}} = 8192$ and smoothed with a narrow Gaussian with FWHM = 1 arcmin.

Maps of Galactic synchrotron, free–free, spinning dust and thermal dust emission are obtained through the PYTHON sky model (PySM, Thorne et al., 2017). The PySM uses the most recent Galactic foreground maps published by the Planck Collaboration (2016c) that were build from the full 2015 *Planck* data together with auxiliary data from the WMAP satellite and the 408 MHz all-sky survey by Haslam et al. (1981, 1982), which has been reprocessed by Remazeilles et al. (2015). These

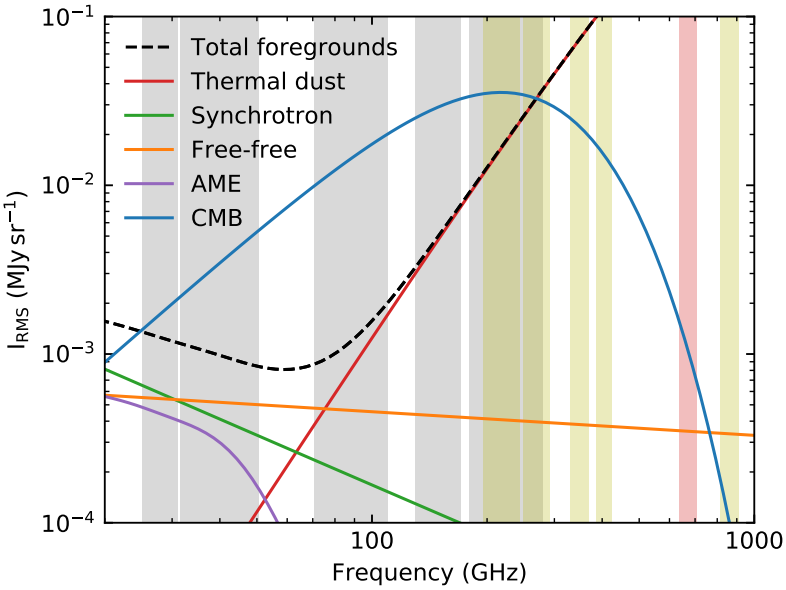


Figure 6.2: Spectra of the Galactic foregrounds used in the CCAT-prime sky model presented in Section 6.3.1, generated using the PySM (Thorne et al., 2017). The coloured curves show the standard deviation of the individual components on a scale of 7 arcmin, defined by the HEALPix resolution of the all-sky templates of $N_{\mathrm{side}} = 512$. The dashed black line gives the sum of all Galactic foregrounds, while the solid blue line shows the spectrum of the primary CMB temperature anisotropies. The grey and yellow bands indicate the proposed frequency channels for AdvACT and a five channel version of CCAT-prime, respectively. The red band shows the location of a potential 670 GHz CCAT-prime channel that would be permitted by a corresponding atmospheric window.

foreground templates were obtained with the COMMANDER algorithm and are provided at a native HEALPix resolution of $N_{\mathrm{side}} = 256$. The PySM upgrades these maps to $N_{\mathrm{side}} = 512$ and adds small scale fluctuations to the maps by extrapolating their power spectra and generating random features according to it, similar to the approach presented by Miville-Deschênes et al. (2007). We use the basic spectral model for each component (i.e. "s1", "f1", "d1", and "a1"; see Fig. 6.2) to compute component maps at a given frequency. These maps are then further upgraded to $N_{\mathrm{side}} = 8192$ and smoothed with a narrow Gaussian (FWHM = 1 arcmin) in order to mitigate pixellation artefacts.

In addition to these diffuse components, we add a realistic population of radio and FIR point sources at 1 arcmin resolution to the sky model. The former are modelled by taking the sky positions and 1.4 GHz fluxes of all $1.7 \times 10^6$ compact sources catalogued by the NVSS (Condon et al., 1998) and extrapolating them to microwave frequencies assuming a power-law SED $I_\nu \propto \nu^{-\alpha}$ with spectral indices $\alpha$ drawn from a Gaussian distribution with a mean of 0.5 and a standard deviation of 0.1.

The FIR point sources are taken from the IRAS point source catalogue (Helou & Walker, 1988), which lists 12, 25, 60, and 100 $\mu$m fluxes and sky positions for $2.5 \times 10^5$ compact objects. Each spectrum is approximated by the modified blackbody SED given by equation (6.1) to extrapolate the measured fluxes to the frequencies of interest.

The analysis presented in this work is restricted to the extragalactic sky, which is targeted by most ground-based CMB experiments. CCAT-prime is currently expected to observe the same, or parts of

the 16 000 deg$^2$ field that will be surveyed by AdvACT and the SO. Since the exact survey strategy was not defined yet, the forecasts presented here will consider all parts of the sky that are not flagged by a 50% Galactic dust mask that also includes the 20% of the sky that has not been observed by the NVSS. From this sky area, we extract 100 $10^\circ \times 10^\circ$ fields centred at random positions that have been sampled uniformly on the sphere using the approach presented in Appendix A.8.

The sky model presented here allows to simulate a wide range of instruments given their frequency bands, their spatial resolution, and their average survey noise. Table 6.2 provides a summary of the specifications of the experiments that are being considered here. In addition to these, we also investigate *Planck* and the version of CCAT-prime presented in Table 4.3. In all cases, the projected fields are convolved with circular Gaussian instrument beams assuming the FWHMs given in the aforementioned tables, while the survey noise is assumed to be Gaussian white noise.

### 6.3.2 Simulating galaxy clusters

The SZ signals of galaxy clusters is simulated in two different ways, by injecting a 'primary' cluster into each map and by populating the sky with realistic background clusters. Our analysis focuses on the extraction of the signal of the primary cluster in the centre of each map. The properties of these primary clusters are assumed to be fully defined by its mass and redshift, which allows us to e.g. map the expected SNR of clusters as a function of these two parameters, which will be described in detail in Section 6.3.3.

We model the tSZ and kSZ effects of these primary galaxy clusters by computing maps of their Comptonization parameter $y$ and the optical depth $\tau_\mathrm{e}$. The Comptonization parameter of each cluster is computed by l.o.s. projection of the pressure profile of the cluster, which is assumed to follow the GNFW profile introduced by Nagai et al. (2007) with the UPP presented by Arnaud et al. (2010). This profile is given by equation (1.70) and was already used in the previous chapters of this work. The clusters are projected assuming spherical symmetry and a maximum radial extent of $r_\mathrm{max} = 5R_{500}$. However the UPP presented by Arnaud et al. (2010) was obtained using X-ray derived pressure profiles, as well as data from hydrodynamic simulations. To ensure that the model reproduces the tSZ signal of clusters seen in actual SZ surveys, we re-normalize the pressure amplitude $P_0$ of the GNFW profile such that the $Y_{500}^\mathrm{sph}$ computed with it matches the one obtained through the *Planck* $Y_{500}$–$M_{500}$ relation that is provided by the Planck Collaboration (2014c, 2016f)

$$E^{-\beta}(z)\left[\frac{D_\mathrm{A}^2(z)\bar{Y}_{500}}{10^{-4}\,\mathrm{Mpc}^2}\right] = Y_*\left[\frac{h}{0.7}\right]^{-2+\alpha}\left[\frac{(1-b)M_{500}}{6\times10^{14}\,\mathrm{M}_\odot}\right]^{\alpha}, \tag{6.2}$$

where $E(z)$ is the cosmic evolution function, $(1+b) = 0.8$ is the hydrostatic mass bias and the values for the parameters $\alpha = 1.79 \pm 0.08$, $\beta = 0.66 \pm 0.5$, and $Y_* = 10^{-0.19\pm0.02}$ were adopted from Table 1 in Planck Collaboration (2016f). This empirical $Y_{500}$–$M_{500}$ relation is tuned further to ensure that the pipeline presented here reproduced the samples sizes of the existing *Planck* and SPT-SZ surveys.

The tSZ signal of the primary clusters is computed including temperature-dependent relativistic corrections using SZPACK (Chluba et al., 2012) under the assumption that clusters are isothermal with the temperature $T_\mathrm{e} \approx T_\mathrm{X}$ computed via the $M$–$T$ scaling relation presented by Reichert et al. (2011)

$$\frac{M_{500}}{10^{14}\,\mathrm{M}_\odot} = (0.291 \pm 0.031)\left(\frac{k_\mathrm{B}T_\mathrm{e}}{\mathrm{keV}}\right)^{1.62\pm0.08} E(z)^{-1.04\pm0.07}. \tag{6.3}$$

| $\nu$ (GHz) | FWHM (arcmin) | $\Delta T$ ($\mu K_{RJ}$-arcmin) | $\Delta T$ ($\mu K_{CMB}$-arcmin) | $\Delta I$ (kJy/sr-arcmin) |
|---|---|---|---|---|
| **SPT-SZ Survey (2500 deg$^2$ survey)** | | | | |
| 95 | 1.6 | 31.8 | 40.0 | 8.8 |
| 150 | 1.1 | 10.4 | 18.0 | 7.2 |
| 220 | 1.0 | 22.8 | 70.0 | 33.8 |
| **Advanced ACT ($10^4$ deg$^2$ survey)** | | | | |
| 28 | 7.1 | 78.4 | 80.0 | 1.9 |
| 41 | 4.8 | 67.0 | 70.0 | 3.5 |
| 90 | 2.2 | 6.5 | 8.0 | 1.6 |
| 150 | 1.4 | 4.0 | 7.0 | 2.8 |
| 230 | 0.9 | 7.4 | 25.0 | 12.0 |
| **CCAT-prime MSIP (4000 h, $10^4$ deg$^2$ survey)** | | | | |
| 226 | 1.0 | 4.8 | 15.5 | 7.5 |
| 273 | 0.8 | 3.8 | 19.6 | 8.6 |
| 350 | 0.6 | 6.4 | 79.1 | 23.9 |
| 405 | 0.5 | 9.3 | 227.7 | 46.7 |
| 862 | 0.3 | 12.4 | $2.1 \times 10^5$ | 282.6 |
| **CCAT-prime v1 (4000 h, $10^4$ deg$^2$ survey)** | | | | |
| 270 | 0.8 | 7.0 | 35.1 | 15.6 |
| 350 | 0.6 | 12.4 | 154.3 | 46.6 |
| 405 | 0.5 | 23.4 | 574.6 | 117.9 |
| **CCAT-prime v2 (4000 h, $10^4$ deg$^2$ survey)** | | | | |
| 350 (2 arrays) | 0.6 | 8.8 | 109.1 | 33.0 |
| 405 | 0.5 | 23.4 | 574.6 | 117.9 |
| **CCAT-prime v3 (4000 h, $10^4$ deg$^2$ survey)** | | | | |
| 350 (3 arrays) | 0.6 | 7.2 | 89.2 | 27.0 |
| **CCAT-prime v4 (4000 h, $10^4$ deg$^2$ survey)** | | | | |
| 350 | 0.6 | 12.4 | 154.3 | 46.6 |
| 405 (2 arrays) | 0.5 | 16.6 | 406.4 | 83.4 |

Table 6.2: Compilation of the band central frequencies, spatial resolution, and map noise of the instruments that are compared in this work. The values for the SPT-SZ survey are given by Bleem et al. (2015), while the specifications of the AdvACT survey are presented by Henderson et al. (2016). Several incarnations of the CCAT-prime bolometer camera called Prime-Cam are compared, all of which are projected to perform a 4000 h, $10^4$ deg$^2$ survey. The collected data is expected to be combined with mm-data ($\nu > 90$ GHz) from the AdvACT survey. In addition to these instruments, we also simulate *Planck* and a 4000 h, $10^3$ deg$^2$ CCAT-prime survey using the numbers given by Erler et al. (2018) that are also given in Table 4.3.

The optical depth $\tau_e$ of each cluster is obtained from the simulated Compton-$y$ map and the ICM electron temperature via

$$\tau_e = \frac{y m_e c^2}{k_B T_e}. \tag{6.4}$$

The optical depth is then used together with a value for the projected l.o.s. component of the peculiar velocity of the clusters to compute their kSZ signal using equation (1.86).

We use the cluster model described here to simulate the SZ signal of clusters as a function of mass and redshift along a logarithmically spaced $64 \times 64$ bin grid with $z \in [0.01, 5]$ and $M_{500} \in [5 \times 10^{13}\,\mathrm{M}_\odot, 2 \times 10^{15}\,\mathrm{M}_\odot]$. The bins are chosen sufficiently small such that the cental redshift and mass of each bin gives a good approximation of the typical redshifts and masses of the clusters within the bin. The predicted central Comptonization parameter $y_0$ and ICM temperature $T_e$ along this grid are shown in Fig. 6.3.

In addition to the SZ signals, we also consider FIR emission from clusters for some forecasts. Since the exact nature of the FIR emission of clusters is not conclusively resolved at the current point in time, we adopt the model used by Erler et al. (2018), who assumed that the FIR signal is is due to warm dust grains in the rest frame of the cluster, the SED of which can be approximated by a modified blackbody with a slightly different parametrization as compared to equation (6.1):

$$I_{\mathrm{FIR}}(\nu) = A_{\mathrm{Dust}} \left(\frac{\nu}{\nu_0}\right)^{\beta_{\mathrm{Dust}}} B(\nu, T_{\mathrm{Dust}}). \tag{6.5}$$

All clusters are assumed to have a dust temperature of 20 K and a spectral index $\beta_{\mathrm{Dust}} = 1.5$. The amplitude $A_{\mathrm{Dust}}$ of the modified blackbody is computed from the total mass of the dust grains in the clusters following the approach presented by Hildebrand (1983)

$$A_{\mathrm{Dust}} = \frac{\kappa_\nu M_{\mathrm{Dust}}}{D_L^2 \Omega}, \tag{6.6}$$

where $\kappa_\nu$ is the mass absorption coefficient, $D_L$ is the angular diameter distance, and $\Omega = \pi(3\theta_{500})^2 / D_A^2$ is the solid angle of the emitting region. We adopt the mass absorption coefficient reported by Draine (2003), $\kappa_{850\mu\mathrm{m}} = 0.0383\,\mathrm{m}^2\,\mathrm{kg}^{-1}$, which was also used by the Planck Collaboration (2016i). The spatial profile of the FIR emission is assumed to follow the Compton-$y$ profile of clusters for easier interpretation of the FIR signal after the simulated maps have been processed by MFs. While the exact radial profile remains unknown, the Planck Collaboration (2016e) found that the FIR emission follows a broader profile compared to the tSZ signal, which is supported by the reported mismatch of the MF- and aperture photometry-based FIR SEDs that was reported by Erler et al. (2018).

Apart from the primary cluster in the centre of each image, we account for the fact that the sky is populated with additional clusters and galaxy groups within a wide mass and redshift range. This is important, since these objects will contribute to the map noise. To model the contribution of other clusters, we again use simulated all-sky maps from the WebSky extragalactic CMB mocks team that were introduced in the previous section. The all-sky $y$- and $\Delta T_{\mathrm{kSZ}}$-maps are provided at a HEALPix resolution of $N_{\mathrm{side}} = 2048$. We upgrade these maps to $N_{\mathrm{side}} = 8192$ and smooth them with a Gaussian with FWHM = 1 arcmin, consistent to the treatment of the CIB maps.

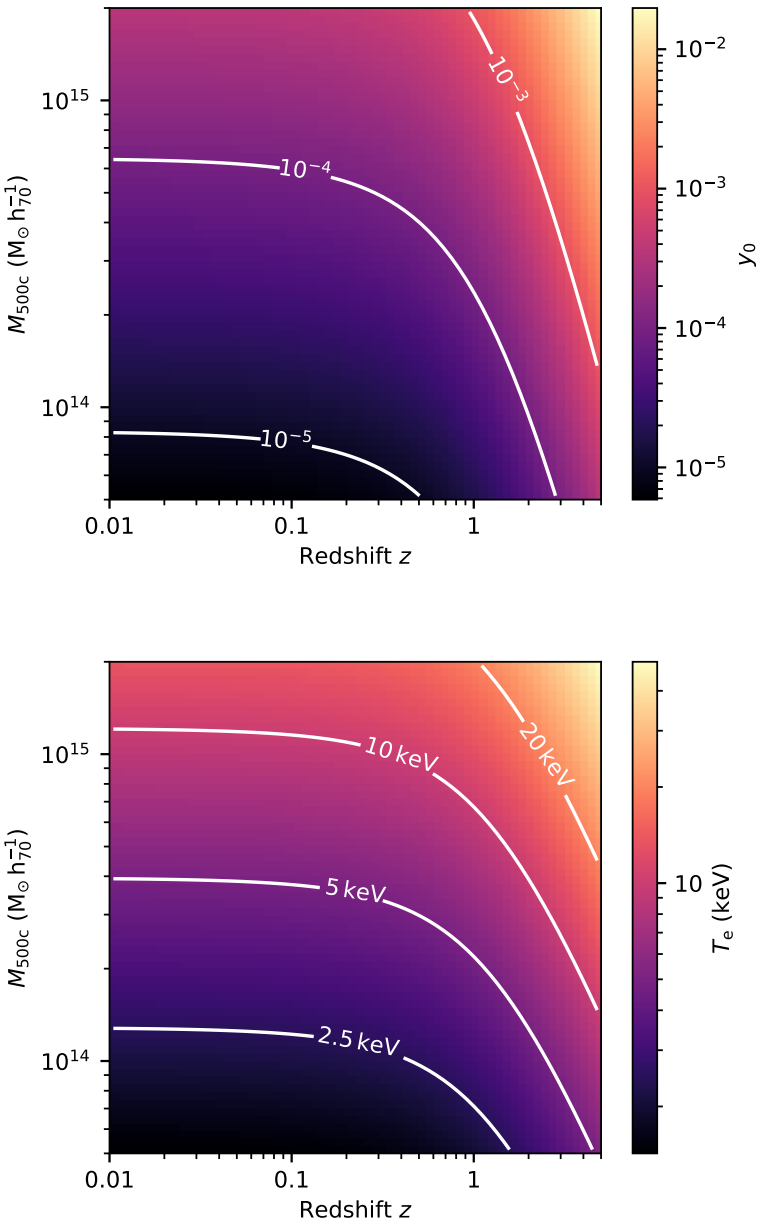


Figure 6.3: CCAT-prime galaxy cluster model. **Upper panel:** Central Comptonization parameter $y_0$ as a function of redshift and mass computed by l.o.s.-projection of a GNFW pressure profile with the best-fit values by Arnaud et al. (2010). **Lower panel:** ICM electron temperature as a function of redshift and mass approximated by the $M$–$T$ scaling relation presented by Reichert et al. (2011).

### 6.3.3 Estimating the SNR of clusters

To estimate the expected SNR of galaxy cluster for a given mass and redshift, we add the relativistic tSZ effect signal of 100 identical clusters, which are simulated using the cluster model presented in the previous section, to 100 mock data sets with varying foregrounds and noise realizations. Each data set is then processed with the MMF from the PyMF package (Erler et al., 2019) to extract the signal of the simulated cluster. We use the non-relativistic approximation of the tSZ effect to build the MMFs to account for the fact that no prior knowledge of a cluster's temperature will be available in a blind cluster survey. The choice of MMFs is motivated by the fact that the same tool is used commonly in current-generation cluster surveys (see Hasselfield et al., 2013; Bleem et al., 2015; Planck Collaboration, 2014d, 2016h). After the multifrequency data sets have been processed with an MMF, the estimated value $y_0$ is extracted at the coordinates of the centres of the primary clusters. An estimate of the noise in the MMF-processed maps is provided directly by equation (5.16). However this estimate corresponds to the standard deviation of the filtered map, which can overestimate the noise level if bright sources like the injected clusters are present in the data. Instead, we estimate the noise level by the standard deviation of a Gaussian that is fit to the pixel value distribution of the filtered map (see Fig. A.3). This effectively excludes extreme map values from the noise estimate. The median of the 100 realizations of the ratio of the values of $y_0$ and the noise levels of the filtered maps provides the expected SNR for a cluster of given mass and redshift. This procedure is repeated for all considered instruments given in Table 4.3 and 6.2. Fig. 6.4 gives an example of the mapped SNR as a function of cluster mass and redshift for a $10^4$ deg$^2$ combined CCAT-prime + AdvACT survey that uses the MSIP version of Prime-Cam. The mapped SNR of clusters will be used in the following step to predict the expected number of clusters that a microwave survey will be able to detect.

### 6.3.4 Predicting the number of clusters

Using the expected average SNR of clusters within given mass and redshift bins we can estimate the number of clusters that a survey should be able to find. To compute the number of clusters, we first need to define a detection threshold, i.e. a minimum SNR that allows for a robust detection. In literature this value is typically 4.5 (e.g. Bleem et al., 2015; Planck Collaboration, 2016h), which we adopt as our threshold in this work and is indicated as a white contour in Fig. 6.4. A detection limit allows to transform the mapped SNR into a binary mask in which no clusters will be detected in redshift and mass bins with SNR $< 4.5$, while all clusters in bins with SNR $\geqslant 4.5$ are assumed to be detected. However, this simple binary mask only allows for a first-order estimate of the expected number of clusters that is likely to underestimate the actual number. The reason for this lies in the peculiar shape of the HMF, which predicts that low-mass clusters are more numerous then high-mass ones at all redshifts, and the fact that the amplitude of the pressure profile of clusters is not constant and will scatter by up to 30% (Arnaud et al., 2010), resulting in a variance in the observed central Compton-$y$ parameter. This scatter is not included in the cluster model presented in Section 6.3.2 for which we assume a re-normalized GNFW pressure profile with the UPP parameter values presented by Arnaud et al. (2010). Additional non-astrophysical scatter is introduced by the noise in the MMF processed maps, which will vary the value of $y_0$ by $\pm 1\sigma_{\mathrm{MMF}}$. This intrinsic variation in the brightness of clusters and the impact of map noise are the two most important sources of variance in the expected SNR of clusters. Assuming that both the map noise and the variance of $y_0$ follow Gaussian distributions, the

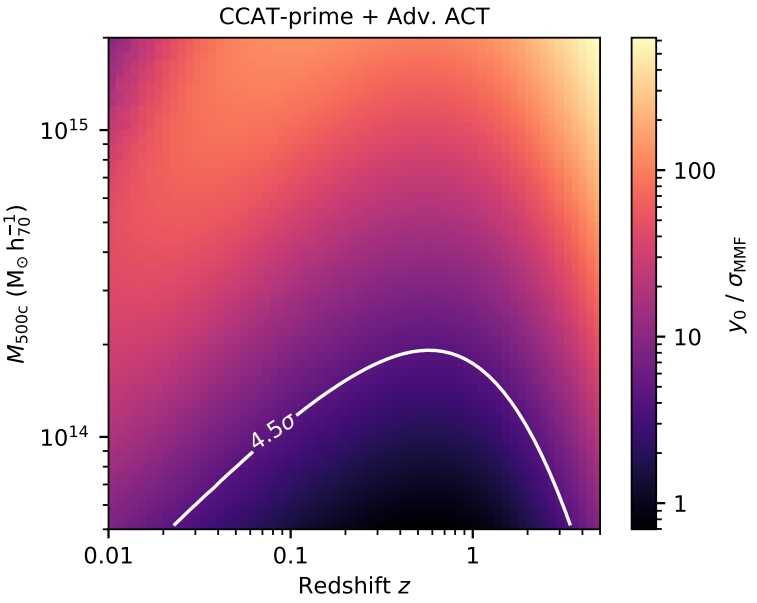


Figure 6.4: Expected SNR of galaxy clusters as a function of mass and redshift for a $10^4$ deg$^2$ CCAT-prime + AdvACT survey. The solid white line indicates the $4.5\sigma_{\mathrm{MMF}}$ detection threshold that is used throughout this work.

probability of detecting a cluster is given by

$$f_{\mathrm{compl}} = \int_{4.5}^{\infty} \mathrm{d}x \, \frac{1}{\sqrt{2\pi}\sigma_{\mathrm{SNR}}} \exp\left(-\frac{(x - \langle \mathrm{SNR} \rangle)^2}{2\sigma_{\mathrm{SNR}}^2}\right), \tag{6.7}$$

where $\sigma_{\mathrm{SNR}}^2 = 1 + (0.3 \langle \mathrm{SNR} \rangle)^2$ gives the width of the combined distribution. This detection probability is commonly referred to as completeness and estimates the fraction of clusters in a mass and redshift bin that a survey is expected to detect. This concept is illustrated in Fig. 6.5.

Although unlikely, a cluster's intrinsic $y_0$ could be twice as high as expected, allowing it to be detected although its mass and redshift suggests that, on average, the cluster should fall below the SNR threshold. Equally, a cluster might be missed because it is intrinsically dimmer than its redshift and mass suggests. However we assume that the $y_0$ of faint clusters can not be boosted by map noise to an arbitrary degree. This assumption is based on the idea that a well-developed source detection algorithm would not only search an MMF-processed map for individual bright pixels, but also take the correlated values of neighbouring pixels into account. We therefore only consider a maximum SNR amplification through uncorrelated noise fluctuations by $\sim 2\sigma_{\mathrm{MMF}}$ and change the width of the Gaussian in equation (6.7) to $\sigma_{\mathrm{SNR}} = 0.3 \langle \mathrm{SNR} \rangle$ for $\langle \mathrm{SNR} \rangle < 2.5$.

Additional sources of scatter will include variation in the remaining GNFW parameters or complete departure from the GNFW model, deviations from spherical symmetry, interacting or merging clusters and misalignment of clusters. However, all of the above are difficult to include in the formalism presented here. The best strategy to do so is to abandon spherical clusters simulated by l.o.s. projection

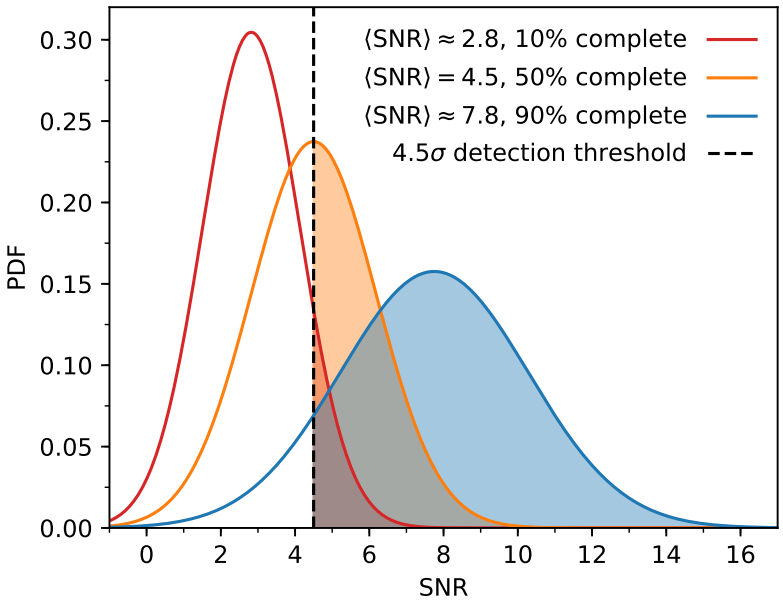


Figure 6.5: Illustration of the concept of sample completeness. The dashed black line marks the SNR threshold of 4.5 that is used to claim a detection. The coloured curves show the distribution of the expected SNR values for three samples with different averages. In all three cases, the shaded regions indicates the fraction of clusters that will be detected. Imagine a hypothetical cluster sample that falls into a very narrow mass and redshift interval and has an average SNR of exactly 4.5. If the cluster properties within the sample scatter such that the result is a symmetric Gaussian distribution for the observed SNR, half of the objects in the sample falls below the detection threshold while the other half falls above it. This sample is, by definition, 50% complete (orange curve). Likewise, if we assume a Gaussian distribution for the observed SNR of the clusters in a given sample it will be 10% complete if the average SNR of the sample is 2.8 (red curve) and 90% complete if the average SNR is 7.8 (blue curve). Note that the numbers given here depend on the assumed scatter in the SZ-observables, as well as the SNR-threshold that is applied.

of a given pressure profile and instead use $y$-maps derived from hydrodynamical simulations, which naturally include a wide range of cluster shapes and use them in a blind detection approach. We leave more sophisticated forecasts using realistic clusters to be explored in future works.

With an estimate of the completeness for each redshift and mass bin all that is left to do is to obtain the predicted total number of galaxy clusters in all bins. The number of dark matter halos in a given mass interval as a function of mass and redshift is given by the HMF $\mathrm{d}n/\mathrm{d}M$, which was introduced in Section 1.5. Using the HMF, the expected number of galaxy clusters for $z_{\mathrm{min}} < z < z_{\mathrm{max}}$ and $M_{\mathrm{min}} < M < M_{\mathrm{max}}$ is given by equation (1.60). We compute the HMF with COLOSSUS (Diemer, 2018) using the model presented by Tinker et al. (2008) and assuming the most recent *Planck* + BAO ΛCDM parameter values presented by the Planck Collaboration (2018b).

The top panel of Fig. 6.7 shows the expected total number of galaxy clusters in the range $0.01 < z < 5$ and $5 \times 10^{13}\,\mathrm{M}_\odot < M_{500\mathrm{c}} < 2 \times 10^{15}\,\mathrm{M}_\odot$ along a $64 \times 64$ bin logarithmically spaced grid. Summing up over all bins, our model predicts a total of 775 269 halos. The distribution follows the characteristics of the HMF, e.g. high-mass halos have not formed yet at high redshifts and are rare at low redshifts due to the small co-moving volume. The expected cluster sample for a given survey can be derived by

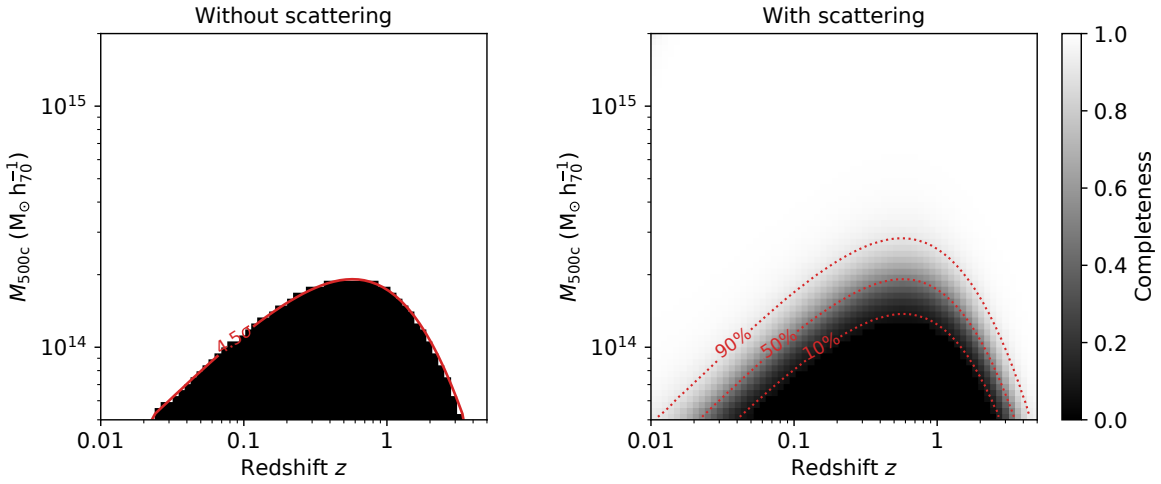


Figure 6.6: Survey mass limits as a function of redshift. **Left-hand panel:** cluster mass limit derived directly from the expected average SNR of galaxy clusters as a function of mass and redshift. All clusters with e.g. SNR $\geqslant 4.5$ (solid red line) are assumed to be detected, while clusters with a lower SNR are assumed to be missed by the survey, resulting in a binary mask. **Right-hand panel:** cluster mass limit obtained by taking the effect of map noise and variance in the intrinsic cluster brightness into account. These two effects lead to a smooth gradient that gives the detection probability for a cluster of a given mass and redshift. The red dotted lines show the estimates of the limiting mass for a $10^4$ deg$^2$ CCAT-prime + AdvACT survey at 10%, 50%, and 90% completeness levels. The corresponding 1D completeness curves as a function of mass and redshift are shown in Fig. C.1.

multiplying the mapped completeness shown in Fig. 6.6 with the expected total number of galaxy clusters, which is demonstrated in the bottom panel of Fig. 6.7 for a $10^4$ deg$^2$ CCAT-prime + AdvACT survey. We find that such a survey should be able to detect $\sim$ 10 000 clusters, the majority of which will be located at $0.13 < z < 0.82$.

The one-dimensional redshift and mass distributions of the clusters samples can be obtained easily by summation of the two-dimensional distributions along their redshift and mass axis, respectively. An example is given in Fig. 6.8, which shows the redshift and mass distributions of the predicted galaxy cluster sample obtainable with a $10^4$ deg$^2$ CCAT-prime + AdvACT survey that is shown in the lower panel of Fig. 6.7. Equivalent one-dimensional distributions are shown in Fig. C.15 for the expected total sample of clusters that is shown in the top panel of Fig. 6.7. Note however that the straightforward summation of the two-dimensional distributions like the ones in Fig. 6.7 will, by definition, adopt the bins that have been used, i.e. logarithmically spaced bins in the example created here. Computing the one-dimensional redshift and mass distributions of the same sample using linearly spaced bins results in histograms that differ in shape, mode, and extent of the 68% interval as is illustrated in Fig. C.2.

### 6.3.5 Creation of random cluster samples

Some specific forecasts require mock cluster samples for a given survey, containing a realistic population of clusters with values of their masses and redshifts. We can generate such samples using two-dimensional distributions in redshift- and mass-space like the one shown in the lower panel of Fig. 6.7. These distributions have the same shape as the expected two-dimensional redshift-mass-PDF,

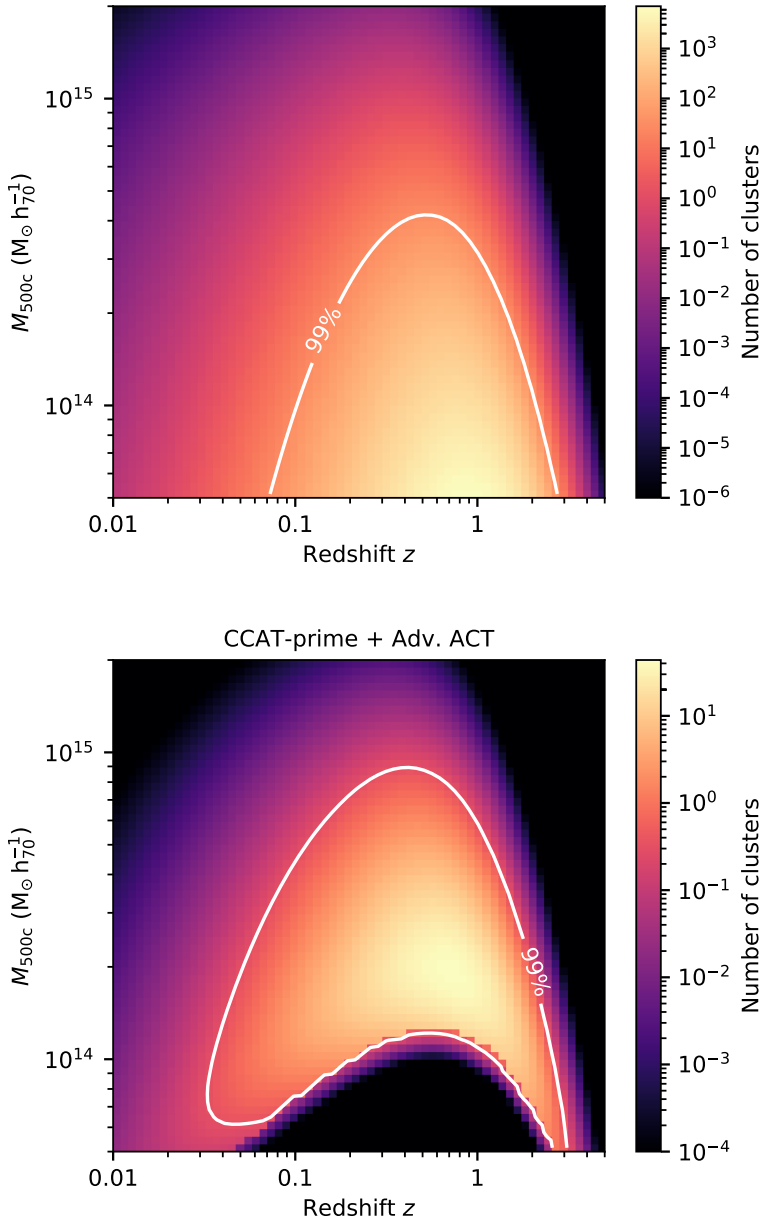


Figure 6.7: Predicted number of galaxy clusters observable with CCAT-prime. **Top-panel:** Expected total number of galaxy clusters in the range $z \in [0.01, 5]$ and $M_{500} \in [5 \times 10^{13}\,\mathrm{M}_\odot, 2 \times 10^{15}\,\mathrm{M}_\odot]$ along a $64 \times 64$ bin logarithmically spaced grid. The numbers are obtained by soving the integral in equation (1.60) numerically using the HMF model presented by Tinker et al. (2008) and adopting the latest 2018 *Planck* + BAO ΛCDM parameter values (Planck Collaboration, 2018b). The solid white line envelopes the region of the diagram that contains 99% of all clusters. **Bottom-panel:** Cluster sample expected for a $10^4$ deg$^2$ CCAT-prime + AdvACT survey. The sample has been obtained through multiplication of the mapped completeness shown in Fig. 6.6 and the expected total number of galaxy clusters given in the panel above.

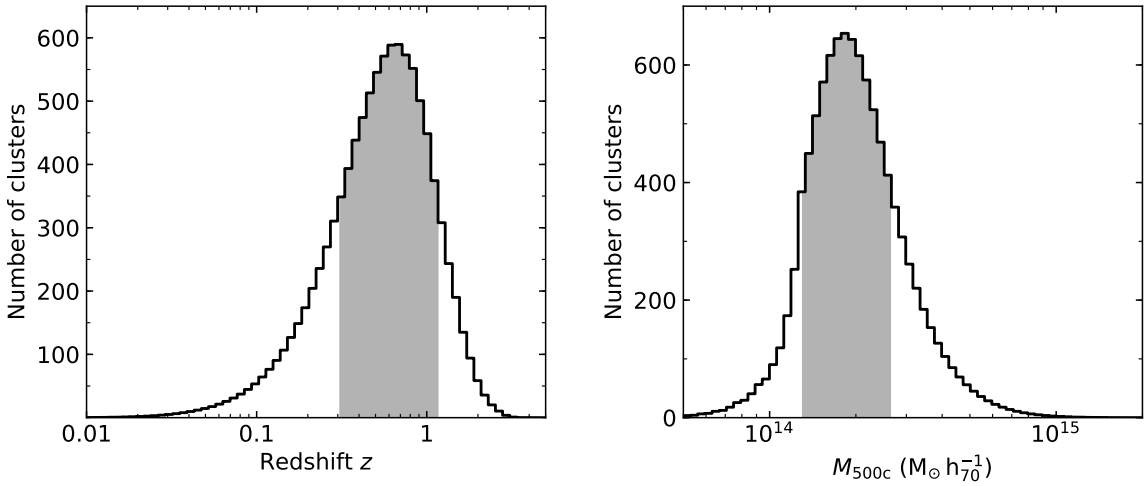


Figure 6.8: Redshift and mass distributions of the predicted galaxy cluster sample obtainable with a $10^4$ deg$^2$ CCAT-prime + AdvACT survey. Both distributions have been obtained by projection of the two-dimensional distribution shown in the bottom panel of Fig. 6.7 and therefore use the same logarithmically spaced bins. The grey area indicates the most compact interval (in logarithmic space) that contains 68% of the simulated cluster sample. **Left-hand panel:** redshift distribution. **Right-hand panel:** mass distribution.

but lack its normalisation to unit integral. The correct normalization can be achieved straightforwardly, but is not required to draw random samples.

Random samples are drawn using a simple Monte-Carlo technique. Uniformly distributed random numbers are drawn in a three-dimensional volume with $\log_{10}(z) \in [-2, 0.7]$, $\log_{10}(M_{500c}) \in [13.7, 15.3]$, and $\log_{10}(n) \in [\log_{10}(n_{\mathrm{min}}), \log_{10}(n_{\mathrm{max}})]$, where $n_{\mathrm{min}}$ and $n_{\mathrm{max}}$ are the minimum and the maximum number of expected clusters in the two-dimensional PDF, respectively. All random samples that lie above the surface defined by the cluster sample PDF are rejected. To determine if a data point lies above or below the surface, we use bi-linear interpolation in logarithmic redshift- and mass-space to fill the gaps between the logarithmically-spaced grid points the PDF is computed on. The procedure is repeated until the desired number of clusters has been generated. An exemplary catalogue generated with this technique is shown in Fig. 6.9.

### 6.3.6 Spectral forecasts

In addition to forecasting the number of clusters that are detectable with a survey or combination of surveys, forecasts on the spectral constraints on the main SZ parameters $y$, $\tau_{\mathrm{e}}$, $v_{\mathrm{pec}}$, and $T_{\mathrm{e}}$ have been prepared. We use the same sky model that has been introduced in Section 6.3.1 but process map of each channel individually using the single-frequency MF from the PyMF package (Erler et al., 2019) in order to extract the spectrum of the simulated clusters. As opposed to the previous forecasts, clusters are now simulated with an additional kSZ component with varying values of $v_{\mathrm{pec}}$. For some forecasts, an additional FIR component will be added to the simulated clusters in order to study its impact on the estimated SZ parameter values. A single mock cluster that is characterised through its mass and redshift is again placed in the centre of each image. The cluster flux is extracted from the MF-processed maps at the cluster position. An example of a simulated spectrum of a massive galaxy cluster with

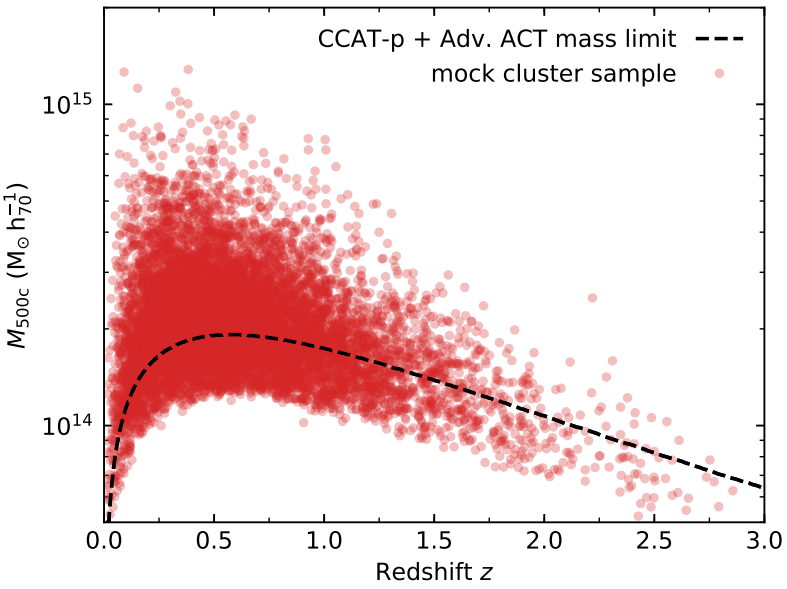


Figure 6.9: Example of a mock cluster sample for a $10^4$ deg$^2$ CCAT-prime + AdvACT survey containing 10121 objects. The sample has been randomly drawn using the Monte-Carlo technique described in Section 6.3.5 from the two-dimensional distribution of clusters in redshift- and mass-space shown in the lower panel of Fig. 6.7. The black dashed line shows the 50% completeness contour for an SNR threshold of 4.5.

$M_{500} = 10^{15}\,\mathrm{M}_\odot$ at $z = 0.23$ and with $v_{\mathrm{pec}} = 1000\,\mathrm{km/s}$, $T_{\mathrm{e}} = 10\,\mathrm{keV}$, $M_{\mathrm{Dust}} = 5 \times 10^{10}\,\mathrm{M}_\odot$, and $T_{\mathrm{Dust}} = 20\,\mathrm{K}$ is shown in Fig. 6.10.

The extracted spectra are fit in a Bayesian approach using the `emcee` package (Foreman-Mackey et al., 2013), which provides an implementation of the affine invariant MCMC ensemble sampler proposed by Goodman & Weare (2010). As introduced in Section 2.4.2 we draw random samples to constrain the posterior probability distribution defined by

$$P(\boldsymbol{p}|\langle \boldsymbol{I}_\nu \rangle) \propto P(\langle \boldsymbol{I}_\nu \rangle|\boldsymbol{p})\, P(\boldsymbol{p}), \tag{6.8}$$

where $\langle \boldsymbol{I}_\nu \rangle$ is the measured average specific intensities after matched filtering, $\boldsymbol{p}$ are the model parameters, $P(\boldsymbol{I}_\nu|\boldsymbol{p})$ is the likelihood function and $P(\boldsymbol{p})$ is the prior. Since the relativistic tSZ spectrum computed with SZPACK's **"COMBO"** runmode is only accurate for $T_{\mathrm{e}} < 75\,\mathrm{keV}$ we restrict the electron temperature to values $0\,\mathrm{keV} < T_{\mathrm{e}} < 75\,\mathrm{keV}$. If not otherwise mentioned, we assume flat and positive priors on the remaining model parameters and use a Gaussian likelihood that is defined by

$$\ln P(\boldsymbol{I}_\nu|\boldsymbol{p}) = -0.5\,[\boldsymbol{I}_\nu(\boldsymbol{p}) - \langle \boldsymbol{I}_\nu \rangle]^{\mathrm{T}} \mathbf{C}^{-1} [\boldsymbol{I}_\nu(\boldsymbol{p}) - \langle \boldsymbol{I}_\nu \rangle]. \tag{6.9}$$

The covariance matrix $\mathbf{C}$ depends on the shape of the MF function used, which is determined by the redshift and mass of the investigated cluster. For a given values of $z$ and $M_{500}$ we estimate the covariance matrix by combining the maps of the 100 sky realizations of each of the $n$ channels into a single array. The matrix obtained this way therefore represents the average sky covariance for a given filter function. As described in Section 6.3.3 using the standard deviation of an MF or MMF processed map can lead to an overestimation of the noise level in the maps because strong sources

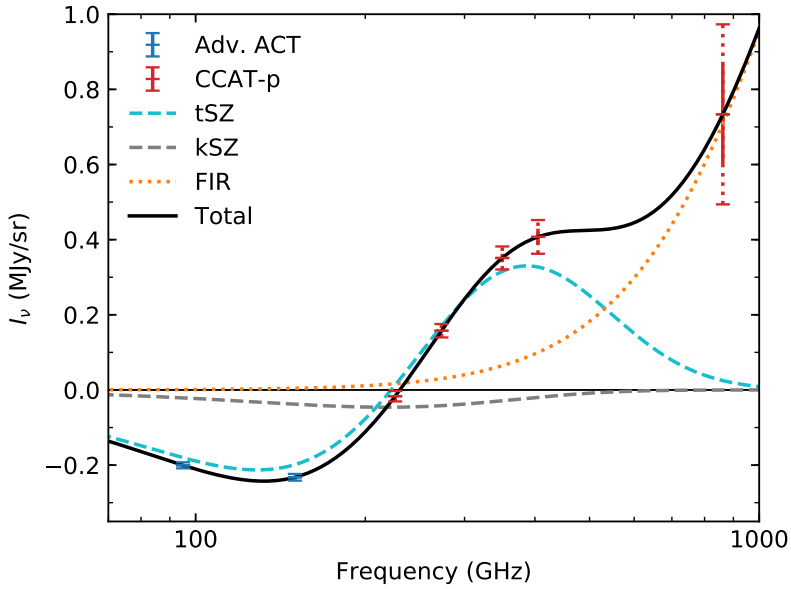


Figure 6.10: Simulated spectrum of a massive galaxy cluster with $M_{500} = 10^{15}\,\mathrm{M}_\odot$, $T_\mathrm{e} = 10\,\mathrm{keV}$ and $v_\mathrm{pec} = 1000\,\mathrm{km/s}$ at $z = 0.23$. The uncertainties of the estimated fluxes correspond the ones expected for a $10^4\,\mathrm{deg}^2$ CCAT-prime (red) + AdvACT (blue) survey. The solid errorbars show the uncertainties if only the instrumental white noise (see Table 6.2) is taken into account, while the dashed ones show the uncertainties obtained by using the sky model introduced in Section 6.3.1. In both cases, single-frequency MFs are applied to simulated multifrequency maps. The dashed lines indicate the simulated tSZ (green), kSZ (grey) and FIR (orange) components of the cluster spectrum while the solid black line shows the combined SED.

like clusters or bright point sources will increase the value of the standard deviation. This has been mitigated previously by estimating the noise level by the width of the distribution of pixel values determined through fitting the histogram of pixel values with a Gaussian (see Fig. A.3). This noise level estimated this way is not impacted by the wide tails seen in the pixel value distributions of many maps. We achieve a similar result during the estimation of the covariance matrices by sigma-clipping the arrays of the combined 100 sky realizations with a threshold of $3\sigma$. An example of a covariance matrix and the corresponding correlation matrix is shown in Fig. 6.11.

The results from the spectral fits are shown either as cornerplots generated using a modified version of the `corner` package (Foreman-Mackey, 2016), or as maps that provide the marginalised uncertainties of a single parameter on the same $64 \times 64$ logarithmically spaced redshift-mass grid that has been used before.

## 6.4 Results

### 6.4.1 Reproducing the *Planck* and SPT-SZ cluster samples

In order to verify the validity of the forecast pipeline presented in the previous section, we use it to predict the number of clusters that are expected for the *Planck* and SPT-SZ cluster surveys, as well as their redshift and mass distributions.

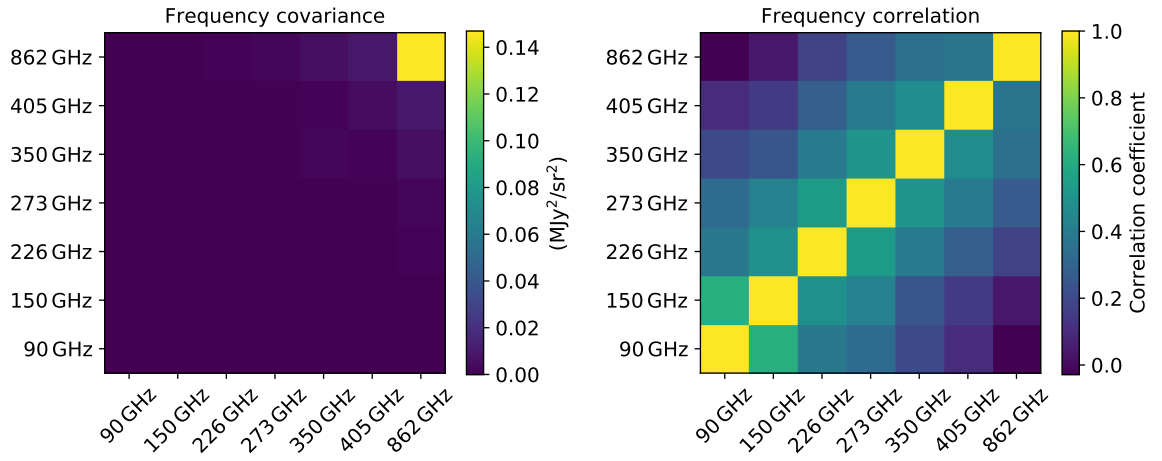


Figure 6.11: Simulated frequency covariance and correlation coefficient matrices obtained from MF processed maps for a $10^4$ deg$^2$ CCAT-prime (226-862 GHz) + AdvACT (90-150 GHz) survey. The MF was constructed to extract the signal of galaxy clusters with $M_{500} = 10^{15}\,M_\odot$ at $z = 0.23$. The matrices show the average frequency-to-frequency covariance and correlation coefficients of 100 mock sky realizations. The maps have been sigma-clipped to prevent bright sources from inflating the estimated values of the covariances and correlation coefficients. **Left-hand panel:** Covariance matrix. **Right-hand panel:** Correlation coefficient matrix.

Using the sky model introduced in Section 6.3.1, we simulate *Planck* maps at the six *Planck* HFI frequencies. We use the same $64 \times 64$ bin grid in redshift and mass as presented before to simulate the tSZ signal of clusters, which are added to the centre of the simulated maps. We assume the average survey noise that is provided by the Planck Collaboration (2016a) for each channel and scale it to a pixel size of 0.4 arcmin assuming it behaves like white noise. After convolution with the *Planck* HFI beams, the maps are re-binned to a pixel size of 1.5 arcmin to match the properties of real Planck data. The maps are then processed with MMFs, as described in Section 6.3.3, to derive the expected SNR of the mock clusters.

A similar procedure is used to simulate SPT-SZ maps. We simulate maps at frequencies of the SPT-SZ survey, i.e. 95, 150, and 220 GHz and assume the average survey noise provided by Bleem et al. (2015). We use the same $64 \times 64$ grid in cluster redshift and mass and estimate their expected SNR from maps processed using an MMF technique.

The mapped SNR for the two surveys are shown in Fig. 6.12. Assuming an SNR threshold of 4.5 for both surveys, we can derive their expected completeness contours and overplot them to the actual samples, which is shown in Fig. 6.13. We find that in both cases the predicted 50% completeness contours fits the true distribution of clusters reasonably well. The apparent lack of low-mass clusters at low redshift seen in the SPT-SZ sample can be understood as the impact of the additional filtering that is applied during the data reduction and is required to mitigate Earth's atmosphere. This additional filtering effectively removes large-scale signals like the one from nearby clusters from the maps. A few massive clusters are detected at low redshifts most likely because their bright compact cores are detected even after filtering.

Following the steps laid out in Section 6.3.4 *Planck* is expected to find 1328 clusters, assuming a sky coverage of 87% that has been adopted from Planck Collaboration (2016h). This number is in good

agreement with the 1203 confirmed galaxy clusters detected by *Planck*, 1096 of which have known redshifts and are listed in the *Planck* PSZ2 union catalogue (R2.08, Planck Collaboration, 2016h). A comparison of the PSZ2 clusters with a *Planck*-like mock cluster sample, shown in the upper panel of Fig. 6.14 and Fig. C.4, reveals that the number of predicted clusters with $z > 0.6$ exceeds those seen in the actual catalogue by a factor of two and our forecasts indicate that *Planck* is expected to be capable of finding $\sim 4$ clusters at $z > 1.0$. Such systems might be included in the remaining unconfirmed 450 cluster candidates reported in the PSZ2. Optical confirmation and redshift estimation of high redshift *Planck* clusters is challenging and was only possible for systems that were observed by the SDSS and are listed in the redMaPPer catalogue (Rykoff et al., 2014b; Planck Collaboration, 2016h). Recently, several *Planck* cluster candidates were confirmed to be high-redshift objects as part of the combined Planck-RASS catalogue of X-ray-SZ clusters (ComPRASS, Tarrío et al., 2019), with the highest reported redshift being 1.2.

We find that the SPT-SZ survey should find $\sim 651$ galaxy clusters within $2500\,\mathrm{deg}^2$ of the sky, which exceed the 516 confirmed clusters presented by Bleem et al. (2015) but are slightly fewer than the 677 reported candidates. The original mass estimates provided by Bleem et al. (2015) for the confirmed SPT-SZ clusters were obtained through the best-fit $Y$-$M$-scaling relation that was optimised by fitting the SPT-SZ number cluster counts to match an assumed, fixed cosmology and could thus not be used for cosmological studies. In recent years, extensive follow-up observations using X-ray and optical facilities have allowed to accurately determine the masses of the SPT-SZ clusters and we use the most recent (marginalized) weak-lensing calibrated estimates presented by Bocquet et al. (2019). We find the median median cluster mass of the SPT-SZ clusters to be $3.57 \times 10^{14}\,\mathrm{M}_\odot\,\mathrm{h}_{70}^{-1}$, which is $\sim 24\%$ higher than our predicted value of $2.88 \times 10^{14}\,\mathrm{M}_\odot\,\mathrm{h}_{70}^{-1}$, while the median redshifts of the real and mock sample are in good agreement with values of 0.55 and 0.53, respectively. In addition, Bocquet et al. (2019) finds a higher limiting mass and significantly higher number of 7 massive clusters with ($M_{500} > 10^{15}\,\mathrm{M}_\odot$) than is predicted by the *Planck* 2018 cosmology that is used in this work, for which we find ~two such systems within $2500\,\mathrm{deg}^2$. The mismatch in predicted and observed cluster masses is seen clearly in the comparison of a mock sample and the SPT-SZ clusters shown in the lower panel of Fig. 6.14 and in Fig. C.5. The same trend is also seen when comparing to the cluster masses originally reported by Bleem et al. (2015). Systematic differences in the masses determined by *Planck* and SPT-SZ have been previously reported by the Planck Collaboration (2016h) and are most likely due to the different mass calibration strategies of the two experiments and the differences in angular resolution of the instruments, which make the SPT sensitive to the bright central regions of clusters, while *Planck* is sensitive to their outskirts.

It is also worth noting that the forecasts presented in this work demonstrate that *Planck* would be able to detect a cluster with $M_{500} \geqslant 10^{15}\,\mathrm{M}_\odot$ at $z \geqslant 4$ with an SNR of $\gtrsim 30$. With its all-sky coverage *Planck* therefore provides strong evidence against the existence of massive clusters at high redshift and for the hierarchical model of structure formation. The SPT-SZ survey provides even more powerful constraints, delivering roughly three times the SNR that *Planck* provides for a cluster of given mass and redshift. However, SPT-SZ only surveyed $\sim 6\%$ of the sky.

### 6.4.2 Forecasts for CCAT-prime

Since the inception of the project in 2016, several variants of CCAT-prime's first-light instrument Prime-Cam were proposed, from an initial seven module design with seven channels ranging from 95 to 862 GHz that would perform a standalone survey, over a submillimetre-exclusive five channel version

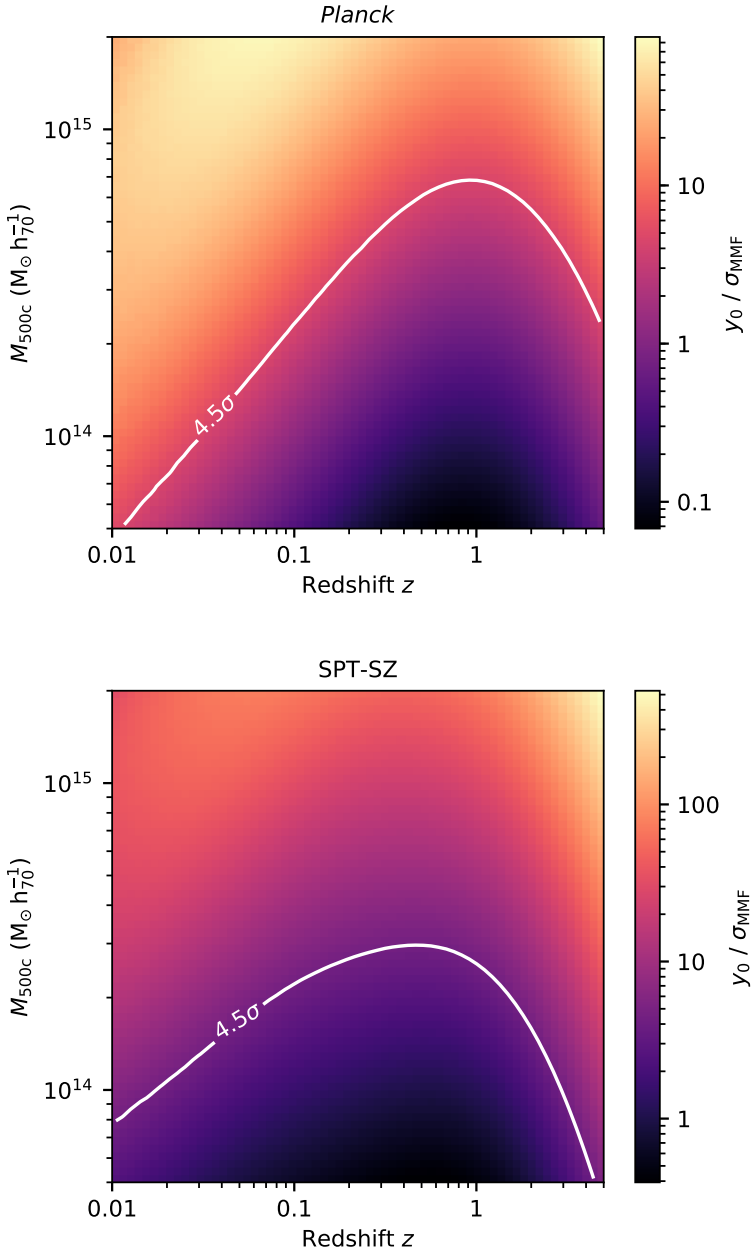


Figure 6.12: **Top panel:** Expected SNR of galaxy clusters in the *Planck* survey computed from simulated *Planck* HFI data using an MMF technique. **Bottom panel:** Expected SNR of galaxy clusters in the SPT-SZ survey computed from simulated SPT data at 95, 150, and 220 GHz using an MMF technique.

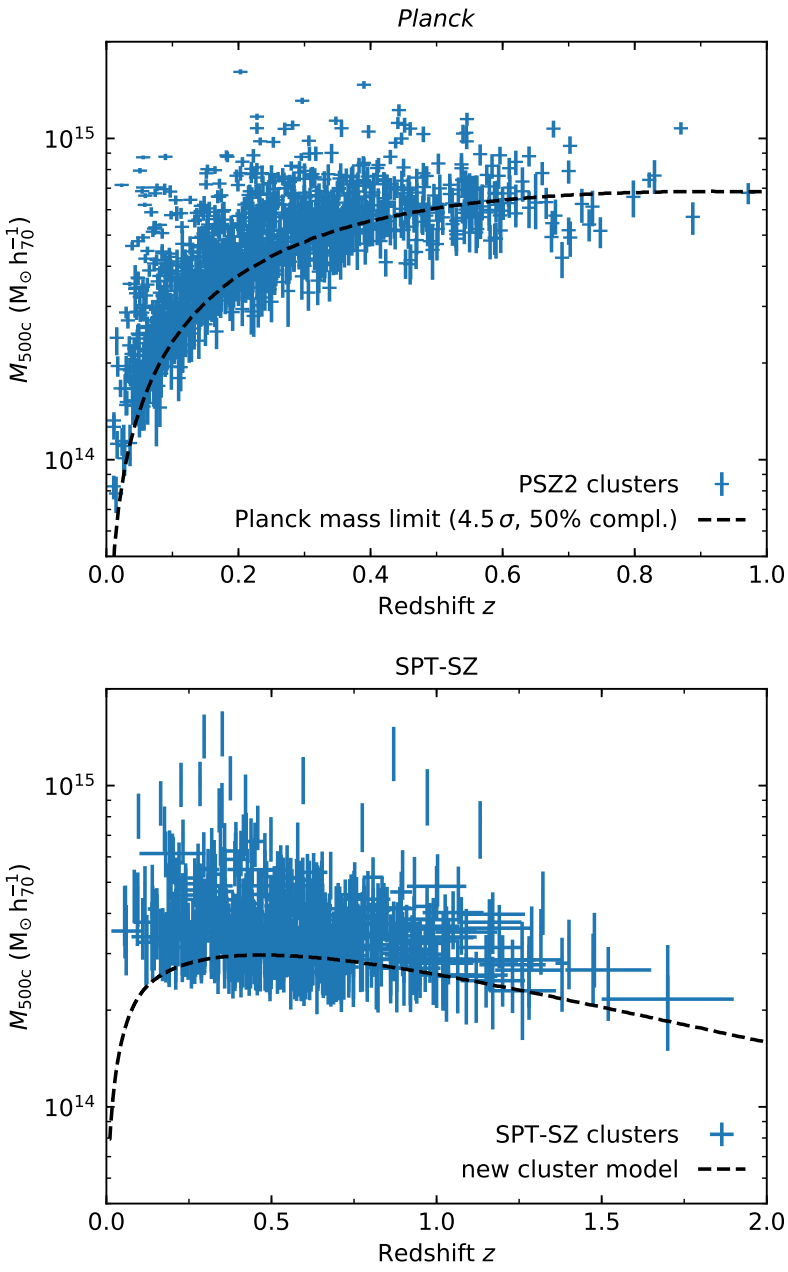


Figure 6.13: *Planck* PSZ2 ($n$ = 1094) and SPT-SZ ($n$ = 516) samples of confirmed galaxy clusters (blue data points). The predicted 50% completeness contour for an SNR threshold of 4.5 that has been derived from Fig. 6.12 is shown by the black dashed line. The predicted mass limits are in good agreement with the two cluster samples. **Top panel:** *Planck* PSZ2. **Bottom panel:** SPT-SZ.

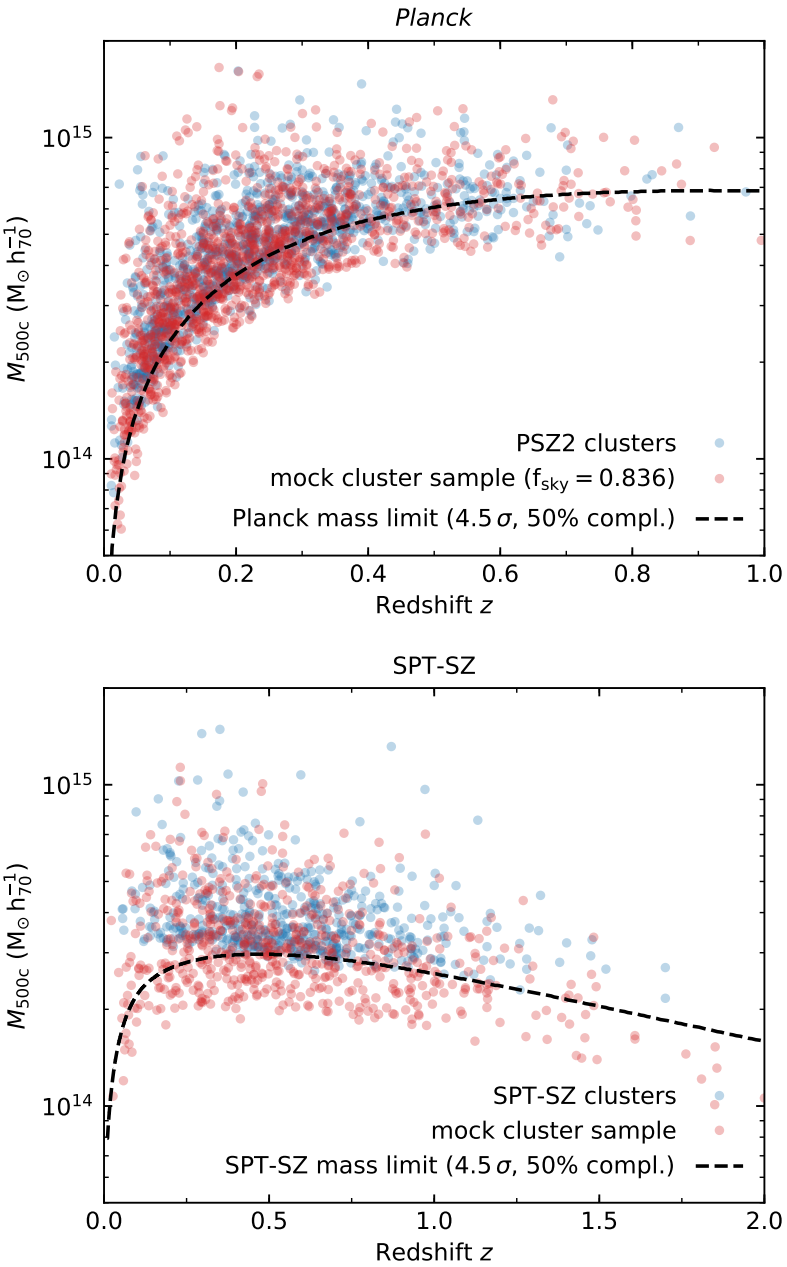


Figure 6.14: *Planck* PSZ2 ($n = 1094$) and SPT-SZ ($n = 516$) samples of confirmed galaxy clusters (blue data points) with overplotted mock cluster samples (red data points) randomly drawn using the Monte-Carlo technique described in Section 6.3.5. Using the predicted SNR of clusters in the two surveys shown in Fig. 6.12, we find that *Planck* is expected to find 1328 clusters, while we expect 651 detections for SPT-SZ. Except for the excess in high redshift objects, which are hard to follow-up in practice, the mock *Planck* sample is in excellent agreement with the real data, while the real SPT-SZ sample contains more higher-mass clusters than expected. **Top panel:** *Planck* PSZ2. **Bottom panel:** SPT-SZ.

that would augment the $10^4$ deg$^2$ AdvACT survey with frequency coverage from 220 to 862 GHz, to the most recently considered budget-limited three module design with one to three channels. The forecasts presented here have followed the evolution of the instrument and were part of the science case presented in several fundraising proposals that have been submitted in this time period.

#### Galaxy cluster sample size

We start our SZ forecasts for CCAT-prime with predictions of the expected galaxy cluster sample size that can be obtained via observations of the tSZ signal of clusters using CCAT-prime's first light instrument Prime-Cam, together with auxilliary data from AdvACT. Initially, CCAT-prime was considered to perform an independent survey of $10^3$ deg$^2$ of the sky using a fully equipped seven-channel version of Prime-Cam. Using the frequencies, expected sensitivities, and beam FWHMs provided in Table 4.3 we expect this deep survey to be able to detect 2304 clusters. The sample has a median redshift of 0.62 and a median mass of $1.5 \times 10^{14}\,\mathrm{M}_\odot$, while 68% of the sample are contained within the marginalized interval $z \in [0.15, 0.92]$ and $M_{500} \in [0.9 \times 10^{14}\,\mathrm{M}_\odot, 1.9 \times 10^{14}\,\mathrm{M}_\odot]$. These results, together with the remaining ones presented in this section, are summarised in Table 6.3, while Fig. 6.15 shows the completeness contours of all surveys considered here.

The plans for a seven-channel first light instrument with millimetre and submillimetre coverage have since been abandoned due to budget constraints and the fact that wide-area millimetre surveys of excellent depth will be performed by facilities like AdvACT and the SO. Currently, CCAT-prime is expected to focus on observations in the submillimetre, performing follow-up observations of the same $10^4$ deg$^2$ that is going to be surveyed by AdvACT. Combining the 90 and 150 GHz channels of AdvACT with a five-channel submillimetre version of Prime-Cam with frequencies from 220 to 857 GHz to restore the originally envisioned frequency coverage of the seven channel instrument would allow to obtain 10121 clusters. The majority of clusters in this sample is expected at slightly lower redshift and higher mass as before with $z \in [0.13, 0.82]$ and $M_{500} \in [1.2 \times 10^{14}\,\mathrm{M}_\odot, 2.5 \times 10^{14}\,\mathrm{M}_\odot]$. The expected results of this combined survey were already presented in Section 6.3 to illustrate each step of the forecast pipeline that is used in this work. It is worth mentioning that the number of clusters expected from this survey is greater than the one expected for a $10^4$ deg$^2$ survey using the seven-channel version of Prime-Cam used earlier, which is expected to find 6464 clusters. The reason for this are the deeper AdvACT millimetre channels that drive the detection of the tSZ signal of clusters.

The most recent proposals called for a further reduced three module version of Prime-Cam with varying frequency coverage. A total of four different layouts were investigated, the specifications of which are given in Table 6.2. We refer to these different layouts as v1, v2, v3, and v4. In all cases, we combine the simulated survey data from these surveys with simulated data from AdvACT at 90, 150, and 230 GHz and assume a survey area of $10^4$ deg$^2$. We find that the three channel v1 survey would yield the largest sample size with 6667 clusters, while the v2, v3, and v4 survey are expected to find slightly fewer clusters, with sample sizes of 5706, 5824, and 5514 clusters, respectively. The redshift and mass distributions of the four different versions are found to be virtually identical. Although shallower, the v1 survey is able to outperform the alternative versions due to featuring a 270 GHz channel close to the tSZ null that proved to be an advantage for cluster detection.

For reference, we also compute the expected sample size for AdvACT alone to understand how many additional clusters the CCAT-prime data is yielding. The baseline is provided by a three channel survey using 90, 150, and 230 GHz for which we expect 5042 clusters. Using all five available channels from

| Experiment | Area ($\mathrm{deg}^2$) | Freq. range (GHz) | $n_{\mathrm{freq.}}$ | $n_{\mathrm{clusters}}$ | $z$ | $M_{500}$ ($10^{14}\,\mathrm{M}_\odot$) |
|---|---|---|---|---|---|---|
| AdvACT | $10^4$ | $[28, 230]$ | 5 | 6185 (58000) | $[0.10, 0.76]$ | $[1.4, 2.9]$ |
| AdvACT | $10^4$ | $[90, 230]$ | 3 | 5042 (57788) | $[0.13, 0.80]$ | $[1.5, 3.1]$ |
| CCAT-p | 200 | $[95, 862]$ | 7 | 1096 (3589) | $[0.21, 1.08]$ | $[0.6, 1.4]$ |
| CCAT-p | $10^3$ | $[95, 862]$ | 7 | 2304 (11491) | $[0.15, 0.92]$ | $[0.9, 1.9]$ |
| CCAT-p | $10^4$ | $[95, 862]$ | 7 | 6464 (21218) | $[0.11, 0.72]$ | $[1.4, 2.9]$ |
| CCAT-p + AdvACT | $10^4$ | $[90, 862]$ | 7 | 10121 (59853) | $[0.13, 0.82]$ | $[1.2, 2.5]$ |
| CCAT-p v1 + AdvACT | $10^4$ | $[90, 405]$ | 6 | 6667 (57400) | $[0.13, 0.81]$ | $[1.4, 2.8]$ |
| CCAT-p v2 + AdvACT | $10^4$ | $[90, 405]$ | 5 | 5706 (56932) | $[0.13, 0.81]$ | $[1.4, 3.0]$ |
| CCAT-p v3 + AdvACT | $10^4$ | $[90, 350]$ | 4 | 5824 (57146) | $[0.13, 0.81]$ | $[1.4, 2.9]$ |
| CCAT-p v4 + AdvACT | $10^4$ | $[90, 405]$ | 5 | 5514 (56716) | $[0.12, 0.80]$ | $[1.5, 3.0]$ |
| *Planck* HFI | 35k | $[100, 857]$ | 6 | 1328 (3084) | $[0.02, 0.28]$ | $[1.9, 5.9]$ |
| SPT-SZ | 2.5k | $[95, 220]$ | 3 | 651 (2252) | $[0.14, 0.78]$ | $[1.8, 3.6]$ |

Table 6.3: Expected number of galaxy clusters and most compact (linear) 68% redshift and mass interval in the range $z \in [0.01, 5]$ and $M_{500} \in [5 \times 10^{13}\,\mathrm{M}_\odot, 2 \times 10^{15}\,\mathrm{M}_\odot]$ for the various surveys that are considered in this work. These numbers were obtained using the formalism presented in Section 6.3.4, assuming the most recent *Planck* 2018 ΛCDM parameter values. The corresponding individual expected cluster samples are shown in Fig. 6.7 and Fig. C.4–C.14. The sample sizes given in round brackets are obtained by dropping all contaminating astrophysical emission from the simulations and thus injecting mock clusters into white-noise-only maps.

28 to 230 GHz leads to a larger sample of 6185 clusters. The predicted redshift and mass distributions of the cluster samples are very similar to the ones obtained for the combined AdvACT + CCAT-prime surveys if an initial three-instrument-module version of Prime-Cam is assumed.

This illustrates that, when focusing on galaxy cluster sample size, CCAT-prime has the potential to double the yield of AdvACT if the five channel version of the survey is considered. Looking at the more recent one to three channel versions, the gain in sample size over an AdvACT only survey is much lower with only a few hundred objects. However the detection of galaxy clusters will always be driven by millimetre observations due to the unique decrement signal of the tSZ effect and the high sensitivities that can be achieved at millimetre wavelengths. The unique aspects of the submillimetre channels provided by CCAT-prime lie in the improved spectral constraints which will be discussed in the next section.

### 6.4.3 SZ spectral constraints

#### Reproduction and update of the CCAT-prime forecasts by Erler et al. (2018)

In addition to the expected galaxy cluster sample size for multiple versions of a CCAT-prime cluster survey, we also investigate the SZ-parameter constraints we can expect to achieve. This is done by simulating and modelling mock galaxy cluster spectra following the steps that were presented in Section 6.3.6.

We start our investigation by reproducing the CCAT-prime spectral forecasts that were presented by Erler et al. (2018). We generate the mock spectrum of a cluster with identical properties, i.e.

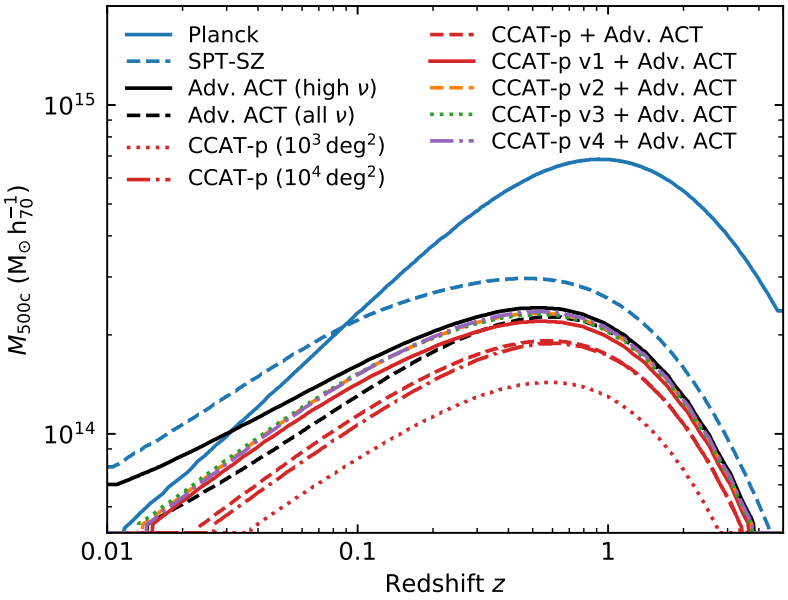


Figure 6.15: Predicted 50% completeness contours for an SNR threshold of 4.5 computed for the various surveys compared in this work. The characteristics of each survey are provided in Table 4.3 and 6.2.

$M_{500} = 10^{15}\,\mathrm{M}_\odot$, $z = 0.23$, $v_{\mathrm{pec}} = 0\,\mathrm{km/s}$ and an FIR component modelled by a modified blackbody that follows the density profile of the ICM with a dust mass of $5 \times 10^{10}\,\mathrm{M}_\odot$, $T_{\mathrm{Dust}} = 20\,\mathrm{K}$, and $\beta = 1.5$. Like Erler et al. (2018) we neglect other astrophysical signals besides the ones from the cluster itself and only add instrumental white noise according to the expected survey sensitivities provided in Table 4.3 to the maps. Extracting the cluster SED by computing the average signal within a circular aperture of radius $\theta_{500}$ and modelling the obtained spectrum leaves us with the parameter constraints shown in Fig C.16 that are consistent with the ones found by Erler et al. (2018), demonstrating agreement between the updated python-implemented pipeline used in this work and the IDL-implemented pipline used by Erler et al. (2018).

An immediate improvement over these forecasts can be achieved by extracting the simulated SED of the cluster from the mock data by using single-frequency MFs instead of computing an aperture average. Single-frequency MFs were used by Erler et al. (2018) for extracting the SED of real clusters from *Planck*, *AKARI* and IRAS all-sky maps, but were not used for the CCAT-prime forecasts because the authors did not have access to an implementation of the MFs in the flat-sky approximation that is used to process small patches of the sky. When using MFs, the extracted cluster SED has a higher SNR at each frequency, improving the parameter constraints by up to a factor of ~two compared to using the aperture average SED. The results are shown in Fig. C.17. This improvement is due to the optimal nature of the MFs and we will thus only use MFs to extract SEDs from mock data for producing the remaining results.

The forecasts presented by Erler et al. (2018) and their reproduction presented here paint a very optimistic picture of the spectral constraints that can be expected for CCAT-p. A major shortcoming of these forecasts is the lack of other astropysical emission like the CMB, CIB, Galactic foregrounds and point sources. Using the sky model that was introduced in Section 6.3.1 we re-run the previous

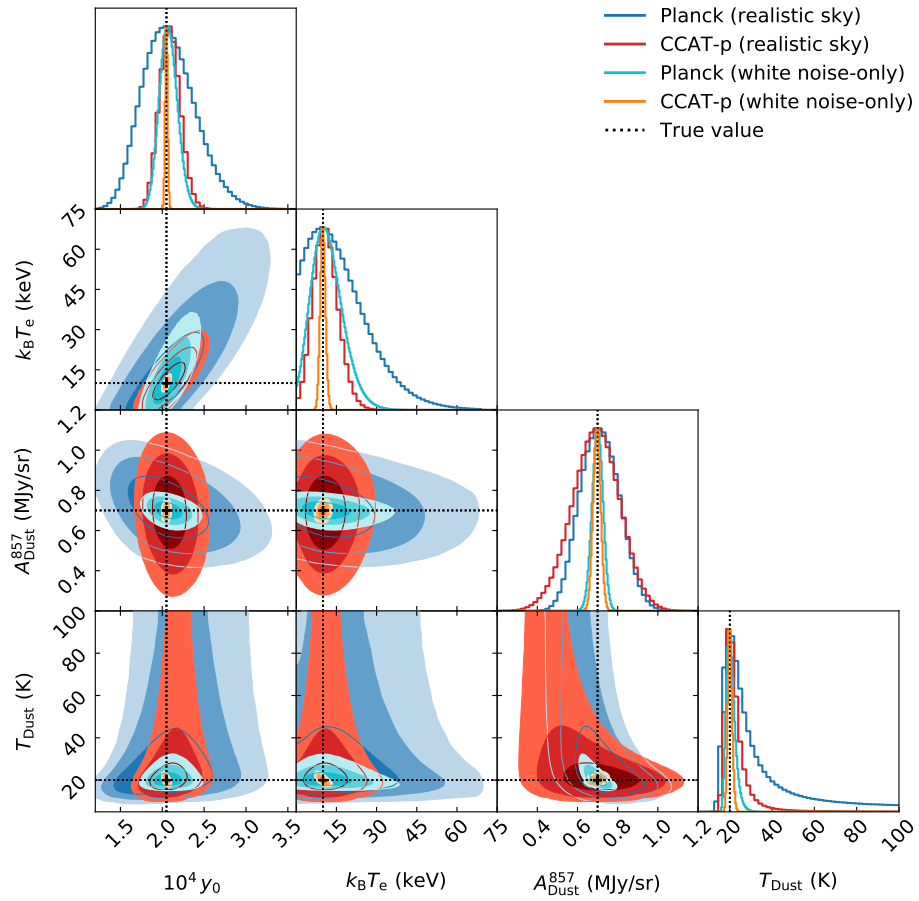


| Instrument | Area ($deg^2$) | Freq. range (GHz) | $10^4\, y_0$ | $k_B T_e$ (keV) | $A^{857}_{Dust}$ (MJy/sr) | $T_{Dust}$ (K) |
|---|---|---|---|---|---|---|
| **realistic sky** | | | | | | |
| *Planck* HFI | 35k | [100, 857] | $2.05^{+0.30}_{-0.32}$ | $10.00^{+12.17}_{-11.00}$ | $0.70^{+0.11}_{-0.09}$ | $20.37^{+13.53}_{-5.24}$ |
| CCAT-p | $10^3$ | [95, 862] | $2.08^{+0.12}_{-0.12}$ | $10.00^{+5.19}_{-3.96}$ | $0.70^{+0.12}_{-0.12}$ | $19.90^{+4.18}_{-2.73}$ |
| **white noise-only** | | | | | | |
| *Planck* HFI | 35k | [100, 857] | $2.07^{+0.11}_{-0.10}$ | $10.00^{+6.39}_{-5.06}$ | $0.70^{+0.03}_{-0.03}$ | $20.00^{+2.01}_{-1.87}$ |
| CCAT-p | $10^3$ | [95, 862] | $2.05^{+0.02}_{-0.01}$ | $9.87^{+1.01}_{-0.90}$ | $0.70^{+0.02}_{-0.02}$ | $20.02^{+1.02}_{-0.97}$ |

Figure 6.16: Comparison of spectral modelling forecasts for CCAT-prime (red, orange) and *Planck* HFI (blue, turquoise) using the realistic sky model presented in Section 6.3.1 (blue, red) and white noise-only data (orange, turquoise). The white noise-only forecasts are shown in detail in Fig. C.17. The results shown here were obtained assuming a single galaxy cluster with $M_{500} = 10^{15}\,M_\odot$ at $z = 0.23$, a dust mass of $5 \times 10^{10}\,M_\odot$, a dust temperature of 20 K, and no l.o.s. peculiar velocity component (i.e. no kSZ signal), identical to the forecasts that have been presented in Erler et al. (2018). We find that the white noise-only forecasts lead to an underestimation of the expected parameter uncertainties of up to a factor of six.

forecasts, leaving the properties of the simulated cluster, as well as the model parameters, unchanged. The obtained parameter constraints from simulated *Planck* HFI data and a simulated CCAT-prime $10^3$ deg$^2$ survey are shown in Fig. 6.16 and compared with the previously presented MF-based white noise-only forecasts that are shown in Fig C.17. We find that simulating mock data using a realistic sky lowers the obtained parameter constraints by up to a factor of six. While the white noise-only forecasts suggested that CCAT-prime should be able to measure the ICM temperature of the simulated cluster at $11\sigma$ significance, the realistic forecasts show that this has been an (expected) overestimation and point towards a significance of $\gtrsim 2\sigma$. Through this comparison, we find that the simulated CCAT-prime survey roughly matches the constraining power of the simulated white noise-only *Planck* HFI data, with the exception of the dust amplitude $A^{857}_{\mathrm{Dust}}$ for which *Planck* provides much tighter constraints. All remaining results in this section were therefore obtained using the realistic sky model from Section 6.3.1.

#### SZ-only forecasts using a realistic sky model

So far, the forecasts presented here have neglected the possibility of a non-zero l.o.s. component of the cluster peculiar velocity and focused on the reproduction and improvement of the constraints on the tSZ and FIR parameters studied by Erler et al. (2018). The study of individual systems will however require to include a kSZ component to the spectral model and the peculiar velocity of clusters is a powerful probe for cosmology. We therefore derive the expected constraints on the three SZ parameters $y_0$, $T_\mathrm{e}$ and $v_\mathrm{pec}$ for a range of different surveys, namely *Planck* HFI, an AdvACT survey covering $10^4$ deg$^2$, a combined CCAT-prime + AdvACT survey covering $10^4$ deg$^2$, and a deeper CCAT-prime survey covering $10^3$ deg$^2$ that extends to millimeter frequencies. Even though we directly draw randomly sampled values for the ICM optical depth $\tau_\mathrm{e}$, its computed posterior distribution is highly degenerate with the value of $T_\mathrm{e}$ and we therefore show the posterior distribution of $y_0$, which is computed from $\tau_\mathrm{e}$ and $T_\mathrm{e}$. We use the same cluster mass and redshift as before and assume a peculiar velocity of 1000 km/s. In order to explore the constraining power on the SZ parameters under the best possible circumstances, we neglect possible FIR contamination for the moment, the effect of which will be discussed in the next section.

The obtained constraints on the SZ parameters are shown in Fig. 6.17. We find that fitting for an additional kSZ component increases the marginalized uncertainties of $y_0$ and $T_\mathrm{e}$ by up to 100% and 50%, respectively, depending on the survey. The corresponding tSZ-only results are presented in Fig. C.18. As previously expected, *Planck* HFI delivers the largest uncertainties, especially on the peculiar velocity. AdvACT improves on *Planck*, even with a lack of high-frequency channels, and is expected to measure the peculiar velocity of massive, fast-moving clusters, like the one simulated, at $\gtrsim 2\sigma$ significance. Combining data from both AdvACT and CCAT-prime allows for tighter constaints, but the gains are relatively small ($\lesssim 30\%$) due to the decreasing sensitivity of ground based instruments at high frequencies. The $10^3$ deg$^2$ CCAT-prime survey is expected to deliver the best constraints and measure the peculiar velocity at $\sim 3$ significance, while the ICM temperature is measured at less than $2\sigma$.

The cluster that has been investigated so far is exceptionally massive and only $\sim 30$ objects with $M_{500} \geqslant 10^{15}\,\mathrm{M}_\odot$ are expected in the entire sky according to the best-fit ΛCMB cosmology presented by the Planck Collaboration (2018b). In order to investigate the number of clusters for which the ICM temperature and peculiar velocity can be directly measured, we simulate and model galaxy cluster SEDs using values for the cluster mass and redshift taken from a $32 \times 32$ logarithmically spaced

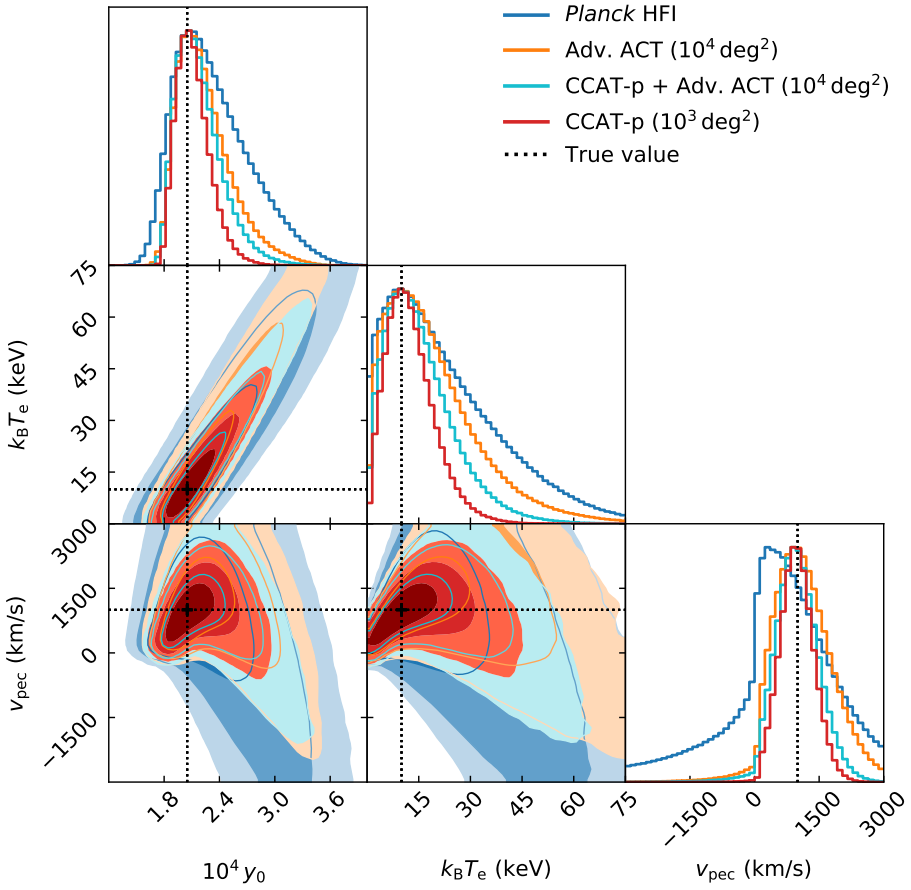


| Instrument | Area (deg$^2$) | Freq. range (GHz) | $10^4\, y_0$ | $k_B T_e$ (keV) | $v_{pec}$ (km/s) |
|---|---|---|---|---|---|
| *Planck* HFI | 35k | [100, 857] | $2.09^{+0.50}_{-0.27}$ | $9.94^{+17.82}_{-9.70}$ | $300^{+1671}_{-368}$ |
| AdvACT | $10^4$ | [28, 230] | $2.05^{+0.34}_{-0.17}$ | $8.71^{+15.12}_{-6.75}$ | $900^{+737}_{-549}$ |
| CCAT-p + AdvACT | $10^4$ | [95, 862] | $2.07^{+0.25}_{-0.19}$ | $10.02^{+10.24}_{-7.24}$ | $900^{+549}_{-431}$ |
| CCAT-p | $10^3$ | [95, 862] | $2.06^{+0.18}_{-0.16}$ | $10.20^{+6.96}_{-6.05}$ | $941^{+419}_{-354}$ |

Figure 6.17: Spectral modelling forecasts for *Planck* HFI (blue), a $10^4$ deg$^2$ AdvACT survey (orange), a $10^4$ deg$^2$ CCAT-prime + AdvACT survey (turquoise), and a $10^3$ deg$^2$ CCAT-prime survey using the realistic sky model presented in Section 6.3.1. The results shown here were obtained from simulated tSZ + kSZ data for a single galaxy cluster with $M_{500} = 10^{15}$ M$_\odot$ at $z = 0.23$ with a l.o.s. peculiar velocity of 1000 km/s. A comparison with the tSZ-only forecasts presented in Fig. C.18 reveals that the addition of a kSZ component to the cluster spectrum lowers the constraining power on both $y$ and $T_e$ by approximately 50% for all four surveys. While none of the surveys is expected to provide a $> 2\sigma$ measurement on the ICM temperature, both versions of a CCAT-prime survey investigated here would be able to constrain the peculiar velocity to be non-zero at $> 2\sigma$.

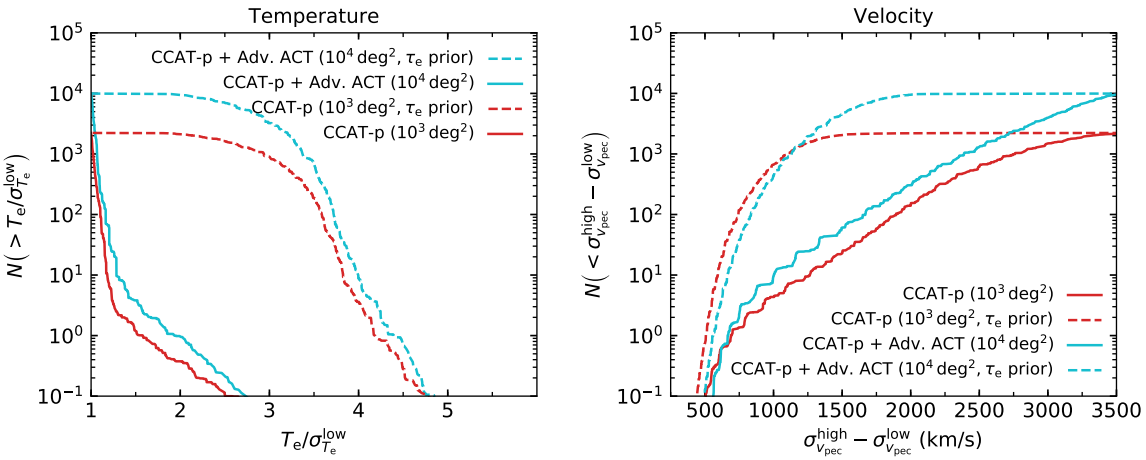


Figure 6.18: Expected cumulative number of clusters as a function of parameter constraints for a $10^4$ deg$^2$ CCAT-prime + AdvACT survey (turquoise), and a $10^3$ deg$^2$ CCAT-prime survey (red). The solid lines indicate the number of clusters that are expected via SZ-only observations, while the dashed lines indicates the number of clusters that are expected in case a 25% Gaussian prior on the ICM optical depth $\tau_e$ can be derived for all clusters and applied in the SZ spectral modelling. The curves were derived by simulating and modelling galaxy cluster spectra on a $32 \times 32$ bin logarithmically spaced grid using the cluster model introduced in Section 6.3.2 and using the realistic sky model presented in Section 6.3.1. Potential cluster FIR emission was neglected for these calculations. **Left-hand panel:** Expected cumulative number of clusters as a function of the significance of the measurement of $T_e$, defined as the value of $T_e$ divided by its lower errorbar. Without additional priors, CCAT-prime is expected to measure the temperature of a few massive clusters at $\gtrsim 2\sigma$. An additional $\tau_e$ prior allows to measure $T_e$ at $\gtrsim 3\sigma$ for more than half of the expected cluster sample. **Right-hand panel:** Expected cumulative number of clusters as a function of the width of the 68% confidence interval of the observed posterior distribution for the l.o.s. component of the peculiar velocity. The simulated clusters are assumed to have a velocity of 0 km/s. With SZ data alone, CCAT-prime will be able to constrain the velocity of a few fast moving and massive clusters, while the addition of a $\tau_e$ prior would increase the number of clusters to several hundred.

grid. All clusters are assumed have a peculiar velocity of 0 km/s. This choice was motivated by the difference in the shape of the posterior distributions of $v_{pec}$ that is observed for different values. This issue is highlighted in Fig. C.19. Our focus lies on the expected constraints on the ICM temperature, which we quantify via the significance of the measurement defined as the value of $T_e$ divided by its lower errorbar, and the peculiar velocity for which we report the width of the 68% confidence interval of the derived posterior distributions. Since the previously presented results already indicate that direct SZ-only measurements of the two parameters will be challenging even for massive clusters, we explore the possibility of a $\tau_e$ prior that could be provided by X-ray surveys like the one that will be performed by eROSITA. The applied prior is a Gaussian centred on the true value of $\tau_e$ with $\sigma = 0.25\,\tau_e$. The limiting masses and redshifts for significant measurements of $T_e$ and $v_{pec}$ are shown in Fig. C.20 and C.21. Fig. 6.18 shows the cumulative number of clusters as a function of the significance of the $T_e$ measurement (left-hand panel) and as a function of the width of the 68% confidence interval of the $v_{pec}$ posterior distributions (right-hand panel).

We find that both a $10^4$ deg$^2$ CCAT-prime + AdvACT survey and a $10^3$ deg$^2$ CCAT-prime can not be expected to measure the ICM temperature of clusters at $\gtrsim 3\sigma$ significance since objects with a sufficiently high mass are not expected for the ΛCDM cosmology used in this work. Both variants of

the survey should however measure the temperature of a few clusters at $\gtrsim 2\sigma$ significance, with a roughly two times higher number expected for the $10^4$ deg$^2$ survey due to the larger cosmic volume that is probed. The constraining power of CCAT-prime on the ICM temperature could however be vastly improved if a 25% $\tau_e$ prior is applied during the spectral modelling. We find that for both versions of the survey such a prior would allow for a $\gtrsim 3\sigma$ measurement of $T_e$ for roughly half of the expected cluster samples. Measurements at $\gtrsim 5\sigma$ significance would require a more informative $\tau_e$ prior, which might be derivable for low-redshift systems.

The situation is similar for measurements of the peculiar velocity of galaxy clusters with the added complication that the projected component of $v_{pec}$ is expected to be random, i.e. the few massive systems that could allow for a significant measurement of $v_{pec}$ are not guaranteed to have large absolute projected speeds. Both versions of a CCAT-prime survey investigated here are able to constrain the velocity $\sim 10$ clusters within $\pm 500$ km/s, assuming symmetric posterior distributions. Introducing a 25% $\tau_e$ prior increases this number to $\sim 1000$ clusters for both surveys.

#### Potential FIR-induced bias on SZ parameters

Although not conclusively proven, evidence has accumulated in recent years that suggests future low-noise submillimetre observations of galaxy clusters to be affected by cluster FIR emission (e.g. Planck Collaboration, 2016i,e; Erler et al., 2018; Hurier, 2016; Melin et al., 2018b). An FIR component was already added and modelled to the simulated cluster spectra presented in Section 6.4.3, but due to their high-frequency coverage, the simulated *Planck* HFI and CCAT-prime surveys were able to obtain unbiased estimates of the SZ-parameters, as well as constraints on the properties of the FIR component. Future ground based surveys that lack submillimetre coverage however might not find clear evidence for the presence of an FIR component and consequently neglect it in their spectral modelling, which can lead to biased estimates of the SZ parameters. We demonstrate this by comparing the SZ parameter estimates obtained through simulated AdvACT-only and CCAT-prime + AdvACT data obtained from the simulated spectrum of a cluster with $M_{500} = 10^{15}$ M$_\odot$, $z = 0.23$, $v_{pec} = 1000$ km/s, and an FIR component modelled by the same modified blackbody as previously with a dust mass of $5 \times 10^{10}$ M$_\odot$, $T_{Dust} = 20$ K, and $\beta = 1.5$ that traces the density profile of the ICM.

If an FIR component is excluded from the spectral model, we find that the obtained parameter estimates are biased. This bias is particularly significant for the peculiar velocity. Adding submillimetre data obtained by CCAT-prime would provide clear evidence of FIR contamination through a comparison of the weak SZ signal at 862 GHz to the FIR dominated observed flux at that frequency. At the same time, CCAT-prime provides the frequency coverage and sensitivity necessary to constrain additional FIR model parameters. Modelling the extracted CCAT-prime + AdvACT spectrum with the sum of an SZ and an FIR component provides unbiased estimates of all parameters. The results are presented in Fig. 6.19. If the same spectral model is used to fit a mock AdvACT-only spectrum, we find the data to be insufficient to provide meaningful constraints on the peculiar velocity and the parameters of the FIR model. The corresponding results are displayed in Fig. C.22.

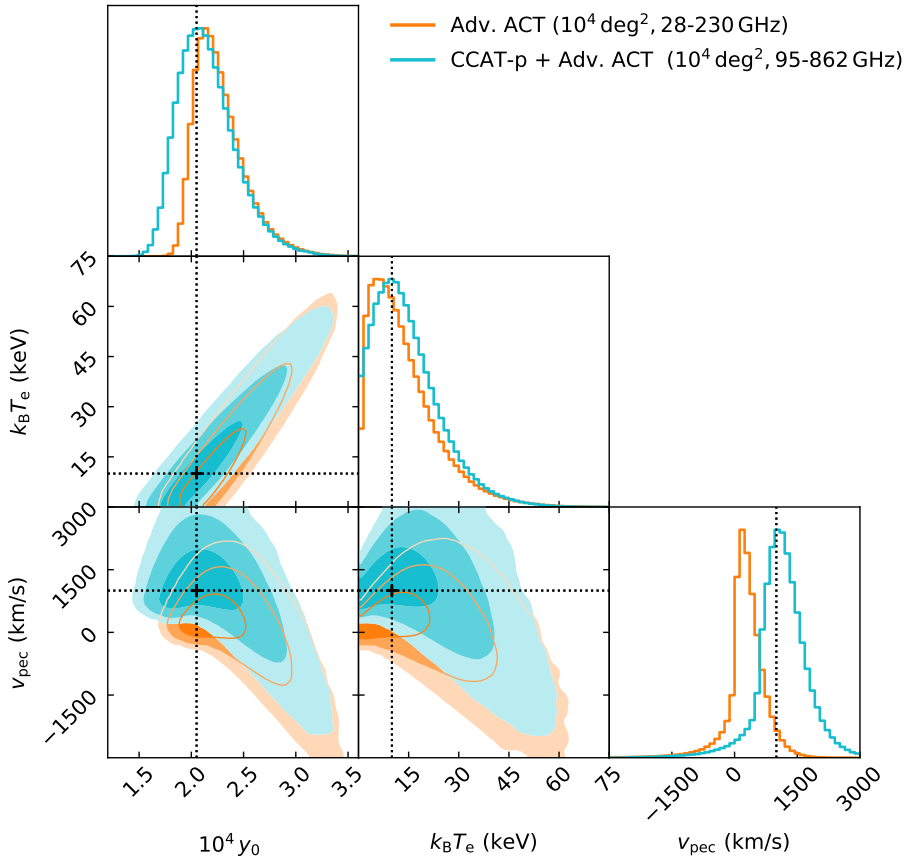


| Instrument | Area ($\mathrm{deg}^2$) | Freq. range (GHz) | $10^4\, y_0$ | $k_\mathrm{B} T_\mathrm{e}$ (keV) | $v_\mathrm{pec}$ (km/s) |
|---|---|---|---|---|---|
| AdvACT | $10^4$ | [28, 230] | $2.15^{+0.26}_{-0.16}$ | $5.85^{+11.22}_{-4.40}$ | $161^{+481}_{-165}$ |
| CCAT-p + AdvACT | $10^4$ | [95, 862] | $2.06^{+0.29}_{-0.23}$ | $9.08^{+10.53}_{-7.85}$ | $1000^{+601}_{-360}$ |

Figure 6.19: Example of biased SZ parameter estimates as a consequence of a neglected cluster-FIR component. We simulate and model the spectrum of a single galaxy cluster with $M_{500} = 10^{15}\,\mathrm{M}_\odot$ at $z = 0.23$, a dust mass of $5 \times 10^{10}\,\mathrm{M}_\odot$, a dust temperature of 20 K, and a l.o.s. peculiar velocity of 1000 km/s and compare the constraints on the model parameters that are expected for a $10^4$ deg$^2$ AdvACT survey (orange) and a $10^4$ deg$^2$ CCAT-prime + AdvACT survey (turquoise). Due to the lack of channels above 230 GHz, the presence of an FIR component is difficult to infer from AdvACT data and we therefore assume that no FIR component is used to model the mock spectrum. As a consequence, we observe the estimated values of all three SZ parameters to be biased. This dust-induced bias is most severe for the peculiar velocity, which is lower than the input value at $1.7\sigma$ significance. If an FIR component is added to the spectral model the constraining power of AdvACT data is strongly reduced, as demonstrated in Fig. C.22. With its submillimetre coverage up to 862 GHz, CCAT-prime will be able to infer the presence of FIR emission in clusters due to the weak expected SZ signal at high frequency and provide unbiased estimates of all SZ parameters.

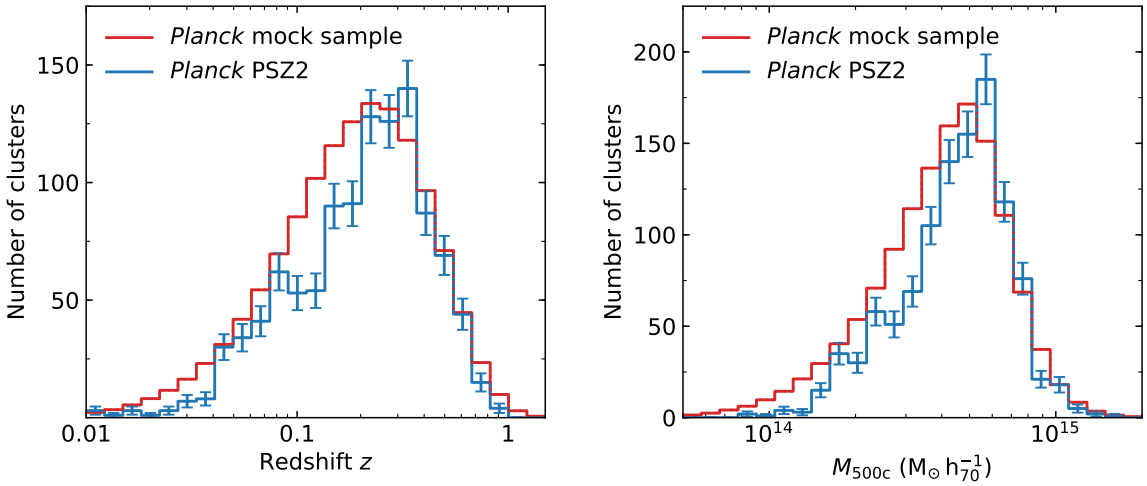


Figure 6.20: Redshift and mass distributions of the *Planck* PSZ2 galaxy clusters (blue lines) and a simulated *Planck* HFI galaxy cluster sample (red lines). The predicted distributions have been obtained from a large mock sample with $10^6$ clusters, generated following the steps laid out in Section 6.3.5, and were re-normalized to contain the expected number of 1328 clusters. The predicted and observed distributions are in good agreement with each other. **Left-hand panel:** redshift distribution. **Right-hand panel:** mass distribution.

## 6.5 Discussion

### 6.5.1 On the difference in predicted and measured SPT-SZ cluster masses

As was demonstrated in Section 6.4.1, we are able to reproduce the galaxy cluster sample sizes that were obtained by the *Planck* and SPT surveys using the forecast-pipeline presented in this work, assuming the best-fit ΛCDM cosmological parameter values obtained from the CMB + BAO analysis presented by the Planck Collaboration (2018b). While this inspires confidence in the forecasted sample sizes for future surveys, we also reported a mismatch in some of the reported sample properties. Specifically, we find that, on average, the weak-lensing calibrated masses of the SPT-SZ clusters reported by Bocquet et al. (2019) exceed the predicted ones by $\sim 20\%$. In contrast, the expected and observed galaxy cluster redshift distributions, as well as the expected and observed mass distribution of *Planck* clusters are in good agreement. The corresponding histograms are shown in Fig. 6.20 and 6.21.

It is important to understand that reproducing the mass distribution of the SPT-SZ cluster sample would require a higher predicted limiting mass, while keeping the predicted sample size constant. This can only be achieved by changing the assumed ΛCDM parameter values that are used to compute the parent distribution of clusters in redshift- and mass-space, which is shown in Fig. 6.7 via the HMF. Changing e.g. the $Y$-$M$-relation that is used to simulate the tSZ signal of cluster would either

- boost the tSZ signal of all clusters, leading to a lower survey limiting mass and thus increase the predicted sample size

–or–

- lower the tSZ signal of all clusters, leading to a higher limiting mass and therefore reduce the predicted sample size.

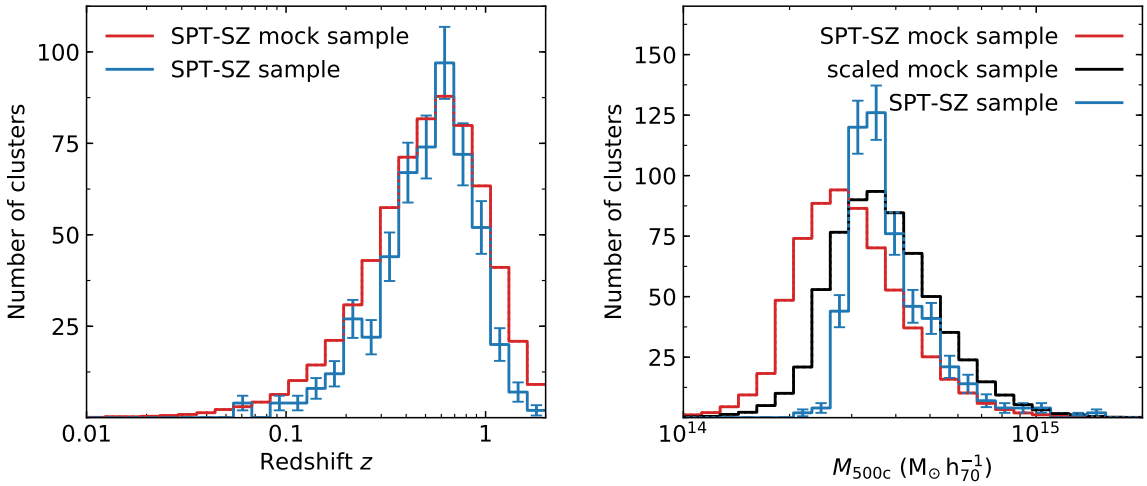


Figure 6.21: Redshift and mass distributions of the real SPT-SZ galaxy clusters (blue lines) and a simulated SPT-SZ galaxy cluster sample (red lines). The predicted distributions have been obtained from a large mock sample with $10^6$ clusters, generated following the steps laid out in Section 6.3.5, and were re-normalized to contain the expected number of 651 clusters. The cluster mass distribution reveals some tension between the observed and expected samples, which is related to systematic differences in the SPT-SZ and *Planck* cluster masses. The latter ones were used to define the cluster model used in this work. The observed and expected distributions can be brought to much better agreement by scaling the expected one to the number of clusters in the SPT-SZ sample and multiplying the predicted masses by a factor of 1.25 (black line). **Left-hand panel:** redshift distribution. **Right-hand panel:** mass distribution.

Since we need to increase the average mass of the predicted clusters we would thus inevitably decrease the predicted sample size and, in addition, no longer match both the observed *Planck* sample size and mass distribution. Changing the assumed cosmology in turn could allow to match the observed SPT-SZ cluster mass distribution and both the SPT-SZ and *Planck* sample sizes, but will likely no longer reproduce the mass distribution reported by *Planck*. We therefore conclude that the masses obtained by the *Planck* and SPT-SZ collaborations can not be correct at the same time and indeed different masses are reported for clusters that are observed by both surveys.

The issue of galaxy cluster mass calibration is a topic of major interest at the current point in time since accurate and precise cluster masses are required for precise cosmological tests. The broad consensus is that weak-lensing offers the most accurate estimates of the mass of galaxy clusters and efforts have been made to re-calibrate the masses of *Planck* clusters using weak-lensing priors, obtaining values that exceed the ones reported by Planck Collaboration (2016h) by 2.5% (Canadian Cluster Comparison Project; Hoekstra et al., 2015) and 16% (Weighing the Giants; von der Linden et al., 2014c). The latter result releaves most of the tension between the constraints on the value of $\sigma_8$ obtained from the CMB power spectrum and galaxy cluster number counts that was reported by Planck Collaboration (2014c). On the contrary, an attempt to re-calibrate the masses of *Planck* clusters using CMB lensing data (Melin & Bartlett, 2015) suggests that the true masses are 20% lower. Similarly, masses for the SPT-SZ cluster sample obtained by Bocquet et al. (2015), de Haan et al. (2016), and Dietrich et al. (2019) are higher, but consistent with the ones reported by Bocquet et al. (2019), as has been demonstrated by Stern et al. (2019). Resolving the tension between different cluster mass

calibration techniques is beyoned the scope of this work and requires larger cluster sample and better follow-up observations.

### 6.5.2 Comparison of the obtained sample sizes with other forecasts

The results presented in Section 6.3.4 suggest that CCAT-prime, depending on the layout of its primary instrument, the survey area, and the availability of external data from e.g. AdvACT, will detect between ~ 2000 and 10 000 galaxy clusters. Similar numbers were obtained by Mittal et al. (2018), who predict ~ 2000 clusters for a $10^3$ deg$^2$ CCAT-prime survey and 10 times more clusters for a survey covering the same area with much greater sensitivity.

A rough estimate for the expected number of clusters that will be observed by AdvACT was given by Henderson et al. (2016), who expect a sample size of ~ 10 000 objects, which is roughly twice the number of clusters that we predict for the AdvACT survey. Unfortunately, the assumed survey area for AdvACT was not provided by Henderson et al. (2016). Through private communication with AdvACT team members we learned that the assumed survey area corresponds to 20 000 deg$^2$, which is twice the area that was assumed in this work using identical sensitivities. Scaling the sample size obtained by us by a factor of two to account for the difference in survey area yields 12370 clusters, which is in excellent agreement with Henderson et al. (2016). However, through the same private channel we also learned that the AdvACT collaboration has revised its expected survey sensitivities, with the new ones being lower and kept confidencial for now. It is therefore possible that the actual number of clusters that will be detected could be fewer than ~ 10 000.

The expected sample size for the SO has been estimated by Ade et al. (2019) to be 16 000 clusters, assuming the baseline sensitivities for the large-aperture telescope (LAT) and $f_{\rm sky} = 0.4$, corresponding to ~ 16 500 deg$^2$. Although we do not simulate the SO in this work, we can get a rough estimate of the number of clusters our pipeline would predict by using the derived numbers for AdvACT as a proxi. The instruments offer comparable sensitivities (ignoring the fact taht the ones for AdvACT have since been revised), with the SO fielding an additional 280 GHz channel. This additional band should offer clear benefits for the detection of clusters and we thus expect the sample size to exceed the one we predict by scaling our value for AdvACT to the SO survey area, which corresponds to 10 205.

Other future ground-based cluster surveys include SPT-3G (Benson et al., 2014), which is projected to find ~ 5 000 clusters within 2 500 deg$^2$, and CMB-S4, which, depending on the spatial resolution, is expected to find between ~ 40 000 and ~ 140 000 clusters (Abazajian et al., 2016). The latter would even surpass the sample size predicted for eROSITA, which was successfully launched on July 13th 2019 and is expected to detect ~ 100 000 clusters (Pillepich et al., 2012; Clerc et al., 2018). Similar sample sizes were prediced for the Cosmic Origins Explorer (COrE, ~ 65 000 clusters, Melin et al., 2018b) and the Probe of Inflation and Cosmic Origins (PICO, ~ 150 000 clusters, Hanany et al., 2019), while the Polarized Radiation Imaging and Spectroscopy Mission (PRISM, André et al., 2014) would conduct the ultimate cluster survey detecting all clusters with $M_{500} > 5 \times 10^{13}$ M$_\odot$ leading to an expected sample size of ~ 1 000 000 objects.

### 6.5.3 The importance of map-based simulations with a realistic sky

A crucial improvement over the previous CCAT-prime forecasts presented by Erler et al. (2018) and Mittal et al. (2018) has been the use of a pipeline that simulates mock maps based on a realistic model of the microwave sky. The model used in this work includes the most relevant Galactic foregrounds

and extragalactic backgrounds and allows to simulate ~arcmin-resolution maps at frequencies ranging from ~ 30 GHz to ~ 1 THz.

When compared to the forecasts presented by Erler et al. (2018) we find that the inclusion of foregrounds lowers the predicted constraining power of CCAT-prime on the ICM temperature by a factor of ~6. While Erler et al. (2018) only used the expected instrumental sensitivities in their map-based forecasts, Mittal et al. (2018) employs a Fisher matrix method that neglects Galactic foregrounds and models the CIB as an additional white-noise component. While the sample size for a $10^3$ deg$^2$ CCAT-prime survey of $\gtrsim$ 2000 clusters predicted by Mittal et al. (2018) is in good agreement with the forecasted 2304 clusters in this work, the derived uncertainties of $T_e$ and $v_{pec}$ for individual clusters lie in between the ones we obtain using white noise-only maps and those that feature a realistic sky.

An important aspect of map-based simulations with a realistic sky is to capture diminishing returns by increases in survey sensitivity, caused by foreground residuals after map processing with e.g. MMFs. In addition to increased sensitivity, improved foreground removal requires additional frequency coverage and spatial resolution. For very deep surveys with limited spatial resolution, source confusion can become a potential limitation as well. We demonstrate the issue of diminishing returns by computing the expected sample size for a CCAT-prime survey covering 200, $10^3$, and $10^4$ deg$^2$ using white noise-only maps and compare them to the realistic numbers presented for the surveys that are given in Table 6.3. For this test, we adjust our $Y$-$M$-relation such that a simulated SPT-SZ survey obtains the same sample size of 651 clusters as was obtained using realistic sky maps. In addition, we provide numbers that are derived from using only the 150 GHz channel of SPT-SZ and CCAT-prime to highlight how multifrequency coverage affects the sensitivity in combined MMF $y$-maps. The results are presented in Table 6.4. Our results demonstrate that comparing a wide but shallow $10^4$ deg$^2$ survey to a deep one covering a much smaller area of 200 deg$^2$ yields a reduction of the sample size by a factor of ~ 2.6 using white noise-only simulations, while the sample size reduces by a factor of 5.9 when a realistic sky is used for the forecasts. As a consequence we recommend that proposed, highly sensitive future observatories field additional frequency bands and, if feasible, increase their apature size in order to mitigate this effect.

The advantages of map-based forecasts over forecasts obtained through a Fisher matrix formalism were recently demonstrated by Hanany et al. (2019), who showed that the predicted uncertainty on the tensor-to-scalar ratio $r$, expected to be obtained with PICO, is underestimated by a factor of five with the latter method. Map-domain forecasts are also the basis of the forecasts for, among others, *Planck* (*Planck* sky model, Delabrouille et al., 2013), PRISM (André et al., 2014), CMB-S4 (Abazajian et al., 2016), COrE (Melin et al., 2018b), and the SO (Ade et al., 2019).

### 6.5.4 Optimizing the frequency coverage of an alternative first light instrument

Recently, a smaller first light instument has been proposed for CCAT-prime due to continued setbacks in the fund raising efforts for Prime-Cam. This alternative instrument would primarily serve as a technology demonstrator of the envisioned detector technologies for Prime-Cam and contain three instrument modules. These three instrument modules could field up to three frequency channels. A total of four variations have been proposed, which were introduced in Table 6.2 as CCAT-prime v1 - v4. By computing the expected galaxy cluster sample sizes for a combined survey of the proposed instruments and AdvACT, covering $10^4$ deg$^2$, we showed that v1, which has the widest frequency coverage raging from 270 GHz up to 405 GHz, can be expected to find 15% more clusters than the

| Experiment | Area ($\mathrm{deg}^2$) | Freq. range (GHz) | $n_{\mathrm{freq.}}$ | $n_{\mathrm{clusters}}^{150\,\mathrm{GHz}}$ white noise-only | $n_{\mathrm{clusters}}^{\mathrm{all}-\nu}$ white noise-only | $n_{\mathrm{clusters}}^{\mathrm{all}-\nu}$ realistic sky |
|---|---|---|---|---|---|---|
| SPT | $2.5k$ | $[95, 220]$ | 3 | 651 | 651 | 651 |
| CCAT-p | 200 | $[95, 862]$ | 7 | 1 173 | 2 668 | 1 096 |
| CCAT-p | $10^3$ | $[95, 862]$ | 7 | 1 580 | 4 756 | 2 304 |
| CCAT-p | $10^4$ | $[95, 862]$ | 7 | 1 838 | 6 912 | 6 464 |

Table 6.4: Expected number of galaxy clusters in the range $z \in [0.01, 5]$ and $M_{500} \in [5 \times 10^{13}\,\mathrm{M}_\odot, 2 \times 10^{15}\,\mathrm{M}_\odot]$. These numbers were obtained using the formalism presented in Section 6.3.4, assuming the most recent *Planck* 2018 ΛCDM parameter values but adjusting the cluster model such that a simulated SPT-SZ survey always obtains a sample size of 651 objects, which was reported in Table 6.3. Decreasing the area of the simulated CCAT-prime survey, and therefore increasing the survey sensitivity, results in a general decrease in expected sample size. This decrease is more drastic if a realistic sky is used for the forecasts and can be attributed to diminishing returns of increases in sensitivity due to foreground residuals, the mitigation of which requires extended frequency coverage. We furthermore find that forecasts using a single channel do not accurately model the changes in sample size with changing survey area.

remaining 3 variants. This contradicts our initial expectation that a single deep 350 GHz band should be the most valuable addition to AdvACT due to the strong tSZ signal expected at that frequency. Instead we find that, although shallow at all frequencies, v1 is the only variant that was proposed to field a 270 GHz channel and offers the highest number of channels. In terms of frequency coverage, when combined with AdvACT, v1 in fact only differs from the originally envisioned Prime-Cam with seven instrument channels through its lack of a 860 GHz channel. From the perspective of the study of galaxy clusters, it is therefore recommended to chose v1 if a smaller-scale first light instrument needs to be build.

### 6.5.5 The importance of high-frequency observations

A unique feature of CCAT-prime is its access to submillimetre wavelengths due to the exceptional atmospheric conditions of its site. In the near-future landscape of next-generation large-aperture CMB instruments, CCAT-prime will be the only instrument capable of accessing frequencies $> 300$ GHz, allowing it to contribute valuable data that will serve e.g. to reduce Galactic foregrounds and emission from the CIB.

In Section 6.4.2 we demonstrated that combining simulated data from CCAT-prime and AdvACT will double the expected galaxy cluster sample size compared to an AdvACT only survey. This improvement is due to the improved handle on high-frequency foregrounds provided by CCAT-p, the separation of which has previously been infeasible for ground-based cluster surveys that traditionally focused on mm-wavelengths.

The extended frequency coverage offered by CCAT-prime furthermore provides a safeguard against biased estimates of the SZ parameters that can be the result of FIR contamination correlated with clusters. In Section 6.4.3, we showed that the undetected presence of cluster-centric FIR emission in AdvACT data will especially bias estimates of $v_{\mathrm{pec}}$, while attempts to model the FIR component using only AdvACT data will drastically reduce its constraining power. The effect of dust in clusters was recently also investigated by Melin et al. (2018a), who concluded that its effect on cosmological

studies with the *Planck* cluster sample is insignificant, but will become relevant for future samples obtained with much more sensitives surveys like CMB-S4.

Besides the advantages for the observations of clusters that are offered by CCAT-p, its capability of observing the polarization of light at all of its frequencies make it an interesting platform for CMB-S4. The main science goal of CMB-S4, a significant measurement of $r$, crucially depends on the mitigation of the $B$-mode polarization signal by Galactic dust (e.g. BICEP2/Keck Collaboration et al., 2015), the inaccurate extrapolation of which lead to the eventual withdrawal of the first detection claim by the BICEP2 collaboration. The most recent demonstration of the importance of high-frequencies has been given in the PICO white paper by Hanany et al. (2019), who showed that a reduced frequency coverage for PICO of 43-462 GHz would make it prone to obtaining a value of $r$ that is biased high, while the proposed range of 21-800 GHz would allow for an unbiased measurement.

### 6.5.6 Future improvements to the cluster forecast pipeline

The presented forecast pipeline was designed to allow for future improvements. The results presented in this section provide an overview over the current capabilities, but are by no means everything the pipeline has to offer.

A potential shortcoming of the current version of our sky model is the use of low-resolution Galactic foreground templates that are generated using the PySM (Thorne et al., 2017), which in turn uses the COMMANDER-separated *Planck* foreground maps. Artificial small scale features could be added to these maps, but require the extrapolation of the powerspectrum of the galactic foregrounds to angular scales that have no been probed by large-scale surveys at the current point in time. It is worth noting that the recently published sky model developed for the forecasts of the SO (Ade et al., 2019) uses the same Galactic foreground templates and does not add artificial small scale features as well. Nevertheless, the addition of small scale features are among the future improvements planed for the simulation pipeline.

Other improvements include the replacement of mock clusters, simulated by l.o.s. projection of a spherically symmetric ICM pressure profile, by tSZ and kSZ maps derived from hydrodynamical simulations. Such maps would cover the full range of dynamical states that are observed in real cluster samples and allow to predict e.g. the constraining power of future instruments on baryonic feedback processes in the ICM.

Finally, shortly after the computations that are the basis for the results presented here were completed the CITA WebSky team released updated, higher-resolution maps for their extragalactic CMB mocks, which will replace the older version of the same maps that have been used in our sky model.

## 6.6 Summary and Conclusions

We presented forecasts of the galaxy cluster sample size and the constraints on tSZ and kSZ effect parameters for the upcoming submillimetre survey telescope CCAT-p. With its novel high-throughput crossed-Dragone optics and its large 6 m diameter aperture, CCAT-prime will be a able to illuminate large multifrequency instruments with up to $\sim 10^5$ detectors, allowing it to survey a large fraction of the sky to ~ten times greater depth than *Planck*.

CCAT-p data is simulated using a self-implemented pipeline for generating and evaluating mock images at a spatial resolution of up to 1 arcmin at frequencies ranging from ~ 30GHz to ~ 1THz. At

the core of the pipeline lies a realistic model of the microwave sky that is build from the most recent Galactic foreground templates provided by the *Planck* telescope, a high resolution artificial CMB map, CIB and SZ all-sky maps from numerical simulations and Galactic, and point sources from the IRAS and NVSS catalogs. Injecting mock clusters into smaller fields projected from our sky model and extracting their signal using matched filtering or ILC techniques allows for a variety of forecasts, which we perform using the expected survey characteristics of CCAT-prime and AdvACT, as well as for the existing *Planck* and SPT-SZ cluster surveys to test the validity of our methods.

Our results indicate that CCAT-p, depending on the details of the survey and primary instrument, will be able to detect between 2000 and 10 000 galaxy clusters, where the latter was derived for a combined CCAT-prime + AdvACT survey. When combined with AdvACT, CCAT-prime will double the number of clusters that can be accessed with AdvACT alone and allow for the detection of all clusters in the survey volume with $M_{500} > 3 \times 10^{14}\,\mathrm{M}_{\odot}$. Approximately half of the expected cluster sample will be located at $z > 0.5$, with several tens of clusters at $z > 2$. Furthermore, we identified 270 GHz to be a crucial frequency for a proposed smaller first-light instrument for CCAT-prime.

Using the same pipeline, we are able to reproduce the sample sizes obtained by the *Planck* and SPT-SZ cluster surveys, as well as the redshift- and mass-distributions of the *Planck* sample. While the redshift distribution of the SPT-SZ clusters could be reproduced as well, the masses of the predicted clusters are $\sim$ 20% lower compared to the ones reported for the actual sample by Bocquet et al. (2019). Adjustments to the pipeline that bring the predicted and observed SPT-SZ masses into closer agreement are found to create tension between the predicted and observed *Planck* masses.

One of the objectives of the forecasts presented in this work has been to determine if CCAT-prime can directly measure the ICM temperature of massive clusters via the relativistic tSZ effect. By comparing the parameter constraints we obtain using a realistic model of the sky to constraints obtained by simulations that only take into account the expected survey noise of CCAT-p, we conclude that direct temperature measurements will only be possible at $\sim 2\sigma$ significance, as opposed to the estimates previously provided by Erler et al. (2018). Furthermore, we showed that only a small number of clusters in the expected sample will have a sufficiently high masses to allow for a $\sim 2\sigma$ measurement of their temperature. Studies of the ICM temperature will therefore continue to rely on statistical techniques like stacking, for which CCAT-prime will offer strong improvements over *Planck*. Similar but slightly more optimistic conclusions can be drawn for the measurements of cluster velocities. Provided that at least some clusters with $M_{500} \gtrsim 10^{15}\,\mathrm{M}_{\odot}$ move at projected speeds in excess of $\pm 1000\,\mathrm{km/s}$, CCAT-prime should be able to directly measure their velocities at $\sim 3\sigma$ significance.

The capability of CCAT-prime to measure cluster temperatures and velocities can be greatly enhanced if an informative prior on the ICM optical depth $\tau_{\mathrm{e}}$ is applied. Such a prior could be constructed from measurements and de-projection of the X-ray surface brightness of clusters. This opens up exciting synergies with the upcoming eROSITA X-ray all-sky survey that will detect 100 000 clusters out to $z \approx 3$, but can only measure the temperature of local clusters. Furthermore, the most massive clusters that will be observed by CCAT-prime are most likely already known and have archival X-ray data taken with XMM-Newton and Chandra.

The coming years will be will be an exciting time for the study of the cosmic microwave background. The next generation of surveys is expected to increase the size of SZ-selected cluster samples by one order of magnitude to many thousands of objects, a large fraction of which will be located at high redshifts. Among the upcoming ground-based facilities, CCAT-prime will be the only one designed to operate in the submillimetre domain. We demonstrated in this work that CCAT-prime will play a crucial role in characterising foregrounds and providing high-frequency data that will allow better

constraints on cluster temperatures and velocities than with any other instrument in the near future. Beyond its first survey, CCAT-prime presents a unique platform for CMB-S4 and could answer some of the most pressing questions of modern cosmology. The coming months and years will tell if CCAT-prime receives the necessary financial support to make this ambitious vision a reality.

CHAPTER 7

# Summary, significance, and outlook

The research presented in this thesis includes a detailed study of the spectrum of the tSZ effect and its relativistic distortions using data from the Planck satellite, the introduction of new matched filtering techniques for improved separation of clusters and point sources in SZ- and X-ray data, and forecasts of the expected galaxy cluster sample size and SZ spectral constraints that will be obtained with CCAT-prime and other near-future experiments. This final Chapter gives a brief summary of each project and outlines the wider implications and impact of the results presented in this work. The thesis is then concluded with an outlook on the near future of SZ observations of galaxy clusters.

## 7.1 Summary of the individual projects

#### Observations of the tSZ spectrum with *Planck*

Chapter 4 of this thesis presented a study of the average tSZ spectrum of 772 massive galaxy clusters using *Planck* data and auxiliary maps from the IRAS and *AKARI* space telescopes with the goal of detecting relativistic distortions. These distortions allow to measure the electron pressure-weighted temperature of the ICM, which has cosmological and astrophysical implications. Individual maps of each cluster were processed with matched filters to remove unwanted bright Galactic and extragalactic emission. After filtering, the maps of the 772 clusters were stacked to boost the SNR and average the clusters' kSZ signal down. The extracted spectrum is the cleanest one to date, clearly revealing the average tSZ effect of the clusters and showing an additional FIR excess, which was attributed to large amounts of warm dust inside the ICM or the clusters' member galaxies. The FIR excess was subsequently modelled with an MBB SED. The average SZ-temperature of the clusters was constrained to $k_\mathrm{B}T_\mathrm{e} = 4.4^{+2.1}_{-2.0}$ keV, giving a $2.2\sigma$ measurement of the relativistic tSZ effect. The analysis of a sub-sample containing the 100 hottest clusters gave a temperature of $k_\mathrm{B}T_\mathrm{e} = 6.0^{+3.8}_{-2.9}$ keV, providing a similar significance of $2.0\sigma$. The additional FIR component was measured $5\sigma$ and $4\sigma$, respectively, with an average dust temperature of $\approx 18$ K in the cluster rest-frame. The matched filtering and spectral modelling pipeline used to obtain these results was thoroughly validated using mock data. The same mock data was used to demonstrate that the usage of the non-relativistic approximation of the tSZ effect will lead to an underestimation of the Compton-$y$ parameter value of clusters. Simplified mock data was used to give a first outlook on the expected performance of the upcoming CCAT-prime telescope, which is expected to deliver a $\sim 5$ times lower uncertainty on $T_\mathrm{SZ}$.

#### Introduction to the constrained matched filter and multifilter

One of the key techniques used in the study of the tSZ spectrum was matched filtering. Chapter 5 of this work introduced multi-component generalisations of the original MF- and MMF-concepts, which allow improved separation of sources that can be approximated by spatial templates. Advantages and limitations of the new techniques are demonstrated on real and mock data sets, focusing on the reduction of contamination by point sources in SZ and X-ray observations of galaxy clusters. It is shown that the new filters allow for an unbiased extraction of the central Comptonization parameter $y_0$ of clusters in the presence of a (radio) point source. The new methods were applied to *Planck* data of the Perseus cluster and gave consistent values with the CMMF-method yielding $y_0 = (10.0 \pm 0.42) \times 10^{-5}$, implying $M_{500} = (6.97 \pm 0.24) \times 10^{14}\,\mathrm{M}_\odot$, while the traditional MF- and MMF-techniques gave strongly biased, negative values for $y_0$. The application of the CMF-method to X-ray data was outlined using eROSITA mock-data.

#### Galaxy cluster science forecasts for CCAT-prime

Chapter 6 of this work presented detailed forecasts of the expected galaxy cluster sample size and SZ-spectral constrains for CCAT-prime and other current and future microwave surveys. The forecasts were based on a self-developed pipeline for the generation of microwave-sky mock observations at a resolution of 1 arcmin, which included the most relevant Galactic foregrounds, the CMB, the CIB, and a population of radio- and FIR point sources. This pipeline was set up to allow for the simulation of any arbitrary survey given its frequency bands, spatial resolution and band sensitivities. Using the MMF-techniques explored in the previous chapter, the SNR of clusters was tabulated as a function of mass and redshift, which allows to characterize the sample properties of a given survey. The simulation and analysis pipeline was validated by reproducing the respective sample sizes obtained by *Planck* and SPT-SZ. It was found that CCAT-prime will detect and characterize between 2000 and 10 000 clusters, depending on the assumed survey area and the combination of CCAT-prime data with that of other surveys like AdvACT. An investigation of the spectral constraints with CCAT-prime revealed clear advantages over *Planck* due to CCAT-prime's comparable frequency coverage but higher spatial resolution and sensitivity. Furthermore, it was demonstrated that the high frequencies accessible with CCAT-prime provide a valuable safeguard against systematic biases introduced by potential cluster FIR emission.

## 7.2 Implications and impact

The results presented in Chapter 4 represent the most detailed study of the full spectrum of the tSZ effect to date and demonstrate that a significant detection of its relativistic distortions is still out of reach for current instruments. Hurier (2016) claims a clear $5\sigma$ detection of the relativistic tSZ effect, but the methods used by the author have clear shortcomings, as has been discussed in Section 4.7.2. Another claim of high-significance detection was made by Hincks et al. (2018), who also investigated a large sample of *Planck* clusters but have since withdrawn their results due to problems with the convergence of the MCMC sampler used for their spectral modelling.

Using mock data, it was demonstrated that the non-relativistic approximation of the tSZ effect leads to a systematic underestimation of the Compton-$y$ parameter. This issue has since been further investigated by Remazeilles et al. (2019), who showed that the bias on the tSZ power spectrum

extracted from *Planck* using the non-relativistic tSZ spectrum results in a power spectrum that is biased by $\sim 1\sigma$. Using the relativistic spectrum relieves some of the tension in the reported values for $\sigma_8$ obtained through analysis of the CMB and tSZ power spectra, implying a lower value of the hydrostatic mass bias that is more in-line with simulations.

A key finding presented in this work is the observed cluster FIR emission, which poses a significant challenge for future SZ observations and will require high frequency coverage. Recently, Vogelsberger et al. (2019) studied the impact of intracluster dust on gas cooling using numerical simulations. The authors report large uncertainties in the abundance of dust and the inferred FIR luminosity due to the poorly constrained lifetime of dust grains in the ICM.

The new CMF- and CMMF-techniques presented in Chapter 5 are very specialized tools and haven't been used in other studies so far. An important property of the new filters is the dependence of their usefulness on the spatial resolution of an instrument, which determines the noise increase in the filtered maps compared to the traditional MF- and CMF-techniques. The next generation of ground-based SZ instruments with their 6 m apertures will provide at least four times the resolution of *Planck*, which opens up the use case for the new filters. It is important to stress again that the CMF- and CMMF-techniques were not designed to replace the traditional filters, but rather represent an additional tool that works best in synergy.

The forecasts for the CCAT-prime cluster science case have been used in several fundraising efforts and recent white papers (Stacey et al., 2018; Aravena et al., 2019). The corresponding simulation pipeline is improved continuously and will help to find the optimal frequency layout for Prime-Cam.

## 7.3 Outlook

The next decade will see major progress in the study of galaxy clusters and cosmological studies with them. In the early 2020s, AdvACT, SPT-3G, the SO, and CCAT-prime will increase the size of SZ selected cluster samples by one order of magnitude. The expected sensitivity of $\lesssim 10\mu\mathrm{K}_{\mathrm{CMB}}$-arcmin for these next-generation surveys was recently demonstrated, for the first time, by the SPT-pol survey over a much smaller area of $100\,\mathrm{deg}^2$ (Huang et al., 2019). Many of these newly discovered objects will be disturbed systems at high redshifts that will allow us to develop a more detailed understanding of cluster formation and feedback mechanisms in the ICM. Progress in X-ray observations of clusters will largely be driven by eROSITA, with the promise to find $10^5$ galaxy clusters. While eROSITA is now beginning to collect data, the aforementioned SZ experiments are currently under construction and their science cases are being prepared and refined.

The preparation of these science cases includes to continual development of simulation tools for the generation and analysis of mock data like the ones presented in Chapter 6. As outlined at the end of that Chapter, several improvements of the simulation pipeline presented in this work are already planed, like the usage of better CIB and all-sky SZ templates, the addition of small-scale features to the Galactic emission templates, as well as the adoption of the recent atmospheric noise model presented by Choi et al. (2019). This updated sky-model will be used to explore other aspects of the galaxy cluster science case. Since the forecasts presented here indicate that CCAT-prime will not be able to measure the temperature of most clusters directly, statistical methods like the stacking approach used for *Planck* data should be explored to predict e.g. the achievable constraints on the $M$–$T_{\mathrm{SZ}}$ relation. Similarly, statistical approaches for the measurement of the kSZ effect, like the pairwise momentum estimator, have to be explored on mock data before applied to real survey data in order to understand

possible systematics and adjust the analysis tools if necessary.

In the more distant future, a large 30–50 m diameter ground based telescope like the proposed AtLAST could revolutionize the study of the SZ effect of clusters, while a future space mission like PICO or PRISM would provide unmatched sensitivity and frequency coverage and allow to measure the relativistic tSZ and kSZ at high significance in many clusters.

# Bibliography


Abadi M. G., Moore B., Bower R. G., 1999, MNRAS, 308, 947

Abazajian K. N., et al., 2016, arXiv e-prints, p. arXiv:1610.02743

Abell G. O., 1958, ApJS, 3, 211

Abell G. O., Corwin Harold G. J., Olowin R. P., 1989, ApJS, 70, 1

Abitbol M. H., Chluba J., Hill J. C., Johnson B. R., 2017, MNRAS, 471, 1126

Addison G. E., Dunkley J., Spergel D. N., 2012, MNRAS, 427, 1741

Ade P., et al., 2019, J. Cosmology Astropart. Phys., 2019, 056

Aghanim N., Hansen S. H., Lagache G., 2005, A&A, 439, 901

Ahmad Q. R., et al., 2001, Phys. Rev. Lett., 87, 071301

Alcock C., et al., 2000, ApJ, 542, 281

Allen S. W., Schmidt R. W., Ebeling H., Fabian A. C., van Speybroeck L., 2004, MNRAS, 353, 457

Allen S. W., Rapetti D. A., Schmidt R. W., Ebeling H., Morris R. G., Fabian A. C., 2008, MNRAS, 383, 879

Allen S. W., Evrard A. E., Mantz A. B., 2011, ARA&A, 49, 409

Alpher R. A., Herman R. C., 1948a, Physical Review, 74, 1737

Alpher R. A., Herman R., 1948b, Nature, 162, 774

Alpher R. A., Bethe H., Gamow G., 1948, Physical Review, 73, 803

Anderson A. J., et al., 2018, Low Temp. Phys., 193, 1057

André P., et al., 2014, J. Cosmology Astropart. Phys., 2014, 006

Angus G. W., Famaey B., Zhao H. S., 2006, MNRAS, 371, 138

Aprile E., et al., 2017, Phys. Rev. Lett., 119, 181301

Aravena M., et al., 2019, arXiv e-prints, p. arXiv:1909.02587

Armengaud E., et al., 2019, Phys. Rev. D, 99, 082003

Arnaud M., Pratt G. W., Piffaretti R., Böhringer H., Croston J. H., Pointecouteau E., 2010, A&A, 517, A92

BICEP2/Keck Collaboration et al., 2015, Phys. Rev. Lett., 114, 101301

Bacchi M., Feretti L., Giovannini G., Govoni F., 2003, A&A, 400, 465

Bartlett J. G., Melin J.-B., 2006, A&A, 447, 405

Bartolo N., Komatsu E., Matarrese S., Riotto A., 2004, Phys. Rep., 402, 103

Basu K., Sommer M., Erler J., Eckert D., Vazza F., Magnelli B., Bertoldi F., Tozzi P., 2016, ApJ, 829, L23

Basu K., et al., 2019, arXiv e-prints, p. arXiv:1903.04944

Beck A. M., et al., 2016, MNRAS, 455, 2110

Beichman C. A., Neugebauer G., Habing H. J., Clegg P. E., Chester T. J., 1988, 1

Bender A. N., et al., 2016, MNRAS, 460, 3432

Bennett C. L., et al., 2003, ApJS, 148, 97

Benson B. A., et al., 2014, Proc. SPIE, 9153, 91531P

Bertone G., Hooper D., Silk J., 2005, Phys. Rep., 405, 279

Biffi V., Sembolini F., De Petris M., Valdarnini R., Yepes G., Gottlöber S., 2014, MNRAS, 439, 588

Biffi V., Dolag K., Merloni A., 2018, MNRAS, 481, 2213

Birkinshaw M., 1999, Phys. Rep., 310, 97

Birkinshaw M., Gull S. F., Northover K. J. E., 1978, MNRAS, 185, 245

Birkinshaw M., Gull S. F., Hardebeck H., 1984, Nature, 309, 34

Blain A. W., 1998, MNRAS, 297, 502

Blandford R., Eichler D., 1987, Phys. Rep., 154, 1

Bleem L. E., et al., 2015, ApJS, 216, 27

Bocquet S., et al., 2015, ApJ, 799, 214

Bocquet S., Saro A., Dolag K., Mohr J. J., 2016, MNRAS, 456, 2361

Bocquet S., et al., 2019, ApJ, 878, 55

Böhringer H., et al., 2007, A&A, 469, 363

Bonamente M., Joy M. K., LaRoque S. J., Carlstrom J. E., Reese E. D., Dawson K. S., 2006, ApJ, 647, 25

Bond J. R., Efstathiou G., 1984, ApJ, 285, L45

Boran S., Desai S., Kahya E. O., Woodard R. P., 2018, Phys. Rev. D, 97, 041501

Borm K., Reiprich T. H., Mohammed I., Lovisari L., 2014, A&A, 567, A65

Brunetti G., Jones T. W., 2014, International Journal of Modern Physics D, 23, 1430007

Bustos R., Rubio M., Otárola A., Nagar N., 2014, PASP, 126, 1126

Butcher H., Oemler A. J., 1978a, ApJ, 219, 18

Butcher H., Oemler A. J., 1978b, ApJ, 226, 559

Butcher H., Oemler A. J., 1984, ApJ, 285, 426

Béthermin M., et al., 2017, A&A, 607, A89

Caldwell R. R., Kamionkowski M., Weinberg N. N., 2003, Phys. Rev. Lett., 91, 071301

Canning R. E. A., et al., 2015, arXiv e-prints, p. arXiv:1505.05790

Carlstrom J. E., Holder G. P., Reese E. D., 2002, ARA&A, 40, 643

Cavaliere A., Fusco-Femiano R., 1976, A&A, 500, 95

Challinor A., Lasenby A., 1998, ApJ, 499, 1

Chluba J., Nagai D., Sazonov S., Nelson K., 2012, MNRAS, 426, 510

Chluba J., Switzer E., Nelson K., Nagai D., 2013, MNRAS, 430, 3054

Chluba J., Hill J. C., Abitbol M. H., 2017, MNRAS, 472, 1195

Choi S. K., et al., 2019, arXiv e-prints, p. arXiv:1908.10451

Clerc N., et al., 2018, A&A, 617, A92

Clowe D., Bradač M., Gonzalez A. H., Markevitch M., Randall S. W., Jones C., Zaritsky D., 2006, ApJ, 648, L109

Colless M., et al., 2001, MNRAS, 328, 1039

Condon J. J., Cotton W. D., Greisen E. W., Yin Q. F., Perley R. A., Taylor G. B., Broderick J. J., 1998, AJ, 115, 1693

Croston J. H., Arnaud M., Pointecouteau E., Pratt G. W., 2006, A&A, 459, 1007

Delabrouille J., Cardoso J. F., Le Jeune M., Betoule M., Fay G., Guilloux F., 2009, A&A, 493, 835

Delabrouille J., et al., 2013, A&A, 553, A96

Delabrouille J., et al., 2018, J. Cosmology Astropart. Phys., 2018, 014

Di Mascolo L., et al., 2019, A&A, 628, A100

Dicker S. R., et al., 2018, Proc.~SPIE, 10700, 107003E

Dickinson C., et al., 2018, New Astron. Rev., 80, 1

Diemer B., 2018, ApJS, 239, 35

Dietrich J. P., et al., 2019, MNRAS, 483, 2871

Doi Y., et al., 2015, PASJ, 67, 50

Draine B. T., 2003, ARA&A, 41, 241

Draine B. T., Salpeter E. E., 1979, ApJ, 231, 77

Dwek E., Arendt R. G., 1992, ARA&A, 30, 11

Dwek E., Rephaeli Y., Mather J. C., 1990, ApJ, 350, 104

Eke V. R., Navarro J. F., Frenk C. S., 1998, ApJ, 503, 569

Enßlin T. A., Kaiser C. R., 2000, A&A, 360, 417

Eriksen H. K., Banday A. J., Górski K. M., Lilje P. B., 2004, ApJ, 612, 633

Erler J., Basu K., Trasatti M., Klein U., Bertoldi F., 2015, MNRAS, 447, 2497

Erler J., Basu K., Chluba J., Bertoldi F., 2018, MNRAS, 476, 3360

Erler J., Ramos-Ceja M. E., Basu K., Bertoldi F., 2019, MNRAS, 484, 1988

Felten J. E., Morrison P., 1966, ApJ, 146, 686

Fixsen D. J., Cheng E. S., Gales J. M., Mather J. C., Shafer R. A., Wright E. L., 1996, ApJ, 473, 576

Foreman-Mackey D., 2016, The Journal of Open Source Software, 24

Foreman-Mackey D., Hogg D. W., Lang D., Goodman J., 2013, PASP, 125, 306

Forman W., Kellogg E., Gursky H., Tananbaum H., Giacconi R., 1972, ApJ, 178, 309

Freeman P. E., Kashyap V., Rosner R., Lamb D. Q., 2002, ApJS, 138, 185

Fukuda Y., et al., 1998, Phys. Rev. Lett., 81, 1562

Gamow G., 1948a, Physical Review, 74, 505

Gamow G., 1948b, Nature, 162, 680

Geman S., Geman D., 1984, IEEE Transactions on Pattern Analysis and Machine Intelligence, PAMI-6, 721

Giard M., Montier L., Pointecouteau E., Simmat E., 2008, A&A, 490, 547

Goodman J., Weare J., 2010, Communications in Applied Mathematics and Computational Science, 5, 65

Green T. S., et al., 2017, MNRAS, 465, 4872

Guth A. H., 1981, Phys. Rev. D, 23, 347

Górski K. M., Hivon E., Banday A. J., Wandelt B. D., Hansen F. K., Reinecke M., Bartelmann M., 2005, ApJ, 622, 759

Haehnelt M. G., Tegmark M., 1996, MNRAS, 279, 545

Hanany S., et al., 2000, ApJ, 545, L5

Hanany S., et al., 2019, arXiv e-prints, p. arXiv:1902.10541

Hand N., et al., 2012, Phys. Rev. Lett., 109, 041101

Hansen S. H., 2004, MNRAS, 351, L5

Harnden F. R. J., Fabricant D. G., Harris D. E., Schwarz J., 1984, SAO Special Report, 393

Haslam C. G. T., Klein U., Salter C. J., Stoffel H., Wilson W. E., Cleary M. N., Cooke D. J., Thomasson P., 1981, A&A, 100, 209

Haslam C. G. T., Salter C. J., Stoffel H., Wilson W. E., 1982, Astronomy and Astrophysics Supplement Series, 47, 1

Hasselfield M., et al., 2013, J. Cosmology Astropart. Phys., 2013, 008

Hastings W. K., 1970, Biometrika, 57, 97

Helou G., Walker D. W., eds, 1988, Infrared astronomical satellite (IRAS) catalogs and atlases. Volume 7: The small scale structure catalog Vol. 7

Henderson S. W., et al., 2016, Journal of Low Temperature Physics, 184, 772

Herbig T., Readhead A. C. S., 1992, ApJS, 81, 83

Hernández-Monteagudo C., Sunyaev R. A., 2010, A&A, 509, A82

Herranz D., Sanz J. L., Hobson M. P., Barreiro R. B., Diego J. M., Martínez-González E., Lasenby A. N., 2002, MNRAS, 336, 1057

Herranz D., Sanz J. L., Barreiro R. B., López- Caniego M., 2005, MNRAS, 356, 944

Hildebrand R. H., 1983, QJRAS, 24, 267

Hill J. C., Battaglia N., Chluba J., Ferraro S., Schaan E., Spergel D. N., 2015, Phys. Rev. Lett., 115, 261301

Hincks A. D., Génova-Santos R., Luzzi G., Battistelli E. S., 2018, arXiv e-prints, p. arXiv:1803.03277

Hoekstra H., Herbonnet R., Muzzin A., Babul A., Mahdavi A., Viola M., Cacciato M., 2015, MNRAS, 449, 685

Hogg D. W., 1999, arXiv e-prints, pp astro–ph/9905116

Hogg D. W., Foreman-Mackey D., 2018, ApJS, 236, 11

Hogg D. W., Bovy J., Lang D., 2010, arXiv e-prints, p. arXiv:1008.4686

Hu W., Dodelson S., 2002, ARA&A, 40, 171

Huang N., et al., 2019, arXiv e-prints, p. arXiv:1907.09621

Hurier G., 2016, A&A, 596, A61

Hurier G., Tchernin C., 2017, A&A, 604, A94

Hurier G., Macías-Pérez J. F., Hildebrandt S., 2013, A&A, 558, A118

Hurier G., Aghanim N., Douspis M., Pointecouteau E., 2014, A&A, 561, A143

Itoh N., Kohyama Y., Nozawa S., 1998, ApJ, 502, 7

Jenkins A., Frenk C. S., White S. D. M., Colberg J. M., Cole S., Evrard A. E., Couchman H. M. P., Yoshida N., 2001, MNRAS, 321, 372

Jüttner F., 1911a, Annalen der Physik, 339, 856

Jüttner F., 1911b, Annalen der Physik, 340, 145

Kaiser N., 1986, MNRAS, 222, 323

Kalberla P. M. W., Burton W. B., Hartmann D., Arnal E. M., Bajaja E., Morras R., Pöppel W. G. L., 2005, A&A, 440, 775

Kauffmann G., White S. D. M., Guiderdoni B., 1993, MNRAS, 264, 201

Kay S. T., Powell L. C., Liddle A. R., Thomas P. A., 2008, MNRAS, 386, 2110

Kellogg E., Gursky H., Tananbaum H., Giacconi R., Pounds K., 1972, ApJ, 174, L65

Knox L., Holder G. P., Church S. E., 2004, ApJ, 612, 96

Kogut A., Banday A. J., Bennett C. L., Gorski K. M., Hinshaw G., Smoot G. F., Wright E. I., 1996, ApJ, 464, L5

Kogut A., et al., 2011, J. Cosmology Astropart. Phys., 2011, 025

Korngut P. M., et al., 2011, ApJ, 734, 10

Koulouridis E., et al., 2018, A&A, 620, A4

Kozmanyan A., Bourdin H., Mazzotta P., Rasia E., Sereno M., 2019, A&A, 621, A34

Lamarre J. M., et al., 1998, ApJ, 507, L5

Lamarre J. M., et al., 2010, A&A, 520, A9

Landsman W. B., 1993, in Hanisch R. J., Brissenden R. J. V., Barnes J., eds, ASP Conf. Ser.Vol. 52, Astronomical Data Analysis Software and Systems II. p. 246

Lanz L. F., Herranz D., Sanz J. L., González- Nuevo J., López-Caniego M., 2010, MNRAS, 403, 2120

Lattanzi M., Gerbino M., 2017, arXiv e-prints, p. arXiv:1712.07109

Lesgourgues J., Pastor S., 2014, New Journal of Physics, 16, 065002

Lewis A., Challinor A., Lasenby A., 2000, ApJ, 538, 473

Lin Y.-T., Mohr J. J., 2007, ApJS, 170, 71

Linde A. D., 1982, Physics Letters B, 108, 389

Lundgren B., et al., 2015, PASP, 127, 776

Mandolesi N., et al., 2010, A&A, 520, A3

Mantz A. B., Allen S. W., Morris R. G., Rapetti D. A., Applegate D. E., Kelly P. L., von der Linden A., Schmidt R. W., 2014, MNRAS, 440, 2077

Mather J. C., et al., 1994, ApJ, 420, 439

Mazzotta P., Rasia E., Moscardini L., Tormen G., 2004, MNRAS, 354, 10

McDonald M., et al., 2016, ApJ, 817, 86

McKinnon R., Torrey P., Vogelsberger M., 2016, MNRAS, 457, 3775

McKinnon R., Torrey P., Vogelsberger M., Hayward C. C., Marinacci F., 2017, MNRAS, 468, 1505

Melin J.-B., Bartlett J. G., 2015, A&A, 578, A21

Melin J.-B., Bartlett J. G., Delabrouille J., 2006, A&A, 459, 341

Melin J.-B., et al., 2012, A&A, 548, A51

Melin J. B., Bartlett J. G., Cai Z. Y., De Zotti G., Delabrouille J., Roman M., Bonaldi A., 2018a, A&A, 617, A75

Melin J. B., et al., 2018b, J. Cosmology Astropart. Phys., 2018, 019

Merloni A., et al., 2012, arXiv e-prints, p. arXiv:1209.3114

Metropolis N., Rosenbluth A. W., Rosenbluth M. N., Teller A. H., Teller E., 1953, J. Chem. Phys., 21, 1087

Meyers J., Meerburg P. D., van Engelen A., Battaglia N., 2018, Phys. Rev. D, 97, 103505

Milgrom M., 1983, ApJ, 270, 365

Mittal A., de Bernardis F., Niemack M. D., 2018, J. Cosmology Astropart. Phys., 2018, 032

Miville-Deschênes M.-A., Lagache G., 2005, ApJS, 157, 302

Miville-Deschênes M. A., Lagache G., Boulanger F., Puget J.-L., 2007, A&A, 469, 595

Montes M., Trujillo I., 2019, MNRAS, 482, 2838

Montier L. A., Giard M., 2005, A&A, 439, 35

Moretti A., Vattakunnel S., Tozzi P., Salvaterra R., Severgnini P., Fugazza D., Haardt F., Gilli R., 2013, Mem. Soc. Astron. Italiana, 84, 653

Mroczkowski T., et al., 2019, Space Science Reviews, 215, 17

Nagai D., Kravtsov A. V., Vikhlinin A., 2007, ApJ, 668, 1

National Research Council 2011, Panel Reports—New Worlds, New Horizons in Astronomy and Astrophysics. The National Academies Press, Washington, DC, doi:10.17226/12982, https://www.nap.edu/catalog/12982/panel-reports-new-worlds-new-horizons-in-astronomy-and-astrophysics

Navarro J. F., Frenk C. S., White S. D. M., 1996, ApJ, 462, 563

Nelson K., Lau E. T., Nagai D., Rudd D. H., Yu L., 2014, ApJ, 782, 107

Netterfield C. B., et al., 2002, ApJ, 571, 604

Neugebauer G., et al., 1984, ApJ, 278, L1

Niemack M. D., 2016, Appl. Opt., 55, 1688

Niikura H., et al., 2019, Nature Astronomy, p. 238

Nozawa S., Itoh N., Kawana Y., Kohyama Y., 2000, ApJ, 536, 31

Ofek E. O., Zackay B., 2018, AJ, 155, 169

Ostriker J., Silk J., 1973, ApJ, 184, L113

Ostriker J. P., Bode P., Babul A., 2005, ApJ, 634, 964

Paradis D., Dobashi K., Shimoikura T., Kawamura A., Onishi T., Fukui Y., Bernard J.-P., 2012, A&A, 543, A103

Pardo J. R., Cernicharo J., Serabyn E., 2001, IEEE Trans. Antennas Propag., 49, 1683

Pariiskii Y. N., 1973, Soviet Ast., 16, 1048

Parshley S. C., et al., 2018a, Proc. SPIE, 10700, 1070041

Parshley S. C., et al., 2018b, Proc. SPIE, 10700, 107005X

Peel A. C., 2006, MNRAS, 365, 1191

Pen U.-L., 1997, New Astron., 2, 309

Penzias A. A., Wilson R. W., 1965, ApJ, 142, 419

Perlmutter S., et al., 1999, ApJ, 517, 565

Piffaretti R., Jetzer P., Schindler S., 2003, A&A, 398, 41

Piffaretti R., Arnaud M., Pratt G. W., Pointecouteau E., Melin J. B., 2011, A&A, 534, A109

Pillepich A., Porciani C., Hahn O., 2010, MNRAS, 402, 191

Pillepich A., Porciani C., Reiprich T. H., 2012, MNRAS, 422, 44

Pillepich A., et al., 2018, MNRAS, 473, 4077

Planck Collaboration 2011, A&A, 536, A8

Planck Collaboration 2013a, A&A, 550, A131

Planck Collaboration 2013b, A&A, 554, A140

Planck Collaboration 2014a, A&A, 571, A1

Planck Collaboration 2014b, A&A, 571, A9

Planck Collaboration 2014c, A&A, 571, A20

Planck Collaboration 2014d, A&A, 571, A29

Planck Collaboration 2016a, A&A, 594, A1

Planck Collaboration 2016b, A&A, 594, A8

Planck Collaboration 2016c, A&A, 594, A10

Planck Collaboration 2016d, A&A, 594, A22

Planck Collaboration 2016e, A&A, 594, A23

Planck Collaboration 2016f, A&A, 594, A24

Planck Collaboration 2016g, A&A, 594, A26

Planck Collaboration 2016h, A&A, 594, A27

Planck Collaboration 2016i, A&A, 596, A104

Planck Collaboration 2018a, arXiv e-prints, p. arXiv:1807.06205

Planck Collaboration 2018b, arXiv e-prints, p. arXiv:1807.06209

Pointecouteau E., Giard M., Barret D., 1998, A&A, 336, 44

Predehl P., 2017, Astronomische Nachrichten, 338, 159

Press W. H., Schechter P., 1974, ApJ, 187, 425

Prokhorov D. A., Colafrancesco S., 2012, MNRAS, 424, L49

Ramos-Ceja M. E., Basu K., Pacaud F., Bertoldi F., 2015, A&A, 583, A111

Reed D., Gardner J., Quinn T., Stadel J., Fardal M., Lake G., Governato F., 2003, MNRAS, 346, 565

Reed D. S., Bower R., Frenk C. S., Jenkins A., Theuns T., 2007, MNRAS, 374, 2

Rees M. J., Sciama D. W., 1968, Nature, 217, 511

Reichert A., Böhringer H., Fassbender R., Mühlegger M., 2011, A&A, 535, A4

Reiprich T. H., Basu K., Ettori S., Israel H., Lovisari L., Molendi S., Pointecouteau E., Roncarelli M., 2013, Space Sci. Rev., 177, 195

Reiss I., Keshet U., 2018, J. Cosmology Astropart. Phys., 2018, 010

Remazeilles M., Delabrouille J., Cardoso J.-F., 2011a, MNRAS, 410, 2481

Remazeilles M., Delabrouille J., Cardoso J.-F., 2011b, MNRAS, 418, 467

Remazeilles M., Dickinson C., Banday A. J., Bigot-Sazy M. A., Ghosh T., 2015, MNRAS, 451, 4311

Remazeilles M., Bolliet B., Rotti A., Chluba J., 2019, MNRAS, 483, 3459

Rephaeli Y., 1995, ApJ, 445, 33

Riess A. G., et al., 1998, AJ, 116, 1009

Robertson H. P., 1935, ApJ, 82, 284

Rogers K. K., Peiris H. V., Leistedt B., McEwen J. D., Pontzen A., 2016, MNRAS, 460, 3014

Rossetti M., Gastaldello F., Eckert D., Della Torre M., Pantiri G., Cazzoletti P., Molendi S., 2017, MNRAS, 468, 1917

Rykoff E. S., et al., 2014a, ApJ, 785, 104

Rykoff E. S., et al., 2014b, ApJ, 785, 104

Sachs R. K., Wolfe A. M., 1967, ApJ, 147, 73

Sarazin C. L., 1986, Reviews of Modern Physics, 58, 1

Sarazin C. L., 1988, X-ray emission from clusters of galaxies. Cambridge University Press

Sasaki S., 1996, PASJ, 48, L119

Sayers J., et al., 2013, ApJ, 778, 52

Sayers J., et al., 2016, ApJ, 832, 26

Sazonov S. Y., Sunyaev R. A., 1998, ApJ, 508, 1

Schellenberger G., Reiprich T. H., 2017, MNRAS, 471, 1370

Schneider P., 2015, Extragalactic Astronomy and Cosmology. Springer-Verlag Berlin Heidelberg

Schumann M., 2019, Journal of Physics G Nuclear Physics, 46, 103003

Schäfer B. M., Pfrommer C., Hell R. M., Bartelmann M., 2006, MNRAS, 370, 1713

Scott D., White M., Cohn J. D., Pierpaoli E., 2001, arXiv e-prints, pp astro–ph/0104435

Sehgal N., Bode P., Das S., Hernandez- Monteagudo C., Huffenberger K., Lin Y.-T., Ostriker J. P., Trac H., 2010, ApJ, 709, 920

Sheth R. K., Tormen G., 1999, MNRAS, 308, 119

Shi X., Komatsu E., 2014, MNRAS, 442, 521

Shimon M., Rephaeli Y., 2002, ApJ, 575, 12

Silk J., 1968, ApJ, 151, 459

Smith R. K., Brickhouse N. S., Liedahl D. A., Raymond J. C., 2001, ApJ, 556, L91

Soergel B., Giannantonio T., Efstathiou G., Puchwein E., Sijacki D., 2017, MNRAS, 468, 577

Springel V., et al., 2005, Nature, 435, 629

Stacey G. J. e. a., 2014, Proc. SPIE, 9153, 91530L

Stacey G. J., et al., 2018, Proc. SPIE, 10700, 107001M

Stern C., et al., 2019, MNRAS, 485, 69

Sunyaev R. A., Chluba J., 2009, Astronomische Nachrichten, 330, 657

Sunyaev R. A., Zeldovich Y. B., 1970, Comments Astrophys. Space Phys., 2, 66

Sunyaev R. A., Zeldovich Y. B., 1972, Comments Astrophys. Space Phys., 4, 173

Sunyaev R. A., Zeldovich I. B., 1980, MNRAS, 190, 413

Sunyaev R. A., Zeldovich I. B., 1981, Astrophysics and Space Physics Reviews, 1, 1

Takita S., et al., 2015, PASJ, 67, 51

Taranu D. S., Hudson M. J., Balogh M. L., Smith R. J., Power C., Oman K. A., Krane B., 2014, MNRAS, 440, 1934

Tarrío P., Melin J. B., Arnaud M., 2019, A&A, 626, A7

Tarrío P., Melin J.-B., Arnaud M., Pratt G. W., 2016, A&A, 591, A39

Tarrío P., Melin J.-B., Arnaud M., 2018, A&A, 614, A82

Tauber J., Pace O., Volonte S., 1994, ESA Journal, 18, 239

Tauber J. A., et al., 2010a, A&A, 520, A1

Tauber J. A., et al., 2010b, A&A, 520, A2

Tegmark M., de Oliveira-Costa A., Hamilton A. J., 2003, Phys. Rev. D, 68, 123523

Tegmark M., et al., 2004, ApJ, 606, 702

Thorne B., Dunkley J., Alonso D., Næss S., 2017, MNRAS, 469, 2821

Tinker J., Kravtsov A. V., Klypin A., Abazajian K., Warren M., Yepes G., Gottlöber S., Holz D. E., 2008, ApJ, 688, 709

Tisserand P., et al., 2007, A&A, 469, 387

Urban O., Werner N., Simionescu A., Allen S. W., Böhringer H., 2011, MNRAS, 414, 2101

Urban O., et al., 2014, MNRAS, 437, 3939

Vavagiakis E. M., et al., 2018, Proc. SPIE, 10708, 107081U

Vikhlinin A., Kravtsov A., Forman W., Jones C., Markevitch M., Murray S. S., Van Speybroeck L., 2006, ApJ, 640, 691

Vikhlinin A., et al., 2009, ApJ, 692, 1060

Vio R., Andreani P., 2018, A&A, 616, A25

Vogelsberger M., et al., 2014, Nature, 509, 177

Vogelsberger M., McKinnon R., O'Neil S., Marinacci F., Torrey P., Kannan R., 2019, MNRAS, 487, 4870

Voit G. M., 2005, Reviews of Modern Physics, 77, 207

Walker A. G., 1935, The Quarterly Journal of Mathematics, 1, 81

Wang X., Tegmark M., Jain B., Zaldarriaga M., 2003, Phys. Rev. D, 68, 123001

Warren M. S., Abazajian K., Holz D. E., Teodoro L., 2006, ApJ, 646, 881

Watson W. A., Iliev I. T., D'Aloisio A., Knebe A., Shapiro P. R., Yepes G., 2013, MNRAS, 433, 1230

White S. D. M., Navarro J. F., Evrard A. E., Frenk C. S., 1993, Nature, 366, 429

Wright E. L., 1979, ApJ, 232, 348

Xi S.-Q., Wang X.-Y., Liang Y.-F., Peng F.-K., Yang R.-Z., Liu R.-Y., 2018, Phys. Rev. D, 98, 063006

Zemcov M., et al., 2012, ApJ, 749, 114

Zwicky F., 1933, Helvetica Physica Acta, 6, 110

de Haan T., et al., 2016, ApJ, 832, 95

van Weeren R. J., de Gasperin F., Akamatsu H., Brüggen M., Feretti L., Kang H., Stroe A., Zandanel F., 2019, Space Sci. Rev., 215, 16

von der Linden A., et al., 2014a, MNRAS, 439, 2

von der Linden A., et al., 2014b, MNRAS, 443, 1973

von der Linden A., et al., 2014c, MNRAS, 443, 1973

APPENDIX A

# Technical remarks

## A.1 Common units and unit conversions in CMB- and SZ-observations

At typical CMB frequencies ($\sim$ 30 GHz to 350 GHz), most data are provided in units of thermodynamic temperature $\Delta T_{\mathrm{CMB}}$ relative to the CMB monopole of 2.7255 K, which are measured in Kelvin and denoted as $\mathrm{K_{CMB}}$. However, at frequencies > 350 GHz these units become impractical. Instead, for extented emission, surveys commonly provide the measured specific intensities $\Delta I$ in units of flux density per solid angle, e.g. MJy/sr with 1 MJy = $10^{-20}\,\mathrm{W\,m^{-2}\,Hz^{-1}}$. The surface brightness of point sources, measured in units of flux density per beam (e.g. Jy/beam) is obtained from the measured specific intensity by integration over the solid angle of the instrument beam:

$$\Delta S = \int \Delta I \,\mathrm{d}\Omega = \langle \Delta I \rangle \Omega_{\mathrm{beam}}, \tag{A.1}$$

with the beam solid angle $\Omega_{\mathrm{beam}}$ defined as

$$\Omega_{\mathrm{beam}} = \frac{\pi \theta_{\mathrm{FWHM}}}{4\ln(2)}, \tag{A.2}$$

where $\theta_{\mathrm{FWHM}}$ is the angle that corresponds to the FWHM of the instrument beam. Conversion from $\mathrm{K_{CMB}}$ to MJy/sr and vice versa is performed via the derivative of the Planckian:

$$\Delta I = \Delta T_{\mathrm{CMB}} \left.\frac{\partial B(\nu, T)}{\partial T}\right|_{T=T_{\mathrm{CMB}}} = \Delta T_{\mathrm{CMB}} \frac{2\mathrm{k_B^3} T_{\mathrm{CMB}}^2}{(\mathrm{h\,c})^2} \frac{x^4 \exp(x)}{(\exp(x)-1)^2}, \tag{A.3}$$

where $x = h\nu/(\mathrm{k_B T_{CMB}})$ is the dimensionless frequency.

Some surveys provide their data in units of brightness temperature, which is computed from the measured specific intensities via the Rayleigh-Jeans approximation of the Planckian

$$\Delta T_{\mathrm{RJ}} = \Delta I \frac{\mathrm{c}^2}{2 k_{\mathrm{B}} \nu^2}. \tag{A.4}$$

For frequencies that are much smaller than the peak-frequency of the 2.7255 K CMB blackbody, the brightness temperature gives a good approximation of $\Delta T_{\mathrm{CMB}}$. A general conversion between the two

temperatures is found by combining equation A.3 and A.4:

$$\Delta T_{\mathrm{RJ}} = \Delta T_{\mathrm{CMB}} \frac{x^2 \exp(x)}{(\exp(x) - 1)^2}. \tag{A.5}$$

Finally, the survey noise of CMB experiments is commonly expressed in units of $\mu\mathrm{K}_{\mathrm{CMB}}$-arcmin, which gives the variance of the map noise measured over pixels with a solid angle of 1 arcmin$^2$. Analogously, the survey noise can be expressed in terms of the variance in surface brightness MJy/sr-arcmin and brightness temperature $\mu\mathrm{K}_{\mathrm{RJ}}$-arcmin in square arcminute pixels.

## A.2 Radius- and mass-conversion using the NFW-profile for dark matter halos

Using the universal NFW profile of dark matter halos, which was introduced in Section 1.4.2, we can convert between halo radii and masses at different overdensities $\Delta$. To do this, we choose $R_s = R_{200}/c = 1$ and equate equation (1.52) and (1.49) to solve for $R_{\mathrm{max}} = R_\Delta$

$$\rho_0(c) \left[ \ln(1 + R_\Delta) - \frac{R_\Delta}{1 + R_\Delta} \right] - \Delta \, \rho_{\mathrm{crit.}}(z) \frac{1}{3} R_\Delta^3 = 0, \tag{A.6}$$

where $\rho_0(c)$ is computed from equation (1.51). We can now compute the ratio of the radii

$$\frac{R_\Delta}{R_{200}} = \frac{R_\Delta}{c}, \tag{A.7}$$

| $c$ | $\frac{R_{100}}{R_{200}}$ | $\frac{R_{178}}{R_{200}}$ | $\frac{R_{500}}{R_{200}}$ | $\frac{R_{1000}}{R_{200}}$ | $\frac{R_{1500}}{R_{200}}$ | $\frac{R_{2500}}{R_{200}}$ | $\frac{M_{100}}{M_{200}}$ | $\frac{M_{178}}{M_{200}}$ | $\frac{M_{500}}{M_{200}}$ | $\frac{M_{1000}}{M_{200}}$ | $\frac{M_{1500}}{M_{200}}$ | $\frac{M_{2500}}{M_{200}}$ |
|---|---|---|---|---|---|---|---|---|---|---|---|---|
| 1 | 1.48 | 1.07 | 0.56 | 0.35 | 0.25 | 0.17 | 1.61 | 1.09 | 0.45 | 0.21 | 0.12 | 0.06 |
| 2 | 1.41 | 1.06 | 0.61 | 0.41 | 0.32 | 0.22 | 1.39 | 1.06 | 0.58 | 0.34 | 0.24 | 0.14 |
| 3 | 1.38 | 1.06 | 0.64 | 0.44 | 0.35 | 0.26 | 1.30 | 1.05 | 0.65 | 0.43 | 0.32 | 0.22 |
| 4 | 1.36 | 1.05 | 0.65 | 0.46 | 0.37 | 0.28 | 1.26 | 1.04 | 0.69 | 0.49 | 0.39 | 0.28 |
| 5 | 1.35 | 1.05 | 0.66 | 0.47 | 0.39 | 0.30 | 1.23 | 1.04 | 0.72 | 0.53 | 0.44 | 0.33 |
| 6 | 1.34 | 1.05 | 0.67 | 0.48 | 0.40 | 0.31 | 1.21 | 1.03 | 0.74 | 0.57 | 0.47 | 0.37 |
| 7 | 1.34 | 1.05 | 0.67 | 0.49 | 0.41 | 0.32 | 1.19 | 1.03 | 0.76 | 0.59 | 0.50 | 0.40 |
| 8 | 1.33 | 1.05 | 0.68 | 0.50 | 0.41 | 0.32 | 1.18 | 1.03 | 0.78 | 0.62 | 0.53 | 0.43 |
| 9 | 1.33 | 1.05 | 0.68 | 0.50 | 0.42 | 0.33 | 1.17 | 1.03 | 0.79 | 0.63 | 0.55 | 0.45 |
| 10 | 1.32 | 1.05 | 0.68 | 0.51 | 0.42 | 0.34 | 1.16 | 1.03 | 0.80 | 0.65 | 0.57 | 0.47 |

Table A.1: Ratio of radii and masses at different average overdensities as a function of the concentration parameter $c$ computed for dark matter halos that follow the NFW profile (Navarro et al., 1996).

which in turn allows us to compute the ratio of the halo masses:

$$\frac{M_\Delta}{M_{200}} = \frac{\Delta}{200}\left(\frac{R_\Delta}{R_{200}}\right)^3 . \tag{A.8}$$

These two ratios have been computed for a number of concentration parameters and overdensities. The results are provided in Table A.1.

## A.3 The many definitions of the integrated Comptonization $Y_{SZ}$

An important observable in studies of galaxy clusters using the tSZ effect is the integrated Comptonization parameter $Y_{SZ}$, which is proportional to the volume integral of the ICM pressure. $Y_{SZ}$ can be related to the total thermal energy of the ICM, making it an important proxy for the total mass of clusters and therefore an interesting probe for cosmological studies. The integrated Comptonization parameter is either defined as the integral of the ICM pressure profile over a spherical or a cylindrical volume, in which case it is referred to as $Y_{sph}$ and $Y_{cyl}$, respectively. The integrated Comptonization parameter within a sphere of radius R is defined as

$$Y_{sph}(R) = \frac{\sigma_T}{m_e c^2} 4\pi \int_0^R P(r) r^2 \, dr, \tag{A.9}$$

while the one within a cylinder of radius R is given by

$$Y_{cyl}(R) = Y_{sph}(R_{max}) - \frac{\sigma_T}{m_e c^2} 4\pi \int_R^{R_{max}} P(r) r \sqrt{r^2 - R^2} \, dr, \tag{A.10}$$

where $R_{max}$ is the total radial extent of the cluster. In this work, we adopt $R_{max} = 5R_{500}$, which is a common choice and supported by numerical simulations (e.g. Arnaud et al., 2010). For $R = R_{max}$, the values obtained for $Y_{sph}$ and $Y_{cyl}$ are identical. For smaller radii, $Y_{cyl}$ always exceeds $Y_{sph}$ due to the larger volume of the cylinder, which covers the whole extent of the cluster along the l.o.s.. Table A.2 provides the ratio $Y_{cyl}/Y_{sph}$ at several common cluster radii.

The values obtained for $Y_{SZ}$ are usually given in units of $Mpc^2$ or $arcmin^2$. The former is obtained by dividing $Y_{SZ}$ by $m^2$ equivalent of a square Mpc, while the latter units are obtained by dividing $Y_{SZ}$

| $\frac{Y_{cyl}(R_{2500})}{Y_{sph}(R_{2500})}$ | $\frac{Y_{cyl}(R_{500})}{Y_{sph}(R_{500})}$ | $\frac{Y_{cyl}(R_{200})}{Y_{sph}(R_{200})}$ | $\frac{Y_{cyl}(R_{5R500})}{Y_{sph}(R_{5R500})}$ |
|---|---|---|---|
| 1.56 | 1.20 | 1.11 | 1.0 |

Table A.2: Ratio $Y_{cyl}/Y_{sph}$ computed using the UPP presented by Arnaud et al. (2010). These ratios are independent of cluster size and redshift. An NFW-profile with a concentration parameter of 4 was assumed to compute the size of clusters at different mean overdensities (see Appendix A.2).

by the square of the distance that corresponds to 1 arcmin at the redshift of the cluster:

$$Y_{\mathrm{SZ}}\,[\mathrm{Mpc}^2] = \frac{Y_{\mathrm{SZ}}}{(10^6\,\mathrm{pc})^2} \tag{A.11}$$

$$Y_{\mathrm{SZ}}\,[\mathrm{arcmin}^2] = \frac{Y_{\mathrm{SZ}}}{\left[\frac{1}{60}\frac{\pi}{180}\,D_{\mathrm{A}}(z)\right]^2} \tag{A.12}$$

Besides volume-integration of the ICM pressure model, $Y_{\mathrm{cyl}}$ can be computed directly from a given $y$-map. The simplest way is through summation of all pixels within the target aperture $\theta$:

$$Y_{\mathrm{cyl}}(\theta) = \pi\,\theta^2 \frac{1}{n_{\mathrm{p}}(<\theta)} \sum_{p(<\theta)} y(p), \tag{A.13}$$

where $y(p)$ denotes the value of the $y$-map at pixel $p$ and $n_{\mathrm{p}}$ is the number of pixels within the probed aperture. Alternatively, $Y_{\mathrm{cyl}}$ can also be obtained by integrating the Compton-$y$ profile in polar coordinates, which is especially useful for MMF-techniques that rely on an input profile and return its estimated amplitude for each cluster (e.g. Planck Collaboration 2014d, 2016h; Bleem et al. 2015, see equation (5.28) for an example that involves MMFs.)

$$Y_{\mathrm{cyl}}(R) = 2\pi \int_0^R y(r) r\,\mathrm{d}r. \tag{A.14}$$

Lastly, some authors, like Arnaud et al. (2010), define a characteristic Compton parameter that is related to the characteristic pressure given in equation 1.67

$$Y_{500} = \frac{\sigma_{\mathrm{T}}}{m_{\mathrm{e}}c^2}\frac{4}{3}\pi R_{500}^3 P_{500}. \tag{A.15}$$

Note however, that most cosmological studies with galaxy clusters, like the one conducted by the (Planck Collaboration, 2011), use $Y_{\mathrm{sph}}$ computed for e.g. $5R_{500}$.

## A.4 Line-of-sight projection

As defined in Section 1.7.1, the Comptonization parameter is the l.o.s. integral of the ICM electron pressure. The tSZ signal of a cluster can therefore be simulated by creating a map of the Comptonization parameter by projection of a parametric model for the electron pressure, e.g. the GNFW model presented by (Nagai et al., 2007). Assuming spherical symmetry, the Compton-$y$ profile of a cluster at redshift $z$ is given by

$$y(\theta) = \frac{2\,\sigma_{\mathrm{T}}}{m_{\mathrm{e}}c^2} \int_0^{l_{\mathrm{max}}} P_{\mathrm{e}}(r)\,\mathrm{d}l \quad \text{with } r = \sqrt{l^2 + \theta^2 D_{\mathrm{A}}(z)^2}, \tag{A.16}$$

where $l$ denotes the coordinate along the l.o.s., $\theta D_{\mathrm{A}}(z)$ is the coordinate in the plane of the sky orthogonal to the l.o.s., and

$$l_{\mathrm{max}} = \sqrt{R_{\mathrm{max}}^2 - \theta^2 D_{\mathrm{A}}(z)^2} \tag{A.17}$$

is the longest path through the cluster along the l.o.s. at the separation $\theta D_{\rm A}(z)$ from the center of a cluster with radius $R_{\rm max}$. Throughout this work, maximum cluster radii are assumed to be 5 $R_{500}$. For the GNFW profile, the integral needs to be solved with numerical techniques. The concept of l.o.s. integration is illustrated in Fig. A.1.

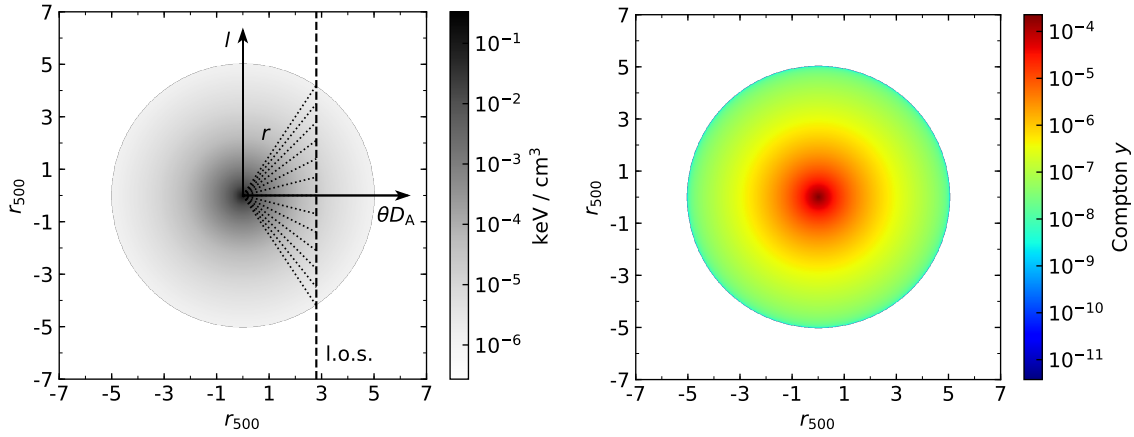


Figure A.1: **Left-hand panel:** Schematic visualisation of the l.o.s. projection of the 3D pressure profile of galaxy clusters that is used to compute the Compton-$y$ profile. For each l.o.s., defined by their angular separation $\theta$ from the cluster centre, the pressure profile is integrated along all $r$ that terminate at their intersection with the l.o.s.. Since the commonly used GNFW pressure model continues indefinitely, it needs to be truncated, which is done at $R_{\rm max} = 5R_{500}$. **Right-hand panel:** Compton-$y$ map of a cluster with $M_{500} = 10^{15}\,{\rm M}_\odot$ at $z = 0.2$ that was created by l.o.s. projection of the GNFW pressure model (Nagai et al., 2007) using the UPP presented by Arnaud et al. (2010) and assuming spherical symmetry.

## A.5 The SZ selection function

Before a sample of clusters can be used in a cosmological study, the survey used to collect the sample needs to be understood and characterized. The selection function of a survey depends both on the underlying physics of the technique that is used to find clusters, as well as on the properties of the observing instrument. This appendix gives a brief overview on the characteristics of the selection function of the tSZ effect and describes how it depends on the aperture size of the observing instrument and its sensitivity.

Although the SZ effect is not dimmed with redshift, the measured signal is affected by the spatial resolution of the survey instrument and the evolution of the pressure of the ICM. For a Compton-$y$ profile of fixed amplitude, moving a cluster from low to high redshift reduces its apparent size $\theta_{500} = R_{500}/D_{\rm A}$. Since the spatial resolution of a survey instrument remains unchanged, convolution with the PSF of the optics does increasingly dilute the signal, lowering the measured peak SZ intensity (see top panel of Fig. C.3). For clusters of a fixed mass, this trend continues even beyoned the turnover point of $D_{\rm A}$ with $\theta_{500} \propto z^{-1/2}$, since $R_{500}$ decreases with the growing matter density at increasing redshift. At the same time, the self-similar evolution of clusters predicts the gas pressure to increase with $\propto E(z)^{8/3}$, boosting $y$ and therefore the tSZ signal (see bottom panel of Fig. C.3). In combination, these two effects lead to the characteristic shape of the curve that gives the limiting mass as a function

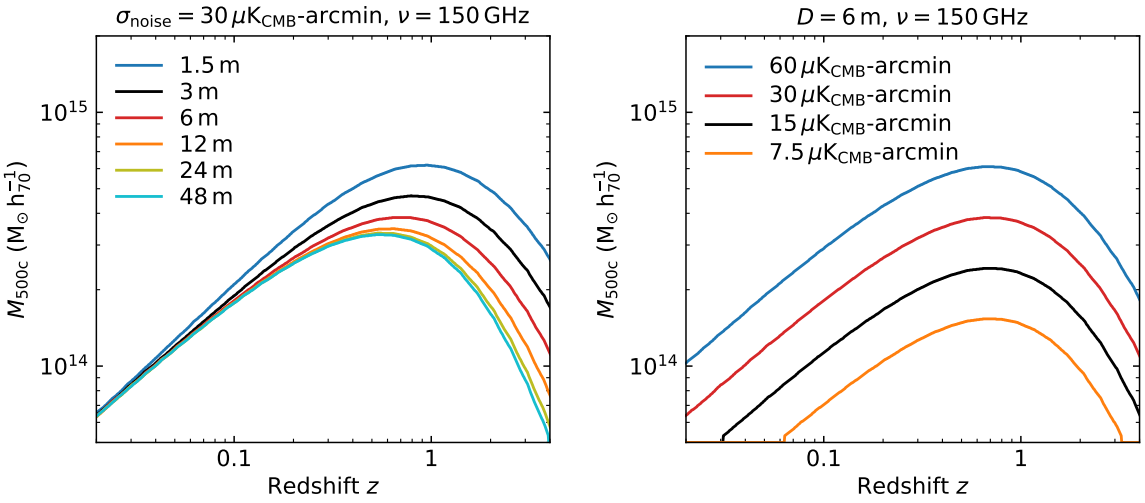


Figure A.2: Predicted limiting galaxy cluster masses as a function of redshift for single-frequency 150 GHz tSZ surveys conducted with telescopes of varying aperture size and noise level. The limiting masses are computed assuming only white noise and a detection threshold of $4.5\sigma$. The cluster model is identical to the one introduced in Section 6.3.2 and the simulated tSZ signal was extracted using single-frequency matched filters. Other astrophysical components have been neglected in order to simulate mock data at arbitrary spatial resolution. **Left-hand panel:** Predicted limiting galaxy cluster masses for a constant sensitivity of $30\,\mu\mathrm{K_{CMB}}$-arcmin but varying aperture size. With increasing telescope diameter, the limiting mass drops at medium and high redshift due to the decreased beam dilution. Low-redshift systems are not affected due to their large apparent sizes. Due to the peculiar behaviour of the angular diameter distance and the slow size evolution of clusters are are diminishing returns for apertures $\gtrsim 10$ m. **Right-hand panel:** Predicted limiting galaxy cluster masses for a constant aperture size of 6 m but varying map noise. Lower map noise boosts the SNR of all clusters and thus the shape of the curves remains unchanged.

of cluster redshift, which is shown in Fig. A.2. After an initial increase of the expected limiting mass of clusters with increasing redshift due to beam dilution, the self-similar pressure evolution leads to a sharp decrease of the limiting mass at $z \gtrsim 0.7$. This makes SZ surveys extremely powerful tools for the search of clusters at high redshift. An increase in aperture size or observed frequency increases the spatial resolution of a survey and mitigates the effect of beam dilution and lower the limiting mass across all redshifts, most notably at high-$z$. For tSZ surveys, there is a noise-dependent limit for the largest practical telescope aperture, beyoned which accessible clusters are always resolved. For current sensitivities, this threshold lies at a diameter of $\sim 12$ m, which is close to the dish size that has been deployed at the ACT and SPT. For a given aperture size, an increase in survey sensitivity increases the SNR of all clusters proportionally, leading to a lower mass limit at all redshifts. The shape of the mass limit remains almost unchanged.

## A.6 ILC offset

As mentioned in section 2.3, maps extracted using ILC-techniques can show an arbitrary offset that is introduced if the input multifrequency maps have a non-zero mean. An example of this offset is shown in Fig. A.3. This offset has to be removed after the map has been produced, which can be done by subtracting:

1. the median of the map,
2. the mean of the map after all sources have been masked,
3. the center of a Gaussian that is fit to the pixel value distribution.

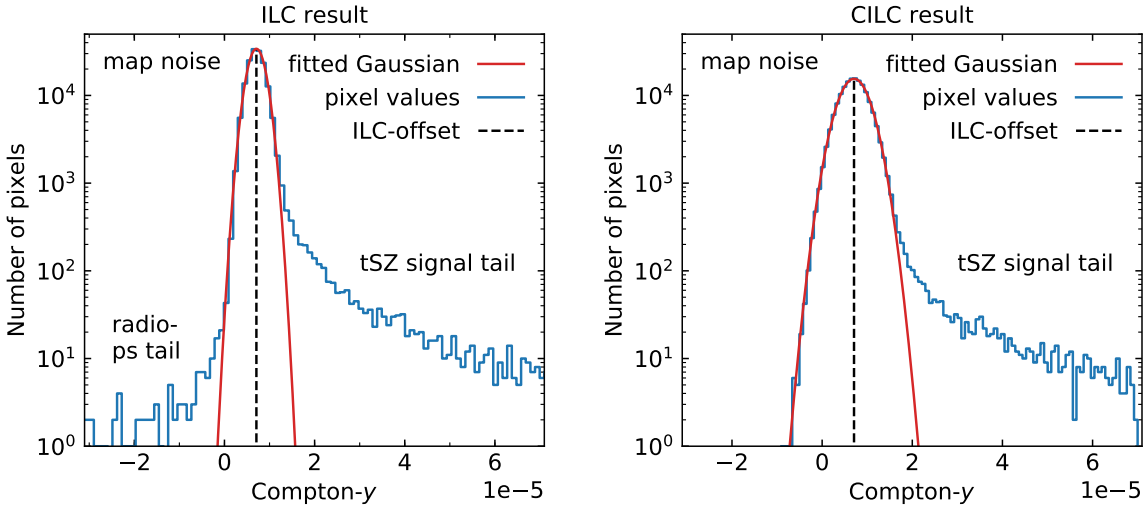


Figure A.3: Illustration of the ILC-offset that is observed when maps of the multifrequency data set that is used have a non-zero mean. Since the variance minimized by the ILC algorithm is invariant to an offset, it has to be removed afterwards. The left-hand panel shows the pixel value distribution of a $10^\circ \times 10^\circ$ $y$-map of the Coma cluster (solid blue line). The distribution was fit with a Gaussian (solid red curve), which matches the central map noise peak well and provides a good estimate of the map noise level. The long positive tail is introduced by the tSZ signal of the cluster while the negative tail is caused by residuals of radio point sources. The ILC-offset is indicated by the dashed black line. The right-hand panel shows a similar pixel value distribution that was obtained from a CILC $y$-map of the same field. An additional spectral constrain on the power SED of radio point sources has been placed in order to remove the negative tail that was seen in the left-hand panel. As a trade off, the map noise level increased by a factor of $\sim 1.7$. The observed offset is similar to the one in the ILC map.

## A.7 Basic properties of HEALPix all-sky maps

The Hierarchical Equal Area isoLatitude Pixelization (HEALPix) of a sphere was introduced by Górski et al. (2005) for the storage and visualization of data sets on the sphere and calculations on them. Since its introduction, HEALPix has become the de-facto standard tool for handling and processing astronomical all-sky data sets like the ones produced by CMB missions like WMAP and *Planck*. At its lowest resolution, HEALPix divides the surface of the sphere into 12 pixels (or curvilinear quadrilaterals to be precise), corresponding to the base resolution parameter $N_{\mathrm{side}} = 1$. Every increase in resolution doubles $N_{\mathrm{side}}$ and divides each pixel into four sub-pixels of equal area. The HEALPix pixelization is illustrated in Fig. A.4. The number of pixels $N_{\mathrm{pix}}$ and pixels size $\theta_{\mathrm{pix}}$ of a HEALPix map as a function of its resolution parameter $N_{\mathrm{side}}$ are summarized in Table A.3.

| $k$ | $N_{\mathrm{side}} = 2^k$ | $N_{\mathrm{pix}} = 12N_{\mathrm{side}}^2$ | $\theta_{\mathrm{pix}} = \sqrt{\Omega_{\mathrm{pix}}}$ | File size |
|---|---|---|---|---|
| 0 | 1 | 12 | 58.6° | 48 B |
| 1 | 2 | 48 | 29.3° | 192 B |
| 2 | 4 | 192 | 14.7° | 768 B |
| 3 | 8 | 768 | 7.3° | 3 KiB |
| 4 | 16 | 3 072 | 3.7° | 12 KiB |
| 5 | 32 | 12 288 | 1.8° | 48 KiB |
| 6 | 64 | 49 152 | 55.0′ | 192 KiB |
| 7 | 128 | 196 608 | 27.5′ | 768 KiB |
| 8 | 256 | 786 432 | 13.7′ | 3 MiB |
| 9 | 512 | 3 145 728 | 6.9′ | 12 MiB |
| 10 | 1 024 | 12 582 912 | 3.4′ | 48 MiB |
| 11 | 2 048 | 50 331 648 | 1.7′ | 192 MiB |
| 12 | 4 096 | 201 326 592 | 51.5″ | 768 MiB |
| 13 | 8 192 | 805 306 368 | 25.8″ | 3 GiB |
| 14 | 16 384 | 3 221 225 472 | 12.9″ | 12 GiB |

Table A.3: Number of pixels $N_{\mathrm{pix}}$ and pixels size $\theta_{\mathrm{pix}}$ of HEALPix maps as a function of the resolution parameter $N_{\mathrm{side}}$. The file size has been computed assuming single-precision floating point numbers, i.e. 32 bit per value.

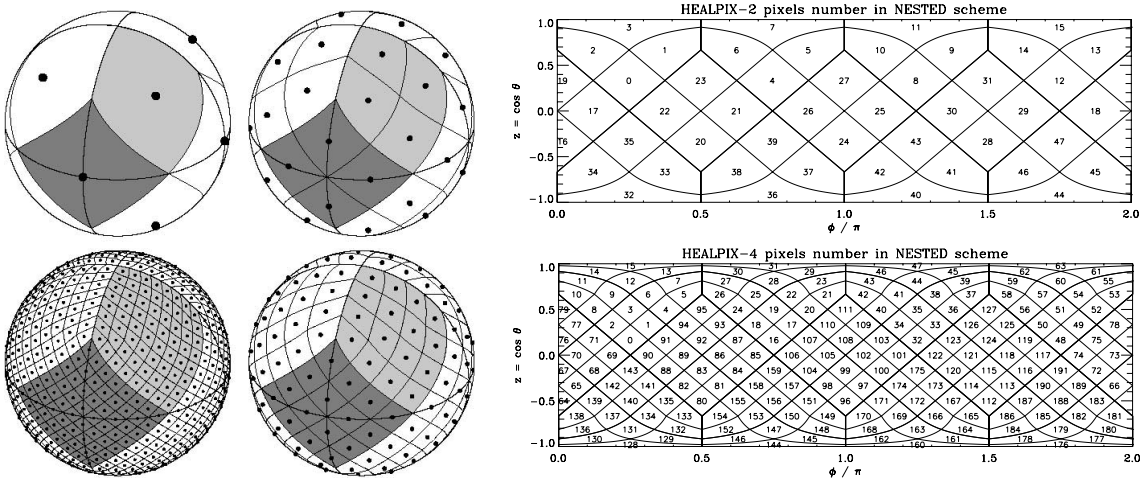


Figure A.4: Illustration of the HEALPix tessellation of the sphere. The left-hand panel shows Orthographic projections of spheres that have been partitioned into (from upper left to lower left) 12 ($N_{\mathrm{side}} = 1$), 48 ($N_{\mathrm{side}} = 2$), 192 ($N_{\mathrm{side}} = 4$), and 768 ($N_{\mathrm{side}} = 8$) pixels of equal area. The right-hand panel shows Cartesian projections of spheres at ($N_{\mathrm{side}} = 2$) (upper panel) and ($N_{\mathrm{side}} = 4$) (lower panel) that demonstrate the nested indexing scheme that is offered by HEALPix. The images have been adopted from Górski et al. (2005).

## A.8 Uniform sampling on the sphere

On several occasions in this work, uniformly distributed samples were drawn on the sphere to represent random sky positions for stacking null-tests or for the creation of mock observations. If pairs of longitude angle $\phi$ and latitude angle $\theta$ are directly drawn from uniform distributions, the data points show two distinct concentrations at the poles of the sphere due to the convergence of parallel longitude lines. This is illustrated in Fig. A.5. In order to draw samples that are uniformly distributed on the sphere, we first chose $a$ and $b$ to be uniformly distributed random numbers on the inverval $(0, 1)$ and then compute $\phi$ and $\theta$ as

$$\begin{aligned} \phi &= 2\pi a, \\ \theta &= \cos^{-1}(2b - 1). \end{aligned} \tag{A.18}$$

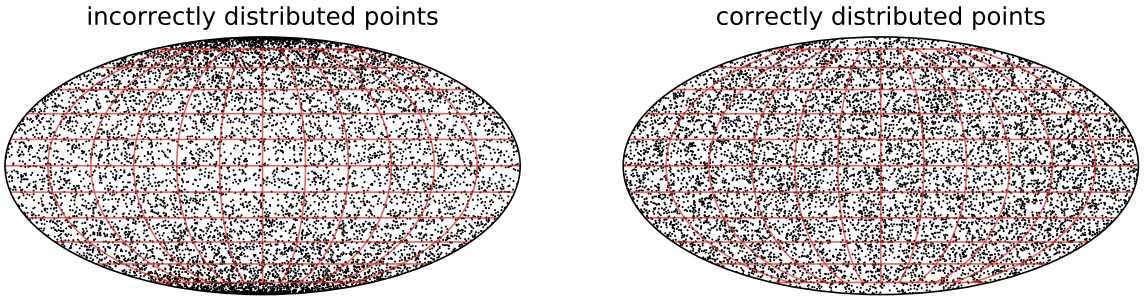


Figure A.5: Mollweide projection of the sphere populated with incorrectly and correctly sampled points. The left-hand panel shows data points ($\phi$, $\theta$) that have been drawn from uniform distributions as $\phi = \mathcal{U}(0, 2\pi)$ and $\theta = \mathcal{U}(-\pi/2, \pi/2)$. This approach leads to clustering of data points at the poles of the sphere due to the convergence of parallel longitude lines. The right-hand panel shows data points that have been correctly sampled following equation (A.18).

APPENDIX B

# Additions to Chapter 5

## B.1 A simple one-dimensional matched filter

When confronted with the idea of an MF for the first time, it is easiest to start with a simple 1D data set. Let us consider a Gaussian spectral line with an amplitude of 1 and a width $\sigma = 50$ that lies in the middle of a data set with 1000 data points. The line shall be hidden below white noise with a standard deviation of 1 such that the amplitude of the line would be measured with an SNR of 1. In order to construct a matched filter, we need to have a template of our signal that matches its expected shape (i.e. a Gaussian of correct width) and is of unit amplitude. If the shape of the template deviates from the true shape of the signal, the SNR amplification that we hope to achieve through the MF is not optimal, but might still be sufficient in practice. If the shape of the signal is roughly known, but a key property remains illusive (e.g. Gaussian of unknown width), the data set can always be processed with a range of filters that are build from different templates. In that case, the template that most closely resembles the true signal yields the strongest SNR amplification, thus allowing to estimate the shape of the signal. Assuming a Gaussian as our template, we find its Fourier transform to be

$$\tau(k) = \mathcal{F}\left(\exp\left(-\frac{x^2}{2\sigma^2}\right)\right)_x = \sqrt{2\pi}\,\sigma \exp\left(-2\pi^2\sigma^2 k^2\right), \tag{B.1}$$

while the power spectrum of white noise is flat and given by

$$P(k) = \sigma^2_{\text{noise}}/n_{\text{samples}}. \tag{B.2}$$

An MF can be computed from the template and the noise power spectrum via

$$\Psi(k) = \left(\sum_k \frac{\tau(k)^2}{P(k)}\right)^{-1} \frac{\tau(k)}{P(k)} \propto \tau(k). \tag{B.3}$$

Since the power spectrum of white noise is independent of $k$, an optimal SNR amplification can be achieved by convolving the data with the template, the amplitude of which has been re-scaled in accordance to the template shape and the standard deviation of the noise. However, the re-scaling of the filter amplitude is only performed in order to ensure that the recovered signal is unbiased and

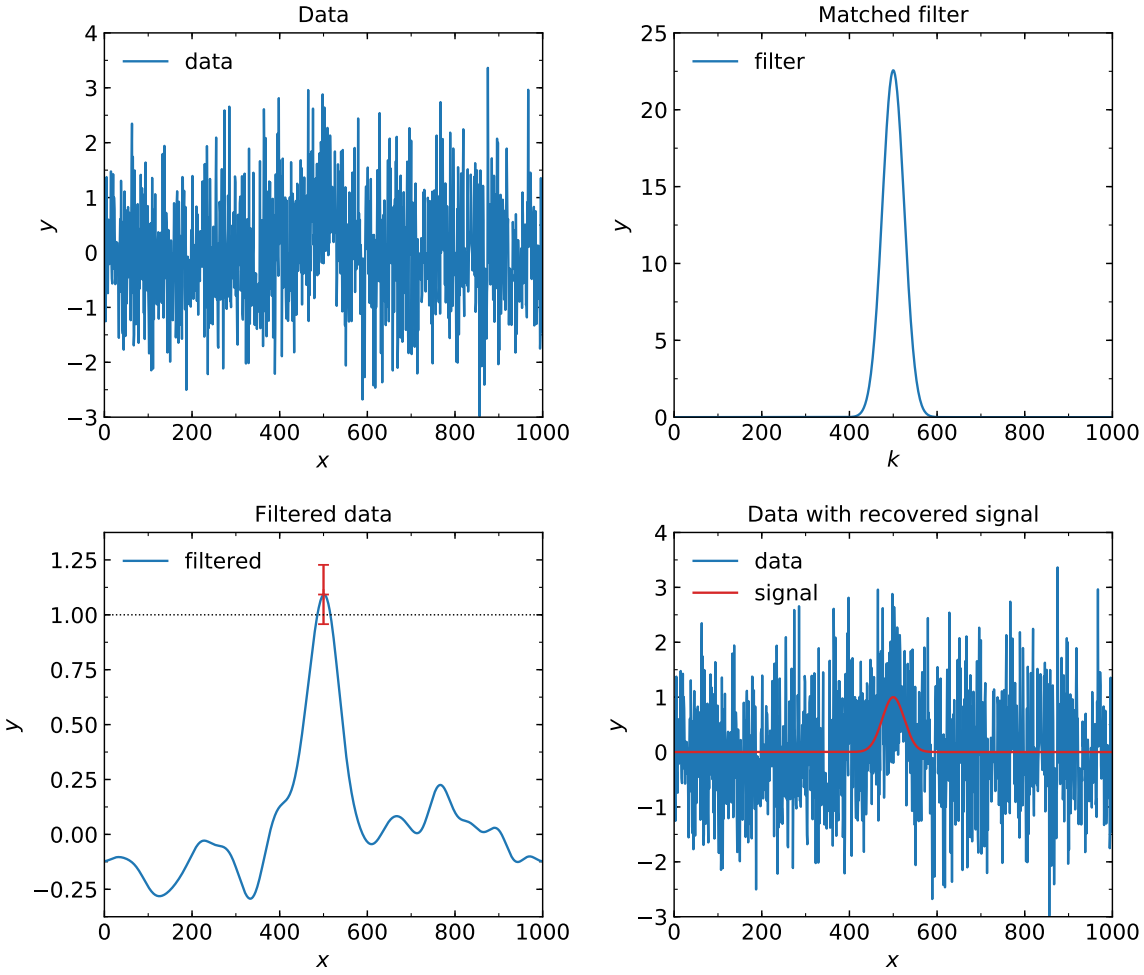


Figure B.1: Example of a one-dimensional matched filter. **Upper left:** Gaussian line centred at $x = 500$ with an amplitude of 1 and $\sigma = 50$, together with white noise with a standard deviation of 1, i.e. the Gaussian line has an SNR of 1. **Upper right:** Optimal matched filter buiied from a Gaussian signal template and the noise power spectrum of the data. In this specific example, the filter takes the same shape as the signal. **Lower left:** Data convolved with the matched filter. The matched filter yields an optimal SNR amplification of the Gaussian line (SNR = 8) and allows an unbiased estimate of its amplitude, which is found to be $1 \pm 0.125$. **Lower right:** Initial data set with the superimposed recovered signal.

does not affect the SNR of the filtered data. It is important to stress that the noise power spectrum of many data sets is not be independent of $k$, in which case the shape of the matched filter is no longer identical to the shape of the assumed signal template. After filtering, the data can be evaluated by searching for significant peaks that exceed a certain arbitrary threshold e.g. $3\sigma_{\mathrm{MF}}$. The location of the peaks coincides with the location of the target signal and the amplitude is an un-biased estimator of the original signal amplitude. The example discussed here is illustrated in Fig. B.1.

## B.2 Two-dimensional visualisation of matched filters

When processing images, spatial filters, like MFs or CMFs, take the shape of images themselves. When working with images of galaxy clusters, the spatial templates are usually assumed to be radially symmetric and thus the filters are fully characterised by their radial profile. However, it is possible to chose a template that is not radially symmetric, e.g. and ellipsoid. Fig. B.2 shows the full two-dimensional pixel-space representation of the MF and CMF that are shown in right-hand panel of Fig. 5.1. These filters are applied either by the convolution of the data with the filter kernels shown here, or by the multiplication of the Fourier transform of the data with the corresponding filter window functions.

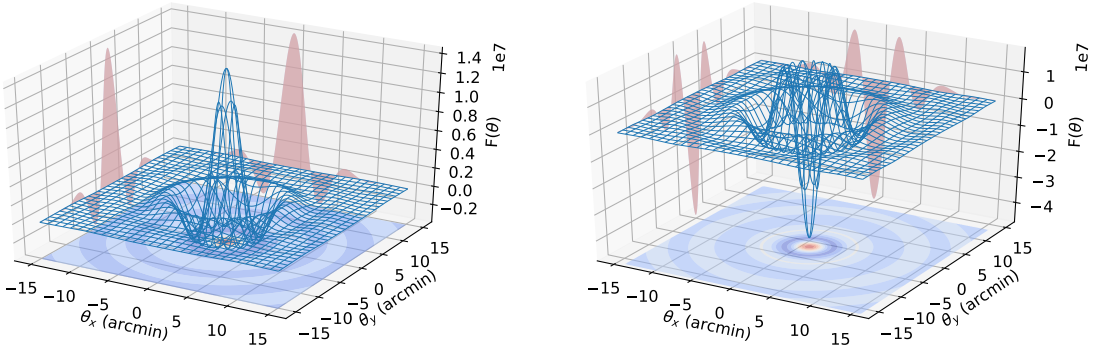


Figure B.2: Two-dimensional representation of the MF and CMF shown in the right-hand panel of Fig. 5.1, with projections along all three axis. The curves shown in the right-hand panel of Fig. 5.1 correspond to the radial profiles of the filters shown here.

## B.3 Exploring the limits of the constrained matched filter

As demonstrated in Section 5.5.1, constraining additional source templates does lead to an increase in the noise of a matched-filtered map. In order to satisfy the demanded response of the filter to an additional template, the degrees of freedom that are available for the minimization of the variance of the filtered map are reduced. For spatial filters, the degrees of freedom are represented by the spatial frequencies of the image, which are determined by the size of the image and its resolution, usually given by the instrument beam and ultimately limited by the pixel size. If an additional template is used to construct a CMF at a fixed map size and resolution, the ratio of the noise level of the map and the noise level of the same map processed with a standard MF depends on the similarity of the two templates. If both templates are given by two-dimensional Gaussians, the ratio $\sigma_{\mathrm{CMF}}/\sigma_{\mathrm{MF}}$ diverges if the width of the two Gaussians approach each other. This behaviour is illustrated in Fig. B.3. It is worth noting that a similar behaviour is expected for CILC algorithms when the spectral shape of two SED templates approach each other.

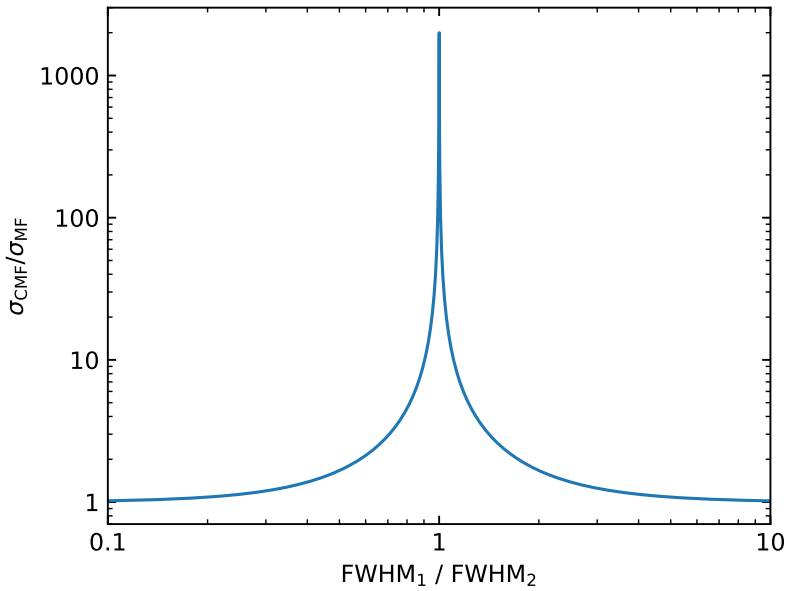


Figure B.3: Noise ratio $\sigma_{CMF}/\sigma_{MF}$ obtained for maps with two different Gaussian sources of width FWHM$_1$ and FWHM$_2$. The noise in the map is assumed to be Gaussian white noise. If FWHM$_1$ > FWHM$_2$ or vice versa, the ratio $\sigma_{CMF}/\sigma_{MF}$ approaches 1 and diverges if FWHM$_1$ approaches FWHM$_2$.

## B.4 Applying different MF and ILC techniques to the Coma cluster

In Section 5.5.2, the new CMF and CMMF methods presented in this work and published in Erler et al. (2018) were applied to the Perseus galaxy cluster in order to demonstrate how these new techniques can allow the SZ photometry of clusters with a bright central radio source. As discussed extensively in Section 5.5.1, constraining additional source templates yields a degradation of the SNR of the target signal, which depends on the spatial resolution (for MFs) or frequency coverage (for ILC methods) of the instrument. When applied to data from the *Planck* satellite, this unfortunately limits the usefulness of the new CMF and CMMF methods. Due to its comparatively low redshift of 0.0179, resulting in a large apparent size of $\theta_{500} \approx 1°$, Perseus represents an ideal target for the comparision of different component separation and filtering techniques. Although the Compton-$y$ values reported in Table 5.2 are reasonable for a cluster of Perseus' mass and redshift, it is surprising to see large differences in the shape of the filtered cluster after applying the MMF and CMMF techniques. In order to investigate if these differences in the filtered images are also observed for other clusters, we apply all six methods on *Planck* HFI data of the Coma cluster. Besides having a similar apparent size of $\theta_{500} \approx 45$ arcmin, the Coma cluster possesses a comparable mass and redshift to Perseus, allowing to infer the Compton-$y$ value and SNR of a Perseus cluster free of radio sources. The latter comparison was already made in Section 5.5.2, where the Compton-$y$ values and SNRs obtained for the two clusters are reported to be consistent with each other. The maps and extracted Compton-$y$ values, which were the basis for this comparison, are shown in Fig. B.4 and Table B.1.

We find that, contrary to the Perseus, the shape of the filtered cluster in the MMF- and CMMF-processed images are almost indistinguishable from the ones obtained from the other four methods. This is more in line with our initial expectation since e.g. the combination of and ILC and MF

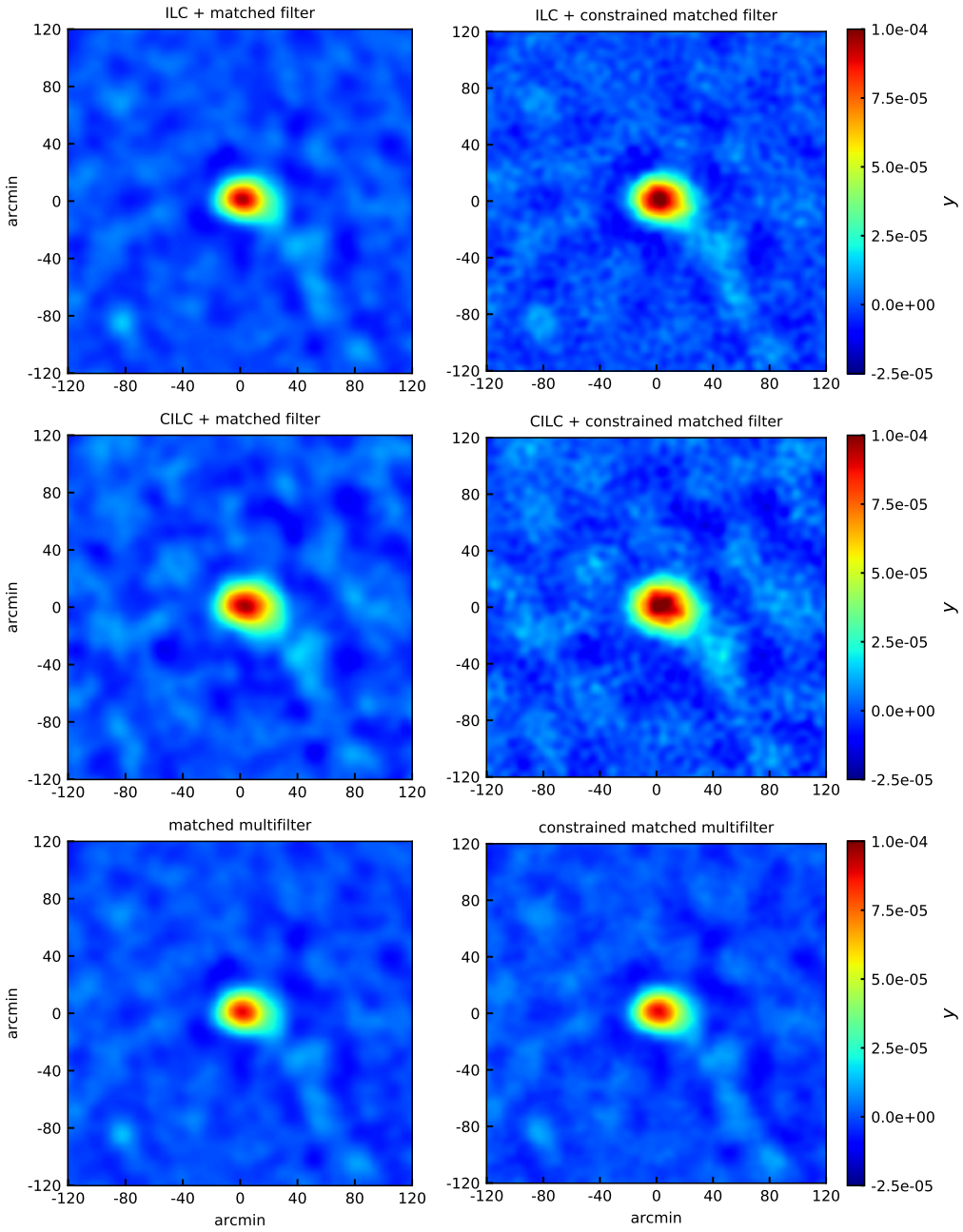


Figure B.4: Filtered maps of the Coma galaxy cluster processed with the same filtering techniques applied to maps of the Perseus galaxy cluster in Section 5.5.2 and are presented in Section 4.4.1. We apply all algorithms to $10^\circ \times 10^\circ$ *Planck* HFI maps centred on (RA, Dec.) = (12h59m48.7s, $+27^\circ 58' 50''$). The maps above show the inner $4^\circ \times 4^\circ$ of the field. In order to apply the single-frequency filters, the six HFI maps were combined into a $y$-map using ILC and CILC algorithms. For a direct comparison with the maps of the Perseus cluster shown in Fig. 5.5, the SED of Perseus A, given in Table 5.1, is used in the CILC, CMF and CMMF techniques with almost no visible impact on the cluster itself due to the lack of a bright radio source in its core. However, we observe that several unassociated radio sources in the surrounding area (outside the field shown here) are strongly reduced, indicating that their SEDs are similar to that of Perseus A. It is worth highlighting that methods which use similar information, like an MMF or an ILC followed by an MF, yield almost identical outcomes with the highest SNR of 22.

| Technique | $y_0$ $10^{-5}$ | $Y_{500}$ $10^{-5}$ Mpc$^2$ | SNR |
|---|---|---|---|
| ILC + MF | 9.43 ± 0.42 | 6.43 ± 0.29 | 22.2 |
| ILC + CMF | 10.09 ± 0.49 | 6.88 ± 0.34 | 20.4 |
| CILC + MF | 9.41 ± 0.54 | 6.41 ± 0.37 | 17.4 |
| CILC + CMF | 10.45 ± 0.61 | 7.12 ± 0.42 | 17.2 |
| MMF | 8.79 ± 0.40 | 5.99 ± 0.27 | 22.1 |
| CMMF | 8.77 ± 0.42 | 5.97 ± 0.28 | 21.1 |

Table B.1: Comparison of the extracted tSZ signal of the Coma galaxy cluster extracted from *Planck* HFI data with various ILC and MMF techniques. The corresponding maps are shown in Fig. B.4. The ILC-based techniques first combine the six HFI maps in an optimal linear combination, after which we apply either an MF or a CMF. The MMF techniques are directly applied to the HFI maps. To allow a direct comparison with the results obtained for the Perseus Cluster presented in Table 5.2, the CILC and CMMF techniques use the SED of Perseus A given in Table 5.1.

technique uses the same information as an MMF. This provides evidence that the differences in the filtered images seen for Perseus either arise from the specific details of the input maps, i.e. the presence of a bright central point source, or from differences in the implementation of the methods. An example for the latter case would be the fact that the MMF is computed and applied in Fourier space, while the implementation of the ILC algorithm used here operates in pixel space.

This choice was made intentionally since performing an ILC in Fourier space at the native resolution of each channel distorts the spatial signature of point sources like Perseus A, which has been seen when applying an MF to the official *Planck* MILCA and NILC $y$-maps provided by the Planck Collaboration (2016d). We conclude the comparison of the different ILC and MF techniques, which was performed on maps of the Perseus and Coma clusters, by noting that the new CMF and CMMF methods fulfill their intended purpose and leave a detailed exploration of the shapes of filtered clusters to future works.

## B.5 Applying the constrained matched filter to a sample of nearby *Planck* clusters

In addition to the results obtained for the Perseus galaxy cluster presented in Section 5.5.2, the CMF has been applied to an additional sample of 64 nearby galaxy clusters with $z < 0.08$, which were extracted from the PSZ2 catalogue. For each object, $10^\circ \times 10^\circ$ Gnomic projections at the six *Planck* HFI frequencies are extracted and then combined using a standard ILC algorithm in order to obtain a $y$-map of each cluster. The $y$-maps are then processed with both an MF and a CMF in order to extract their deconvolved tSZ signal amplitude $y_0$. Both filters use identical cluster templates build from a GNFW pressure profile with the Arnaud et al. (2010) best-fit parameters and the cluster masses and redshifts from the PSZ2. Additionally, the CMF is set up to have zero-response to the 10 arcmin *Planck* beam in order to mitigate potential contamination from radio point sources in the centres of clusters. The results are shown in Fig B.5.

On average, we find that the values obtained for $y_0$ through the CMF method are higher than the ones

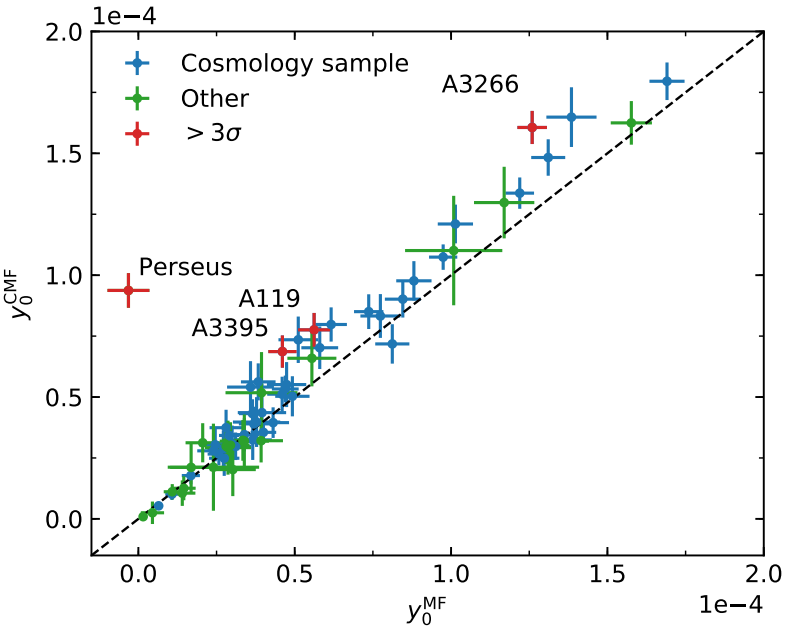


Figure B.5: Central Compton-$y$ parameter $y_0$ extracted using MFs and CMFs applied to *Planck* HFI data of 64 nearby galaxy clusters with $z < 0.08$, which are part of the PSZ2 catalogue. For comparison, the Perseus cluster was added to the plot. The black dashed line indicates the one-to-one relation. Both filters use a GNFW cluster template, in addition to which the CMF also uses a point source template. Galaxy clusters that are part of the *Planck* cluster cosmology sample are shown in blue, the remaining ones in green. Of the 64 clusters, three objects, marked in red, show a significant discrepancy between the $y_0$ values obtained using the MF and CMF methods, defined by $(y_0^{CMF} - y_0^{MF})/\sigma_{CMF} > 3$. On average, we observe that the values obtained through the CMF are larger than the ones returned by the MF. Both findings provide evidence for previously unaccounted radio sources in the centres of these clusters that can bias the measured tSZ amplitude $y_0$.

returned by a standard MF by a factor of $1.08 \pm 0.2$. This effect is stronger, but still overall insignificant, for clusters that belong to the *Planck* cluster cosmology sample with $y_0^{CMF}/y_0^{MF} = 1.13 \pm 0.16$, as opposed to $y_0^{CMF}/y_0^{MF} = 0.98 \pm 0.23$ for the remaining clusters. For three objects, namely A119, A3266, and A3395, we find a significant discrepancy with $(y_0^{CMF} - y_0^{MF})/\sigma_{CMF} > 3$. As stated in Section 2.3.2, radio sources with a falling power law SED appear in ILC and MF $y$-maps as sources with negative $y$ values and thus introduce a negative bias to the tSZ signal from clusters. The findings presented here provide some evidence that the tSZ data of at least some clusters are affected by compact radio sources.

Besides the possibility that these findings are pure coincidence, an alternative explanation might be differences in the bias that is introduced by both the MF and the CMF if the source template does not exactly match the true shape of the source. A more rigorous investigation of the observed mismatch of the MF and CMF results will be done in future works.

## B.6 Additional results obtained from applying the constrained matched filter to eROSITA mock data

In addition to the X-ray mock data presented in Section 5.4.3, we applied the combined MF plus CMF pipeline introduced in Section 5.5.3 to the more realistic mocks that were used by Clerc et al. (2018). The most important improvement these data offer over the X-ray mock data used in this work are a realistic AGN population as well as an energy and off-axis-separation dependent PSF, which was simulated using ray-tracing. However, point sources are still uniformly distributed and clusters are simulated using $\beta$-models of varying core radii and $\beta = 0.67$. The expected count rates from the simulated clusters were computed assuming $z = 0.3$, $T_X \in [1\,\mathrm{keV}, 5\,\mathrm{keV}]$, and $Z \in [0.3\,Z_\odot, 0.8\,Z_\odot]$ for fluxes in the 0.5–2 keV band ranging from $2 \times 10^{-15}$ erg s$^{-1}$ cm$^{-2}$ to $5 \times 10^{-13}$ erg s$^{-1}$ cm$^{-2}$. However, the temperature $T_X$ and metal abundance $Z$ only have a minor impact on the simulated count rates and were therefore marginalized over.

All mock images were first processed by an MF that uses a projected $\beta$-model cluster template with the same values for $\beta$ and $r_c$ as were used to simulated the clusters in the image. Bright sources above a threshold of $3\sigma_{MF}$ are then identified using the `find_peaks()` function of the python PHOTUTILS package. We then evaluate the values in a map processed with a CMF, that is designed to minimise point sources, at the positions of the candidate sources. If the values in both the MF and the CMF map surpass the threshold of $3\sigma_{MF}$, the source is classified as a galaxy cluster, otherwise as a point source. Sources that have no actual counterpart are labeled spurious sources. Except for the slightly lower detection threshold, this procedure is identical to the one presented in Section 5.5.3. Fig. B.6 shows the detection efficiency of the pipeline, defined as the fraction of simulated clusters that were correctly identified as such by the algorithm.

We find that the detection efficiency of the MF + CMF pipeline is comparable to existing pipelines in the literature (e.g. the eSASS pipeline, see Clerc et al., 2018) only for equatorial and intermediate fields. For the eROSITA deep fields, the pipeline performs even worse than for the other two. The reason for the surprisingly bad performance of the MF plus CMF pipeline is that the mock images become signal dominated and their power spectra are therefore no longer a sufficient estimators of the noise power spectrum. A significant decrease of the SNR after filtering is also seen in high SNR SZ mock data. This issue can be addressed by estimating the noise power spectrum in an alternative manner, e.g. from dedicated background maps (Tarrío et al., 2016, 2018). Besides the incorrect estimation of the noise power spectrum, the implementation of the MF and CMF used in this work make use of Gaussian statistics. As discussed in Section 5.6, a matched filter for the Poissonian low-count regime has been derived recently by Ofek & Zackay (2018). However, we note that Gaussian statistics become more applicable for high count rates and thus non-Gaussianity can not be the reason for the bad performance of the pipeline for the eROSITA deep fields. Finally, it is worth mentioning that the detection threshold used by e.g. `find_peaks()` can be tuned in order to optimise the detection of clusters while keeping the rate of spurious sources at an acceptable level.

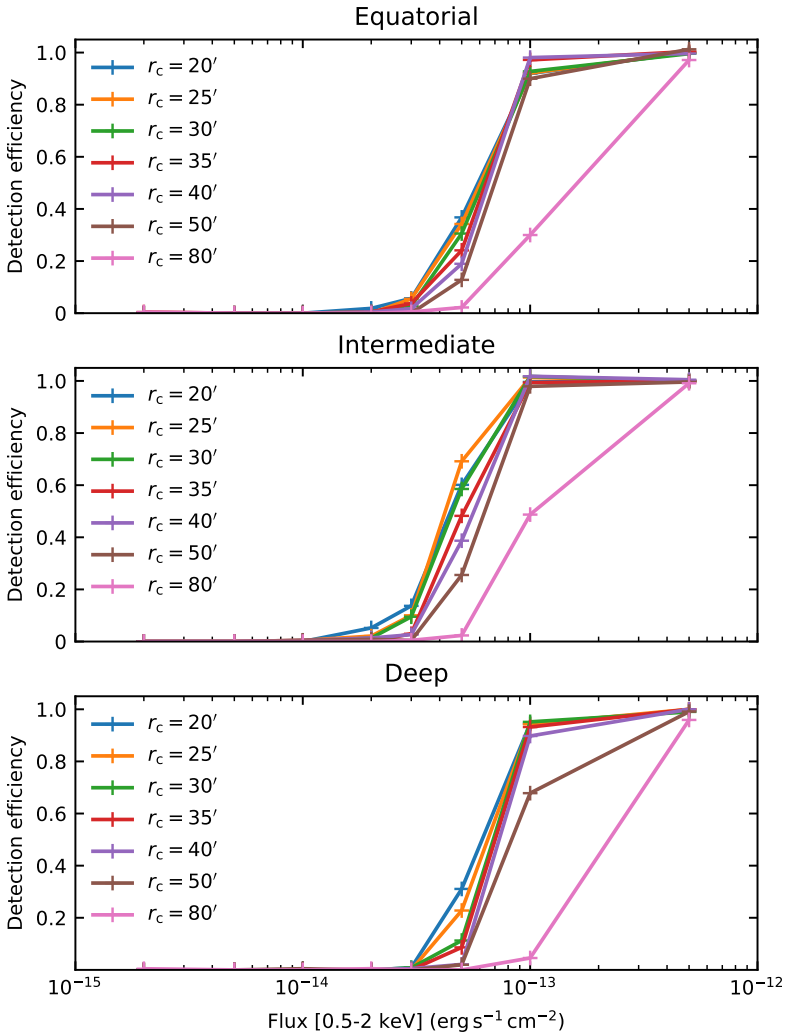


Figure B.6: Source detection efficiency of a combined MF plus CMF pipeline as a function of input flux for a range of simulated core radii. The pipeline has been applied to simulated eROSITA maps with exposure times corresponding to the expected depth of the equatorial ($\sim 2$ ks), intermediate ($\sim 4$ ks) and deep ($\sim 10$ ks) surveys. We find that, although the MF techniques offer conceptual advantages for the separation of clusters from point sources, the current implementation only provides a comparable detection efficiency to established methods in the literature (e.g. the eSASS pipeline, see Clerc et al., 2018) for mock images of the equatorial and intermediate surveys.

# APPENDIX C

# Additions to Chapter 6

This Appendix contains additional results and figures for the CCAT-prime cluster science forecasts that are presented in Chapter 6. Detailed information are given in the respective figure captions.

Fig. C.1 shows the one expected survey completeness of a $10^4$ deg$^2$ CCAT-prime + AdvACT survey as a function of mass (left-hand panel) and redshift (right-hand panel). The two panels show cross-cuts through the two-dimensional completeness shown in the right-hand panel of Fig. 6.6.

The two upper panels of Fig. C.2 show the same predicted redshift and mass distributions for a $10^4$ deg$^2$ CCAT-prime + AdvACT survey that are presented in Fig. 6.7. The two lower panels illustrate how the shape and mode of these distributions change when linear instead of logarithmic bins are used to draw the respective histograms.

Fig. C.3 illustrates how the size- and ICM pressure-evolution of galaxy clusters give rise to the characteristic shape of the tSZ limiting cluster mass curve.

Fig. C.4 and C.5 show the 2D redshift and mass distributions of the predicted and observed *Planck* and SPT-SZ cluster samples. The corresponding 1D distributions are shown in Fig. 6.20 and 6.21 of Section 6.5.1.

One of the main results presented in Chapter 6 are the expected galaxy cluster sample sizes and properties for multiple variations and combinations of CCAT-prime and AdvACT, as well as for *Planck* and SPT-SZ. All these results are summarized in Table 6.3. The corresponding mapped SNR and distributions of clusters in redshift and mass are shown in Fig. C.4–C.14.

The predicted samples reported in Table 6.3 are sub-samples of a parent sample computed via the HMF using the model presented by Tinker et al. (2008) and assuming the 2018 *Planck* + BAO ΛCDM parameter values (Planck Collaboration, 2018b). The 2D redshift and mass distribution of this parent sample are shown in Fig. 6.7, while Fig. C.15 shows the corresponding 1D distributions.

Besides predicting the galaxy cluster samples size of a CCAT-prime survey, Chapter 6 presents the spectral constraints on the SZ parameters that are achievable. Since previous forecasts were already presented by Erler et al. (2018) (Chapter 4 of this work), we begin the discussion of updated forecasts with the reproduction of these results using an updated simulation pipeline. Fig. C.16 presents the results of a spectral forecast that closely reproduces the one presented in Fig. 12 of Erler et al. (2018) (Fig. 4.12 of this work). On the other hand, Fig. C.17 shows updated results that are obtained using the same cluster model as before, but extracting the spectra of the simulated cluster with an MF technique as opposed to aperture photometry.

The close and the improved reproductions of the forecasts presented by Erler et al. (2018) both only

add white noise, according to the expected survey noise for CCAT-prime, to the simulated cluster images. One of the major improvements of the work presented here is the addition of a realistic sky model, which led to an adjustment of the expected parameter constraints to a level that is consistent with the ones obtained by current-generation instruments. Including a previously neglected kSZ component to the cluster model further degraded the constraints on the remaining tSZ parameters due to spectral degeneracies (see Fig. 6.17). In order to understand to which degree the inclusion of a kSZ component affects the remaining parameters constraints for different surveys, the simulations were repeated without a kSZ component and the results are shown in Fig. C.18.

One of the challenges in simulating the kSZ effect of clusters is the choice of the assumed l.o.s. peculiar velocity $v_{\mathrm{pec}}$. Fig. C.19 demonstrates that the constraining power on positive velocities is better than on negative velocities and that the absolute errors are tighter for small absolute values of the velocity.

Besides the detailed spectral forecasts presented for a single massive cluster, Fig. 6.18 of Section 6.4.3 shows the expected cumulative number of clusters as a function of parameter uncertainty obtained from by simulating and modeling clusters over a wide range of redshits and masses. The corresponding parameter constraints are mapped on an $z$-$M_{500c}$ grid and are shown as contours in Fig. C.20 and C.21 with and without the addition of a hypothetical X-ray $\tau_{\mathrm{e}}$ prior.

Finally, Fig. C.22 demonstrates how the addition of a cluster FIR component leads to larger parameter uncertainties and biases if the frequency coverage of the observing instrument is insufficient.

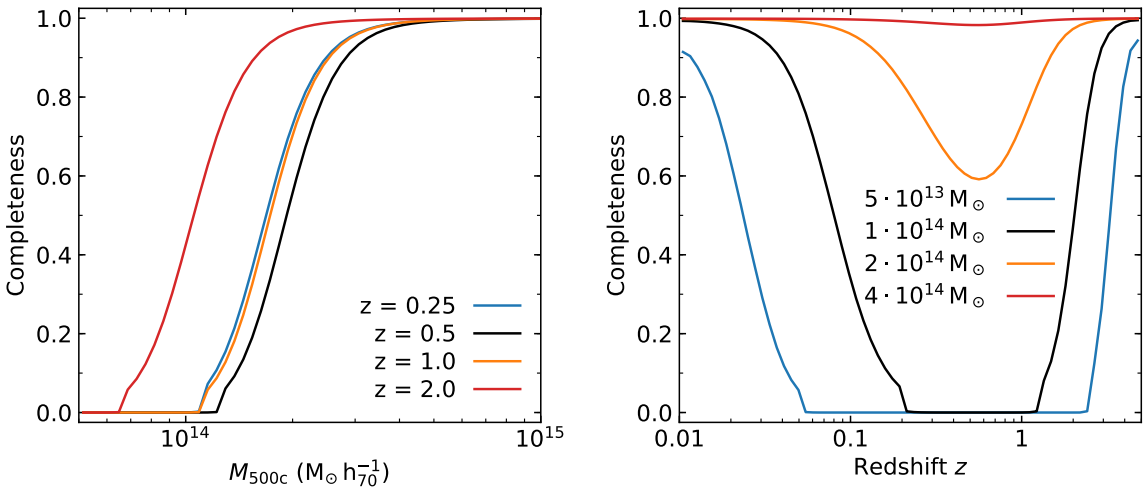


Figure C.1: Survey completeness as a function of mass and redshift. The two panels show cross-cuts through the two-dimensional completeness shown in the right-hand panel of Fig. 6.6. **Left-hand panel:** Survey completeness as a function of mass at four distinct redshifts. The kink at low completeness values is caused by the changing width of the Gaussian in equation 6.7 for low values of the SNR, which is explained in Section 6.3.4. **Right-hand panel:** Survey completeness as a function of redshift at four distinct cluster masses $M_{500c}$.

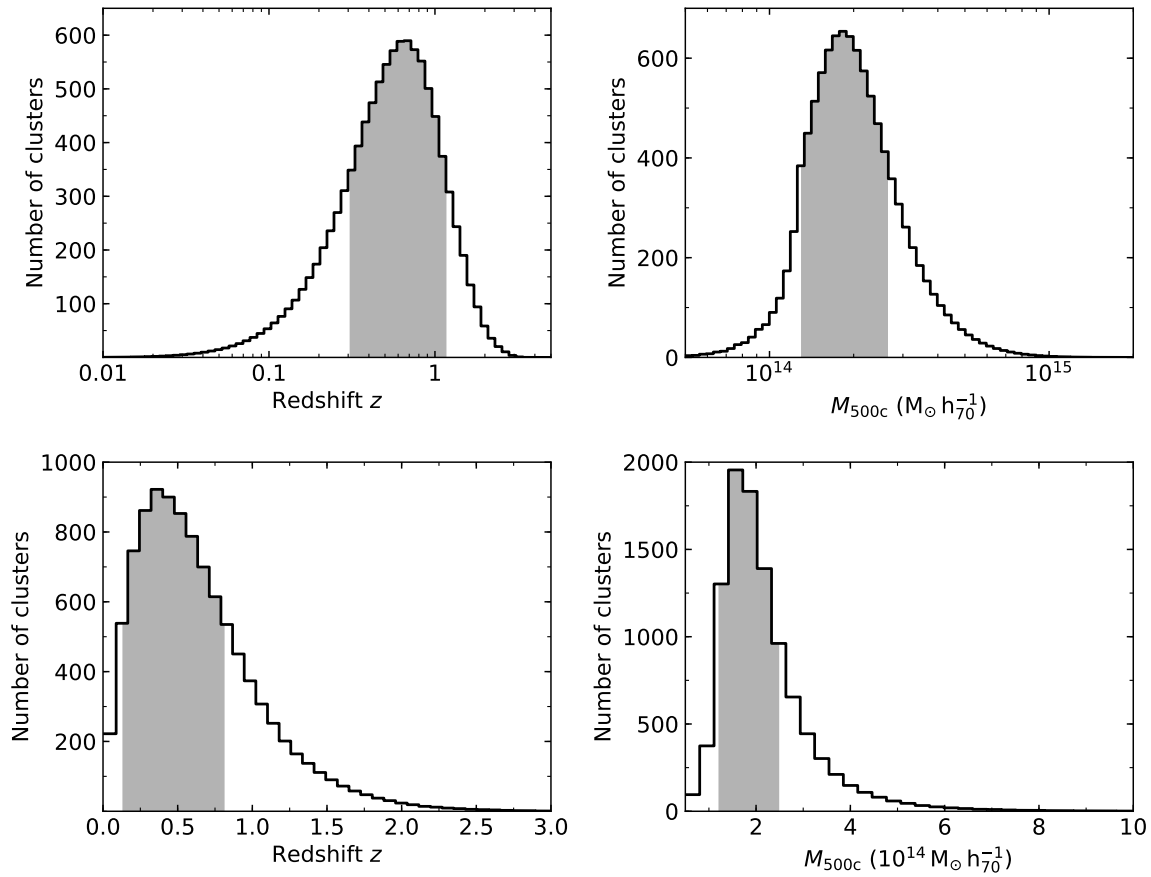


Figure C.2: Redshift and mass distributions of the predicted galaxy cluster sample obtainable with a $10^4$ deg$^2$ CCAT-prime + AdvACT survey. The two upper panels are identical to those shown in Fig. 6.8 and have been obtained by projection of the two-dimensional distribution shown in the bottom panel of Fig. 6.7 using the same logarithmically spaced bins. The two lower panels show the predicted redshift and mass distributions of the same CCAT-prime + AdvACT survey but using linearly spaced bins. The change from logarithmic to linear binning has been conducted by generating a mock catalogue with $10^6$ clusters using the method described in Section 6.3.5. The obtained one-dimensional redshift and mass histograms were normalized to contain the same number of clusters as the logarithmically binned ones above. The linearly spaced histograms have been cropped along their x-axis to highlight the central parts of the distributions. The grey area indicates the most compact interval (in logarithmic and linear space, respectively) that contains 68% of the simulated cluster sample. Note that the mode of the distributions, their shape and the extent of the 68% interval all change when linear bins are used instead of logarithmic ones. **Upper left-hand panel:** redshift distribution using logarithmic bins. **Upper right-hand panel:** mass distribution using logarithmic bins. **Lower left-hand panel:** redshift distribution using linear bins. **Lower right-hand panel:** mass distribution using linear bins.

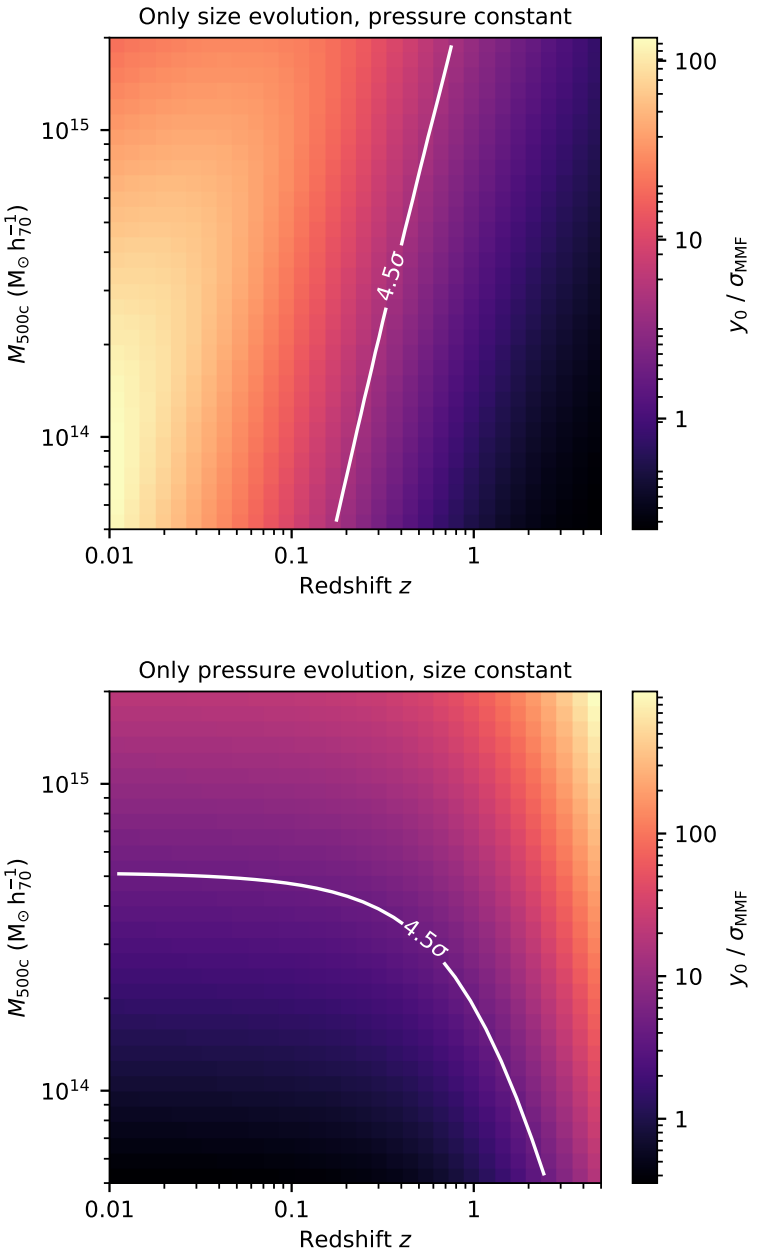


Figure C.3: **Top panel:** Expected SNR of tSZ observations of galaxy clusters defined by $y_0/\sigma_{\rm MMF}$ computed as a function of redshift and mass assuming a fixed value for $y_0$ (i.e. no pressure evolution). The expected decrease of the SNR is due to the decreasing angular size of the clusters as determined by their angular diameter distance and the intrinsic evolution of the size of clusters. When combined, these two effects lead to a monotonic decease of the observed angular size. With decreasing angular size the bright cluster cores are increasingly diluted by the fixed beam of the observing instrument, leading to a decrease in observed SNR with redshift. **Bottom panel:** Expected SNR of tSZ observations of galaxy clusters assuming a constant mass-dependent size at all redshifts, combined with a realistic evolution of the central Comptonization parameter $y_0$. Assuming a self-similar evolution of the ICM pressure, the value of $y_0$ increases with redshift, leading to an increase of the observed SNR. Combining the effects seen in the top and bottom panel leads to the characteristic shape of the tSZ limiting mass curve.

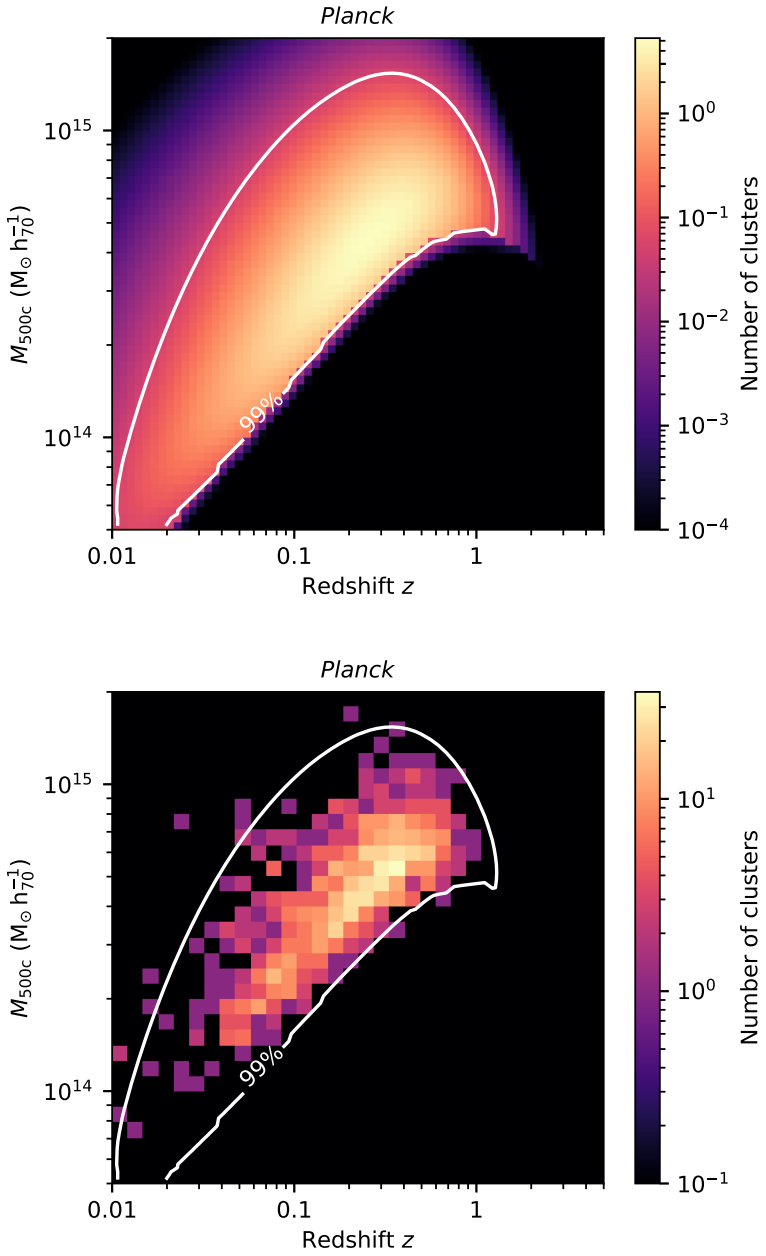


Figure C.4: **Top panel:** Galaxy cluster sample expected for a *Planck* HFI all-sky survey with six frequency bands from 100 to 857 GHz assuming $f_{\rm sky} = 0.836$. The white contour envelops the region that contains 99% of the clusters in the sample. **Bottom panel:** Distribution of the galaxy clusters from the *Planck* PSZ2 catalogue in redshift- and mass-space. The white contour envelops the region that contains 99% of the clusters in the mock sample that is presented in the top-panel of this figure. Except for the predicted high-redshift tail, the real and predicted samples are in good agreement.

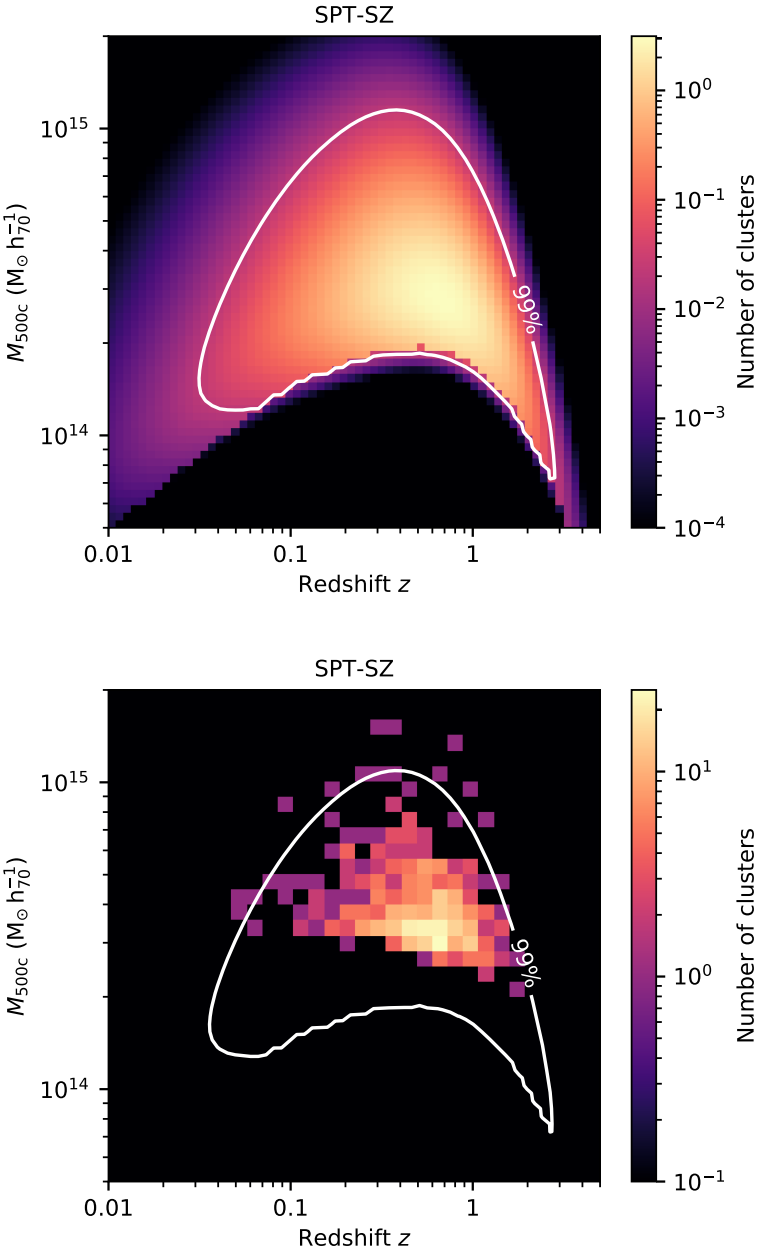


Figure C.5: **Top panel:** Galaxy cluster sample expected for the SPT-SZ survey with three frequency bands from 95 to 220 GHz. The white contour envelops the region that contains 99% of the clusters in the sample. **Bottom panel:** Distribution of the galaxy clusters from the SPT-SZ cluster catalog in redshift- and mass-space. The white contour envelops the region that contains 99% of the clusters in the mock sample that is presented in the top-panel of this figure. As argued in the main text, the systematic differences in the *Planck* and SPT-SZ mass calibration lead to a mismatch of the predicted and actual sample. The lack of low-mass clusters at low-redshift can be attributed to the spatial filtering that is applied to remove atmospheric contamination from the SPT maps.

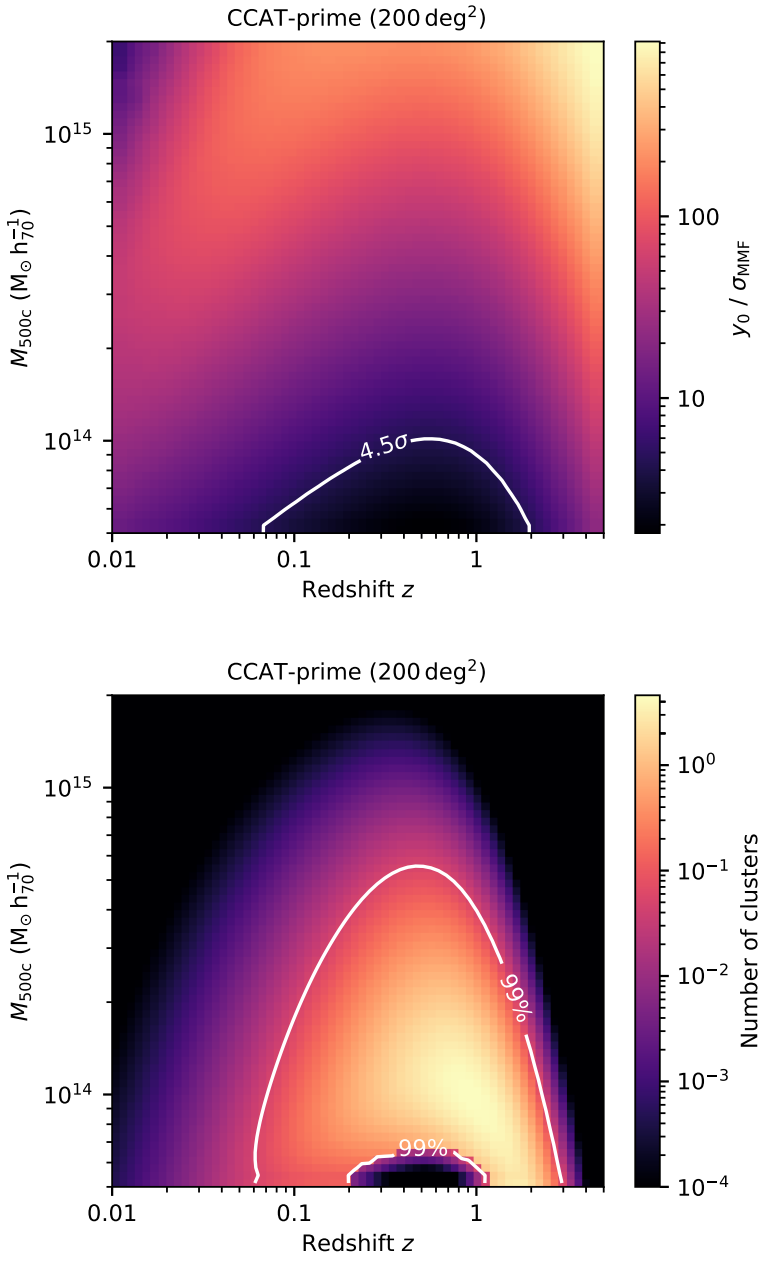


Figure C.6: **Top panel:** Expected SNR of galaxy clusters as a function of mass and redshift for a $10^3$ deg$^2$ CCAT-prime survey with seven frequency bands from 95 to 862 GHz. The solid white line indicates the $4.5\sigma_{\rm MMF}$ detection threshold. **Bottom panel:** Galaxy cluster sample expected for a $10^3$ deg$^2$ CCAT-prime survey with seven frequency bands from 95 to 862 GHz. The white contour envelops the region that contains 99% of the clusters in the sample.

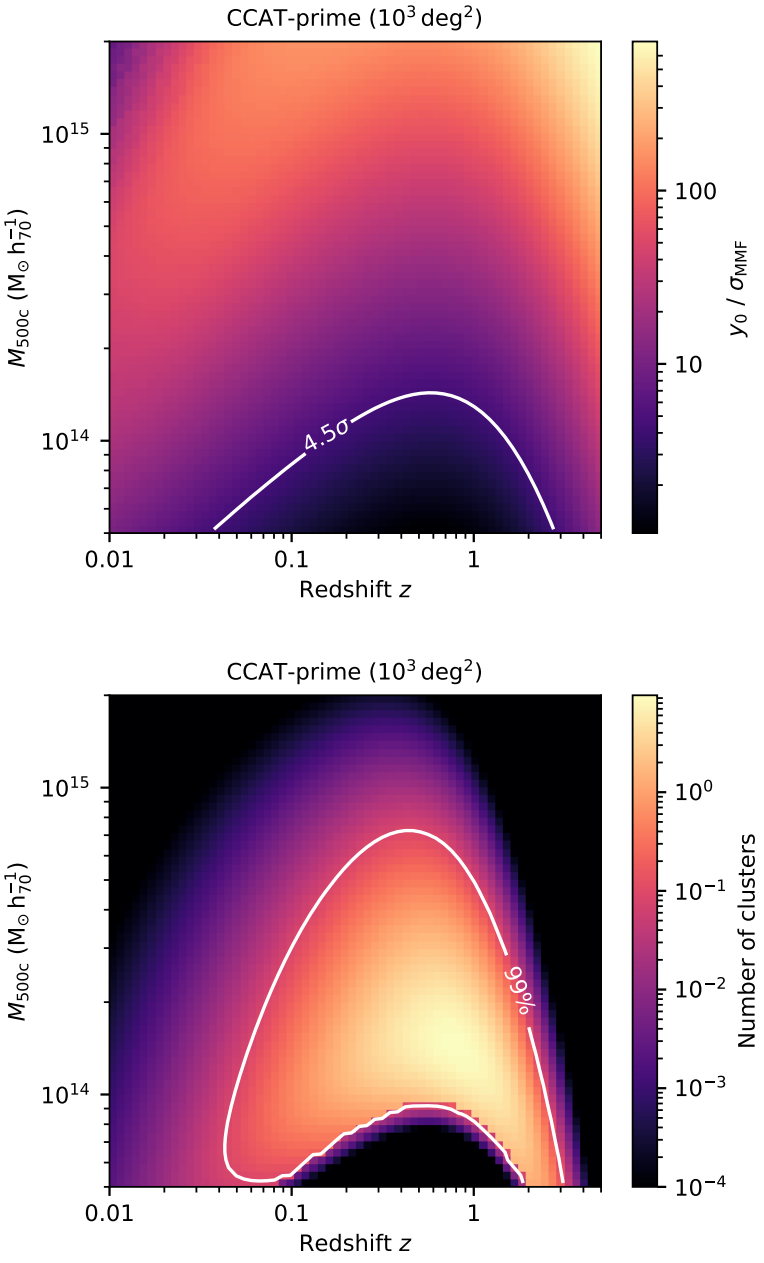


Figure C.7: **Top panel:** Expected SNR of galaxy clusters as a function of mass and redshift for a $10^3$ deg$^2$ CCAT-prime survey with seven frequency bands from 95 to 862 GHz. The solid white line indicates the $4.5\sigma_{\mathrm{MMF}}$ detection threshold. **Bottom panel:** Galaxy cluster sample expected for a $10^3$ deg$^2$ CCAT-prime survey with seven frequency bands from 95 to 862 GHz. The white contour envelops the region that contains 99% of the clusters in the sample.

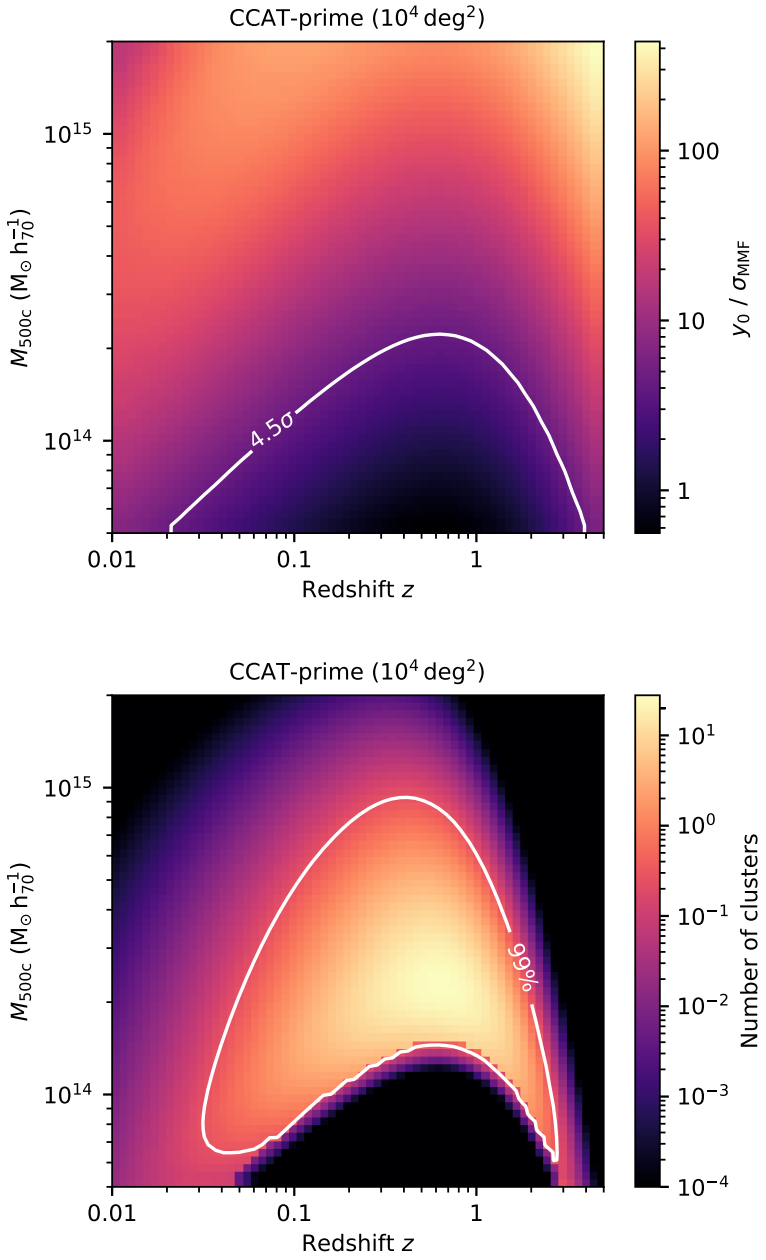


Figure C.8: **Top panel:** Expected SNR of galaxy clusters as a function of mass and redshift for a $10^4$ deg$^2$ CCAT-prime survey with seven frequency bands from 95 to 862 GHz. The solid white line indicates the $4.5\sigma_{\rm MMF}$ detection threshold. **Bottom panel:** Galaxy cluster sample expected for a $10^4$ deg$^2$ CCAT-prime survey with seven frequency bands from 95 to 862 GHz. The white contour envelops the region that contains 99% of the clusters in the sample.

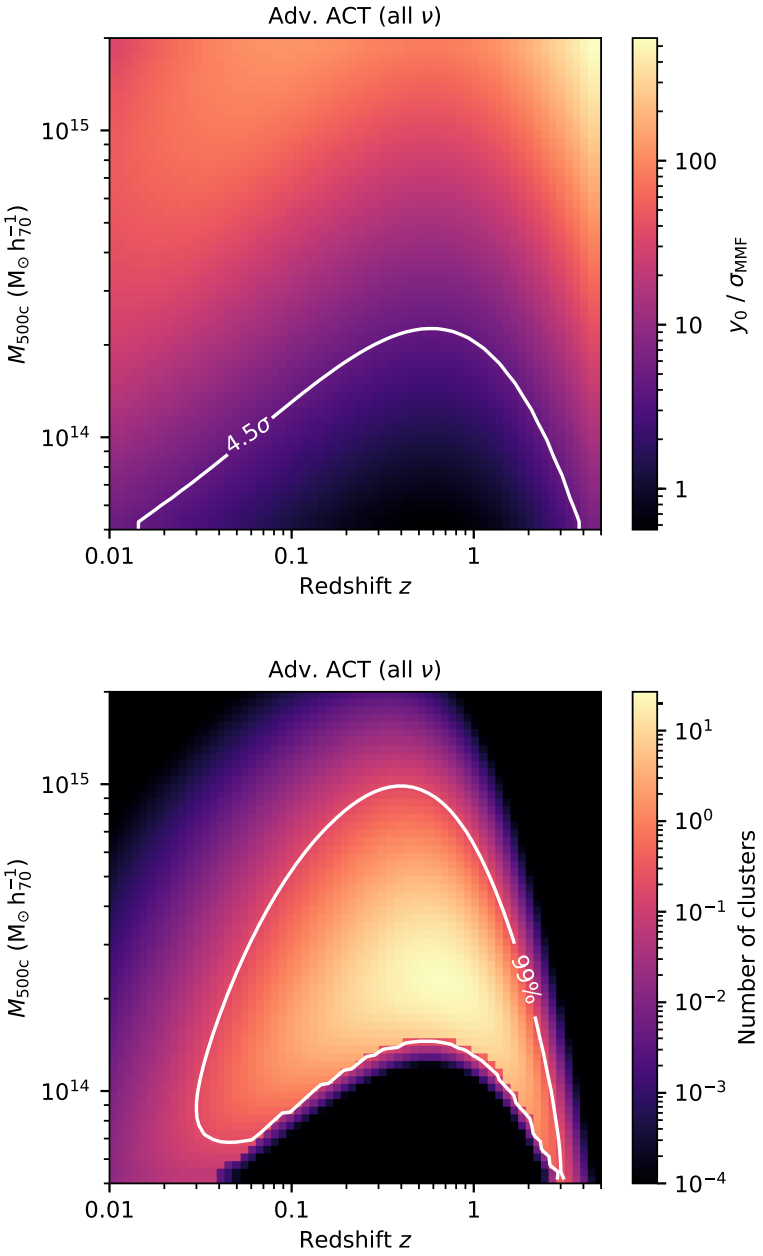


Figure C.9: **Top panel:** Expected SNR of galaxy clusters as a function of mass and redshift for a $10^4$ deg$^2$ AdvACT survey with five frequency bands from 28 to 230 GHz. The solid white line indicates the $4.5\sigma_{\rm MMF}$ detection threshold. **Bottom panel:** Galaxy cluster sample expected for a $10^4$ deg$^2$ AdvACT survey with five frequency bands from 28 to 230 GHz. The white contour envelops the region that contains 99% of the clusters in the sample.

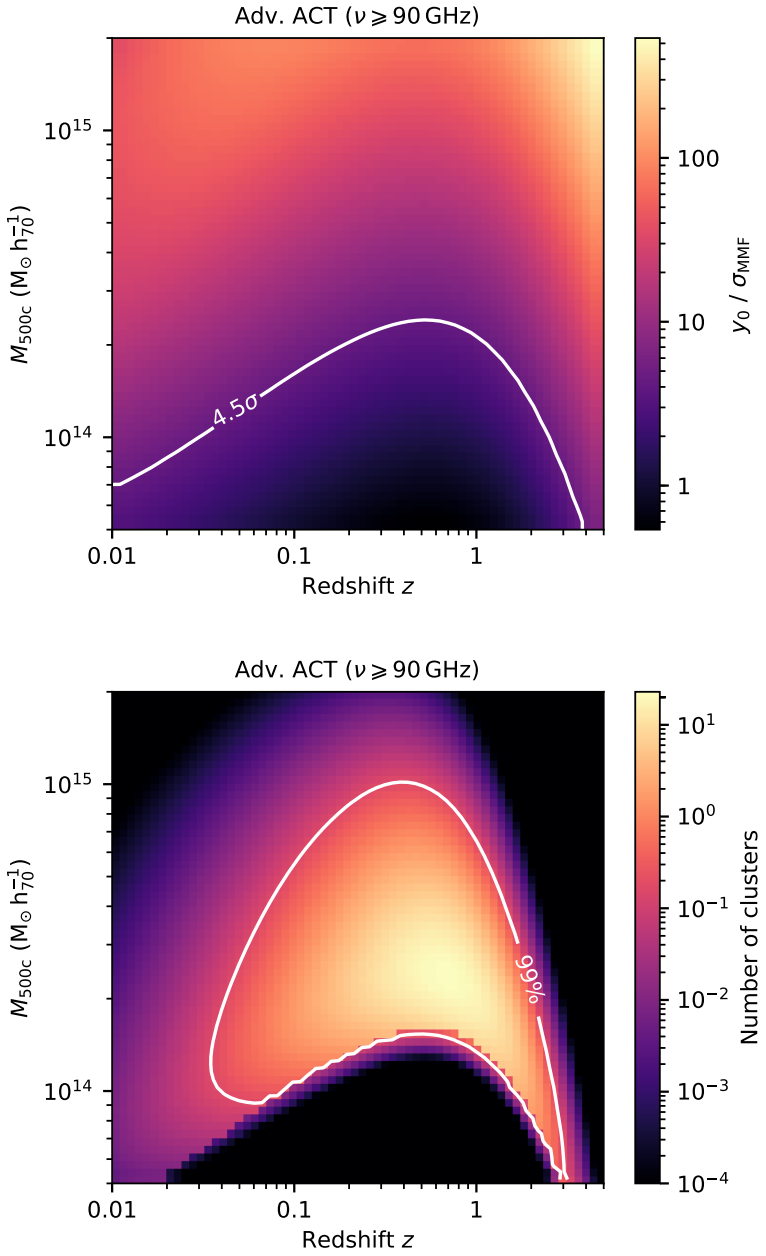


Figure C.10: **Top panel:** Expected SNR of galaxy clusters as a function of mass and redshift for a $10^4$ deg$^2$ AdvACT survey with three frequency bands from 90 to 230 GHz. The solid white line indicates the $4.5\sigma_{\rm MMF}$ detection threshold. **Bottom panel:** Galaxy cluster sample expected for a $10^4$ deg$^2$ AdvACT survey with three frequency bands from 90 to 230 GHz. The white contour envelops the region that contains 99% of the clusters in the sample.

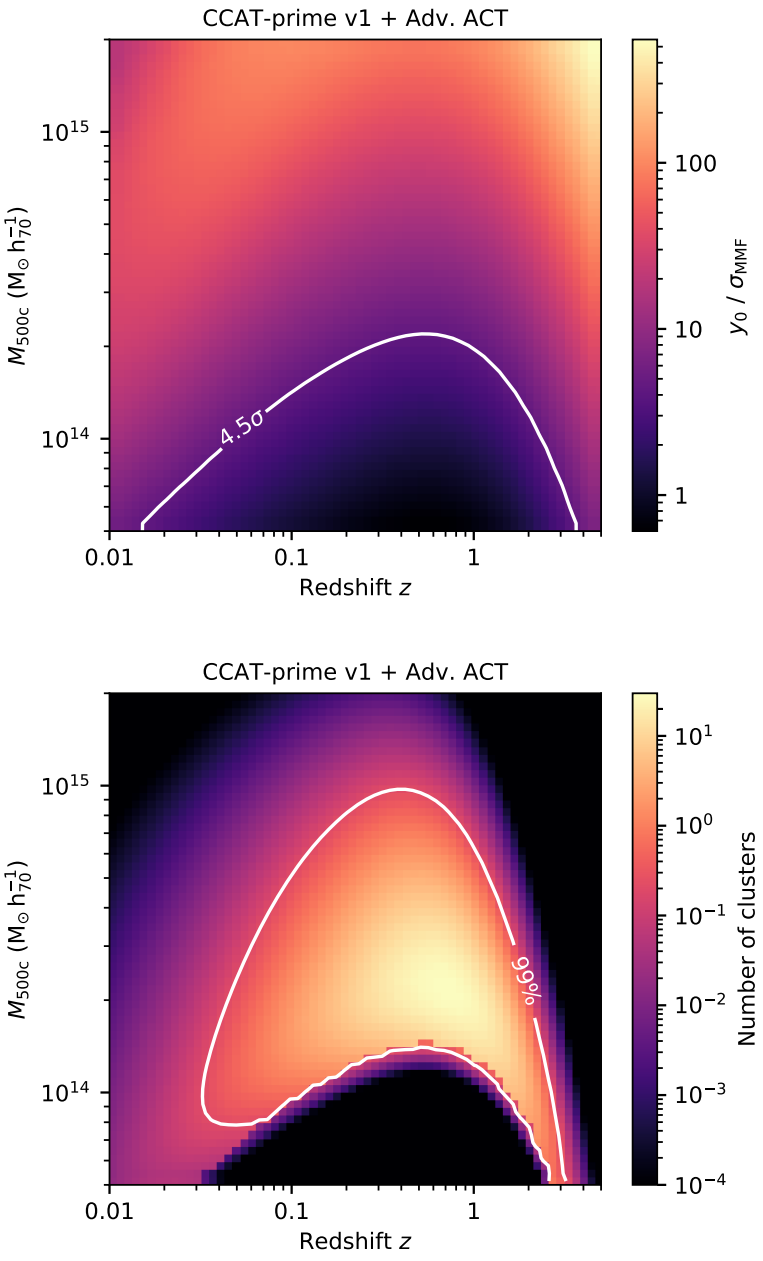


Figure C.11: **Top panel:** Expected SNR of galaxy clusters as a function of mass and redshift for a $10^4$ deg$^2$ CCAT-prime v1 + AdvACT survey with six frequency bands from 90 to 405 GHz. The solid white line indicates the $4.5\sigma_{\rm MMF}$ detection threshold. **Bottom panel:** Galaxy cluster sample expected for a $10^4$ deg$^2$ CCAT-prime v1 + AdvACT survey with six frequency bands from 90 to 405 GHz. The white contour envelops the region that contains 99% of the clusters in the sample.

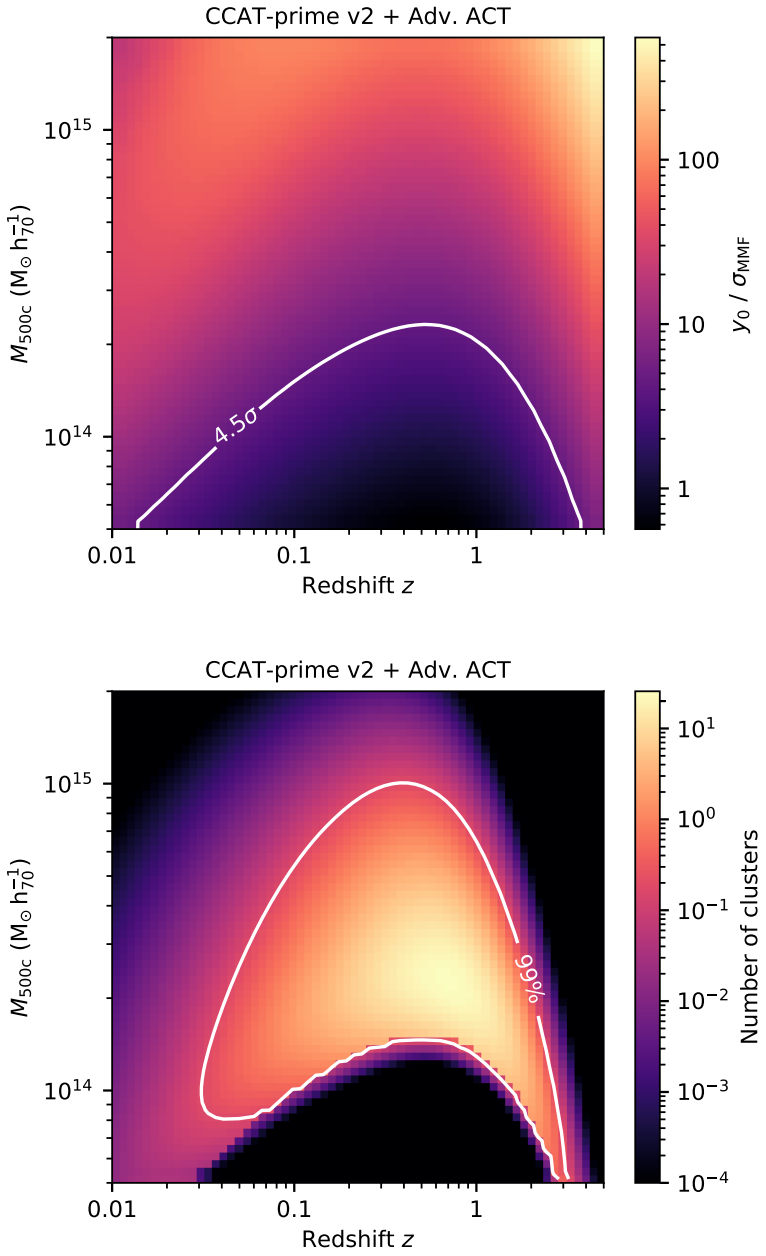


Figure C.12: **Top panel:** Expected SNR of galaxy clusters as a function of mass and redshift for a $10^4$ deg$^2$ CCAT-prime v1 + AdvACT survey with five frequency bands from 90 to 405 GHz. The solid white line indicates the $4.5\sigma_{\rm MMF}$ detection threshold. **Bottom panel:** Galaxy cluster sample expected for a $10^4$ deg$^2$ CCAT-prime v2 + AdvACT survey with five frequency bands from 90 to 405 GHz. The white contour envelops the region that contains 99% of the clusters in the sample.

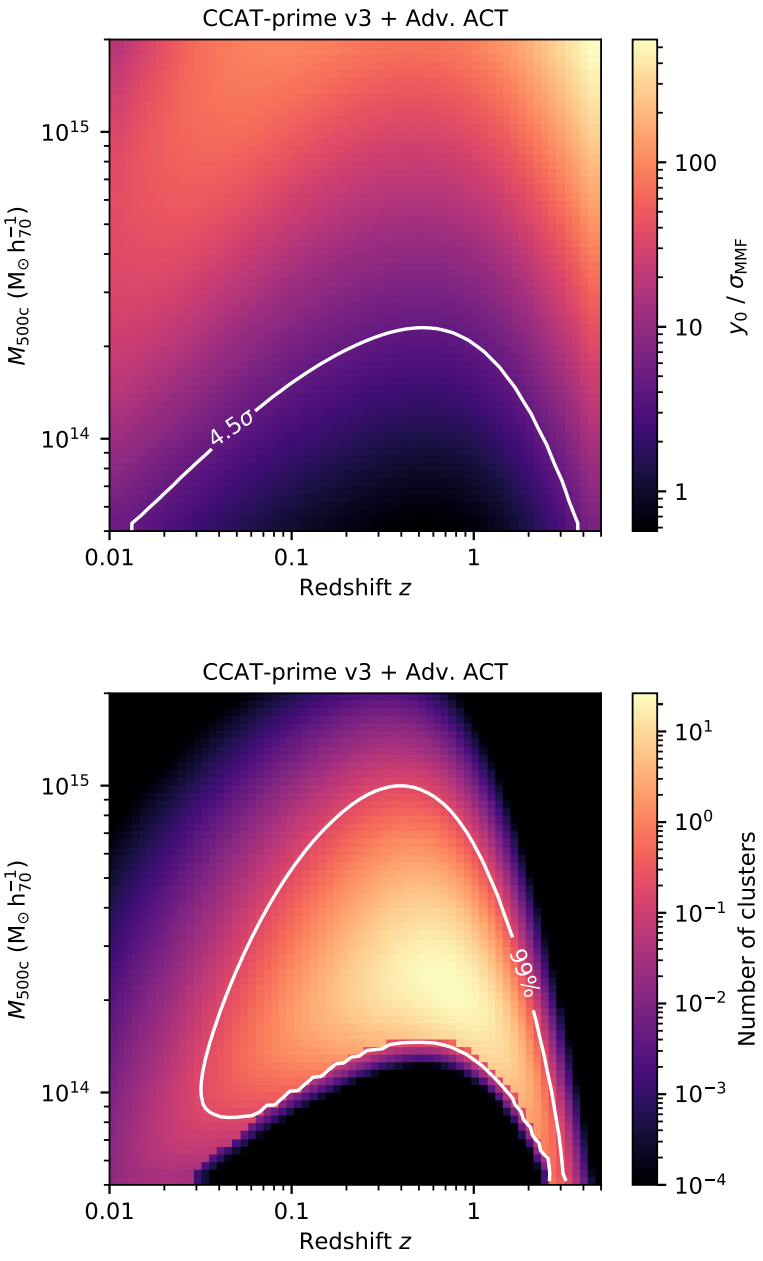


Figure C.13: **Top panel:** Expected SNR of galaxy clusters as a function of mass and redshift for a $10^4$ deg$^2$ CCAT-prime v1 + AdvACT survey with four frequency bands from 90 to 350 GHz. The solid white line indicates the $4.5\sigma_{\mathrm{MMF}}$ detection threshold. **Bottom panel:** Galaxy cluster sample expected for a $10^4$ deg$^2$ CCAT-prime v3 + AdvACT survey with four frequency bands from 90 to 350 GHz. The white contour envelops the region that contains 99% of the clusters in the sample.

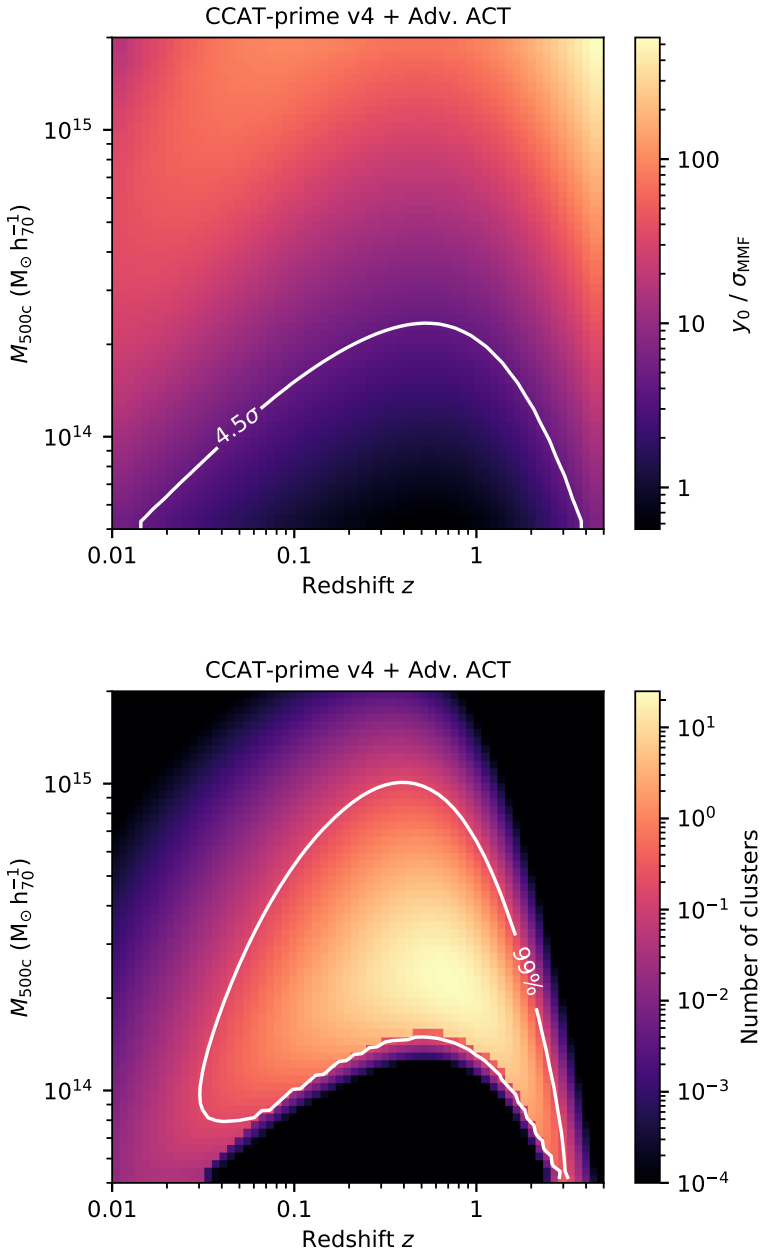


Figure C.14: **Top panel:** Expected SNR of galaxy clusters as a function of mass and redshift for a $10^4$ deg$^2$ CCAT-prime v1 + AdvACT survey with five frequency bands from 90 to 405 GHz. The solid white line indicates the $4.5\sigma_{\rm MMF}$ detection threshold. **Bottom panel:** Galaxy cluster sample expected for a $10^4$ deg$^2$ CCAT-prime v4 + AdvACT survey with five frequency bands from 90 to 405 GHz. The white contour envelops the region that contains 99% of the clusters in the sample.

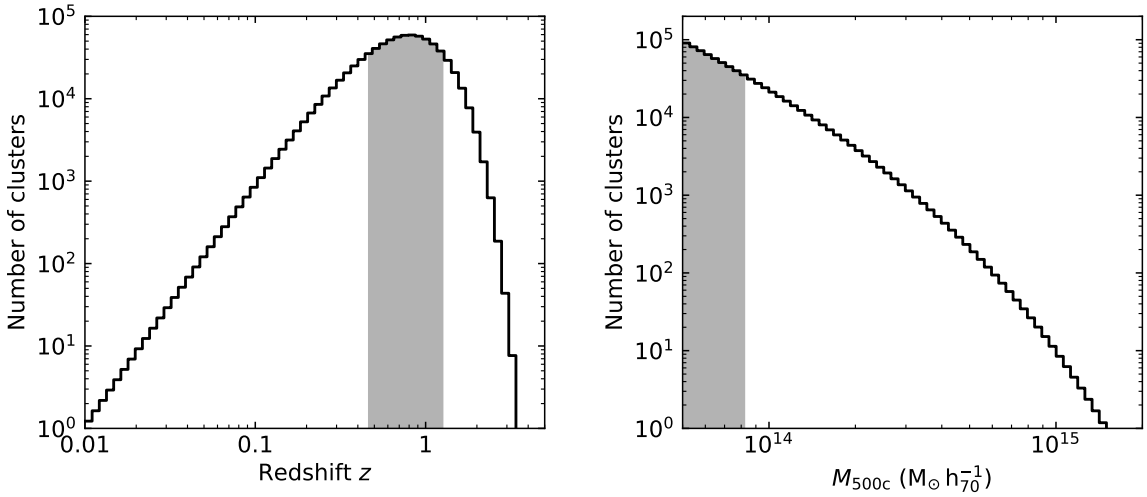


Figure C.15: Redshift and mass distributions of the complete predicted galaxy cluster sample in the range $z \in [0.01, 5]$ and $M_{500} \in [5 \times 10^{13}\,\mathrm{M}_\odot, 2 \times 10^{15}\,\mathrm{M}_\odot]$. Using the halo mass function model presented by Tinker et al. (2008) and adopting the latest 2018 *Planck* + BAO ΛCDM parameter values (Planck Collaboration, 2018b), we expect a total of 775 269 galaxy clusters in the entire sky. Both distributions have been obtained by projection of the two-dimensional distribution shown in the top panel of Fig. 6.7 and therefore use the same logarithmically spaced bins. The grey area indicates the most compact interval (in logarithmic space) that contains 68% of the simulated cluster sample. **Left-hand panel:** redshift distribution. **Right-hand panel:** mass distribution.

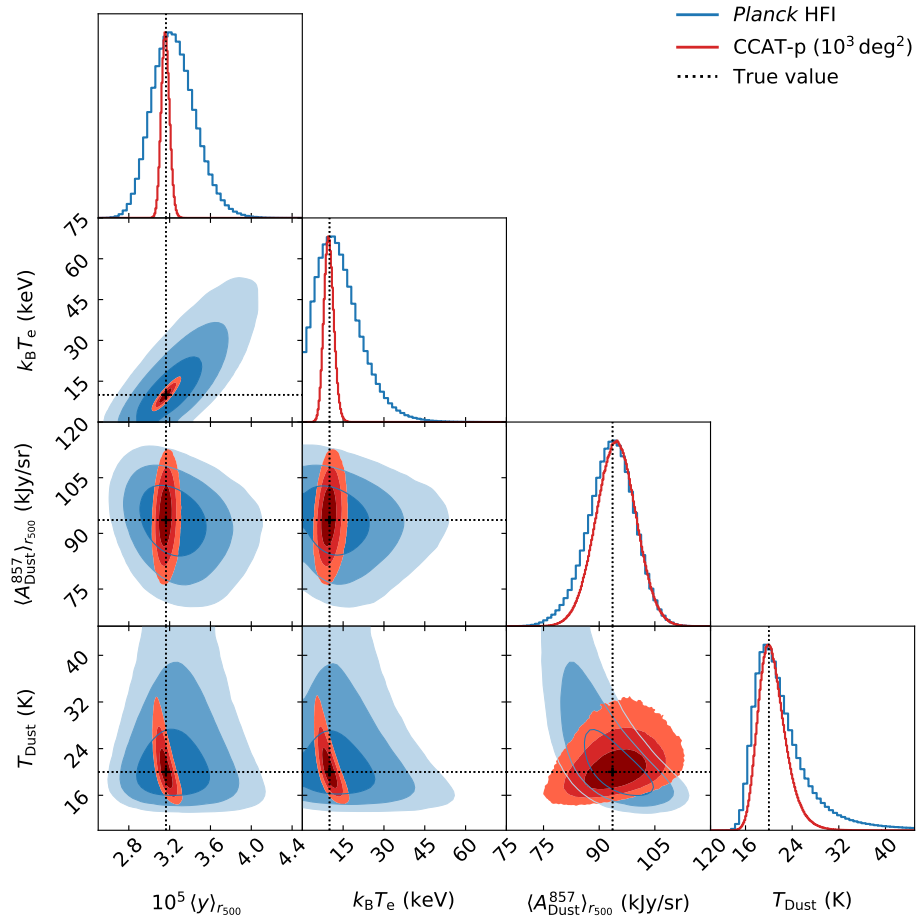


| Instrument | Area ($\mathrm{deg}^2$) | Freq. range (GHz) | $10^5\,\langle y\rangle_{r_{500}}$ | $k_\mathrm{B}T_\mathrm{e}$ (keV) | $\langle A^{857}_\mathrm{Dust}\rangle_{r_{500}}$ (kJy/sr) | $T_\mathrm{Dust}$ (K) |
|---|---|---|---|---|---|---|
| *Planck* HFI | 35k | [100, 857] | $3.20^{+0.23}_{-0.19}$ | $11.25^{+7.70}_{-7.81}$ | $94.15^{+5.55}_{-6.67}$ | $19.45^{+4.73}_{-2.73}$ |
| CCAT-p | $10^3$ | [95, 862] | $3.16^{+0.04}_{-0.04}$ | $9.52^{+1.90}_{-1.63}$ | $95.12^{+4.75}_{-5.88}$ | $20.07^{+2.39}_{-2.11}$ |

Figure C.16: Reproduction of the spectral modelling forecasts for CCAT-prime (red) and *Planck* HFI (blue) that were presented by Erler et al. (2018). The reproduced forecasts shown here assume an identical single galaxy cluster with $M_{500} = 10^{15}\,\mathrm{M}_\odot$ at $z = 0.23$, a dust mass of $5 \times 10^{10}\,\mathrm{M}_\odot$, a dust temperature of 20 K, and no l.o.s. peculiar velocity component (i.e. no kSZ signal). All astrophysical signals besides the clusters tSZ and FIR components are neglected and only instrumental white noise is added to the data according to the instument sensitivies presented in Table 4.3. The spectrum is extracted from the simulated maps by averaging the signal within a circular aperture of radius $\theta_{500}$. The data were simulated using a new python-based pipeline that is also used for the more realistic forecasts presented in this work and the parameter constraints are obtained using the `emcee` package (Foreman-Mackey et al., 2013). We find the reproduced parameter constraints shown here to be in good agreement with those presented by Erler et al. (2018).

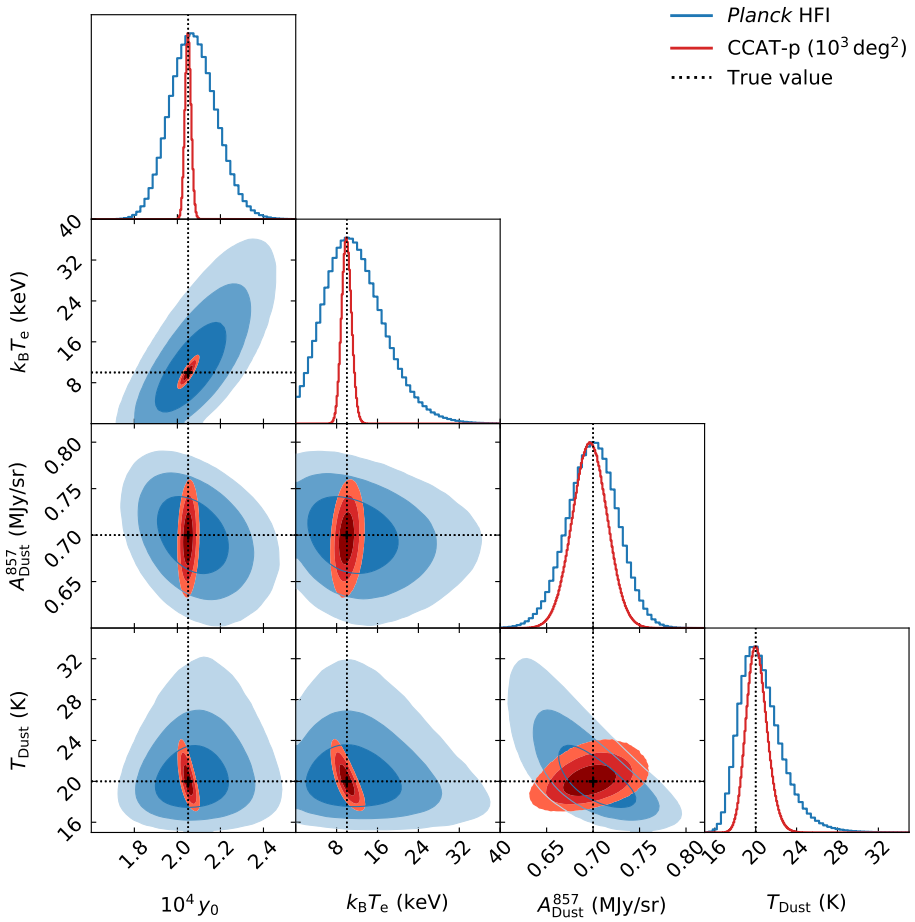


| Instrument | Area ($\mathrm{deg}^2$) | Freq. range (GHz) | $10^4\, y_0$ | $k_\mathrm{B}T_\mathrm{e}$ (keV) | $A^{857}_{\mathrm{Dust}}$ (MJy/sr) | $T_{\mathrm{Dust}}$ (K) |
|---|---|---|---|---|---|---|
| *Planck* HFI | 35k | [100, 857] | $2.07^{+0.11}_{-0.10}$ | $10.00^{+6.39}_{-5.06}$ | $0.70^{+0.03}_{-0.03}$ | $20.00^{+2.01}_{-1.87}$ |
| CCAT-p | $10^3$ | [95, 862] | $2.05^{+0.02}_{-0.01}$ | $9.87^{+1.01}_{-0.90}$ | $0.70^{+0.02}_{-0.02}$ | $20.02^{+1.02}_{-0.97}$ |

Figure C.17: Improved reproduction of the spectral modelling forecasts for CCAT-prime (red) and *Planck* HFI (blue) that were presented by Erler et al. (2018). The improved forecasts shown here were created using the same simulation pipeline and cluster model as was used for the exact reproduction shown in Fig. C.16, but the spectra where extracted using single-frequency MFs as opposed to computing the average signal within a circular aperture of radius $\theta_{500}$. Due to their optimal nature, the MFs provide a higher SNR at all frequencies, leading to improvements in the parameter constraints by up to a factor of ~two. A consequence of switching to MF extracted spectra is that instead of giving the constraints on the average $y$ and $A_{\mathrm{Dust}}$ in a given aperture one obtains constraints on the central l.o.s. peak value of both parameters.

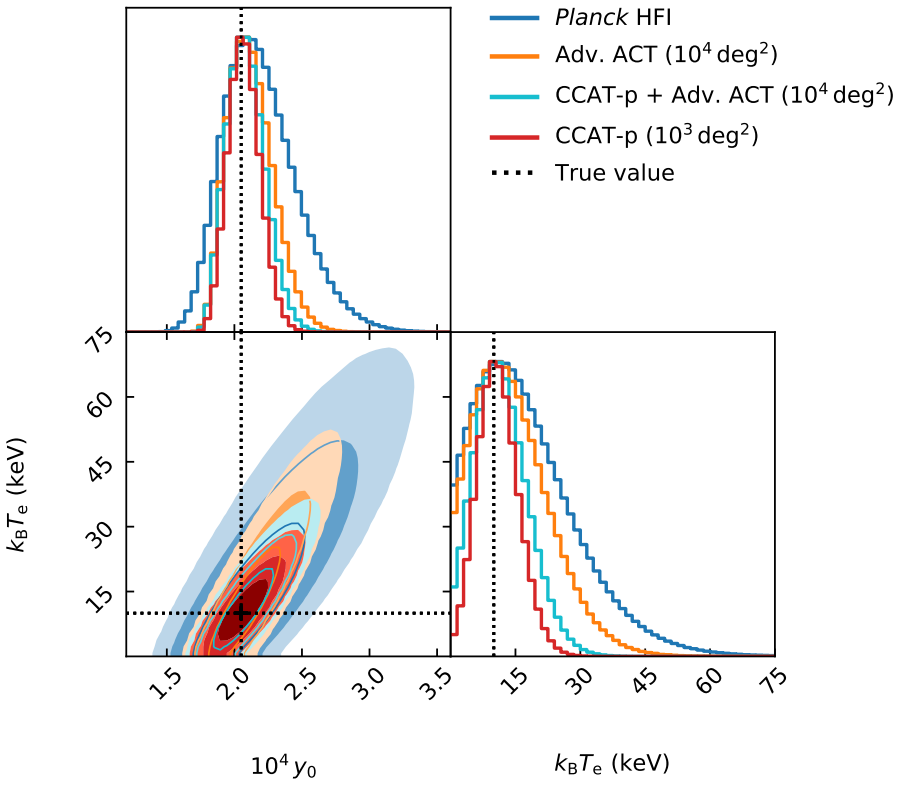


| Instrument | Area (deg$^2$) | Freq. range (GHz) | $10^4\, y_0$ | $k_B T_e$ (keV) |
|---|---|---|---|---|
| *Planck* HFI | 35k | [100, 857] | $2.10^{+0.30}_{-0.22}$ | $11.25^{+11.90}_{-9.38}$ |
| AdvACT | $10^4$ | [28, 230] | $2.07^{+0.18}_{-0.15}$ | $9.48^{+10.65}_{-6.25}$ |
| CCAT-p + AdvACT | $10^4$ | [95, 862] | $2.05^{+0.16}_{-0.12}$ | $10.72^{+6.16}_{-6.01}$ |
| CCAT-p | $10^3$ | [95, 862] | $2.05^{+0.12}_{-0.11}$ | $10.11^{+5.07}_{-4.25}$ |

Figure C.18: Spectral modelling forecasts for *Planck* HFI (blue), a $10^4$ deg$^2$ AdvACT survey (orange), a $10^4$ deg$^2$ CCAT-prime + AdvACT survey (turquoise), and a $10^3$ deg$^2$ CCAT-prime survey (red) using the realistic sky model presented in Section 6.3.1. The results shown here were obtained from simulated tSZ-only data for a single galaxy cluster with $M_{500} = 10^{15}$ M$_\odot$ at $z = 0.23$. If both the kSZ effect and cluster FIR emission are assumed to be neglectable, we expect a deep $10^3$ deg$^2$ CCAT-prime survey to measure the temperature of massive clusters at $\gtrsim 2\sigma$. This is a 50% improvement over the expected constraints for a $10^4$ deg$^2$ survey and a 100% improvement over *Planck* HFI. The latter is expected to improve further with increasing redshift due to the effect of beam dilution, which is more severe for *Planck* due to its low angular resolution.

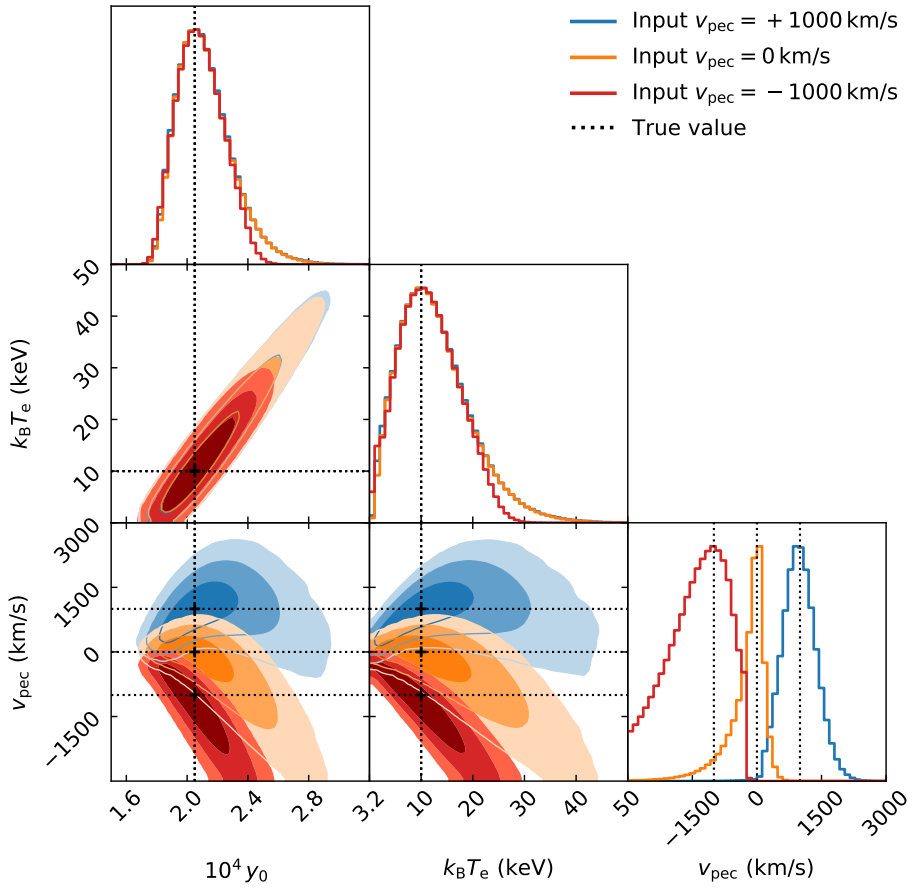


| Instrument | Area ($\mathrm{deg}^2$) | Freq. range (GHz) | Input $v_{pec}$ (km/s) | $10^4\, y_0$ | $k_B T_e$ (keV) | $v_{pec}$ (km/s) |
|---|---|---|---|---|---|---|
| CCAT-p | $10^3$ | [95, 862] | +1000 | $2.06^{+0.18}_{-0.16}$ | $10.20^{+6.96}_{-6.05}$ | $+941^{+419}_{-354}$ |
| CCAT-p | $10^3$ | [95, 862] | 0 | $2.04^{+0.19}_{-0.14}$ | $10.14^{+6.92}_{-5.88}$ | $+21^{+198}_{-417}$ |
| CCAT-p | $10^3$ | [95, 862] | -1000 | $2.06^{+0.16}_{-0.14}$ | $10.02^{+6.53}_{-5.27}$ | $-991^{+510}_{-908}$ |

Figure C.19: Spectral modelling forecasts for a $10^3$ deg$^2$ CCAT-prime survey using the realistic sky model presented in Section 6.3.1. The results shown here were obtained from simulated tSZ + kSZ data for a single galaxy cluster with $M_{500} = 10^{15}$ $M_\odot$ at $z = 0.23$ with three different values for the l.o.s. component of the peculiar velocity, −1000 km/s (red), 0 km/s (orange), and +1000 km/s (blue). The results for $v_{pec} = +1000$ km/s are also presented in Fig. 6.17. The examples given here serve to illustrate differences in the shapes of the marginalized one-dimensional $v_{pec}$ posterior distributions. We find that in general, negative peculiar velocities are harder to constrain than positive ones. In both cases, the upper bound of the 68% confidence interval (in absolute terms) is larger than the lower bound. The narrowest posterior is found to be the one for $v_{pec} = 0$ km/s. The marginalised uncertainties on the remaining two SZ parameters are mostly independent from the value of $v_{pec}$ with slightly improved errors for $v_{pec} = -1000$ km/s.

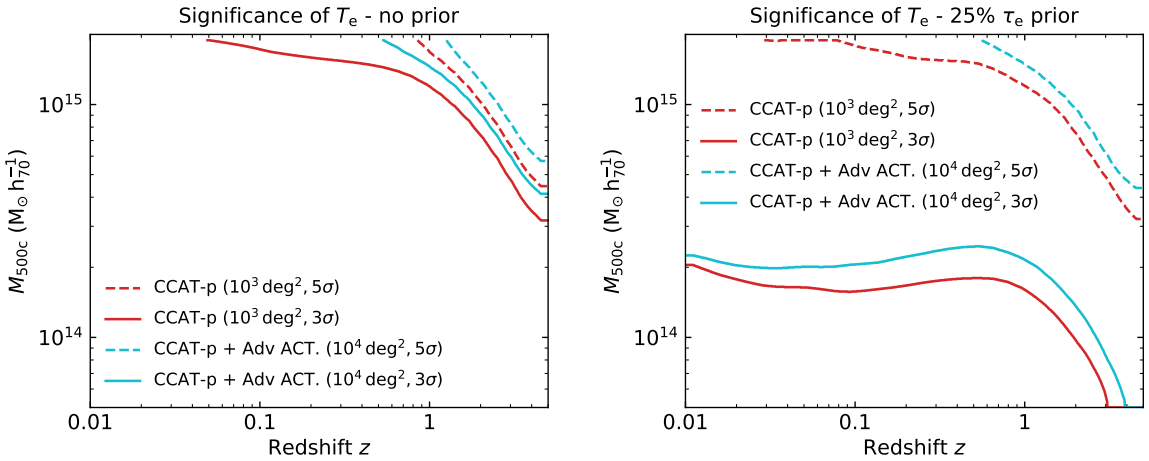


Figure C.20: Expected significance of ICM temperature measurements for a $10^4$ deg$^2$ CCAT-prime + AdvACT survey (turquoise), and a $10^3$ deg$^2$ CCAT-prime survey (red). The significance of the $T_e$ measurement is defined as the value of $T_e$ divided by its lower errorbar. The solid lines indicate the mass and redshift above which $T_e$ will be measured at $\geqslant 3\sigma$ significance, while the dashed lines indicate the minimum mass and redshift required for a measurement with $\geqslant 5\sigma$ significance. The curves were derived by simulating and modelling galaxy cluster spectra on a $32 \times 32$ logarithmically spaced grid using the cluster model introduced in Section 6.3.2 and using the realistic sky model presented in Section 6.3.1. Potential cluster FIR emission was neglected for these calculations. **Left-hand panel:** SZ-only derived significance of $T_e$ measurements. Even for a deep survey CCAT-prime we expect CCAT-prime to only measure the temperatures of the most massive clusters directly at $\gtrsim 3\sigma$ significance. **Right-hand panel:** Expected significance of $T_e$ measurements assuming a 25% Gaussian $\tau_e$ prior at all masses and redshifts. The $\tau_e$ prior allows for a $\gtrsim 3\sigma$ measurement of $T_e$ for all clusters $\gtrsim 3 \times 10^{14}$ $M_\odot$.

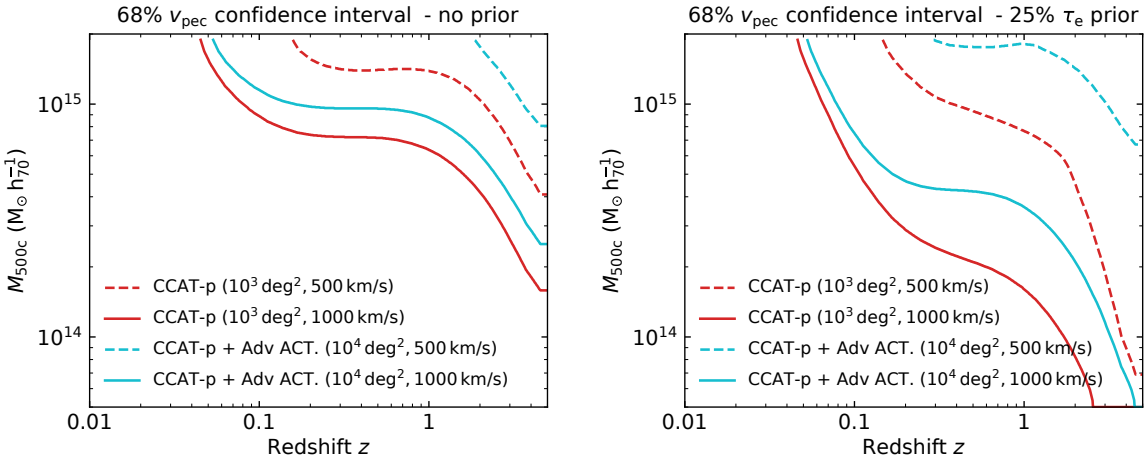


Figure C.21: Expected width of the 68% confidence interval of the measured $v_{pec}$ posterior distribution for a $10^4$ deg$^2$ CCAT-prime + AdvACT survey (turquoise), and a $10^3$ deg$^2$ CCAT-prime survey (red). The solid lines indicate the mass and redshift above which the 68% confidence interval has a width of $\leqslant 1000$ km/s, while the dashed lines indicate the minimum mass and redshift required for a measurement with $\leqslant 500$ km/s. The curves were derived by simulating and modelling galaxy cluster spectra on a $32 \times 32$ logarithmically spaced grid assuming a peculiar velocity of 0 km/s and using the cluster model introduced in Section 6.3.2 and the realistic sky model presented in Section 6.3.1. Potential cluster FIR emission was neglected for these calculations. **Left-hand panel:** SZ-only derived constraints on $v_{pec}$. Direct measurements of the peculiar velocity at $\gtrsim 3\sigma$ significance is only possible for the most massive clusters and for large (absolute) speeds. **Right-hand panel:** Expected width of the 68% confidence interval of $v_{pec}$ measurements assuming a 25% Gaussian $\tau_e$ prior at all masses and redshifts. The $\tau_e$ prior allows precise measurements of $v_{pec}$ in a much larger range in mass and redshift.

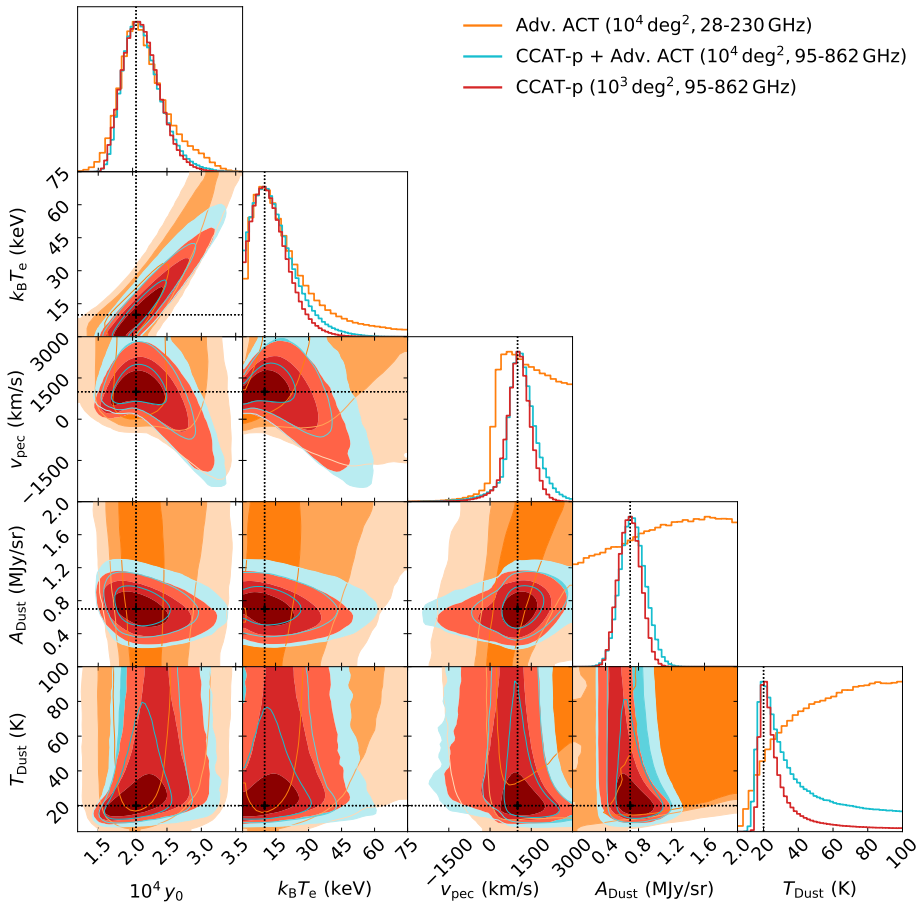


| Instrument | Area ($\mathrm{deg}^2$) | Freq. range (GHz) | $10^4\,y_0$ | $k_\mathrm{B}T_\mathrm{e}$ (keV) | $v_\mathrm{pec}$ (km/s) | $A_\mathrm{Dust}$ (MJy/sr) | $T_\mathrm{Dust}$ (K) |
|---|---|---|---|---|---|---|---|
| AdvACT | $10^4$ | [28, 230] | $2.02^{+0.41}_{-0.24}$ | $8.71^{+14.64}_{-7.10}$ | $660^{+1535}_{-424}$ | $1.75^{+0.84}_{-1.41}$ | $99.05^{+0.93}_{-51.42}$ |
| CCAT-p + AdvACT | $10^4$ | [95, 862] | $2.06^{+0.29}_{-0.23}$ | $9.08^{+10.53}_{-7.85}$ | $1000^{+601}_{-360}$ | $0.70^{+0.18}_{-0.13}$ | $19.64^{+29.24}_{-5.75}$ |
| CCAT-p | $10^3$ | [95, 862] | $2.05^{+0.30}_{-0.21}$ | $9.23^{+9.38}_{-7.27}$ | $998^{+474}_{-358}$ | $0.70^{+0.13}_{-0.14}$ | $20.77^{+10.06}_{-4.56}$ |

Figure C.22: Comparison of spectral modelling forecasts for a $10^4$ deg$^2$ AdvACT survey (orange), a $10^4$ deg$^2$ CCAT-prime + AdvACT survey (turquoise), and a $10^3$ deg$^2$ CCAT-prime survey using the realistic sky model presented in Section 6.3.1. The results shown here were obtained assuming a single galaxy cluster with $M_{500} = 10^{15}\,\mathrm{M}_\odot$ at $z = 0.23$, a dust mass of $5 \times 10^{10}\,\mathrm{M}_\odot$, a dust temperature of 20 K, and an l.o.s. peculiar velocity of 1000 km/s. We find that the addition of a cluster FIR component to the simulated spectrum (see Fig. 6.17 for SZ-only results) greatly reduced the ability of AdvACT to measure the peculiar velocity of the cluster. In addition, due to its limited high-frequency coverage, AdvACT provides no constraints on the parameters of the FIR component itself. If the FIR component is excluded from the spectral model, the estimated SZ parameter values obtained by AdvACT are biased as demonstrated in Fig. 6.19. Combining additional submillimetre channels from CCAT-prime with the data from AdvACT allows to measure the velocity of the cluster at $\gtrsim 2\sigma$ significance, while providing strong constraints on the FIR model parameters.

# List of Figures

# List of Tables

# Acronyms

**ΛCDM** Lambda cold dark matter. 1, 6–10, 15, 21, 22, 26, 36, 68, 128, 137, 139, 149, 154, 155, 157, 160, 203, 218

**HEALPix** Hierarchical Equal Area isoLatitude Pixelization. 54–56, 68–72, 75, 77, 107, 114, 128–130, 133, 190, 191

**APEC** Astrophysical Plasma Emission Code. 115

**2dFGRS** 2 Degree Field Galaxy Redshift Survey. 17, 19

**ACBAR** Arcminute Cosmology Bolometer Array Receiver. 67

**ACT** Atacama Cosmology Telescope. 43, 48, 63, 71, 106, 110, 122, 126, 132, 188

**AdvACT** Advanced Atacama Cosmology Telescope. 126, 130, 135, 137–144, 148, 149, 152–156, 158, 159, 161, 162, 166, 167, 203, 205, 212–217, 221, 223–225

**AGN** active galactic nucleus. 28, 63, 115, 120, 122, 123, 200

**ALMA** Atacama Large Millimeter Array. 48, 49

**AME** Anomalous Microwave Emission. 17, 79, 129

**AtLAST** Atacama Large-Aperture Submm/mm Telescope. 50, 168

**BAO** baryon acoustic oscillation. 13, 15, 26, 137, 139, 155, 203, 218

**BBN** Big Bang nucleosynthesis. 13, 37

**BCG** brightest cluster galaxy. 27, 116, 119, 123

**CAD** computer aided design. 48

**CAMB** Code for Anisotropies in the Microwave Background. 20, 112, 128

**CARMA** Combined Array for Research in Millimeter-Wave Astronomy. 29

**CDM** cold dark matter. 5, 6, 11, 15, 26

**CHAI** CCAT Heterodyne Array Instrument. 48, 49

**CIB** Cosmic Infrared Background. 17, 46, 68, 79, 80, 90, 112, 126, 128, 129, 133, 150, 159, 161, 162, 166, 167

**CILC** constrained internal linear combination. 53, 54, 63, 117–119, 189, 196–198

**CMB** Cosmic Microwave Background. 5–8, 10–18, 28, 30, 32, 37–43, 45–47, 50, 52, 53, 55, 57, 63, 64, 66, 67, 69, 77, 90, 93, 99, 101, 106, 109, 111, 112, 128–130, 133, 150, 155, 158, 160–162, 166, 167, 183, 184, 190

**CMB-S4** Cosmic Microwave Background Stage 4. 93, 159, 161, 163

**CMF** constrained matched filter. 106, 108, 109, 111, 114–118, 120–124, 166, 167, 195–201

**CMMF** constrained matched multifilter. 110, 111, 116–119, 121–123, 166, 167, 196–198

**COBE** Cosmic Background Explorer. 13, 14, 16, 46, 93

**COBRAS** Cosmic Background Radiation Anisotropy Satellite. 45, 46

**ComPRASS** Combined Planck-RASS catalogue of X-ray–SZ sources. 144

**COrE** Cosmic ORigins Explorer. 89, 93, 159, 160

**DM** dark matter. 32

**DMR** Differential Microwave Radiometer. 16

**DSA** diffusive shock acceleration. 28

**EdS** Einstein–de Sitter. 22, 36

**EOS** equation of state. 4, 6, 8

**eROSITA** extended ROentgen Survey with an Imaging Telescope Array. 64, 106, 114, 115, 120–123, 126, 154, 159, 163, 166, 167, 200–202

**ESA** European Space Agency. 45

**ESO** European Southern Observatory. 50

**FIR** far-infrarred. 49, 65, 67, 68, 70, 74, 76, 78–81, 84–88, 90–93, 96, 118, 128–130, 133, 140, 142, 149, 152, 154–156, 161, 165–167, 204, 219, 221, 223–225

**FIRAS** Differential Microwave Radiometer. 14, 16, 93

**FLRW** Friedmann–Lemaître–Robertson–Walkerr. 1, 7

**FWHM** full width at half maximum. 55, 56, 69, 72, 79, 94, 109, 114–117, 122, 128, 131, 148, 183

**GNFW** generalised Navarro-Frenk-White. 34, 40, 78, 80, 112, 114, 117, 131, 134, 136, 186, 187, 199

**HFI** (*Planck*) High Frequency Instrument. 2, 46, 47, 52, 54–56, 69, 72, 75, 79, 96, 111, 116–119, 123, 127, 128, 142, 145, 149–153, 155, 157, 196–199, 207, 219–221

**HL-LHC** High-Luminosity Large Hadron Collider. 5

**HMF** halo mass function. 23, 25, 26, 35, 203

**ICM** intracluster medium. 27, 28, 30–33, 35, 37–39, 42–44, 48, 63, 66–68, 89, 90, 94, 97, 104, 111, 112, 117, 122, 127, 133, 134, 149, 150, 152–155, 159, 162, 163, 165, 167, 185–187, 203, 206, 223

**IDL** Interactive data language. 54, 68, 150

**ILC** internal linear combination. 2, 50–57, 63, 82, 83, 89, 99–102, 106, 108, 117–119, 162, 189, 196–200

**IRAS** Infrared Astronomical Satellite. 65, 69, 70, 72, 77–79, 84, 85, 87, 88, 96–98, 112, 129, 130, 150, 162, 165

**IRIS** Improved Reprocessing of the IRAS Survey. 69, 70, 79, 97

**ISM** interstellar medium. 30, 68, 78

**KID** kinetic inductance detector. 48

**kSZ** kinetic Sunyaev–Zeldovich (effect). 38, 40–44, 63, 66, 67, 71, 78, 82, 93–96, 106, 111, 122, 123, 129, 131, 133, 140, 142, 151–153, 162, 165, 167, 168, 204, 219, 221, 222

**l.o.s.** line of sight. 38–43, 112, 131, 134, 136, 151–154, 156, 162, 185–187, 204, 219, 220, 222, 225

**LFI** (*Planck*) Low Frequency Instrument. 46, 47, 69, 127

**LSS** last scattering surface. 13

**MACHO** massive compact halo object. 5

**MACS** Massive Cluster Survey. 43

**MBB** modified blackbody. 129, 165

**MCMC** Markov-Chain Monte Carlo. 58–61, 76, 81, 87, 88, 140, 166

**MCXC** Meta-Catalog of X-Ray Detected Clusters of Galaxies. 89

**MF** matched filter. 105–109, 111, 114–118, 120–124, 133, 140–143, 150, 166, 167, 193, 195–201, 203, 220

**MILCA** Modified Internal Linear Combination. 57, 101, 117, 197

**MMF** matched multifilter. 105, 106, 109, 110, 116–118, 122, 123, 128, 133, 135, 136, 141, 143, 145, 160, 166, 186, 196–198

**MOND** Modified Newtonian Dynamics. 5

**MSIP** Mid-Scale Innovations Program. 132, 135

**NFW** Navarro-Frenk-White. 23, 33, 184, 185

**NGC** New General Catalogue. 116

**NILC** Needlet Internal Linear Combination. 57, 101, 117, 197

**NSF** National Science Foundation. 49

**ntSZ** non-thermal Sunyaev–Zeldovich (effect). 38, 42, 43

**NVSS** NRAO VLA Sky Survey. 112–114, 129, 130, 162

**PICO** Probe of Inflation and Cosmic Origins. 159–161, 168

**PIXIE** Primordial Inflation Explorer. 93

**PRISM** Polarized Radiation Imaging and Spectroscopy Mission. 159, 160, 168

**PS** point source. 129

**PSF** point spread function. 33, 64, 115, 120, 123, 187, 200

**PySM** Python sky model. 112, 129, 130, 162

**pSZ** polarised Sunyaev–Zeldovich (effect). 43

**PWV** precipitable water vapour. 48, 126

**QSO** quasi-stellar objects. 97

**RASS** ROSAT all-sky survey. 144

**redMaPPer** red-sequence Matched-filter Probabilistic Percolation (cluster finding algorithmn). 144

**ROSAT** Röntgensatellit. 123

**rSZ** relativistic Sunyaev–Zeldovich (effect). 66, 85, 111, 123

**SAMBA** Satellite for Measurement of Background Anisotropies. 45, 46

**SDSS** Sloan Digital Sky Survey. 17, 30, 144

**SED** spectral energy distribution. 12, 16, 17, 38, 47, 50–54, 77, 78, 84, 85, 90, 91, 111, 112, 117–119, 123, 129, 130, 133, 142, 149, 150, 152, 165, 189, 196–198, 200

**SILC** Scale-Discretised Internal Linear Combination. 57

**SMBH** supermassive black hole. 23

**SNR** signal-to-noise ratio. 53, 106, 108, 118–121, 123, 128, 131, 133, 135–138, 141, 143–147, 150, 165, 166, 188, 193, 194, 196–198, 200, 203, 204, 206, 209–217, 220

**SO** Simons Observatory. 64, 126, 130, 148, 159, 160, 162, 167

**SPH** smooth particle hydrodynamical. 103

**SPIRE** Spectral and Photometric Image Receiver. 67

**SPT** South Pole Telescope. 34, 43, 63, 71, 106, 110, 122, 125, 126, 128, 132, 142–147, 149, 155, 157, 158, 160, 162, 163, 166, 167, 188, 203, 208

**SPT-3G** South Pole Telescope third-generation (receiver). 126, 159, 167

**SZ** Sunyaev–Zeldovich (effect). 32–35, 37–40, 42, 43, 48, 53, 63–70, 78, 80, 82, 89, 92–97, 101, 104, 106, 107, 111, 117, 121–123, 125–128, 131–133, 137, 140, 142–149, 152, 154–158, 160–163, 165–168, 187, 188, 196, 200, 203, 208, 222–225

**TES** transition edge sensor. 48, 126

**tSZ** thermal Sunyaev–Zeldovich (effect). 38–44, 46, 50, 52, 53, 63, 65–74, 78–85, 87–90, 92–94, 96–98, 100–102, 106, 108, 111, 114, 117–120, 122, 126, 127, 129, 131, 133, 141, 142, 148, 149, 152, 153, 157, 161–163, 165–168, 185–189, 197, 199, 200, 203, 204, 219, 221, 222

**UPP** universal pressure profile. 33, 131, 136, 185, 187

**UV** ultraviolet. 13, 17, 30

**WIMP** weakly interacting massive particle. 5, 20

**WMAP** Wilkinson Microwave Anisotropy Probe. 16, 46, 50, 129, 190

# Acknowledgements

I would like to thank my supervisor Frank Bertoldi for providing me with the opportunity to join his research group as a doctoral student. I am grateful for his support of my work over the past five years and for the chance of pursuing my own research interests during that time. I also thank my secondary supervisor Thomas Reiprich for his engagement during my studies.

The research I conducted would not have been possible without the supervision and guidance of my advisor Kaustuv Basu, who contributed countless ideas and helped me to become a scientist.

I am grateful to my collaborator Jens Chluba for his help in analyzing and interpreting the SZ spectrum of *Planck* clusters. I furthermore would like to thank Mathieu Remazeilles and Jean-Baptiste Melin, whose work on ILC techniques and matched filters form the very foundation of my own research, for helpful advice and discussions.

I gratefully acknowledge the support I have received from the BCGS through an H2 scholarship and travel allowances, both of which aided my research and personal development. I am equally thankful for the support through the IMPRS, which allowed me to participate in workshops and conferences across Europe and in the United States. Being a member of these two graduate schools gave me the opportunity to meet and connect to people from all across the planet, which was the most enriching experience during my time as a doctoral student.

I am in dept to our secretary Christina Stein-Schmitz, who helped me on many occasions with various paperwork and who always stands up for me and the other students.

Special thanks goes to my office mates and friends Kevin Harrington, Eric Faustino Jiménez-Andrade, and Ana Paola Mikler Celis for the many helpful discussions, entertaining lunch breaks and activities such as our infamous all-day hikes. I wouldn't have shared my office with anyone other than you.

A valuable part of my time as a doctoral student was the chance of participating in the supervision of the master students Vyoma Muralidhara, Rovina Pinto, and Devika Sharma, who I enjoyed working with and thank for their trust.

Working in the field of astronomy gave me the privilege of meeting and connecting to many diverse and brilliant people. Among them, I would like to especially thank Douglas Applegate, Katharina Borm, Maude Charmetant, Melani Hampel, Henning Hilmarsson, Behnam Javanmardi, Alexander Karim, Christos Karoumpis, Joseph Kuruvilla, Benjamin Magnelli, Aarti Nagarajan, Hans Nguyen, Prajwal Padmanabh, Fatimah Raihan, Miriam Ramos Ceja, Armin Rasekh, Gerrit Schellenberger, Basilio Solis Castillo, Pablo Torné, Sandra Unruh, Bharad Vijaysarathy, and Victoria Yankelevich for sharing their insights, the occasional beer, and for challenging me on the badminton court.

Ganz herzlich möchte ich auch meinen Eltern Bärbel und Herbert Erler, sowie meiner Schwester Ellen danken, welche mich stets unterstützt haben und mir immer mit Rat zur Seite standen.

I am not certain if I could have finished this work without the support of my girlfriend Katharina Bey, who through her love, patience, and many flat jokes helped me keep my sanity in difficult times and who taught me that the human body is able to run 170 km and climb 11 km in 50 hours. I am forever grateful to have you at my side during all these years, Kathi.

Finally, I was deeply touched by the passing of colleagues, friends, and family during my studies. I would like to conclude my acknowledgements in memory of Yu-Ying Zhang, Julia Hampel, and my grandmother Luzie Klinkhammer.